Continuum Mechanics Modelling of Corrugated Board

Nyman, Ulf

2004

Document Version:
Publisher's PDF, also known as Version of record

LUND UNIVERSITY

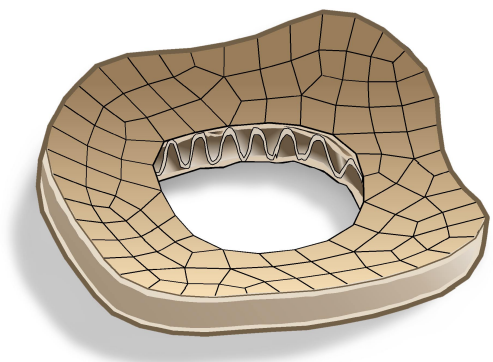

CONTINUUM MECHANICS MODELLING OF CORRUGATED BOARD

ULF NYMAN

Structural Mechanics

Doctoral Thesis

Structural Mechanics

ISRN LUTVDG/TVSM--04/1017--SE (1-215)
ISBN 91-628-6111-5 ISSN 0281-6679

CONTINUUM MECHANICS MODELLING OF CORRUGATED BOARD

Doctoral Thesis by

ULF NYMAN

Printed by KFS i Lund AB, Lund, Sweden, April 2004.

For information, address:
Division of Structural Mechanics, LTH, Lund University, Box 118, SE-221 00 Lund, Sweden.
Homepage: http://www.byggmek.lth.se

Till mamma, pappa och mina systrar

Preface

The work presented in this thesis was carried out at the Division of Structural Mechanics, Lund University. The project was performed in collaboration with the industrial partner SCA Packaging Research. Supplementary, the initial part of the project was a portion of a participating program with FPIRC, Forest Products Industry Research College. The economic support from Bo Rydins stiftelse för vetenskaplig forskning and the Foundation for Strategic Research (SSF), Forest Products Industry Research College is gratefully acknowledged.

Firstly, I would like to express my gratitude to Prof. Per Johan Gustafsson, for his support and open minded guidance of this work. He has a profound knowledge within the field of mechanics of materials and a particular scientific nerve. There is of course a multitude of colleagues at Structural Mechanics, who contributed in some way to the work. For example Mr. Thord Lundgren who provided electronic equipment for measurements and Mr. Bo Zadig who completed some illustrations, inter alia the front cover of the thesis. I am also grateful to the people at Asa Försökspark, especially Mr. Kjell Rosén who elaborately assisted the lifetime measurements. I would also like to thank Dr. Christer Nilsson for sharing valuable viewpoints within the field of continuum mechanics and Dr. Björn Johannesson for the discussions concerning modelling of mixtures.

Finally, I would like to thank my family for their impartial support and consideration during the course of this work.

Lund, May 2004

Ulf Nyman

Abstract

The aim of this work is to elaborate on methods relating to the simulation of lifetime of corrugated board boxes. The storage of compressive loaded boxes in an environment with naturally varying humidity is a practical issue in corrugated board employment. Time dependent variables such as moisture content, strain fields, stress fields and material strength play important roles for the time to failure. Supplementary, the stochastic nature of material and moisture load is obstructing the prediction of a reliable measure of lifetime. This work is composed of a number of portion proposals, each aiming on a method for a specific subproblem of the numerical modelling of time to failure.

Firstly, the focus is the problem of finite deformation hygro-elasticity. The assumption of kinematics is based on an additive split of the stretch in an elastic part and a non-elastic part. In time stepping sequences the elastic stretch is updated by the use of the total stretch from the polar decomposed deformation gradient. As a consequence, in the linearized virtual work equation appears a hygroscopic contribution to the stiffness matrix as well as a hygroscopic load vector. Particularly, a numerical procedure for analyzing layered shells is developed.

Further, a numerical method for the transient moisture flow in porous cellulosic materials like paper and wood is examined. The derivation of the model is based on mass conservation for a mixture containing a vapour phase and an adsorbed water phase embedded in a porous solid material. A model for the development of higher order sorption hysteresis is also developed. The model is capable of describing cyclic hardening as well as cyclic softening of the equilibrium water concentration. The model is verified by comparison with the measured response to natural variations in temperature and humidity. A close agreement of the simulated results to measured data is found.

The reliability of geometrically non-linear composite shells is studied by use of the First Order Reliability Method (FORM). A finite difference method is employed in order to find the gradients of the limit state function. A failure stress criterion for corrugated board facings is also proposed. The failure criterion is based on material failure and structural local buckling failure. The structural failure stress is evaluated using a novel analytical solution for the buckling of long orthotropic plates under combined in-plane loading. The failure stress is compared with collapse experiments on corrugated board cylinders and the failure stress presented herein is seen to be in significantly better agreement with the measured stresses than the Tsai-Wu failure criterion alone.

Alongside with the numerical predictive methods, a number of testing procedures on individual paper materials and corrugated board boxes are performed. Firstly, mechanical second order stochastic field parameters of liner and fluting materials are estimated for a variety of materials used for commercial boards. Secondly, reliability testing of corrugated board boxes in a natural dynamic humidity environment is performed. A large number of boxes are loaded with a constant compressive force in an untempered airy indoor climate. Contemporary with the record of time to failures, the moisture transport in individual paper sheets and a sealed corrugated board box is measured.

Keywords: corrugated board, hygro-elasticity, sorption hysteresis, moisture transport, reliability, lifetime, failure criterion, assumed natural strain shell

Contents

1 Background

The origin of corrugated board dates back to the beginning of the 20:th century. Though manufacturing of board first took place around the turn of the century extended use remained to the mid century, due to lack of experience in packaging with the new material. The need for transporting necessities of life during the wartime -39 to -45 hastened the usage of rationally produced packaging materials. Today it is the prevailing material used for transport packaging of consumer goods, see Figure 1. The growth of corrugated board usage is mainly owing to its low price in relation to board stiffness and strength [1]. In fact, not including economic effects the relative stiffness and strength to weight is higher than most materials.

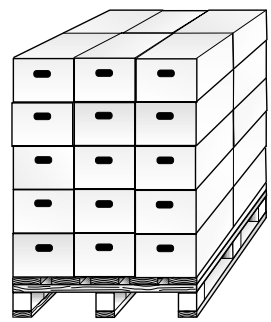

Figure 1: Stack of corrugated board boxes.

Having in mind the widespread popularity of the material, nevertheless, engineering use of the material is a complex task. Among the essential unfavourable properties of corrugated board is the definite sensitivity to exposure of moisture. Therefore, the performance of a box in a naturally varying climate accommodates to a large extent uncertainties. Also, duration of load effects such as material damage growth and creep play important roles in the use of paper materials. Supplementary, the subtle and unappraisable mechanical load environment of packages, e.g. mishandling and stacking on irregular support, is generally hard to define in engineering measures.

Traditionally, the design of corrugated board packages, in terms of material strength and box load resistance, is devoted to empirical research and relatively simple models. One example of an empirical result is the formula for box compression strength proposed by Maltenfort [2], which is derived from statistical test data of box compression strength. Another extensively used empirical design formula is the one proposed by McKee [3].

For a package to endure the complete chain of load events and climate conditions during a distribution cycle, the engineering design is obliged to incorporate the effect of strength reduction of such events. In the packaging industry it is customary to accomplish this by the entry of correction factors in the determination of a specifically required box strength. The procedure is to define a referential box strength at ideal load and climate conditions. For example, a pertinent referential box strength is the short term ultimate compression load at 50% relative humidity. Each deviating condition from the ideal load condition is then assigned an individual load correction factor. Commonly, correction

is introduced for long term loading, eccentric loading due to misalignment in stacking, moisture induced reduction of strength and rough handling or dynamic loading. As an example, consider a corrugated board box to be stored in 4 weeks in 90% relative humidity. The individual correction factors are 1.7 and 2.6. Furthermore, an interlocking stacking pattern is used and during piling up the boxes a dynamic loading is introduced. The equivalent individual correction factors are 1.5 and 1.3, respectively, see [4]. If strict independence between the individual correction factors is assumed and the content in the box carries no load, this implies that the referential load of the box is $1.7 \times 2.6 \times 1.5 \times 1.3 = 8.6$ times greater than the actual compressive loading at storing, i.e. the box must be designed to carry a load which is 8.6 times greater than the actual load. If safety against failure is desired an additional correction is needed. For a package weight of x kilogram, each unit of excessive correction factor quantitatively implies an increase of superfluous material of the same amount, x kilogram. The analogous economic sequel is obvious.

2 Continuum mechanics properties of paper and board

At a micro-scale level paper materials consists of randomly plane-oriented wood fibers. The distribution function of the direction of fibers is a polar function of the angle of deviation from the machine direction (MD). Typically, this two-dimensional distribution function has maximum at zero angle, MD, and minimum at the perpendicular angle, cross direction (CD). At a macro-scale continuum level a general assumption is that three mutually orthogonal planes of elastic symmetry exist, i.e. orthotropic symmetry. Under ideal manufacturing conditions the symmetry planes are co-linear with MD, CD and the transverse direction (ZD). Properties of the random fiber network that will influence the elastic continuum properties are individual fiber properties, fiber to fiber bonding strength and the fiber distribution function. Due to the randomness in distribution and connectivity of fibers the material will exhibit varying stiffness and strength properties in the sheet plane. A basic assumption on the joint probability density function is homogeneity and isotropy, i.e. rotational invariance. This means that the joint probability density function between different material points will only depend on the relative distance between the points and not on the absolute locations.

In a short term perspective and provided that the strains are moderately large paper appear as an elastic material. In view of the discussed structure of the fibers paper can for this limited case properly be modelled as an orthotropic elastic material. An important observation is that the transverse normal and shear elastic properties deviate substantially from the in-plane elastic properties. Particularly, consideration to this is crucial in numerical continuum models for the determination of deformations and strength of shell structures. Under extended strains paper will exhibit non-linear plastic deformation. The typical form of the complete load versus deformation curve, from compressive fracture to tensile fracture, is S-shaped. In the forthcoming numerical modelling in this work the load levels in the material prior to collapse are assumed to be analogous to linear elastic strains only.

In a long term perspective paper display dissipative and non-recoverable properties.

As an example, under a prescribed load the material will suffer from considerable visco-elastic/plastic creep and damage growth during time. The dissipative release rate will to a large extent vary with moisture content as given within normal natural relative humidity levels. A well known effect is that an altering humidity environment will accelerate the dissipative effects in the material, though the absolute cycle humidity levels are less than a specific constant level of humidity. This is termed the mechanosorptive effect. It is also known that the rate of change of humidity is of small importance compared to the number of humidity cycles.

So far, the inquest has been devoted to the individual material layers of corrugated board only. The bending stiffness and strength of corrugated board is, due to the oriented properties of the individual layers, obviously oriented. However, the corrugated structure of the medium layer additionally contribute to orientation of the board bending properties. Under in-plane loading of board panels, with customary side length to thickness ratios, the initial global buckling load provide a conservative measure of ultimate load. Commonly, the panel will sustain considerably larger load levels than the initial buckling load. When the limit load is reached material creases will develop on the concave side of the panel. However, in the immediate precedence to crease development local buckling of the liner is observed. Accordingly, the detailed load deformation relation is exceedingly complex, involving a large number of possible bifurcation branches.

The numerical modelling of corrugated board and boxes comprises the formulation of structural finite elements in terms of plates or shells. In practical situations it is plausible to use a laminate shell element in which the corrugated core is replaced by equivalent homogenized stiffness properties. A thorough investigation and development of equivalent stiffness properties can be found in [5].

3 Previous contributions on corrugated board

The traditional design of corrugated board boxes is based on empirical research and relatively simple models for load resistance. Quantitatively, empirical measures of bending stiffnesses is used together with the box perimeter to predict the top to bottom ultimate compressive load. One example of an empirical result is the formula for box compression strength proposed by Maltenfort [2], which is derived from statistical data from tests of box compression strength. Another example is the design formula presented by McKee [3]. Of later decades the finite element technique has become the prevailing method for the evaluation of deformation and stress fields, facilitating work on more fundamental and rational methods for strength analysis. Studies of the strength of corrugated board based on structural analysis has been performed by Patel [6], who both numerically and experimentally examined the biaxial strength. It was found that the failure of the board is influenced by local instability of the facings and a strength analysis based solely on material failure therefore is a conservative measure of the ultimate strength. The prolonged exploration of finite element methods for strength analysis was presented by Nordstrand [7], who inter alia formulated a finite element procedure utilizing homogenized section properties of the board.

The strength of corrugated board due to localized buckling was previously also studied

by Johnson and Urbanik [8]. In the work, a non-linear finite element method was used to examine the instability. Furthermore, Johnson and Urbanik [9] developed a non-linear elastic plate theory with the application to paper bending properties.

4 Contributions in this work

The overarching object of this work is to elaborate on methods for the prediction of lifetime of corrugated board boxes. The storage of compressive loaded boxes in a naturally varying surrounding humidity environment is a practical issue in corrugated board employment. Time dependent variables such as moisture content, strain fields, stress fields and material strength play important roles for the time to failure. In addition, the stochastic nature of material and moisture load is obstructing the prediction of a reliable measure of lifetime. This work is composed of a number of portion proposals, each aiming on a method for a specific subproblem of the numerical modelling of time to failure. In the following is rendered the contributions in the form of scientific publications.

In Paper I a class of problems of finite deformation hygro-elasticity is examined. The kinematics of contemporary non-elastic swelling and elastic deformations is considered and a framework for the construction of finite elements is established. Particularly, a numerical procedure for analyzing layered shells is developed. In the Lagrangian frame the stretch is additively split up in an elastic part and a non-elastic part. In time stepping sequences the elastic stretch is updated by the use of the total stretch from the polar decomposed deformation gradient. As a consequence, in the linearized virtual work equation appear a hygroscopic contribution to the stiffness matrix as well as a hygroscopic load vector. The methodology derived here applies equally well for thermo-elastic problems provided that the elastic deformation is independent of an altered temperature. Some numerical finite deformation examples are provided to demonstrate the performance of the method. In addition, a reference boundary value solution of the hygroscopic elastica, for the case of constant and linearly varying through-the-thickness swelling, is derived.

In Paper II a numerical method for the transient moisture flow in porous cellulosic materials like paper and wood is proposed. The derivation of the model is based on mass conservation for a mixture containing a vapour phase and an adsorbed water phase embedded in a porous solid material. The principle of virtual moisture concentrations in conjunction with a consistent linearization procedure is used to produce the iterative finite element equations. A monolithic solution strategy is chosen in order to solve the coupled non-symmetric equation system. A model for the development of higher order sorption hysteresis is also developed. The model is capable of describing cyclic hardening as well as cyclic softening of the equilibrium water concentration. The model is verified by comparison with the measured response to natural variations in temperature and humidity. A close agreement of the simulated results to measured data is found.

In Paper III a finite element procedure for the reliability of geometrically non-linear composite shells is presented. The formulation and implementation of the finite element procedure is described as well as the finite difference method in order to find the gradients of the limit state function. Numerical examples are performed on an in-plane loaded corrugated board panel involving uncertainties in geometrical imperfection, material properties

and load.

In Paper IV the problem of buckling of long orthotropic plates under combined in-plane loading is considered. An approximate analytical solution is presented. The concept of a mixed Rayleigh-Ritz method is used considering higher-order shear deformations. The achieved load function of the half buckling wavelength and the inclination of the nodal lines is minimized via a simplex search method. For low transverse shear stiffnesses the model predicts buckling coefficients under in-plane shear load that are of the same order of magnitude as those resulting from a uniaxial compressive load. For a thin plate the critical shear load is larger by 42% compared to the uniaxial case. The model also suggests that for highly anisotropic materials, such as paper, the critical load solution is still influenced by the shear deformation effect at width-to-thickness ratios above 100.

In Paper V the local buckling of corrugated board facings is studied numerically through finite element calculations. The analytical solution developed in Paper IV is compared with the numerical solution. The facings are modeled as infinite orthotropic plates, resting on parallel free supports and subjected to an arbitrary in-plane stress state. The deflection shape is defined by wave length and displacement of the periodic deflection pattern. In the finite element solution periodic boundary conditions are used on the repetitive cells studied. Transverse shear strain is considered by first (FEM) and higher order (analytical) shape functions. The results imply that the analytical solution of Paper IV is correct for the periodic deflection pattern of long plates.

In Paper VI a failure stress criterion for corrugated board facings is presented. The failure criterion is based on material failure and structural local buckling failure, which are evaluated in a combined analysis procedure. The failure stress is compared with collapse experiments on corrugated board cylinders and the failure stress presented herein is seen to be in significantly better agreement with the measured stresses than the Tsai-Wu failure criterion alone. The fluting wavelength of the corrugated board is also varied for the purpose of strength sensitivity analysis of corrugated board.

In Paper VII the reliability of corrugated board is studied by finite element Monte Carlo simulations and by a first order reliability method, with the use of a failure criterion that includes both material failure and structural failure. The stiffness and strength parameters of the board are given as scalar multipliers of a geometrically distributed stochastic field. For the case of pure bending stresses, it is concluded that the failure is almost completely governed by structural failure. It is also seen that the board is very sensitive to compressive stresses in the machine direction.

Alongside with the numerical predictive methods described is performed a number of testing procedures on individual paper materials and corrugated board boxes. Firstly, mechanical stochastic field parameters of liner and fluting materials are estimated for a variety of materials used for board lay-up. In conjunction with the estimation of stochastic parameters short term strength of corrugated board boxes according to standard test procedures are performed. The short term strength is used to verify box compression strength under ideal, i.e. controlled stationary climate conditions. In Appendix A the measurement procedures for stochastic parameters is outlined. The testing procedure for short term box strength is described in the section below concerning modelling of box strength with stationary environment conditions.

The principal part of test procedures is the measurement of time to failure of corru-

gated board boxes in a natural dynamic humidity environment. A large number of boxes are loaded with a constant compressive force in an untempered airy indoor climate. Along with the long term loading, the moisture transport in individual paper sheets and a sealed corrugated board box is recorded. In Appendix B the testing procedures for long term strength in naturally varying humidity is described.

In addition to long term measurements in varying climate measurements on time to failure of boxes in a controlled climate is performed. The purpose of this test procedure is to fit damage growth parameters for a number of constant humidity and load levels. The long term measurements in controlled climate are not brought to end as this work is written.

5 Modelling examples

In this section some examples of numerical modelling of strength and lifetime of corrugated board boxes is presented. The implemented computer code employs a unification of the methods proposed in the individual papers. In a first subsequence of the code the incremental moisture content is determined according to the procedure described in Paper II, for the case of varying relative humidity. In a second subsequence the deformation and stress fields are determined using the shell finite element developed for hygro-elastic problems in Paper I. In a final subsequence, the onset of material failure and localized buckling failure is evaluated using the combined failure threshold presented in Paper VI. Reliability analysis and damage growth are not considered in the examples.

5.1 Stationary environment conditions

The short term strength of corrugated board boxes subject to stationary temperature and humidity is examined for six types of boxes. The box compression strength is experimentally determined from a standard test procedure where the box is compressed between two rigid plates. The rate of relative movement of the plates is 10 mm/s and the climate conditions are 23°C and 50% relative humidity. The types of boxes and boards included in the test procedure is listed in Tables 1 and 2. In Table 1 the mean values and coefficients of variation of the measured compression strength are also listed. The stiffness and strength properties equivalent with the materials in Table 2 can be found in Appendix A. An effective stiffness of the medium layers is obtained by multiplying the paper modulus with $\gamma t_2/h_2$, where γ is the ratio of the corrugated wave intrinsic length to the wavelength. Moreover t_2 and h_2 is the paper and core thickness, respectively. The values of core thickness and wavelength of corrugations are 3.68 mm and 7.77 mm for the C flute boards and 2.0 mm and 6.49 mm for the B flute board, respectivley. The stiffness of the core in the direction along the corrugations is assigned a very small value.

Considering the symmetry of the geometry and load conditions one eighth of the boxes is used in the finite element model, excluding the top flaps. It is noted that this implies an enforcement of the lowest buckling mode of the panels. The two panels are divided in an uniform element mesh, see Figure 2.

The translational degrees of freedom at the junction edges of the two flat portions are

Table 1: Types of boxes.

Box type	Dimension, L×W×H [mm]	Board	Compr. strength [kN]	C.O.V.
1	400×400×400	171C	3.706	0.052
2	400×400×400	140C	2.120	0.036
3	500×300×400	171C	3.995	0.044
4	500×300×400	140C	2.520	0.050
5	300×300×300	162B	2.781	0.052

Table 2: Types of boards.

Board	Outer liner[a]	Fluting[a]	Inner liner[a]
SCA 171C	200WT	150HK	200KL
SCA 140C	150TL	112RF	150TL
SCA 162B	200WT	112HK	200WT

[a]Numbers indicate the grammage [g/m^2].

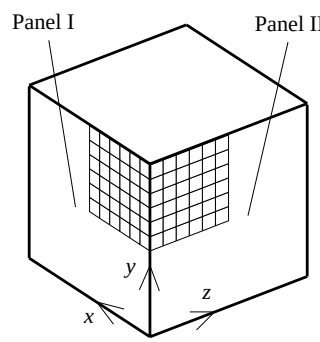

Figure 2: Element mesh.

rigidly connected using Lagrange multipliers while the rotational degrees of freedom are left free. In addition, the translations of the upper (loaded) edge are constrained to be equal in the vertical direction. In Figure 3a the convergence of the finite element mesh resolution is plotted. It is concluded that a six by six mesh for each flat portion is enough. As the failure load is not a linear function the size of the load increment will influence the evaluation of the failure threshold. From Figure 3b, where the normalized failure load with decreasing increment size is plotted, it can be concluded that ten load increments is sufficient.

To account for the eccentricity introduced by the weak creases of the board an edge moment is applied. The edge moment is applied to act on outwards deformation on the inner flap panel, denoted panel I in Figure 2, and inwards deformation on the outer flap

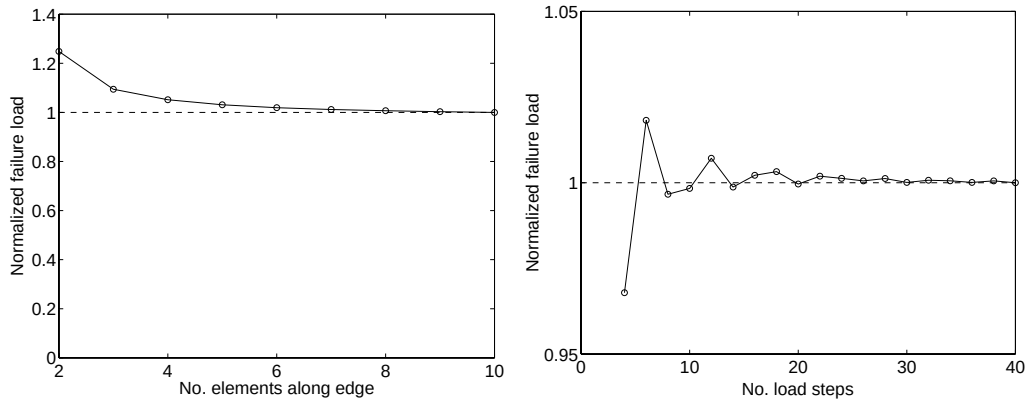

Figure 3: Convergence of a) element resolution and b) load increment size.

panel, denoted panel II in the figure. The value of the moment is given as equivalent to the offset of the edge load from the system line of the shell. The eccentricity value $0.2h$ is used throughout the examples, where h is the total thickness of the board.

In Figure 4 the simulated failure loads are compared with measured failure loads. The measured failure loads are presented as rectangular plots in which statistics are estimated from ten tested failure loads for each box type. The rectangles have lines at the lower quartile, median, and upper quartile values. The whiskers are lines extending from each end of the box to show the extent of the rest of the data. The simulated failure loads are presented as pentagrams. It is seen that for box types one to four the simulated failure load is reasonably close to the measured values. For box type 5 the present simulation over predicts the median value of the measured failure load by 20%.

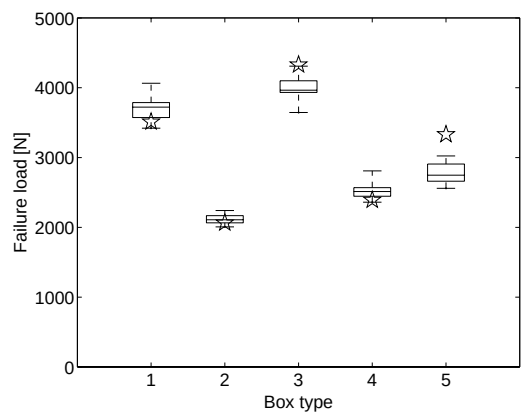

Figure 4: Failure loads for stationary environment conditions.

5.2 Dynamic environment conditions

The long term strength of corrugated board boxes subject to a dynamic temperature and humidity environment is examined for two types of boxes, 1 and 2, see the previous section. The lifetime of corrugated board boxes with a static compressive top load is also experimentally determined, see Appendix B. An identical finite element mesh and eccentricity load to the previous section is used for the hygro-elastic problem of the dynamic moisture load case. The moisture content and hygro-elastic deformations are calculated for two types of boxes and time variations of moisture load, experimental set 2a and 3a, see Appendix B. The beginning of the test period is February 15, 2000, for set 2a and May 8, 2000, for set 3a. An instantaneous failure threshold reduction due to moisture content is employed according to

$$S_f^R = {}^{\text{ref}}S_f^R(1 - \gamma \Delta c) \tag{1}$$

where S_f^R is the failure stress introduced in Paper VI and $\Delta c = c - c_{\text{ref}}$. The reference value of the moisture content, $c_{\text{ref}} = 0.06$, is the adsorption equilibrium value, i.e. the lower boundary sorption value, at 50% relative humidity, see Paper II. The reference failure stress, ${}^{\text{ref}}S_f^R$, is the prevailing value when the moisture content is $c = c_{\text{ref}}$, as determined by the measured strength parameters in Appendix A. The coefficient of strength reduction is $\gamma = 6.65$, see [10].

In each time increment, prior to the solution of the hygro-elastic deformations, the moisture content is determined according to the method described in Paper II. Five equispaced one-dimensional moisture flow elements are used for each of the three liner and fluting layers. The measured relative humidity outside the box is via a convective layer used as moisture load, whereas isolated conditions is assumed for the node on the inside surface of the box. As initial condition for the void moisture concentration the value equivalent with the relative humidity at the beginning of the test period is applied. The equilibrium boundary adsorption value corresponding to the initial relative humidity is used for the fiber moisture content. The material properties for the moisture flow problem can be found in Table 1 and Table 2 in Paper II. The measured thicknesses and densities of the inner liners, flutings and outer liners can be found in Appendix A. The hysteresis parameters $K_a = K_d = 3/4$ are used. The hygro-elastic stretch is assumed to be proportional to the deviation in moisture content from the initial value of moisture content, with the proportionality parameters $\alpha_{MD} = 0.039$ and $\alpha_{CD} = 0.117$, see [11].

In Figures 5a and 5b is plotted the moisture content at four node locations in the corrugated board, the outside surface of the box, the interface of the outer liner and the fluting, the interface of the inner liner and the fluting and the inside surface of the box. It is seen that the maximum relative difference in moisture content between the outside surface and the inside surface is approximately 0.01 for load case 2a and 0.015 for load case 3a.

In Figures 6a and 6b is plotted the deflections of the center points of the panels initially located in the xy-plane and the yz-plane, respectively. The deflections are defined to be positive when inwards directed. In the first incremental step the deflections are -0.3 and 0.3 mm for load case 2a and -0.8 and 0.7 mm for load case 3a, mainly caused by the applied top mechanical compressive load. In the subsequent increments the maximum

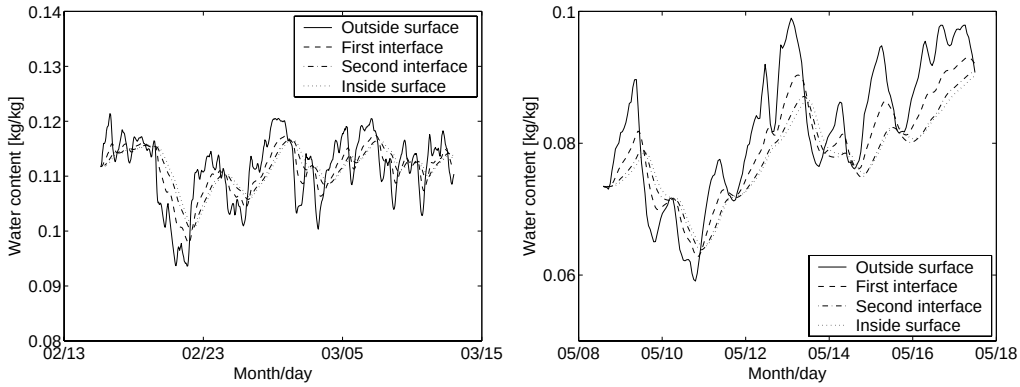

Figure 5: Moisture content for hygroscopic load case a) 2a and b) 3a.

peak to peak hygroscopic deflections are approximately 5 mm for load case 2a and 7 mm for load case 3a.

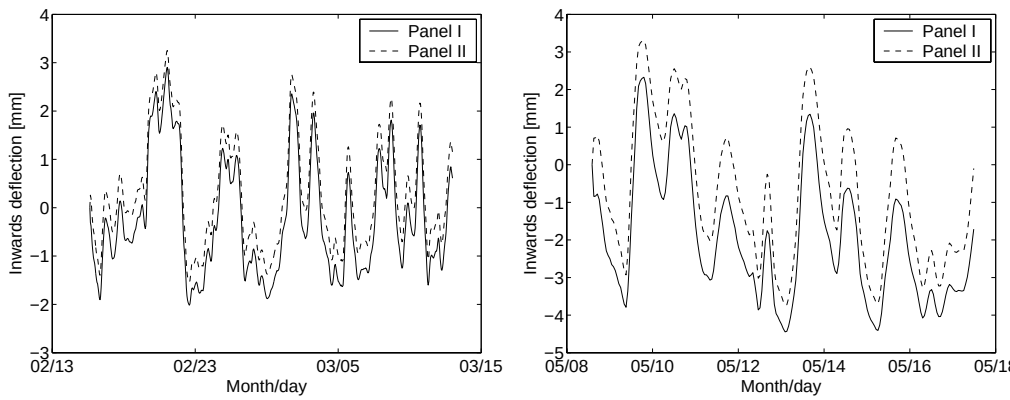

Figure 6: Deflections for hygroscopic load case a) 2a and b) 3a.

In Figures 7a to 8b the failure threshold index is plotted for the case of no reduction due to the moisture content level in the material. The evaluation points are the center points and center points of the upper edges of the panels, determined as mean values of two gauss points in the thickness direction of the inner layer and outer layer of the panels, respectively. It is seen that without reduction the peak to peak failure threshold is varying as a maximum between 0.05 and 0.13 at the center points and between 0.02 and 0.38 at the edge points for load case 2a and between 0.1 and 0.34 at the center points and between 0.08 and 0.6 at the edge points for load case 3a. Note that in the first incremental step the maximum failure threshold at the center points is 0.08 for load case 2a and 0.17 for load case 3a.

In Figures 9a to 10b the failure threshold index is plotted for the case of reduction due to the moisture content level in the material. It is seen that with reduction the failure

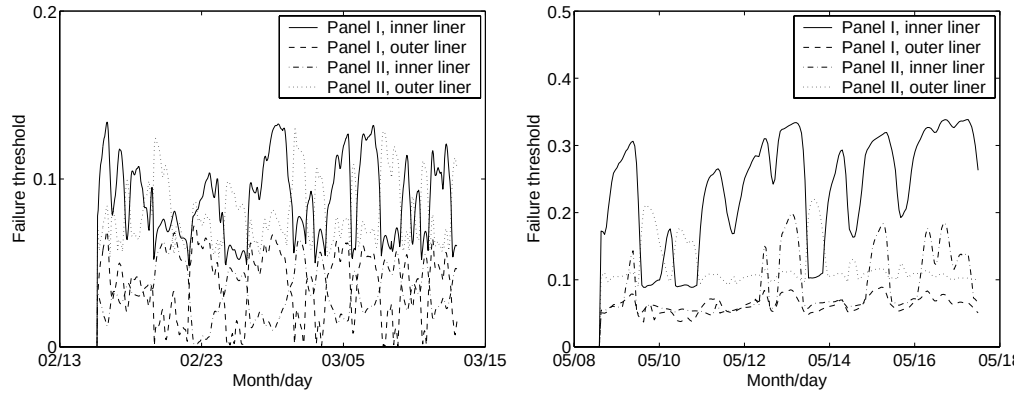

Figure 7: Failure threshold at center of panels for hygroscopic load case a) 2a and b) 3a.

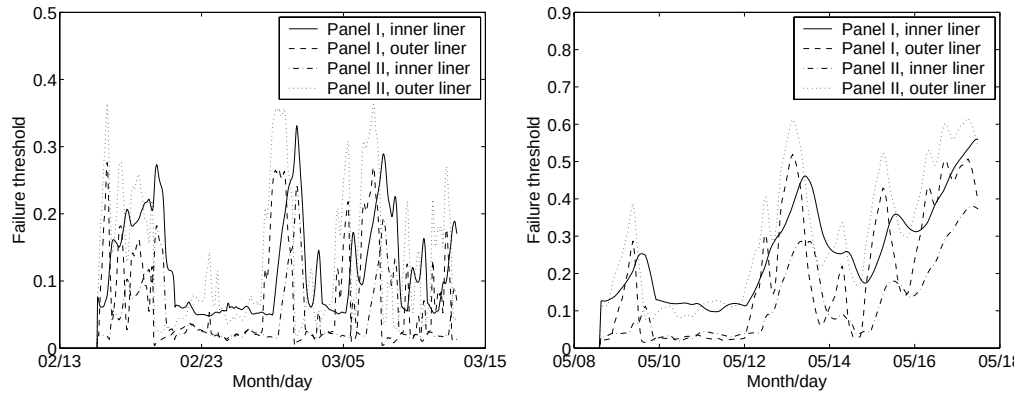

Figure 8: Failure threshold at upper edges of panels for hygroscopic load case a) 2a and b) 3a.

index is varying as a maximum between 0.07 and 0.21 at the center points and between 0.03 and 0.6 at the edge points for load case 2a and between 0.1 and 0.42 at the center points and between 0.08 and 0.8 at the edge points for load case 3a.

As a conclusion, the failure index is substantially influenced not only by the reduction of strength due to moisture content level, but also by the hygroscopic deformations caused by the variations in relative humidity.

6 Future work

A limitation in this work is the momentaneous evaluation of the failure threshold, i.e. damage growth is not considered in the predictive model. To this point, therefore, only a qualitative judgment can be made from the simulations whether a box is likely to fail or not, for example from the failure threshold curves shown in the previous section. A

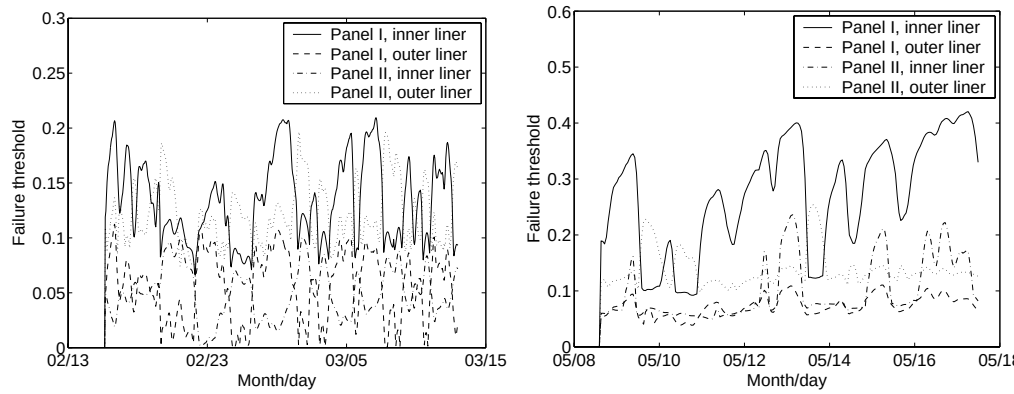

Figure 9: Failure threshold at center of panels for hygroscopic load case a) 2a and b) 3a.

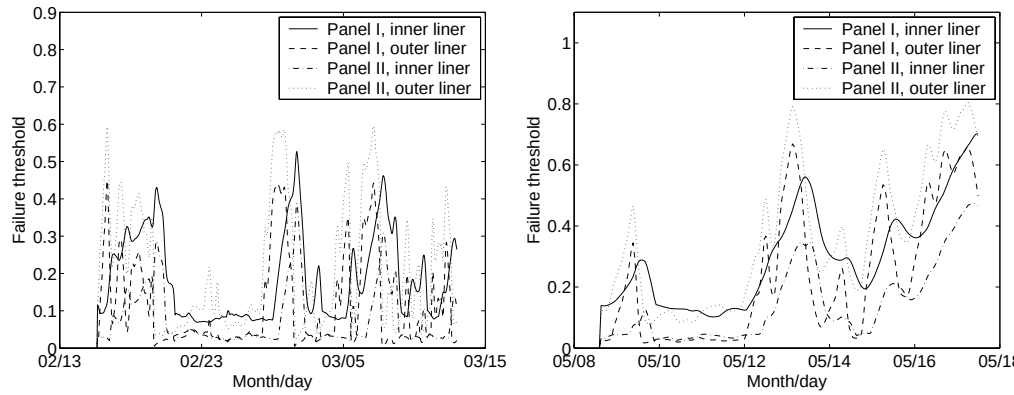

Figure 10: Failure threshold at upper edges of panels for hygroscopic load case a) 2a and b) 3a.

preliminary work towards considering the effect of damage growth has been initiated. Firstly, an introductory numerical model for integration of accumulated damage is developed. Secondly, long term measurements of box strength in controlled climate for the calibration of damage parameters are almost completed. Further measurements on time to failure should also be performed in a controlled fluctuating humidity environment, in order to consider the mechanosorptive effect.

The reliability analysis covered in this work determines the instantaneous probability of failures only, i.e. the probability of failure of short term loaded boxes. The practical case of long term loaded boxes in a naturally varying climate implies a time dependent (cumulative) probability of failure, influenced by the fluctuating humidity environment (time dependent stochastic process). It is envisaged that the extension of the reliability analysis to time integration of the probability of failure is a rather intricate problem.

Concerning the short term strength under ideal climate conditions, for some box types, there are deviations in simulated and measured compression strength. In a future work a

detailed experimental investigation of the deformations caused by a compressive top load will presumably clarify the discrepancies.

7 Concluding remarks

In this work is considered the modelling of long term strength of corrugated board boxes. Apart from traditional methodology for design and prediction of box strength the selected course is general methods adopting fundamental principles consistent with continuum mechanics. Concerning the numerical methods treated in this work novelty in predictive capability is introduced by the procedures for determination of the moisture content in naturally varying humidity environments, as well as the consideration of the effect of hygroscopic deformations on the long term strength. In addition, the failure threshold criterion accommodating both material failure and local buckling failure of the liner improves the predictive capability. Concerning the experimental methods the reliability/lifetime testing of a large number of simultaneously loaded boxes facilitates the qualitative engineering judgment of the long term strength.

In view of the discussed improvements, a detailed analysis of corrugated board boxes can be conducted. For example the influence on box strength of all practical material properties and dimensions, including parameters for moisture transport and moisture barriers, can be examined. This is not feasible in the employment of simple design formulas. In addition, in an extended reliability analysis the influence of variability of load and strength variables can be investigated. As pointed out earlier, however, further research on numerical methods for the modelling of time varying failure probability is crucial for the realization of a complete reliability model.

References

[1] Steenberg, B., Kubat, J., Martin-Löf, S., Rudström, L., (1970) *Competition in Rigid Packaging Materials*, Svensk papperstidning, 4, 77.

[2] Maltenfort, G. G., (1956) *Compression Strength of Corrugated Containers*, Fibre Containers, Vol. 41, No. 7.

[3] McKee, R. C., Cander, J. W., Wachuta, J. R., (1963) *Compression Strength Formula for Corrugated boxes*, Paperboard Packaging, 48, 149-159.

[4] Jönsson, G., (1999) *Corrugated Board Packaging*, Second edition.

[5] Nordstrand, T., Carlsson, L. A., and Allen, H. G., (1994) *Transverse Shear Stiffness of Structural Core Sandwich*, Composite Structures, **27**, pp 317-329.

[6] Patel, P., (1996) *Biaxial Failure of Corrugated Board*, Licentiate thesis, Dept. of Eng. Logistics, Lund University.

[7] Nordstrand, T., (2003) *Basic Testing and Strength Design of Corrugated Board and Containers*, TVSM 1015, Doctoral thesis, Lund University, Sweden

[8] Johnson, M. W. and Urbanik, T. J., (1989) *Analysis of the Localized Buckling in Composite Plate Structures with application to Determining the Strength of Corrugated Fiberboard*, J. of Composites Technology and Research, Vol. 11, No. 4, pp. 121-127.

[9] Johnson, M. W. and Urbanik, T. J., (1984) *A Nonlinear Theory for Elastic Plates With Application to Characterizing Paper Properties*, J. of Applied Mechanics, Vol. 51, pp 146-152.

[10] Norman, B. et. al., (1992) *Pappersteknik*, KTH, Stockholm.

[11] Niskanen, K. J., Kuskowski, S. J. and Bronkhorst, C. A., (1997) *Dynamic hygroexpansion of paperboards*, Nordic Pulp and Paper Res. Jou., Vol. 12, pp 103-110.

Paper I

Finite Deformation Hygro-Elasticity of Shells

Ulf Nyman

Submitted to International Journal for Numerical Methods in Engineering

FINITE DEFORMATION HYGRO-ELASTICITY OF SHELLS

Ulf Nyman[1]

ABSTRACT: A class of problems of finite deformation hygro-elasticity is investigated. The kinematics of contemporary non-elastic swelling and elastic deformations is considered and a framework for the construction of finite elements is established. Particularly, a numerical procedure for analyzing layered shells is developed.

In the Lagrangian frame the stretch is additively split up in an elastic part and a non-elastic part. In time stepping sequences the elastic stretch is updated by the use of the total stretch from the polar decomposed deformation gradient. As a consequence, in the linearized virtual work equation appear a hygroscopic contribution to the stiffness matrix as well as a hygroscopic load vector. The methodology derived here applies equally well for thermo-elastic problems provided that the elastic deformation is independent of an altered temperature.

Some numerical finite deformation examples are provided to demonstrate the performance of the method. In addition, a reference boundary value solution of the hygroscopic elastica, for the case of constant and linearly varying through-the-thickness swelling, is derived.

Introduction

Modelling of materials undergoing swelling due to either an increase in moisture or a temperature rise forms a well posed problem. The deformation of shells subjected to external mechanical loads accompanied by a volumetric increase of volume is the focus of this work. Specifically, the primary purpose is to develop a numerical methodology for the problem of buckling of layered shells exposed to variations in surrounding humidity. Inherently, the methods proposed here also hold for the modelling of thermoelastic buckling of shells.

During the past decades the effort of finding a shell quadrilateral element formulation which is general and robust has escalated and a large number of element procedures have been presented. It is well known that fully integrated elements exhibit shear locking as the shell thickness reaches the thin limit. To overcome this many techniques have been proposed that exploit various kinds of reduced integration. In the most trivial case the element is uniformly underintegrated with one gauss point over the shell plane. This, however, leads to severe spurious modes due to rank deficiency of the stiffness matrix. The number of spurious modes can be reduced by utilizing selective underintegration of the transverse shear terms, see for example [1]. An attractive course of line is to enable vanishing of transverse shear stress by interpolating the corresponding shear strains with a priori chosen sampling points, as proposed in [2, 3]. This method, the Assumed Natural Strain method (ANS), is used for the shell element formulation in the present work.

[1]Division of Structural Mechanics, Lund University, PO Box 118, S-221 00 Lund, Sweden

The concept of a multiplicative decomposition of the deformation gradient into an elastic part and a non-elastic part was introduced in [4] and specifically addressed to the modelling of elasto-plastic materials. Using this approach the elastic deformation of the material is referred to an intermediate configuration. Therefore, the elastic stretch of a material fiber is not independent of a purely non-elastic deformation though a purely elastic deformation does not alter the non-elastic stretch of the fiber. A second approach is to decompose the deformation gradient additively, which implies that the same reference (initial) configuration is used both for the elastic and non-elastic deformation. As a consequence, the only dependence between the elastic and non-elastic stretch is imposed by external kinematic constraints. This approach was first introduced in [5]. Unfortunately the total stretch is related to the elastic stretch and non-elastic stretch by a material rotation, an implication which is not either unambiguous. A third approach is to decompose the material stretch additively, as introduced in [6, 7]. This implies that the elastic and non-elastic stretch are independent variables and that strain measures can be established which are independent of material rotations. The latter approach will be followed here for the implementation of a numerical procedure for non-elastic swelling of materials.

The apparent resemblance of hygro-elasticity with a restricted type of thermo-elasticity draws the attention to published papers within the latter field. As a matter of fact, a remarkably low number of works are found within this field. In [8] postbuckling of composite laminates under compressive load and temperature is analyzed. A triangular element is used together with a procedure for integration of nodal forces for the case of constantly or linearly varying temperatures over the shell thickness. In [9] the von Kármán-type of non-linear strains is used for the thermo-mechanical stability analysis of plates. Interestingly, an arc-length method is prominently introduced for the solution of the non-linear equations.

Elaborately, a more formal approach to the modelling of hygro/thermal-elasticity at finite deformations is developed. The versatility of the approach used here is particularly obvious as the inherent description of kinematics allows for an arbitrary variation of non-elastic stretch over the shell thickness. In addition, the extension to the use of non-linear relations between stress and elastic strain is quite amenable since an explicit expression for the stress in terms of total and hygroscopic stretch is derived.

The following disposition of the paper is used. In the second section the kinematic relations pertinent to hygro-elastic problems are established. A finite deformation elastic strain measure is also introduced. The third and fourth section are devoted to balance principles and linearization, respectively. In the fifth section the continuum mechanics equations are formulated in terms of finite element matrices for a layered shell. Finally, in the sixth section some numerical examples show the performance of the derived theory. As an introductory of this section a reference boundary value solution of the hygroscopic elastica, for the case of constant and linearly varying through-the-thickness swelling, is derived.

Decomposition of kinematic variables and measures of strain

Let an initial state $\mathcal{C}_0$, of a body $\mathcal{B} \in \mathbb{R}^3$, denote the reference configuration of the body. The reference configuration is understood to be a state of zero stress and deformation. Let also particles in $\mathcal{C}_0$ be denoted by the position vector $\mathbf{X}$ and the neighborhood of $\mathbf{X}$ be denoted by $\mathcal{N}_0$. Then, the nonlinear map $\chi(\mathbf{X})$ transports $\mathbf{X}$ to $\mathbf{x}$ in the current configuration according to $\chi : \mathcal{C}_0 \rightarrow \mathcal{C} \in \mathbb{R}^3$. Furthermore, the linear map $\mathbf{F}(\mathbf{X}) = \text{Grad}\chi(\mathbf{X})$ transports a material line segment $\text{d}\mathbf{X} \in \mathcal{N}_0$ to a current line segment $\text{d}\mathbf{x} \in \mathcal{N}$. According to the polar decomposition theorem an invertible $\mathbf{F}$ can uniquely be represented by

$$\mathbf{F} = \mathbf{R}\mathbf{U}, \qquad \mathbf{U} = \sqrt{\mathbf{C}}, \qquad \mathbf{R} = \mathbf{F}\mathbf{U}^{-1} \tag{1}$$

where $\mathbf{R}$ is an orthogonal rotation tensor and $\mathbf{U}$ and $\mathbf{C}$ are positive definite symmetric tensors termed the right stretch tensor and the right Cauchy-Green strain tensor, respectively. The elements of $\mathbf{U}$ and $\mathbf{C}$ are Lagrangian measures, i.e. referring to $\mathcal{C}_0$. The spectral form of $\mathbf{U}$ is

$$\mathbf{U} = \sum_{i=1}^{3} \lambda_i \hat{\mathbf{N}}_i \otimes \hat{\mathbf{N}}_i \tag{2}$$

where λ_i and $\hat{\mathbf{N}}_i$ are the principal referential stretches and directions of $\mathbf{U}$, respectively.

Introducing now two imaginable and rotationally free configurations, $\mathcal{C}_e$ and $\mathcal{C}_h$, $\text{d}\mathbf{X}$ is transported to a third configuration $\mathcal{C}_U$, also free from material rotation, by the mapping function $\mathbf{U}(\mathbf{X})$ decomposed as,

$$\mathbf{U} = \mathbf{U}_e + \mathbf{U}_h - \mathbf{I} \tag{3}$$

see Figure 1. Here $\mathcal{C}_e$ is referred to as an elastic configuration and $\mathcal{C}_h$ is referred to as an hygroscopic and stress free configuration. It is noted that for a deformation the principal stretches are given by

$$\lambda_i = \lambda_i^e + \lambda_i^h - 1 = \frac{l_i^e}{L} + \frac{l_i^h}{L} - 1 \tag{4}$$

in which l_i^e and l_i^h are deformed measures of length and L is the initial length, implying that the same reference configuration is referred to. It is here assumed that the hygroscopic deformation is purely dilatational, which implies that $\mathbf{U}_h$ is

$$\mathbf{U}_h = \sum_{i=1}^{3} \lambda_i^h \mathbf{e}_i \otimes \mathbf{e}_i \tag{5}$$

The Cauchy stress or true stress is defined over a spatial surface element and denoted by $\boldsymbol{\sigma}$. The nominal stress, $\mathbf{P}$, is found by using (1) and (3)

$$\mathbf{P} = J\boldsymbol{\sigma}\mathbf{F}^{-T} = J\boldsymbol{\sigma}\mathbf{R}(\mathbf{U}_e + \mathbf{U}_h - \mathbf{I})^{-1} \tag{6}$$

and the 2:nd Piola-Kirchhoff stress, $\mathbf{S}$, is given by

$$\mathbf{S} = J\mathbf{F}^{-1}\boldsymbol{\sigma}\mathbf{F}^{-T} = (\mathbf{U}_e + \mathbf{U}_h - \mathbf{I})^{-1}\mathbf{R}^T\mathbf{P} \tag{7}$$

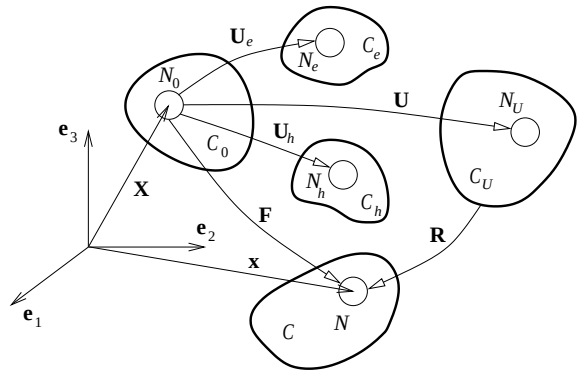

Figure 1: Different configurations in hygro-elasticity.

where $J = \det \mathbf{F} = \det(\mathbf{U}_e + \mathbf{U}_h - \mathbf{I})$.

At this point it is essential two form a measure of strain that comprises the foundation of kinematics established in (3). Since the purpose is to develop a numerical procedure in which all the variables refer to $\mathcal{C}_0$, it is natural to adopt a Lagrangian strain measure. Also, even though the displacements are large in the structural analysis of shells, commonly, the strains are moderately large. As a suitable strain measure is the Green-Lagrange strain adopted. Firstly, from (3) it follows that the total right Cauchy-Green strain is given by

$$\mathbf{C} = \mathbf{F}^T\mathbf{F} = \mathbf{U}_e^2 + \mathbf{U}_h^2 + 2\,\mathrm{sym}(\mathbf{U}_e\mathbf{U}_h) - 2\,\mathbf{U}_e - 2\,\mathbf{U}_h + \mathbf{I} \tag{8}$$

and the total Green-Lagrange strain appears as

$$\mathbf{E} = \frac{1}{2}(\mathbf{C} - \mathbf{I}) = \frac{1}{2}\mathbf{U}_e^2 + \frac{1}{2}\mathbf{U}_h^2 + \mathrm{sym}(\mathbf{U}_e\mathbf{U}_h) - \mathbf{U}_e - \mathbf{U}_h \tag{9}$$

It is then advantageous to establish an elastic strain isolated from the presence of hygroscopic deformations. From

$$\mathbf{E}_e = \frac{1}{2}(\mathbf{U}_e^2 - \mathbf{I}) \tag{10}$$

and (3) it follows that the elastic strain is given by

$$\mathbf{E}_e = \frac{1}{2}(\mathbf{U}^2 - \mathbf{I}) + \frac{1}{2}\mathbf{U}_h^2 - \mathrm{sym}(\mathbf{U}\mathbf{U}_h) + \mathbf{U} - \mathbf{U}_h + \frac{1}{2}\mathbf{I} \tag{11}$$

where the term $\frac{1}{2}(\mathbf{U}^2 - \mathbf{I})$ contains the partial derivatives of total displacements in $\mathcal{B}$, $\mathrm{Grad}\,\mathbf{u}$.

Remark 1 *Define numbers b_i close to zero and let the principal stretches of $\mathbf{U}_e$ and $\mathbf{U}_h$ be denoted by λ_i^e and λ_i^h, $i = 1, 2, 3$. Then, from (9) it can be concluded that*

$$\lim_{\lambda_i^e, \lambda_i^h \to 1 + b_i} \mathbf{E} = \frac{1}{2}(\mathbf{I} + \boldsymbol{\varepsilon}_e)^2 + \frac{1}{2}(\mathbf{I} + \boldsymbol{\varepsilon}_h)^2 + \mathrm{sym}((\mathbf{I} + \boldsymbol{\varepsilon}_e)(\mathbf{I} + \boldsymbol{\varepsilon}_h)) - (\mathbf{I} + \boldsymbol{\varepsilon}_e) - (\mathbf{I} + \boldsymbol{\varepsilon}_h) = \boldsymbol{\varepsilon}_e + \boldsymbol{\varepsilon}_h \tag{12}$$

where $\boldsymbol{\varepsilon}_e$ and $\boldsymbol{\varepsilon}_h$ contain the tensorial components of the engineering (small) elastic and hygroscopic strain.

Remark 2 *An important property that follows directly from (9) and (11) is that both* $\mathbf{E}$ *and* $\mathbf{E}_e$ *fulfil the attributes of symmetric and rotationally invariant tensors.*

A key issue in the formulation of a shell element is the auxiliar interpolation of transverse shear strains over the quadrilateral. This is accomplished by the interpolation of strains in a convected coordinate system, with base vectors $\mathbf{g}_i$

$$\mathbf{g}_1 = \frac{\partial \mathbf{x}}{\partial \xi} \qquad \mathbf{g}_2 = \frac{\partial \mathbf{x}}{\partial \eta} \qquad \mathbf{g}_3 = \frac{\partial \mathbf{x}}{\partial \zeta} \tag{13}$$

where ξ, η and ζ are the natural element coordinates. The referential convective base vectors, $\mathbf{G}_i$, are given by

$$\mathbf{G}_1 = \frac{\partial \mathbf{X}}{\partial \xi} \qquad \mathbf{G}_2 = \frac{\partial \mathbf{X}}{\partial \eta} \qquad \mathbf{G}_3 = \frac{\partial \mathbf{X}}{\partial \zeta} \tag{14}$$

At this stage it is essential to establish relations between the Cartesian form and the convected form of the Green Lagrange strain tensor. The convected components of the strain are given by

$$\tilde{E}_{ij} = \frac{1}{2}(\mathbf{g}_i \cdot \mathbf{g}_j - \mathbf{G}_i \cdot \mathbf{G}_j) \tag{15}$$

The Cartesian components of the strain, E_{ij}, are related to $\tilde{E}_{ij}$ by

$$E_{ij} = \tilde{E}_{mn}(\mathbf{G}^m \cdot \mathbf{e}_i)(\mathbf{G}^n \cdot \mathbf{e}_j) \tag{16}$$

or

$$E_{ij} = \tilde{E}_{mn}(\mathbf{G}^m \otimes \mathbf{G}^n) : (\mathbf{e}_i \otimes \mathbf{e}_j) \tag{17}$$

where $\mathbf{G}^i$ is the contravariant counterpart of $\mathbf{G}_j$ given by

$$\mathbf{G}^i = G^{ij}\mathbf{G}_j, \qquad [G^{ij}] = [G_{ij}]^{-1}, \qquad G_{ij} = \mathbf{G}_i \cdot \mathbf{G}_j \tag{18}$$

Introducing the following convective measure, $\tilde{\mathbf{F}}$, defined as

$$\tilde{\mathbf{F}} = \mathrm{Grad}_{\xi}\mathbf{x} = \mathrm{Grad}_{X}\mathbf{x}\,\mathrm{Grad}_{\xi}\mathbf{X} = \mathbf{F}\mathbf{J} \tag{19}$$

where $\mathbf{J}$ is the Jacobian matrix, (15) can be written as

$$\tilde{\mathbf{E}} = \frac{1}{2}(\tilde{\mathbf{F}}^T\tilde{\mathbf{F}} - \mathbf{J}^T\mathbf{J}) \tag{20}$$

In a numerical procedure $\tilde{\mathbf{F}}$ can be obtained as

$$\tilde{\mathbf{F}} = [\mathbf{g}_1\ \mathbf{g}_2\ \mathbf{g}_3] \tag{21}$$

Virtual work equation

Apart from the conventional form of the virtual work equation the mission is here to arrive at an expression that embodies the assumption of kinematics emanating from (3). The Lagrangian form of Cauchy's equation of motion reads

$$\begin{aligned} \mathrm{Div}\mathbf{P} + \mathbf{B} = 0, \qquad & \mathbf{X} \in \Omega_0 \\ \mathbf{u} = \hat{\mathbf{u}}, \qquad & \mathbf{X} \in \partial\Omega_{u0} \\ \mathbf{T} = \mathbf{P}\mathbf{N} = \hat{\mathbf{T}}, \qquad & \mathbf{X} \in \partial\Omega_{T0} \end{aligned} \tag{22}$$

where $\mathbf{B}$ are body forces acting on $\mathcal{B}$ in the referential volume, Ω_0. $\hat{\mathbf{u}}$ and $\hat{\mathbf{T}}$ are prescribed displacements and nominal tractions on $\partial\Omega_{u0}$ and $\partial\Omega_{T0}$, respectively, whereas $\mathbf{N}$ is the referential outward normal on $\partial\Omega_{T0}$. By defining a set of admissible virtual displacements $\delta\mathbf{u}$ according to the map $\chi : \mathcal{C}_0 \rightarrow \mathcal{C}_U \rightarrow \mathcal{C}$, (22) can be written on the global form

$$\int_{\Omega_0} \mathrm{Div}(\mathbf{P}^T\delta\mathbf{u})\,\mathrm{d}V - \int_{\Omega_0} \mathbf{P} : \mathrm{Grad}\delta\mathbf{u}\,\mathrm{d}V + \int_{\Omega_0} \delta\mathbf{u}^T\mathbf{B}\,\mathrm{d}V = 0 \tag{23}$$

where the identity $\mathrm{Div}(\mathbf{P}^T\delta\mathbf{u}) = \mathrm{Div}\mathbf{P}\cdot\delta\mathbf{u} + \mathbf{P} : \mathrm{Grad}\delta\mathbf{u}$ was used. The divergence theorem implies that

$$\int_{\partial\Omega_0} \delta\mathbf{u}^T\mathbf{P}\mathbf{N}\,\mathrm{d}S - \int_{\Omega_0} \mathbf{P} : \mathrm{Grad}\delta\mathbf{u}\,\mathrm{d}V + \int_{\Omega_0} \delta\mathbf{u}^T\mathbf{B}\,\mathrm{d}V = 0 \tag{24}$$

By using (6) together with (7), (24) takes the form

$$\delta\Pi = \int_{\Omega_0} \mathbf{S} : \mathrm{sym}(\mathbf{F}^T\mathrm{Grad}\delta\mathbf{u})\,\mathrm{d}V - \int_{\partial\Omega_0} \delta\mathbf{u}^T\mathbf{T}\,\mathrm{d}S - \int_{\Omega_0} \delta\mathbf{u}^T\mathbf{B}\,\mathrm{d}V = 0, \tag{25}$$

which is the hygro-elastic virtual work equation. It is stressed that (25) embodies the compound motion $\mathcal{C}_0 \rightarrow \mathcal{C}_e$ and $\mathcal{C}_0 \rightarrow \mathcal{C}_h$ in terms of $\mathbf{F}$.

Variation of virtual work

A prerequisite for the numerical solution of the hygro-elastic problem is to obtain the variational form of (25). A restriction to the class of problems in which the external mechanical loads can be considered as conservative is introduced on (25). In this case the variation of $\delta\Pi$ is

$$\begin{aligned} \Delta\delta\Pi = & \left(\int_{\Omega_0} \mathrm{sym}(\mathbf{F}^T\mathrm{Grad}\delta\mathbf{u}) : \frac{\partial\mathbf{S}}{\partial\mathbf{E}_e} : \frac{\partial\mathbf{E}_e}{\partial\mathbf{u}}\,\mathrm{d}V + \right. \\ & \left. \int_{\Omega_0} \mathbf{S} : \frac{\partial}{\partial\mathbf{u}}\mathrm{sym}(\mathbf{F}^T\mathrm{Grad}\delta\mathbf{u})\,\mathrm{d}V \right) \cdot \Delta\mathbf{u} = \\ & \int_{\Omega_0} \mathrm{sym}(\mathbf{F}^T\mathrm{Grad}\delta\mathbf{u}) : \mathbb{C} : \Delta\mathbf{E}_e\,\mathrm{d}V + \int_{\Omega_0} \mathbf{S} : \Delta\mathrm{sym}(\mathbf{F}^T\mathrm{Grad}\delta\mathbf{u})\,\mathrm{d}V \end{aligned} \tag{26}$$

Subsequently, the following linear relationship between $\mathbf{S}$ and $\mathbf{E}_e$ is assumed

$$\mathbf{S} = \mathbb{C} : \mathbf{E}_e \tag{27}$$

By using

$$\delta\mathbf{U}^2 = \delta\mathbf{C} = \delta\mathbf{F}^T\mathbf{F} + \mathbf{F}^T\delta\mathbf{F} \tag{28}$$

and recalling (11) the variation of $\mathbf{E}_e$ reads

$$\delta\mathbf{E}_e = \mathrm{sym}(\mathbf{F}^T\mathrm{Grad}\delta\mathbf{u}) + \mathrm{sym}((\mathbf{I} - \mathbf{U}_h)\delta\mathbf{U}) - \mathrm{sym}((\mathbf{U} - \mathbf{U}_h + \mathbf{I})\delta\mathbf{U}_h) \tag{29}$$

Noting that $\mathrm{sym}(\mathbf{F}^T\mathrm{Grad}\delta\mathbf{u}) = \delta\mathbf{E}$ and the symmetry properties of $\mathbb{C}$, the incremental equilibrium equation can be written

$$\begin{aligned}&\int_{\Omega_0} \delta\mathbf{E} : \mathbb{C} : \Delta\mathbf{E}\,\mathrm{d}V + \int_{\Omega_0} \mathbf{S} : \Delta\delta\mathbf{E}\,\mathrm{d}V + \int_{\Omega_0} \delta\mathbf{E} : \mathbb{C} : ((\mathbf{I} - \mathbf{U}_h)\Delta\mathbf{U})\,\mathrm{d}V = \\ &\int_{\partial\Omega_0} \delta\mathbf{u}^T\mathbf{T}\,\mathrm{d}S + \int_{\Omega_0} \delta\mathbf{u}^T\mathbf{B}\,\mathrm{d}V + \int_{\Omega_0} \delta\mathbf{E} : \mathbb{C} : (\mathbf{U}_e\Delta\mathbf{U}_h)\,\mathrm{d}V - \int_{\Omega_0} \delta\mathbf{E} : \mathbf{S}\,\mathrm{d}V\end{aligned} \tag{30}$$

The third and sixth term in (30) are newly appearing terms with respect to a pure elastic formulation. It is accentuated that the above expression holds also for a restricted class of large deformation thermo-elasticity problems, under the provision of a prescribed thermal stretch matrix $\mathbf{U}_t$, replacing $\mathbf{U}_h$.

The variation of the stretch requires the solution of the tensor equation

$$\delta\mathbf{U}\,\mathbf{U} + \mathbf{U}\,\delta\mathbf{U} = \delta\mathbf{C} \tag{31}$$

in which $\delta\mathbf{U}, \mathbf{U}, \delta\mathbf{C} \in \mathrm{sym}$. Assume that $\mathbf{U}$ commutes with $\delta\mathbf{U}$, then (31) has the simple solution

$$\delta\mathbf{U} = \mathrm{sym}(\mathbf{F}^T\delta\mathbf{F})\mathbf{U}^{-1} \tag{32}$$

which implies

$$\begin{aligned}\delta\mathbf{E}_e = \mathrm{sym}(\mathbf{F}^T\mathrm{Grad}\delta\mathbf{u}) + \frac{1}{2}\mathrm{sym}((\mathbf{I} - \mathbf{U}_h)(\delta\mathbf{F}^T\mathbf{F} + \mathbf{F}^T\delta\mathbf{F})\mathbf{U}^{-1}) - \\ \mathrm{sym}((\mathbf{U} - \mathbf{U}_h + \mathbf{I})\delta\mathbf{U}_h)\end{aligned} \tag{33}$$

The second variation of the Green-Lagrange strain is

$$\Delta\delta\mathbf{E} = \mathrm{sym}((\mathrm{Grad}\delta\mathbf{u})^T\mathrm{Grad}\Delta\mathbf{u}) \tag{34}$$

where higher order terms have been neglected. By virtue of (33) and (34), (30) takes the form

$$\begin{aligned}&\int_{\Omega_0} (\mathbf{F}^T\mathrm{Grad}\delta\mathbf{u}) : \mathbb{C} : (\mathbf{F}^T\mathrm{Grad}\Delta\mathbf{u})\,\mathrm{d}V + \int_{\Omega_0} \mathbf{S} : ((\mathrm{Grad}\delta\mathbf{u})^T\mathrm{Grad}\Delta\mathbf{u})\,\mathrm{d}V + \\ &\frac{1}{2}\int_{\Omega_0} (\mathbf{F}^T\mathrm{Grad}\delta\mathbf{u}) : \mathbb{C} : ((\mathbf{I} - \mathbf{U}_h)((\mathrm{Grad}\Delta\mathbf{u})^T\mathbf{F} + \mathbf{F}^T\mathrm{Grad}\Delta\mathbf{u})\mathbf{U}^{-1})\,\mathrm{d}V = \\ &\int_{\partial\Omega_0} \delta\mathbf{u}^T\mathbf{T}\,\mathrm{d}S + \int_{\Omega_0} \delta\mathbf{u}^T\mathbf{B}\,\mathrm{d}V + \int_{\Omega_0} (\mathbf{F}^T\mathrm{Grad}\delta\mathbf{u}) : \mathbb{C} : (\mathbf{U}_e\Delta\mathbf{U}_h)\,\mathrm{d}V - \\ &\qquad\qquad \int_{\Omega_0} (\mathbf{F}^T\mathrm{Grad}\delta\mathbf{u}) : \mathbf{S}\,\mathrm{d}V\end{aligned} \tag{35}$$

Remark 3 *When* $\{\mathbf{F},\mathbf{U},\mathbf{U}_e,\mathbf{U}_h : t=0\}=\mathbf{I}$*, (35) reduces to*

$$\int_{\Omega_0}\delta\boldsymbol{\varepsilon}:\mathbb{C}:\Delta\boldsymbol{\varepsilon}\,\mathrm{d}V=\int_{\partial\Omega_0}\delta\mathbf{u}^T\mathbf{t}\,\mathrm{d}S+\int_{\Omega_0}\delta\mathbf{u}^T\mathbf{b}\,\mathrm{d}V+\int_{\Omega_0}\delta\boldsymbol{\varepsilon}:\mathbb{C}:\Delta\boldsymbol{\varepsilon}_h\,\mathrm{d}V \tag{36}$$

which is pertinent to the observation in Remark 1.

FE-matrices for the quadrilateral shell

Adopting the standard Galerkin approach the individual terms in (35) can be identified as assembled FE-matrices, which yields the incremental form

$$^t(\mathbf{K}_L+\mathbf{K}_{NL}+\mathbf{K}_H)\Delta\mathbf{a}=\Delta\mathbf{R}+\Delta\mathbf{R}_H \tag{37}$$

in which

$$\begin{aligned}\Delta\mathbf{R}&=^{t+\Delta t}\mathbf{R}_{ext}-{}^t\mathbf{F}_{int}\\ \Delta\mathbf{R}_H&=^{t+\Delta t}\mathbf{R}_H-{}^t\mathbf{R}_H\end{aligned} \tag{38}$$

In the establishment of the element matrices the tensors will be referred to three coordinate frames; the global Cartesian frame, $\{e_1,e_2,e_3\}\in$ orth, a local material oriented frame, $\{\bar\xi,\bar\eta,\bar\zeta\}\in$ orth and a tangential natural frame $\{\xi,\eta,\zeta\}\in$ cov. A four node element is employed, using five degrees of freedom at each node. $\mathbf{K}_L$, $\mathbf{K}_{NL}$ and $\Delta\mathbf{R}$ are formed by following the procedure in [3], though the numerical integration is performed in the local material frame, and will not be given here. The element version of the hygroscopic stiffness matrix $\mathbf{K}_H$ is given by

$$\mathbf{K}_H^e=\int_{\Omega_0^e}\tilde{\mathbf{B}}_L^T\mathbf{A}^T\mathbf{D}\bar{\mathbf{F}}_H\mathbf{A}_H\bar{\mathbf{J}}^{-T}\tilde{\mathbf{B}}_{NL}\,\mathrm{d}V \tag{39}$$

where $\mathbf{D}$ is the constitutive matrix and $\tilde{\mathbf{B}}_L$, $\tilde{\mathbf{B}}_{NL}$ are the covariant interpolation matrices

$$\tilde{\mathbf{B}}_L=\begin{bmatrix}\frac{\partial N_k}{\partial\xi}\mathbf{g}_1^T & \frac{\zeta}{2}h_k\frac{\partial N_k}{\partial\xi}\mathbf{g}_1^T[-\mathbf{v}_2^k\ \ \mathbf{v}_1^k]\\ \frac{\partial N_k}{\partial\eta}\mathbf{g}_2^T & \frac{\zeta}{2}h_k\frac{\partial N_k}{\partial\eta}\mathbf{g}_2^T[-\mathbf{v}_2^k\ \ \mathbf{v}_1^k]\\ \mathbf{0}_{1,3} & \mathbf{0}_{1,2}\\ \frac{\partial N_k}{\partial\eta}\mathbf{g}_1^T+\frac{\partial N_k}{\partial\xi}\mathbf{g}_2^T & \frac{\zeta}{2}h_k\left(\frac{\partial N_k}{\partial\eta}\mathbf{g}_1^T+\frac{\partial N_k}{\partial\xi}\mathbf{g}_2^T\right)[-\mathbf{v}_2^k\ \ \mathbf{v}_1^k]\\ N_A\frac{\partial N_k}{\partial\xi}\Big|_A{}^A\mathbf{g}_3^T+N_B\frac{\partial N_k}{\partial\xi}\Big|_B{}^B\mathbf{g}_3^T & \frac{1}{2}h_k\left(N_AN_k^{AA}\mathbf{g}_1^T+N_BN_k^{BB}\mathbf{g}_1^T\right)[-\mathbf{v}_2^k\ \ \mathbf{v}_1^k]\\ N_C\frac{\partial N_k}{\partial\eta}\Big|_C{}^C\mathbf{g}_3^T+N_D\frac{\partial N_k}{\partial\eta}\Big|_D{}^D\mathbf{g}_3^T & \frac{1}{2}h_k\left(N_CN_k^{CC}\mathbf{g}_2^T+N_DN_k^{DD}\mathbf{g}_2^T\right)[-\mathbf{v}_2^k\ \ \mathbf{v}_1^k]\end{bmatrix} \tag{40}$$

and

$$\tilde{\mathbf{B}}_{NL}=\begin{bmatrix}\frac{\partial N_k}{\partial\xi}\mathbf{I}_{3,3} & -\frac{\zeta}{2}h_k\frac{\partial N_k}{\partial\xi}\mathbf{v}_2^k & \frac{\zeta}{2}h_k\frac{\partial N_k}{\partial\xi}\mathbf{v}_1^k\\ \frac{\partial N_k}{\partial\eta}\mathbf{I}_{3,3} & -\frac{\zeta}{2}h_k\frac{\partial N_k}{\partial\eta}\mathbf{v}_2^k & \frac{\zeta}{2}h_k\frac{\partial N_k}{\partial\eta}\mathbf{v}_1^k\\ \mathbf{0}_{3,3} & -\frac{1}{2}h_kN_k\mathbf{v}_2^k & \frac{1}{2}h_kN_k\mathbf{v}_1^k\end{bmatrix} \tag{41}$$

where N_A,N_B,N_C,N_D are the auxiliar shape functions pertinent to the transverse shear sampling points A,B,C,D, evaluated at gauss points. Superscripts of A,B,C,D means

evaluation in sampling points. $\mathbf{v}_1$ and $\mathbf{v}_2$ are the surface-coherent nodal vectors of the shell. $\bar{\mathbf{F}}_H$ is the matrix

$$\bar{\mathbf{F}}_H = \frac{1}{2}\begin{bmatrix} 2(1-U_{11}^h)U_{11}^{-1}\begin{bmatrix}\mathbf{f}_1^T & \mathbf{0}_{1,3} & \mathbf{0}_{1,3}\end{bmatrix} \\ 2(1-U_{22}^h)U_{22}^{-1}\begin{bmatrix}\mathbf{0}_{1,3} & \mathbf{f}_2^T & \mathbf{0}_{1,3}\end{bmatrix} \\ 2(1-U_{33}^h)U_{33}^{-1}\begin{bmatrix}\mathbf{0}_{1,3} & \mathbf{0}_{1,3} & \mathbf{f}_3^T\end{bmatrix} \\ \left((1-U_{22}^h)U_{11}^{-1}+(1-U_{11}^h)U_{22}^{-1}\right)\begin{bmatrix}\mathbf{f}_2^T & \mathbf{f}_1^T & \mathbf{0}_{1,3}\end{bmatrix} \\ \left((1-U_{33}^h)U_{11}^{-1}+(1-U_{11}^h)U_{33}^{-1}\right)\begin{bmatrix}\mathbf{f}_3^T & \mathbf{0}_{1,3} & \mathbf{f}_1^T\end{bmatrix} \\ \left((1-U_{33}^h)U_{22}^{-1}+(1-U_{22}^h)U_{33}^{-1}\right)\begin{bmatrix}\mathbf{0}_{1,3} & \mathbf{f}_3^T & \mathbf{f}_2^T\end{bmatrix} \end{bmatrix} \tag{42}$$

where $\mathbf{f}_1, \mathbf{f}_2$ and $\mathbf{f}_3$ are formed by the columns of $\mathbf{F}$

$$\mathbf{f}_1 = \begin{bmatrix} F_{11} \\ F_{21} \\ F_{31} \end{bmatrix} \qquad \mathbf{f}_2 = \begin{bmatrix} F_{12} \\ F_{22} \\ F_{32} \end{bmatrix} \qquad \mathbf{f}_3 = \begin{bmatrix} F_{13} \\ F_{23} \\ F_{33} \end{bmatrix} \tag{43}$$

$\mathbf{A}$, $\mathbf{A}_H$ and $\bar{\mathbf{J}}$ are transformation matrices given in Appendix. The element version of the incremental hygroscopic load vector, $\Delta\mathbf{R}_H$, reads

$$\Delta\mathbf{R}_H^e = \int_{\Omega_0^e} \tilde{\mathbf{B}}_L^T \mathbf{A}^T \mathbf{D} \Delta\bar{\mathbf{F}}_H \, \mathrm{d}V \tag{44}$$

where $\Delta\bar{\mathbf{F}}_H$ is

$$\Delta\bar{\mathbf{F}}_H = \begin{bmatrix} U_{11}^e \Delta\lambda_{11}^h \\ U_{22}^e \Delta\lambda_{22}^h \\ 0 \\ U_{12}^e \Delta\lambda_{22}^h + U_{21}^e \Delta\lambda_{11}^h \\ U_{31}^e \Delta\lambda_{11}^h \\ U_{32}^e \Delta\lambda_{22}^h \end{bmatrix} \tag{45}$$

Observe that $\Delta\bar{\mathbf{F}}_H$ is non-zero only in the first iteration of the current incremental step.

Numerical examples

A cantilever beam subject to an end-point load and hygroscopic swelling is first examined. A reference boundary value solution for the case of constant and linearly varying hygroscopic stretch is introductory derived. In a second example the hygroscopic buckling of a composite panel is analyzed for an increasing surrounding humidity.

Variable arc-length hygro-elastica

Consider a cantilever beam with length L in the initial state, subject to an end-point load and a contemporary constant or linearly varying hygroscopic stretch over the beam thickness. It is assumed that the only stretching of the neutral beam axis is due to hygroscopic swelling. Furthermore, it is assumed that cross-sections initially plane and perpendicular to the neutral axis remain plane and perpendicular to the deformed axis. In addition, the shape and area of the section is preserved during deformation.

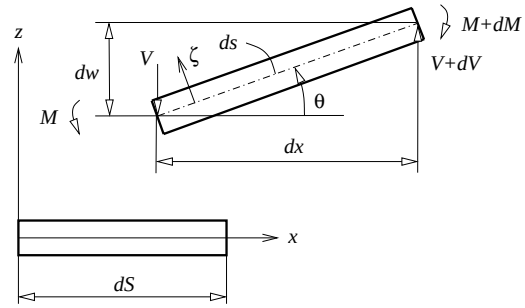

Figure 2: Lagrangian and Eulerian beam segments.

Let $\mathrm{d}S$ and $\mathrm{d}s$ denote the infinitesimal Lagrangian (initial) and Eulerian (deformed) neutral beam segments, respectively, see Figure 2. Let also λ_0^h denote the stretching of the beam neutral axis so that $\mathrm{d}s = \lambda_0^h \mathrm{d}S$ and

$$\mathrm{d}x = \lambda_0^h \cos\theta \, \mathrm{d}S, \qquad \mathrm{d}w = \lambda_0^h \sin\theta \, \mathrm{d}S \tag{46}$$

in which θ is the angle of the initial beam axis to the deformed beam axis. The total curvature, κ, and hygroscopic curvature, κ_h, both defined over a stretched segment $\mathrm{d}s$, can be used to express the generic material total and hygroscopic stretch over the beam thickness

$$\lambda(\zeta) = \lambda_0^h(1 - \kappa\zeta), \qquad \lambda_h(\zeta) = \lambda_0^h(1 - \kappa_h\zeta) \tag{47}$$

where ζ is the thickness coordinate of the beam. The elastic stretch is then given by

$$\lambda_e(\zeta) = \lambda - \lambda_h + 1 = 1 - \lambda_0^h\zeta(\kappa - \kappa_h) \tag{48}$$

In the case of conservative loading, the static equilibrium of the beam is

$$\frac{\mathrm{d}M}{\mathrm{d}S} - P\cos\theta = 0 \tag{49}$$

Using the Green-Lagrange strain the constitutive relation yields

$$S = \frac{1}{2}E\lambda_0^h\zeta(\kappa - \kappa_h)[\lambda_0^h\zeta(\kappa - \kappa_h) - 2] \tag{50}$$

where E is the Young's modulus. By virtue of (50) the moment can be determined

$$M = \int_{-h/2}^{h/2} S\zeta \, \mathrm{d}\zeta = -EI\lambda_0^h(\kappa - \kappa_h) \tag{51}$$

where I is the moment of inertia. Recalling (49) and using

$$\kappa = \frac{\mathrm{d}\theta}{\mathrm{d}s} = \frac{1}{\lambda_0^h}\frac{\mathrm{d}\theta}{\mathrm{d}S} \tag{52}$$

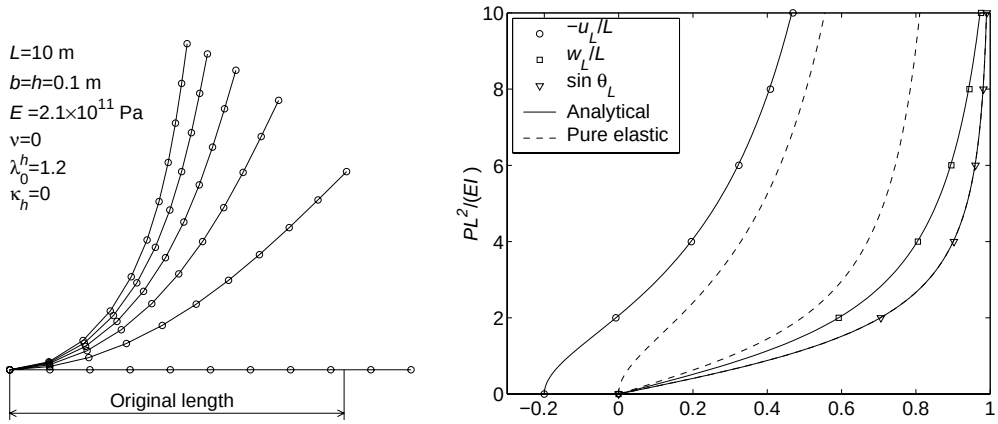

Figure 3: a) Deformed beam and b) load deformation path for a constant through-the-thickness hygroscopic swelling.

the boundary value problem becomes

$$EI\frac{\mathrm{d}^2M}{\mathrm{d}S^2} + P\cos\theta = 0, \qquad \theta(0) = 0, \qquad \left.\frac{\mathrm{d}\theta}{\mathrm{d}S}\right|_L = \kappa_h \tag{53}$$

It is seen that the only departure of (53) compared to the pure elastic solution is the boundary condition at $S = L$. By parametrization (53) can be converted to the system

$$\begin{aligned} \frac{\mathrm{d}\theta}{\mathrm{d}S} &= \vartheta, & \theta(0) &= 0 \\ \frac{\mathrm{d}\vartheta}{\mathrm{d}S} &= -\frac{P\cos\theta}{EI}, & \vartheta(L) &= \kappa_h \end{aligned} \tag{54}$$

which is easily solved using a numerical package. The displacement at $S = L$ can then be found by integration of (46) and using

$$u_L = x_L - L \tag{55}$$

The problem is also solved using ten shell elements and compared to the reference solution for the case $\lambda_0^h = 1.2$, $\kappa_h = 0$ and $\lambda_0^h = 1$, $\kappa_h = 0.0346$, see Figures 3 and 4. It is seen that the agreement between the present formulation and the reference solution is very good.

Moisture buckling of a panel

A 3-layer composite material is analyzed with respect to out of plane deflection for an increasing surrounding humidity. The dimensions and material properties are chosen from a corrugated board panel, where the corrugated core is approximated as a homogenized section with equivalent stiffness parameters, see [10]. The panel is quadratic with side

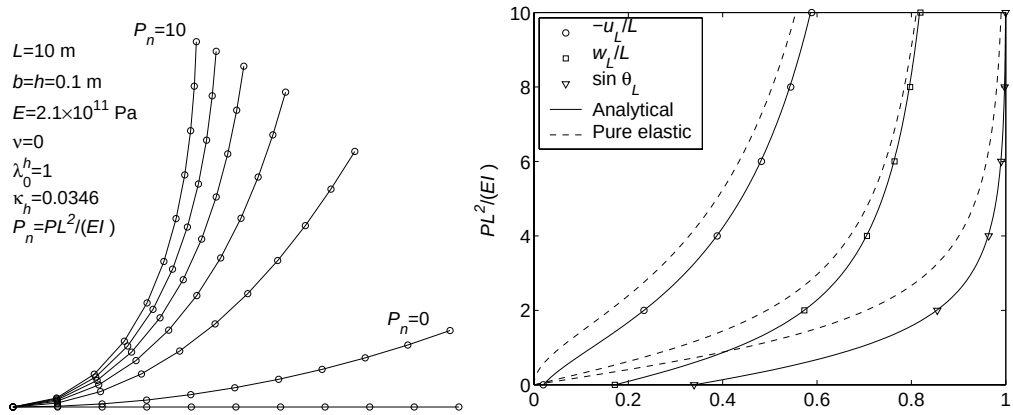

Figure 4: a) Deformed beam and b) load deformation path for a linearly through-the-thickness hygroscopic swelling.

length 0.4 m. The facings are of equal thickness, 0.2 mm, and the thickness of the medium layer is 3.6 mm. The stiffness parameters for the facings are E_{xx}=7×10^9, E_{yy}=3.5×10^9, G_{xy}=3×10^9, G_{xz}=G_{yz}=0.045×10^9 Pa and ν_{xy}=0.2. The stiffness parameters for the core are E_{xx}=0.005×10^9, E_{yy}=0.2×10^9, G_{xy}=0.005×10^9, G_{xz}=G_{yz}=0.0035×10^9 Pa and ν_{xy}=0.05. The hygroscopic stretch is assumed to be given by

$$\lambda_h = 1 + \alpha \Delta \mathcal{R} \tag{56}$$

where $\Delta\mathcal{R}$ is the deviation of relative humidity from a reference state $\mathcal{R}_{\text{ref}}$, given by $\Delta\mathcal{R} = \mathcal{R} - \mathcal{R}_{\text{ref}}$. The linear relationship between hygroscopic stretch and relative humidity in (56) is questionable at large values of $\Delta\mathcal{R}$. However, this anomaly is here discarded since the example serves as a demonstration of the numerical procedure only. The hygroexpansivity parameters are $\alpha_{xx} = 3 \times 10^{-5}$ and $\alpha_{yy} = 15 \times 10^{-5}$ %$^{-1}$, see [11]. Due to symmetry only one quarter of the panel is analyzed, using a 6 by 6 element mesh.

In Figure 5 the relative humidity against center deflection is plotted both for hinged edges and clamped edges. For the hinged panel instability occurs at $\Delta\mathcal{R} \approx 4$ % and for the clamped panel instability occurs at $\Delta\mathcal{R} \approx 8$ %. In the hinged case a turning point is observed at $\Delta\mathcal{R} \approx 30$ %.

Conclusions

The class of problems of finite deformation hygro-elasticity is investigated. Elaborately, the kinematics of contemporary non-elastic swelling and elastic deformations is considered and a theoretical framework for the construction of finite elements is established. Particularly, a numerical procedure for analyzing layered shells is developed.

In the Lagrangian frame the stretch is additively split up in an elastic part and a non-elastic part. In time stepping sequences the elastic stretch is updated by the use of

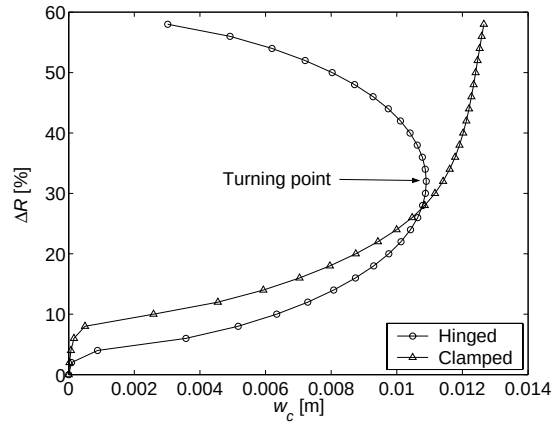

Figure 5: Moisture buckling of panel.

the total stretch from the polar decomposed deformation gradient. As a consequence, in the linearized weak form of equilibrium appear a hygroscopic contribution to the stiffness matrix as well as a hygroscopic load vector.

The methodology derived here applies equally well for thermo-elastic problems provided that the elastic deformation is independent of an altered temperature.

Acknowledgements

The financial support from "Bo Rydins stiftelse för vetenskaplig forskning" [The Bo Rydin Foundation for Scientific Research] is gratefully acknowledged. Special thankfulness is addressed to Prof. Per Johan Gustafsson and Dr. Christer Nilsson for valuable discussions on the topic.

References

[1] Hughes T. J. R., Cohen M., Haroun M., *Reduced and selective integration techniques in the finite element analysis.* Nucl. Engng. Des. **46**, 206-222, 1978.

[2] MacNeal R. H., *Derivation of element stiffness matrices by assumed strain distributions.* Nucl. Engng. Des. **70**, 3-12, 1982.

[3] Dvorkin E. N. and Bathe K-J., *A continuum mechanics based four-node shell element for general non-linear analysis.* Eng. Comput., **1**, 77-88, 1984.

[4] Lee E. H., *Elastic-plastic deformation at finite strains.* J. Appl. Mech., **36**, 1-6, 1969.

[5] Nemat-Nasser S., *A Decomposition of strain measures and their rates in finite deformation elastoplasticity.* Int. J. Solids Structures., **15**, 155-166, 1978.

[6] Simo J. C. and Marsden J. E., *On the rotated stress tensor and the material version of the Doyle-Ericksen formula.* Arch. Rat. Mech. Anal., 8b 213-231, 1984.

[7] Kim S. J. and Oden J. T., *Finite element analysis of a class of problems in finite elastoplasticity based on the thermodynamical theory of materials of type N.* Comp. Meth. Appl. Mech. Eng., **53**, 277-302, 1985.

[8] Argyris J. and Tenek L., *Postbuckling of composite laminates under compressive load and temperature.* Comp. Meth. Appl. Mech. Eng., **128**, 49-80, 1995.

[9] Carrera E. and Librescu L., *Large deflection FEM analysis of thermally loaded, stiffened, shear deformable plates.* Recent advances in solids/structures and application of metallic materials, PVP-Vol 369 141-154, 1997.

[10] Nordstrand T. M., *Parametric Study of the Postbuckling Strength of Structural Core Sandwich Panels*, Composite Structures, 30, 441-451, (1995)

[11] Kolseth P. et al, *Design criteria for paper performance*, Seminar on progress in paper physics, (1987)

Appendix

The transformation matrix $\mathbf{A}$

$$\mathbf{A} = \begin{bmatrix} l_1^2 & m_1^2 & n_1^2 & l_1m_1 & l_1n_1 & m_1n_1 \\ l_2^2 & m_2^2 & n_2^2 & l_2m_2 & l_2n_2 & m_2n_2 \\ l_3^2 & m_3^2 & n_3^2 & l_3m_3 & l_3n_3 & m_3n_3 \\ 2l_1l_2 & 2m_1m_2 & 2n_1n_2 & l_1m_2+l_2m_1 & l_1n_2+l_2n_1 & m_1n_2+m_2n_1 \\ 2l_1l_3 & 2m_1m_3 & 2n_1n_3 & l_1m_3+l_3m_1 & l_1n_3+l_3n_1 & m_1n_3+m_3n_1 \\ 2l_2l_3 & 2m_2m_3 & 2n_2n_3 & l_2m_3+l_3m_2 & l_2n_3+l_3n_2 & m_2n_3+m_3n_2 \end{bmatrix} \tag{57}$$

where

$$\begin{array}{lll} l_1 = (\mathbf{G}^1)^{T\,0}\mathbf{v}_1 & m_1 = (\mathbf{G}^2)^{T\,0}\mathbf{v}_1 & n_1 = (\mathbf{G}^3)^{T\,0}\mathbf{v}_1 \\ l_2 = (\mathbf{G}^1)^{T\,0}\mathbf{v}_2 & m_2 = (\mathbf{G}^2)^{T\,0}\mathbf{v}_2 & n_2 = (\mathbf{G}^3)^{T\,0}\mathbf{v}_2 \\ l_3 = (\mathbf{G}^1)^{T\,0}\mathbf{v}_3 & m_3 = (\mathbf{G}^2)^{T\,0}\mathbf{v}_3 & n_3 = (\mathbf{G}^3)^{T\,0}\mathbf{v}_3 \end{array} \tag{58}$$

The transformation matrix $\mathbf{A}_H$

$$\mathbf{A}_H = \begin{bmatrix} r_1r_1 & r_1s_1 & r_1t_1 & r_1s_1 & s_1s_1 & s_1t_1 & r_1t_1 & s_1t_1 & t_1t_1 \\ r_1r_2 & r_1s_2 & r_1t_2 & r_2s_1 & s_1s_2 & s_1t_2 & r_2t_1 & s_2t_1 & t_1t_2 \\ r_1r_3 & r_1s_3 & r_1t_3 & r_3s_1 & s_1s_3 & s_1t_3 & r_3t_1 & s_3t_1 & t_1t_3 \\ r_1r_2 & r_2s_1 & r_2t_1 & r_1s_2 & s_1s_2 & s_2t_1 & r_1t_2 & s_1t_2 & t_1t_2 \\ r_2r_2 & r_2s_2 & r_2t_2 & r_2s_2 & s_2s_2 & s_2t_2 & r_2t_2 & s_2t_2 & t_2t_2 \\ r_2r_3 & r_2s_3 & r_2t_3 & r_3s_2 & s_2s_3 & s_2t_3 & r_3t_2 & s_3t_2 & t_2t_3 \\ r_1r_3 & r_3s_1 & r_3t_1 & r_1s_3 & s_1s_3 & s_3t_1 & r_1t_3 & s_1t_3 & t_1t_3 \\ r_2r_3 & r_3s_2 & r_3t_2 & r_3s_2 & s_2s_3 & s_3t_2 & r_2t_3 & s_2t_3 & t_2t_3 \\ r_3r_3 & r_3s_3 & r_3t_3 & r_3s_3 & s_3s_3 & s_3t_3 & r_3t_3 & s_3t_3 & t_3t_3 \end{bmatrix} \tag{59}$$

where

$$\begin{array}{lll} r_1 = \mathbf{e}_1^{T\,0}\mathbf{v}_1 & s_1 = \mathbf{e}_2^{T\,0}\mathbf{v}_1 & t_1 = \mathbf{e}_3^{T\,0}\mathbf{v}_1 \\ r_2 = \mathbf{e}_1^{T\,0}\mathbf{v}_2 & s_2 = \mathbf{e}_2^{T\,0}\mathbf{v}_2 & t_2 = \mathbf{e}_3^{T\,0}\mathbf{v}_2 \\ r_3 = \mathbf{e}_1^{T\,0}\mathbf{v}_3 & s_3 = \mathbf{e}_2^{T\,0}\mathbf{v}_3 & t_3 = \mathbf{e}_3^{T\,0}\mathbf{v}_3 \end{array} \tag{60}$$

The Jacobian matrix $\bar{\mathbf{J}}$

$$\bar{\mathbf{J}} = \begin{bmatrix} \frac{\partial X_1}{\partial \xi} & 0 & 0 & \frac{\partial X_1}{\partial \eta} & 0 & 0 & \frac{\partial X_1}{\partial \zeta} & 0 & 0 \\ 0 & \frac{\partial X_1}{\partial \xi} & 0 & 0 & \frac{\partial X_1}{\partial \eta} & 0 & 0 & \frac{\partial X_1}{\partial \zeta} & 0 \\ 0 & 0 & \frac{\partial X_1}{\partial \xi} & 0 & 0 & \frac{\partial X_1}{\partial \eta} & 0 & 0 & \frac{\partial X_1}{\partial \zeta} \\ \frac{\partial X_2}{\partial \xi} & 0 & 0 & \frac{\partial X_2}{\partial \eta} & 0 & 0 & \frac{\partial X_2}{\partial \zeta} & 0 & 0 \\ 0 & \frac{\partial X_2}{\partial \xi} & 0 & 0 & \frac{\partial X_2}{\partial \eta} & 0 & 0 & \frac{\partial X_2}{\partial \zeta} & 0 \\ 0 & 0 & \frac{\partial X_2}{\partial \xi} & 0 & 0 & \frac{\partial X_2}{\partial \eta} & 0 & 0 & \frac{\partial X_2}{\partial \zeta} \\ \frac{\partial X_3}{\partial \xi} & 0 & 0 & \frac{\partial X_3}{\partial \eta} & 0 & 0 & \frac{\partial X_3}{\partial \zeta} & 0 & 0 \\ 0 & \frac{\partial X_3}{\partial \xi} & 0 & 0 & \frac{\partial X_3}{\partial \eta} & 0 & 0 & \frac{\partial X_3}{\partial \zeta} & 0 \\ 0 & 0 & \frac{\partial X_3}{\partial \xi} & 0 & 0 & \frac{\partial X_3}{\partial \eta} & 0 & 0 & \frac{\partial X_3}{\partial \zeta} \end{bmatrix} \tag{61}$$

Paper II

A Numerical Method for Nonlinear Transient Moisture Flow in Cellulosic Materials

Ulf Nyman, Per Johan Gustafsson, Björn Johannesson and Rickard Hägglund

Submitted to International Journal for Numerical Methods in Engineering

A NUMERICAL METHOD FOR NONLINEAR TRANSIENT MOISTURE FLOW IN CELLULOSIC MATERIALS

U. Nyman[1], P. J. Gustafsson[2], B. Johannesson[3] and R. Hägglund[4]

ABSTRACT: A numerical method for the transient moisture flow in porous cellulosic materials like paper and wood is presented. The derivation of the model is based on mass conservation for a mixture containing a vapour phase and an adsorbed water phase embedded in a porous solid material. The principle of virtual moisture concentrations in conjunction with a consistent linearization procedure is used to produce the iterative finite element equations. A monolithic solution strategy is chosen in order to solve the coupled non-symmetric equation system.

A model for the development of higher order sorption hysteresis is also developed. The model is capable of describing cyclic hardening as well as cyclic softening of the equilibrium water concentration. The model is verified by comparison with the measured response to natural variations in temperature and humidity. A close agreement of the simulated results to measured data is found.

Introduction

Moisture flow in porous materials is encountered in a number of engineering applications and in a wide variety of materials. Examples of porous materials are concrete, soil, wood and fiber networks as textiles and paper. Classically, moisture flow among other diffusional processes, is modelled by using Fick's law, where the rate of particle motion is governed by the concentration gradient. This relation constitutes a constitutive dependence between the diffusion velocity and the concentration gradient. By using Fick's law a simplified continuum representation of the physical medium is adopted. However, moisture flow in a porous material may be a very complex course of events such as phase changes, sorption of vapour in the bulk solid and capillary suction i.e. flow of a liquid water phase. This leads to the use of more extensive and detailed modelling of the natural events, such as the use of multiphase modelling of matter. In a multiphase model the state variables describing the system is accounted for on a microscale level of the material. This means that the complete response is achieved for the natural events. Often, this is referred to as mixture models and can involve state variables such as stress, strain, velocity, solute concentrations and temperature. The key idea in the modelling of mixtures is that the heterogeneous material is apparently smoothened so that at a generic point all the constituents are coexisting. The choice of such a detailed modelling incorporating multiple state variables

[1]Division of Structural Mechanics, Lund University, PO Box 118, S-221 00 Lund, Sweden
[2]Division of Structural Mechanics, Lund University, Sweden.
[3]Division of Building Materials, Lund University, Sweden.
[4]SCA Packaging Research, SCA Packaging, Sundsvall, Sweden

implies that the response and interaction between different constituents in the mixture is logically achieved, nevertheless on the expense on complexity of the model.

Multiphase modelling of heat and mass transport problems in materials has been treated by several authors. In [1], [2] and [3] the fundamental theories of thermodynamics and mixture problems are treated in terms of continuum conservation equations. In [4] a comprehensive presentation of transport processes in concrete is found. Coupled heat and moisture transfer in building walls is found in [5]. In [6] a multiphase transport model for drying of wood is analyzed. Modelling of heat and moisture transfer in multilayer wall constructions can be found in [7]. In [8] the effects of temperature, stress and damage (matrix cracks) are considered in order to form a moisture diffusion model for stress loaded polymer matrix composites.

The moisture concentration level has an extremely large influence on the strength of paper. Moreover, in the manufacturing processes involved in papermaking or in the converting process of corrugated board the level of moisture concentration is crucial in order to achieve the desired properties of the material. In view of this, considerable efforts has been made within the field of modelling the moisture transport process in paper. In [9] and [10] effective moisture diffusivities were measured for paper. The works presented material parameters relying on Fickian transport within the material with concentration independent diffusivity. This is only a valid approximation in the relative humidity range of about 0 - 60%. Thereafter a strong nonlinear dependency is observed [11].

Five different transport mechanisms may be postulated for paper (porous materials) [9]; gas diffusion (vapour phase in the pores), Knudsen diffusion (vapour phase in pores with diameter less than 100 Å), surface diffusion (adsorbed phase at the surface of the fibers), bulk - solid diffusion (adsorbed phase within the fibers), capillary transport (condensed phase in the pores). At low or medium moisture concentrations, i.e. 0 - 0.2 weight fraction water per dry material, gas diffusion is the predominant mode of transport.

A step toward a two phase physical model is given by [12], in which both the moisture level in the pores and in the fibers is considered. However, the sorption process in the fibers was considered not to be extended in time, which is the case in [13]. In the work by [13] it is concluded that the transport velocity within the fiber is slow compared to the velocity in the pores. They developed a physical model however, were the moisture movement within the fibers is included. Several works based on similar equations are done in [14, 15, 16]. In [17] an optimization procedure is used in order to fit the transport model to a number of paper materials.

At low levels of relative humidity the process of sorption in the fibers is addressed to molecular bonding (hydrogen bonding) of hydrogen atoms to the hydroxyl groups, or OH sites, into the cellulose molecule, $(C_6H_{10}O_5)_n$. At an increased level of relative humidity sorption is addressed to multilayer adsorption, as free water molecules attaches to already fixed water molecules by hydrogen bonds. In addition, capillary condensation might be present at high levels of relative humidity.

In this work the focus is moisture transport and sorption of water in paper materials. The primary purpose is to form a finite element model suitable for one and two dimensional modelling based on a two phase representation of flow in the material. In addition the sorption hysteresis effect in the fibers is accounted for and a sorption law for higher order processes is developed. The coupled equation system is solved for in a monolithic

iteration matrix format rather than a staggered solution scheme. The advantage of this is that no restriction of time step length is produced by staggering steps. Nevertheless, the monolithic iteration format produces a non-symmetric stiffness matrix. In several numerical examples and by comparison with test results it is shown that modelling of moisture flow and sorption under cyclic variation in ambient moisture levels can adequately be performed.

Mixture balance equations

In a Lagrangian frame the current position, $\mathbf{x}_i$, of a particle i is a function of the original position, $\mathbf{X}_i$, and time

$$\mathbf{x}_i = \chi(\mathbf{X}_i, t) \tag{1}$$

where χ denotes the motion of the particle and $\mathbf{X}_i$ is termed the reference frame.

The conservation of mass for an open volume, Ω, on rate form is given by

$$\frac{\partial}{\partial t}\int_\Omega \rho_i \, dV + \oint_{\partial\Omega} \rho_i \dot{\mathbf{x}}_i \cdot \mathbf{n} \, dA - \int_\Omega m_i \, dV = 0 \qquad i = 1..n \tag{2}$$

where index i refers to the i:th constituent in a mixture of n constituents, the last term is the rate of mass exchange from the other constituents and $\dot{\mathbf{x}}_i \cdot \mathbf{n}$ is the normal time derivative of the particle position $\mathbf{x}_i$. In this case the mixture is considered to consist of a gas phase (vapour), liquid phase (water) and solid phase (fibers). The individual mass densities for each phase is denoted ρ_g, ρ_l, and ρ_s, respectively, defined over a unit volume element in Ω. The corresponding balance equations can be written

$$\begin{aligned}
\frac{\partial}{\partial t}\int_\Omega \rho_g \, dV + \oint_{\partial\Omega} \rho_g \dot{\mathbf{x}}_g \cdot \mathbf{n} \, dA - \int_\Omega m_g \, dV = 0 \\
\frac{\partial}{\partial t}\int_\Omega \rho_l \, dV + \oint_{\partial\Omega} \rho_l \dot{\mathbf{x}}_l \cdot \mathbf{n} \, dA - \int_\Omega m_l \, dV = 0 \\
\frac{\partial}{\partial t}\int_\Omega \rho_s \, dV + \oint_{\partial\Omega} \rho_s \dot{\mathbf{x}}_s \cdot \mathbf{n} \, dA - \int_\Omega m_s \, dV = 0
\end{aligned} \tag{3}$$

If there is no motion of the solid, or mass exchange occurs from other phases to or from the solid, the third equation in (4) can be omitted, thus

$$\begin{aligned}
\frac{\partial}{\partial t}\int_\Omega \rho_g \, dV + \oint_{\partial\Omega} \rho_g \dot{\mathbf{x}}_g \cdot \mathbf{n} \, dA - \int_\Omega m_g \, dV = 0 \\
\frac{\partial}{\partial t}\int_\Omega \rho_l \, dV + \oint_{\partial\Omega} \rho_l \dot{\mathbf{x}}_l \cdot \mathbf{n} \, dA - \int_\Omega m_l \, dV = 0
\end{aligned} \tag{4}$$

By defining the density of the mixture as

$$\rho_m = \rho_g + \rho_l + \rho_s \tag{5}$$

the mass weighted average velocity of the mixture is given by

$$\dot{\mathbf{x}}_m = \frac{\rho_g \dot{\mathbf{x}}_g + \rho_l \dot{\mathbf{x}}_l + \rho_s \dot{\mathbf{x}}_s}{\rho_m} \tag{6}$$

It might be advantageous to define the velocity of the different constituents in terms of relative velocity. This is justified by reasons of achieving descriptions of flow of material that is frame indifferent, a restriction which must be followed when constitutive laws are formed for the material behaviour. The relative velocity of the i:th constituent is

$$\mathbf{v}_i = \dot{\mathbf{x}}_i - \dot{\mathbf{x}}_m \tag{7}$$

By using (7) and applying the divergence theorem, (4) can be written on the form

$$\begin{aligned} \int_\Omega (\dot{\rho}_g + \mathrm{div}(\rho_g \mathbf{v}_g) + \rho_g \mathrm{div}(\dot{\mathbf{x}}_m) + \dot{\mathbf{x}}_m \cdot \mathrm{grad}(\rho_g) - m_g)\, dV = 0 \\ \int_\Omega (\dot{\rho}_l + \mathrm{div}(\rho_l \mathbf{v}_l) + \rho_l \mathrm{div}(\dot{\mathbf{x}}_m) + \dot{\mathbf{x}}_m \cdot \mathrm{grad}(\rho_l) - m_l)\, dV = 0 \end{aligned} \tag{8}$$

where the dot on ρ_g and ρ_l means the spatial time derivative. The third and fourth (convective) terms in (8) influence the mass flow only when the average velocity in the mixture is considerable, e.g. when capillary flow is present. In this case, spatial mass transport is assumed only to take place in the gas phase by vapour diffusion. Thus, since $\dot{\mathbf{x}}_s$ and $\dot{\mathbf{x}}_l$ are assumed to be zero and $\rho_g << \rho_m$ it can be concluded from (6) that $\dot{\mathbf{x}}_m$ is small, which implies that $\mathbf{v}_g \approx \dot{\mathbf{x}}_g$. Yet, mass exchange is considered to take place in the form of condensation and evaporation of water molecules, which means

$$m_g = -m_l \neq 0 \tag{9}$$

(8) now reduces to

$$\begin{aligned} \int_\Omega (\dot{\rho}_g + \mathrm{div}(\rho_g \mathbf{v}_g) - m_g)\, dV = 0 \\ \int_\Omega (\dot{\rho}_l - m_l)\, dV = 0 \end{aligned} \tag{10}$$

In a porous material, i.e. consisting of both bulk material and void spaces, the porosity is defined as

$$\varepsilon_v = \frac{\int_{\Omega_v} dV}{\int_\Omega dV} \tag{11}$$

in which Ω_v is the volume occupied by the voids in Ω. By using ε_v the mass density of, for example the gas phase, can be defined over a void unit volume element instead of over the entire volume element as

$$\rho_v = \frac{\rho_g}{\varepsilon_v} \tag{12}$$

and (10) can be written as

$$\begin{aligned} \int_\Omega (\varepsilon_v \dot{\rho}_v + \mathrm{div}(\varepsilon_v \rho_v \mathbf{v}_g) - m_g)\, dV = 0 \\ \int_\Omega (\dot{\rho}_l - m_l)\, dV = 0 \end{aligned} \tag{13}$$

since ε_v is independent of time in a non-deformable body. Note that this is an approximation which might not be valid if the bulk material undergoes considerable swelling. The reason for rewriting (10) using (12) is that boundary conditions in the form of ambient mass density can be applied directly on (13). It is convenient to express the mass flow of gas relative to the mixture as

$$\mathbf{j}_g = \varepsilon_v \rho_v \mathbf{v}_g \tag{14}$$

It is noted that any constitutive relation applied on (14) will result in material parameters referred either to values of ρ_v, or gradient thereof, or ρ_g, depending on the choice of state variable. The mass concentration of water in the liquid phase, which is assumed to solely take place within the fibers, can be related to the water mass density by

$$c_l = \frac{\rho_l}{\rho_m} \tag{15}$$

Assuming that (13) is valid for all parts of Ω, the strong form of (13) is

$$\begin{gathered}
\varepsilon_v \dot{\rho}_v + \operatorname{div}(\mathbf{j}_g) - m_g = 0 \qquad \mathbf{x}_g \in \Omega_v \subset \Omega,\ t > 0 \\
\dot{\overline{\rho_m\, c_l}} - m_l = 0 \qquad \mathbf{x}_l, \mathbf{x}_s \ni \Omega_v,\ \mathbf{x}_l, \mathbf{x}_s \in \Omega\ t > 0 \\
\mathbf{j}_g \cdot \mathbf{n} - \mathbf{j}_{\partial\Omega} = 0 \qquad \mathbf{x}_g \in \partial\Omega_v \subset \partial\Omega,\ t > 0 \\
\rho_v(\mathbf{x}_g, 0) = \rho_0(\mathbf{x}_g),\ c_l(\mathbf{x}_l, 0) = c_0(\mathbf{x}_l) \qquad \mathbf{x}_g \in \Omega_v,\ \mathbf{x}_l \ni \Omega_v,\ \mathbf{x}_l \in \Omega,\ t = 0
\end{gathered} \tag{16}$$

In (16) the boundary conditions and initial conditions are added to the balance equations. It is noted that, inherently, for a porous material the solid phase is forming the main part of the mixture density. Thus, in (16) the rate of change of ρ_m is very small, i.e. $\dot{\overline{\rho_m\, c_l}} \approx \rho_m \dot{c}_l$. In order to completely describe the system, (16) must also be supplemented by proper constitutive relations which is done in a following section. Further on, the indices denoting vapour phase and liquid phase on ρ and c is dropped since there is no confusion between mass density and mass concentration in the different phases.

Weak form of balance equations

As can be concluded from (9), there is a coupling between the first two equations in (16). However, in creating the weak form of (16) no assumptions are introduced since the solution of a weak form is exactly that of the strong form. Hence, special care need not be taken due to coupling. By using an arbitrary weighting factor, δc, the standard Galerkin weak form of (16) is obtained as

$$\int_\Omega \delta\rho\, \varepsilon_v \dot{\rho}\, dV - \int_\Omega (\operatorname{grad} \delta\rho) \cdot \mathbf{j}\, dV + \oint_{\partial\Omega_v \cup \partial\Omega} (\delta\rho\, \mathbf{j}) \cdot \mathbf{n}\, dS + \int_\Omega \delta\rho\, m_l\, dV = 0 \tag{17}$$

and

$$\int_\Omega \delta\rho\, \rho_m\, \dot{q}\, dV - \int_\Omega \delta\rho\, m_l\, dV = 0 \tag{18}$$

In the derivation of (17), the divergence theorem and the identity

$$\operatorname{div}(\delta\rho\, \mathbf{j}) = (\operatorname{grad}\delta\rho) \cdot \mathbf{j} + \delta\rho \operatorname{div}(\mathbf{j}) \tag{19}$$

was used together with (9). By using the third equation in (16), (17) takes the form

$$\int_\Omega \delta\rho\,\varepsilon_v\dot{\rho}dV - \int_\Omega (\mathrm{grad}\,\delta\rho)\cdot\mathbf{j}dV + \oint_{\partial\Omega_b} \delta\rho\,k_b\rho_{\partial\Omega_b}dS - \oint_{\partial\Omega_b} \delta\rho\,k_b\rho_\infty dS + \int_\Omega \delta\rho\,m_l dV = 0 \quad (20)$$

where $\partial\Omega_b = \partial\Omega_v \cup \partial\Omega$. Note that in (18) the same weighting is used in Ω, in a consistent manner. In regarding $\delta\rho$ as a virtual mass density field the weak form, (18) and (20), of the initial-boundary value problem given by (16), is be said to form the principle of virtual moisture concentration. This is general in terms of possible non-uniqueness of solutions introduced by for example hysteresis effects in the mass transport problem. In other words, (18) and (20) are not seen as the stationarity condition of an existing functional.

At this point it is suitable to incorporate material specific expressions for $\mathbf{j}$ and m_l. For $\mathbf{j}$ a gradient dependency is taken as

$$\mathbf{j} = -\mathbf{D}\,\mathrm{grad}\rho \quad (21)$$

where the Soret effect is neglected, i.e. $\mathbf{j}$ is independent of a possible temperature gradient. This assumption is confirmed in [1]. In (21) $\mathbf{D}$ is assumed isotropic

$$\mathbf{D} = D_v\mathbf{I} \quad (22)$$

Furthermore, at the boundary the following relation is assumed to hold

$$\mathbf{j}_{\partial\Omega} = k_b(\rho_v - \rho_\infty) \quad (23)$$

where k_b is the boundary mass transfer coefficient. The constitutive relation for m_l can be given by, e.g. [18],

$$m_l = \rho_m k_c(c_{eq} - c) \quad (24)$$

where c_{eq} is the equilibrium mass concentration of water in fibers and k_c is a mass transfer coefficient. This implies that (20) and (18) takes the form

$$\int_\Omega \delta\rho\,\varepsilon_v\dot{\rho}\,dV - \int_\Omega (\mathrm{grad}\,\delta\rho)\cdot(\mathbf{D}\,\mathrm{grad}\rho)\,dV + \oint_{\partial\Omega_b} \delta\rho\,k_b(\rho_{\partial\Omega_b} - \rho_\infty)\,dS + \int_\Omega \delta\rho\,\rho_m\,k_c(c_{eq} - c)\,dV = 0 \quad (25)$$

and

$$\int_\Omega \delta\rho\,\dot{c}\,dV - \int_\Omega \delta\rho\,k_c(c_{eq} - c)\,dV = 0 \quad (26)$$

Consistent linearization

The problem remains to find a sequence of linearized equations, from which the solution for mass density and mass concentration can be advanced in time. If the left hand sides of (25) and (26) is denoted $\delta\mathcal{F}_a$ and $\delta\mathcal{F}_b$, respectively, the set of equations can be given by

$$\begin{aligned}\delta\mathcal{F}_a({}^{t+\Delta t}\rho, {}^{t+\Delta t}c) &= \delta\mathcal{F}_a({}^t\rho, {}^tc) + \Delta\delta\mathcal{F}_a + O(|\Delta\rho|^2) + O(|\Delta c|^2)\\ \delta\mathcal{F}_b({}^{t+\Delta t}\rho, {}^{t+\Delta t}c) &= \delta\mathcal{F}_b({}^t\rho, {}^tc) + \Delta\delta\mathcal{F}_b + O(|\Delta\rho|^2) + O(|\Delta c|^2)\end{aligned} \quad (27)$$

where

$$\Delta\delta\mathcal{F}_a = \frac{\partial\delta\,{}^t\mathcal{F}_a}{\partial\rho}\Delta\rho + \frac{\partial\delta\,{}^t\mathcal{F}_a}{\partial c}\Delta c \tag{28}$$

and

$$\Delta\delta\mathcal{F}_b = \frac{\partial\delta\,{}^t\mathcal{F}_b}{\partial\rho}\Delta\rho + \frac{\partial\delta\,{}^t\mathcal{F}_b}{\partial c}\Delta c \tag{29}$$

If the explicit partial derivatives are available in (28) and (29), the process is termed a consistent linearization procedure. This may be crucial in order to achieve convergence in solutions if strong non-linearities is encountered or large increments in time are used in the numerical procedure. In $\delta\mathcal{F}_a$ and $\delta\mathcal{F}_b$ a strong non-linearity in m_l is expected.

Using the chain rule and neglecting higher order variations of the state variables the first increment in (28) is found to be

$$\frac{\partial\delta\,{}^t\mathcal{F}_a}{\partial\rho}\Delta\rho = \int_\Omega \delta\rho\,\varepsilon_v\Delta\dot{\rho}\,dV - \int_\Omega (\operatorname{grad}\delta\rho)\cdot(\mathbf{D}\operatorname{grad}\Delta\rho)\,dV + \oint_{\partial\Omega_b}\delta\rho\,k_b\Delta\rho_{\partial\Omega_b}\,dS + \int_\Omega \delta\rho\,\rho_m\,k_c\frac{\partial c_{eq}}{\partial\rho}\Delta\rho\,dV \tag{30}$$

and the second

$$\frac{\partial\delta\,{}^t\mathcal{F}_a}{\partial c}\Delta c = -\int_\Omega \delta\rho\,\rho_m\,k_c\Delta c\,dV \tag{31}$$

whereas the first increment of (29) is found to be

$$\frac{\partial\delta\,{}^t\mathcal{F}_b}{\partial\rho}\Delta\rho = -\int_\Omega \delta\rho\,k_c\frac{\partial c_{eq}}{\partial\rho}\Delta\rho\,dV \tag{32}$$

and the second

$$\frac{\partial\delta\,{}^t\mathcal{F}_b}{\partial c}\Delta c = \int_\Omega \delta\rho\,\Delta\dot{c}\,dV + \int_\Omega \delta\rho\,k_c\Delta c\,dV \tag{33}$$

Noting that at time t all quantities are known, and neglecting higher order terms in (27), the equations (25)-(33) can be summarized as

$$\begin{aligned}\int_\Omega \delta\rho\,\varepsilon_v\Delta\dot{\rho}\,dV + \int_\Omega (\operatorname{grad}\delta\rho)\cdot(\mathbf{D}\operatorname{grad}\Delta\rho)\,dV + \\ \oint_{\partial\Omega_b}\delta\rho\,k_b\Delta\rho_{\partial\Omega_b}\,dS + \int_\Omega \delta\rho\,\rho\,k_q\frac{\partial c_{eq}}{\partial\rho}\Delta\rho\,dV - \int_\Omega \delta\rho\,\rho\,k_q\Delta c\,dV = \\ -\int_\Omega \delta\rho\,\varepsilon_v\dot{\rho}\,dV - \int_\Omega (\operatorname{grad}\delta\rho)\cdot(\mathbf{D}\operatorname{grad}\rho)\,dV - \\ \oint_{\partial\Omega_b}\delta\rho\,k_b(\rho_{\partial\Omega_b}-\rho_\infty)\,dS - \int_\Omega \delta\rho\,\rho_m\,k_c(c_{eq}-c)\,dV\end{aligned} \tag{34}$$

and

$$\int_\Omega \delta\rho\,\Delta\dot{c}dV - \int_\Omega \delta\rho\,k_c\frac{\partial c_{eq}}{\partial\rho}\Delta\rho dV + \int_\Omega \delta\rho\,k_c\Delta c dV = -\int_\Omega \delta\rho\,\dot{c}dV + \int_\Omega \delta\rho\,k_c(c_{eq}-c)dV \tag{35}$$

in which unknown integrals are collected on the left hand side whereas the known integrals are collected on the right hand side of (34) and (35). It is noted that in (34) and (35) a consistent linearization is achieved provided that an explicit relation can be found for $\frac{\partial c_{eq}}{\partial \rho}$. Under transient thermal conditions the expressions in (27) is furthermore a function of the variation in temperature, ΔT. Then, (27) can be given on the modified form

$$\begin{aligned}\delta\mathcal{F}_a({}^{t+\Delta t}\rho, {}^{t+\Delta t}c, {}^{t+\Delta t}T) &= \delta\mathcal{F}_a({}^{t+\Delta t}\rho, {}^{t+\Delta t}c, {}^{t}T) + \Delta_T\delta\mathcal{F}_a + O(|\Delta T|^2)\\ \delta\mathcal{F}_b({}^{t+\Delta t}\rho, {}^{t+\Delta t}c, {}^{t+\Delta t}T) &= \delta\mathcal{F}_b({}^{t+\Delta t}\rho, {}^{t+\Delta t}c, {}^{t}T) + \Delta_T\delta\mathcal{F}_b + O(|\Delta T|^2)\end{aligned} \tag{36}$$

It is assumed that the only pertinent dependency on T in (36) is given by the variable saturation vapour density in air, $\rho_{\text{sat}}(T)$. The equilibrium mass concentration of water in the fibers is mainly a function of the vapour density relative to the saturation vapour concentration, or the relative humidity, $\mathcal{R} = \rho/\rho_{\text{sat}}$. Thus, using the chain rule

$$\frac{dc_{eq}}{d\rho} = \frac{\partial c_{eq}}{\partial \rho} + \frac{\partial c_{eq}}{\partial T}\frac{\partial T}{\partial \rho} \tag{37}$$

the extra terms

$$\int_\Omega \delta\rho\, \rho_m\, k_c \frac{\partial c_{eq}}{\partial T}\Delta T\, dV, \qquad -\int_\Omega \delta\rho\, k_c \frac{\partial c_{eq}}{\partial T}\Delta T\, dV \tag{38}$$

can be identified in (30) and (32), respectively. Regarding (38) as load terms, c_{eq} on the right hand side of (34) and (35) can be replaced by ${}^{t+\Delta t}\bar{c}_{eq}$, where the approximate relation

$${}^{t+\Delta t}\bar{c}_{eq} = {}^{t}c_{eq} + \frac{\partial c_{eq}}{\partial T}\Delta T = c_{eq}({}^{t}\rho, {}^{t+\Delta t}T) \tag{39}$$

is used.

Iterational matrix format

The solution of equations (34) and (35) is complicated by the coupling terms due to the mass transport between the vapour phase and the liquid phase. In the solution of coupled equations a staggered solution procedure can be chosen, in which the system is solved partly for the first state variable while the second is restricted to be constant and vice versa. The advantage of this method is that existing codes can be used for the solution of coupled problems. Moreover, the non-symmetry introduced by the coupling terms is avoided. However, in this work a monolithic solution strategy is chosen rather than a staggered procedure. By this choice no accuracy or stability degradation is inferred to the system.

Employing the α-family of time integration methods, e.g. [19], (34) and (35) together

with (38) and (39) can be cast in the form

$$\frac{1}{\Delta t}\int_\Omega \delta\rho\,\varepsilon_v \Delta\rho^{(i)}\,dV + \alpha\int_\Omega (\mathrm{grad}\,\delta\rho)\cdot(\mathbf{D}\,\mathrm{grad}\Delta\rho^{(i)})\,dV +$$
$$\alpha\oint_{\partial\Omega_b}\delta\rho\,k_b\Delta\rho^{(i)}_{\partial\Omega_b}\,dS + \alpha\int_\Omega \delta\rho\,\rho_m\,k_c\frac{\partial c_{eq}}{\partial\rho}\Delta\rho^{(i)}\,dV - \alpha\int_\Omega \delta\rho\,\rho_m\,k_c\Delta c^{(i)}\,dV =$$
$$\oint_{\partial\Omega_b}\delta\rho\,k_b\,{}^{t+\Delta t}\rho_\infty\,dS - \int_\Omega \delta\rho\,\varepsilon_v\,{}^{t+\alpha\Delta t}\dot\rho^{(i-1)}\,dV - \int_\Omega(\mathrm{grad}\,\delta\rho)\cdot(\mathbf{D}\,\mathrm{grad}\,{}^{t+\alpha\Delta t}\rho^{(i-1)})\,dV -$$
$$\oint_{\partial\Omega_b}\delta\rho\,k_b\,{}^{t+\alpha\Delta t}\rho^{(i-1)}_{\partial\Omega_b}\,dS - \int_\Omega \delta\rho\,\rho_m\,k_c\,{}^{t+\alpha\Delta t}\bar c^{(i-1)}_{eq}\,dV + \int_\Omega \delta\rho\,\rho_m\,k_c\,{}^{t+\alpha\Delta t}c^{(i-1)}\,dV \quad (40)$$

and

$$\frac{1}{\Delta t}\int_\Omega \delta\rho\,\Delta c^{(i)}\,dV - \alpha\int_\Omega \delta\rho\,k_c\frac{\partial c_{eq}}{\partial\rho}\Delta\rho^{(i)}\,dV + \alpha\int_\Omega \delta\rho\,k_c\Delta c^{(i)}\,dV =$$
$$-\int_\Omega \delta\rho\,{}^{t+\alpha\Delta t}\dot c^{(i-1)}\,dV + \int_\Omega \delta\rho\,k_c\,{}^{t+\alpha\Delta t}\bar c^{(i-1)}_{eq}\,dV - \int_\Omega \delta\rho\,k_c\,{}^{t+\alpha\Delta t}c^{(i-1)}\,dV \quad (41)$$

together with

$$\begin{aligned} {}^{t+\alpha\Delta t}\dot\rho^{(i-1)} &= ({}^{t+\Delta t}\rho^{(i-1)} - {}^t\rho)/\Delta t \\ {}^{t+\alpha\Delta t}\rho^{(i-1)} &= \alpha\,{}^{t+\Delta t}\rho^{(i-1)} + (1-\alpha)\,{}^t\rho \end{aligned} \quad (42)$$

where the left superscript t refers to a state of numerical equilibrium and the right superscript i refers to the i:th iteration. In (42) the same expressions hold for ρ interchanged with c.

In context of finite element matrices, (40) and (41) can be put in the compact iterational format

$$(\frac{1}{\Delta t}\mathbf{C} + \alpha\mathbf{K})\Delta\mathbf{a} = \mathbf{Q}_{\mathrm{ext}} - \mathbf{Q}_{\mathrm{int}} \quad (43)$$

where $\Delta\mathbf{a}$ contains the increments in ρ and c. $\mathbf{C}$ and $\mathbf{K}$ are given by

$$\begin{aligned} \mathbf{C} &= \mathbf{C}_{a\rho} + \mathbf{C}_{bc} \\ \mathbf{K} &= \mathbf{K}_{av} + \mathbf{K}_{ab} + \mathbf{K}_{ai} + \mathbf{K}_{ac} + \mathbf{K}_{bi} + \mathbf{K}_{bc} \end{aligned} \quad (44)$$

where $\mathbf{C}_{a\rho}$ and $\mathbf{C}_{bc}$ are the first two terms of (40) and (41). $\mathbf{K}_{av}$ to $\mathbf{K}_{ac}$ are the second until the fifth term of (40) and $\mathbf{K}_{b\rho}$ and $\mathbf{K}_{bc}$ are the second and third term of (41). Moreover

$$\begin{aligned} \mathbf{Q}_{\mathrm{ext}} &= \mathbf{Q}_\infty \\ \mathbf{Q}_{\mathrm{int}} &= \dot{\mathbf{Q}}_{a\rho} + \mathbf{Q}_{av} + \mathbf{Q}_{\partial\Omega} + \mathbf{Q}_{ai} + \mathbf{Q}_{ac} + \dot{\mathbf{Q}}_{bc} + \mathbf{Q}_{bi} + \mathbf{Q}_{bc} \end{aligned} \quad (45)$$

where $\dot{\mathbf{Q}}_{a\rho}$ to $\mathbf{Q}_{ac}$ are the 7:th until 11:th term of (40) and $\dot{\mathbf{Q}}_{bc}$ to $\mathbf{Q}_{bc}$ are the fourth until the 6:th term of (41). In Appendix the element matrices corresponding to (44) and (45) are given explicitly for the one dimensional case. A generalization to isoparametric quadrilateral elements is presented in [20].

Stability of time integration

The solution of (43) is known to be unconditionally stable for values of α larger that 1/2. Chosing $\alpha = 0$ (explicit integration) will provide an equation system with all off diagonal terms of $\mathbf{C}$ equal to zero if the lumped form of $\mathbf{C}$ is used. The solution is then very efficient without the need for factorization of $\mathbf{C}$ (Cholesky factorization is possible since $\mathbf{C}$ is positive definite). However, the stability of an explicit time stepping procedure needs to be investigated. In the analysis of moisture flow processes long time periods of interest might appear. For example, in natural outside climate variations the time period of investigation is typically 24 hours. In an explicit time integration procedure the condition for stability of the uncoupled liquid phase is

$$\left|\frac{^{t+\Delta t}C}{^{t}C}\right| \leq 1 \quad \Rightarrow \quad |1 - \Delta t_b k_c| \leq 1 \quad \Rightarrow \quad t_b \leq \frac{2}{k_c} \tag{46}$$

and for the uncoupled vapour phase with lumped $\mathbf{C}$

$$t_a \leq \frac{\varepsilon_v}{D_v}\frac{(\Delta x)^2}{2} \tag{47}$$

where Δx is the finite element length. Typical values of the parameters in (46) and (47) are $k_c = 1 \times 10^{-2}$ 1/s, $\Delta x = 3 \times 10^{-5}$ m, $\varepsilon_v = 0.5$ and $D_v = 3 \times 10^{-8}$ m^2/s. This gives $t_a \leq 7.5$ ms and $t_b \leq 200$ s which is of course not acceptable. In the numerical examples the performance of implicit time integration with $1/2 \leq \alpha \leq 1$ will be investigated only.

Development of higher order sorption law

In an environment with fluctuating relative humidity, $\mathcal{R}$, the sorption evolution of materials is a function of the history of humidity. This holds for most hygroscopic materials such as concrete, textiles and wood fiber materials. Hysteresis is manifested in a branch switch of the equilibrium sorption path whenever a change in direction of evolution of relative humidity occur. This history dependent path can be tracked by the use of a set of discrete memory variables, $\kappa = \{\kappa_1, \kappa_2, ...\}$. This means that the sorption equilibrium is a function of vapour mass concentration, temperature, κ and $\mathcal{H}$, as

$$c_{eq} = f(\mathcal{R}(\rho, T), \mathcal{H}, \kappa) \tag{48}$$

where $\mathcal{H} = \mathcal{H}(\kappa)$ is defined as a sequence of material specific hardening parameters

$$\mathcal{H} = \{H_1, H_2, ...\} \tag{49}$$

The relation in (48) is assumed to hold for all locations in a material, each one independent of another. Assume now that a general sorption law can be described by

$$c_{eq}(\mathcal{R}) = \sum_{j=1}^{3} c_j \mathcal{R}^j \qquad 0 \leq \mathcal{R} \leq 1 \tag{50}$$

This choice of sorption law is a result of the measured response on a global level rather than based on the rate of chemical or physical bonding of adsorbate. In addition, in the use of (50) and (24) thermodynamic effects such as latent heat of condensation are neglected. In (50) the parameters c_j are fitted to the boundary sorption curves found from measurements. Boundary sorption is denoted ${}^{a}c_{eq}$ for adsorption and ${}^{d}c_{eq}$ for desorption, whereas interior sorption is denoted ${}^{i}c_{eq}$. With this notation the sorption law at time $t - \Delta t$, ${}^{c}c_{eq}$, can be either of ${}^{a}c_{eq}$, ${}^{d}c_{eq}$ or ${}^{i}c_{eq}$. Whenever a scanning curve, or higher order sorption, occur the corresponding interior sorption parameters are assumed to be explicitly given by the boundary curve parameters and the level of the current $\mathcal{R}$. At a given time t the differential relative humidity is

$$\Delta^t \mathcal{R} = \left.\frac{d\mathcal{R}}{dt}\right|_t \Delta t \tag{51}$$

With the aid of (51) the value of the memory variable at t can be found from

$${}^{t}\kappa = \mathrm{sgn}|\Delta^t \mathcal{R}| \tag{52}$$

where the value of κ is explained as

$$\begin{aligned} {}^{t}\kappa = 1 \qquad & \text{adsorption at } t \text{ (primary, secondary, tertiary, ...)} \\ {}^{t}\kappa = -1 \qquad & \text{desorption at } t \text{ (primary, secondary, tertiary, ...)} \end{aligned} \tag{53}$$

It is possible to define, as a simple case to (48) and (49), $\mathcal{H} = \{K_a, K_d\}$ as history independent initial slopes of a new branch, relative to an old branch, at a candidate reversal point. Then, a conditional development of c_{eq} can be defined as follows. If κ do not change sign from $t - \Delta t$ to t the current equilibrium path is identical to the previous path. If, however, κ changes sign and ${}^{t}\kappa < 0$ secondary or higher order sorption develops according to the following conditions

$$\begin{aligned} &\left.\frac{d^i c_{eq}}{d\mathcal{R}}\right|_{\mathcal{R}={}^{t-\Delta t}\mathcal{R}} = K_d \left.\frac{d^c c_{eq}}{d\mathcal{R}}\right|_{\mathcal{R}={}^{t-\Delta t}\mathcal{R}} \qquad 0 \le K_d \le 1 \\ &\left.\frac{d^i c_{eq}}{d\mathcal{R}}\right|_{\mathcal{R}=\mathcal{R}_b} = \left.\frac{d^d c_{eq}}{d\mathcal{R}}\right|_{\mathcal{R}=\mathcal{R}_b} \qquad \mathcal{R}_b < {}^{t-\Delta t}\mathcal{R} \\ &{}^{i}c_{eq}({}^{t-\Delta t}\mathcal{R}) = {}^{c}c_{eq}({}^{t-\Delta t}\mathcal{R}) \\ &{}^{i}c_{eq}(\mathcal{R}_b) = {}^{d}c_{eq}(\mathcal{R}_b) \end{aligned} \tag{54}$$

and if ${}^{t}\kappa > 0$ according to

$$\begin{aligned} &\left.\frac{d^i c_{eq}}{d\mathcal{R}}\right|_{\mathcal{R}={}^{t-\Delta t}\mathcal{R}} = K_a \left.\frac{d^c c_{eq}}{d\mathcal{R}}\right|_{\mathcal{R}={}^{t-\Delta t}\mathcal{R}} \qquad 0 \le K_a \le 1 \\ &\left.\frac{d^i c_{eq}}{d\mathcal{R}}\right|_{\mathcal{R}=\mathcal{R}_b} = \left.\frac{d^a c_{eq}}{d\mathcal{R}}\right|_{\mathcal{R}=\mathcal{R}_b} \qquad \mathcal{R}_b > {}^{t-\Delta t}\mathcal{R} \\ &{}^{i}c_{eq}({}^{t-\Delta t}\mathcal{R}) = {}^{c}c_{eq}({}^{t-\Delta t}\mathcal{R}) \\ &{}^{i}c_{eq}(\mathcal{R}_b) = {}^{a}c_{eq}(\mathcal{R}_b) \end{aligned} \tag{55}$$

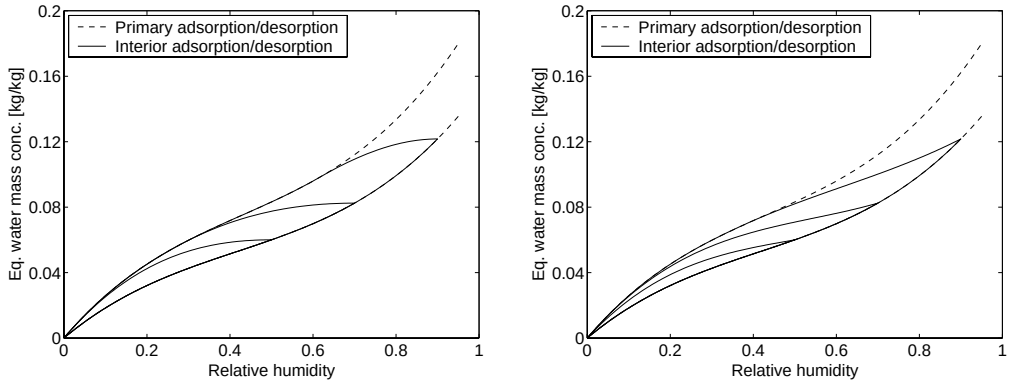

Figure 1: Hysteresis loop curves; a) $K_a = K_d = 0$, b) $K_a = K_d = 3/4$.

where $\mathcal{R}_b$ is the junction point of interior sorption and boundary sorption. From (54) or (55) the parameters ${}^ic_1, {}^ic_2, {}^ic_3$ and $\mathcal{R}_b$ can be explicitly found, see Appendix. The solution of $\mathcal{R}_b$ in (54) and (55) may or may not be larger than zero or smaller than one, respectively. It is recognized that a physical restriction on the parameters ${}^ac_1, {}^ac_2, {}^ac_3$ and ${}^dc_1, {}^dc_2, {}^dc_3$ apply, namely

$$\frac{d^ic_{eq}}{d\mathcal{R}} \geq 0 \qquad \mathcal{R} \in [{}^{t-\Delta t}\mathcal{R}, \mathcal{R}_b] \tag{56}$$

This condition is invoked in the procedure for fitting the parameters on material data.

In Figures 1a and 1b principle examples of hysteresis curves are shown as a sequence of scanning curves, starting at $\mathcal{R} = 0$ and turning at $\mathcal{R} = 0.5$, $\mathcal{R} = 0.7$ and $\mathcal{R} = 0.9$, respectively. In Figures 2a and 2b examples of loop curves are shown for a sequence of 20 cycles in $\mathcal{R}$, starting at $\mathcal{R} = 0$. In Figures 3a and 3b examples of loop curves are shown for a sequence of 6 cycles in $\mathcal{R}$, starting at $\mathcal{R} = 0.95$ and $\mathcal{R} = 0$, respectively.

Numerical examples

In a number of numerical examples the one dimensional moisture transport in paper materials is investigated. The numerical performance of time integration is analyzed for the purpose of selection of an appropriate value of α. In addition, comparison of simulations and measured natural moisture response is performed. The same geometrical and material parameters are used throughout the examples, relevant to the parameters for the test results, see Table 1. In the test a liner material, commonly used in corrugated board boxes, is used. The fitted adsorption and desorption parameters [20] are listed in Table 2. In Figure 4 a comparison of the sorption law given by (50) is compared to the measured levels of equilibrium water concentration. Note that the restriction (56) is invoked in the fitting procedure, for possible reversal points in the interval ${}^{t-\Delta t}\mathcal{R} = [0.5, 0.9]$. The same interval was applied both for secondary adsorption and secondary desorption.

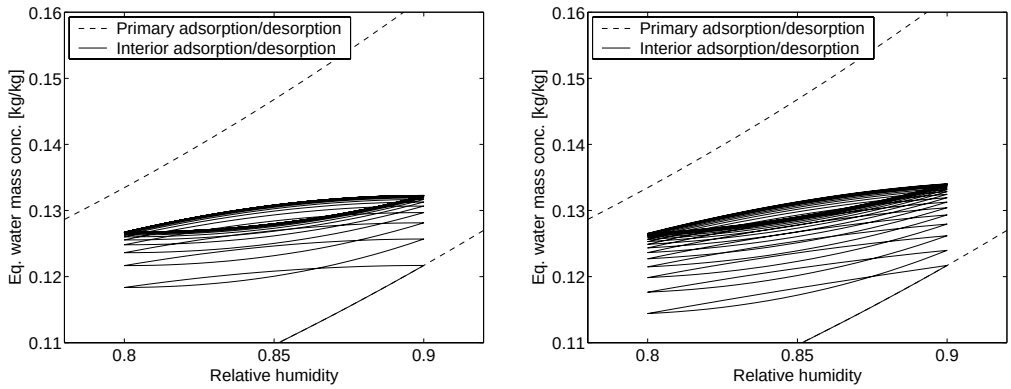

Figure 2: Cycled hysteresis curves; a) $K_a = K_d = 0$, b) $K_a = K_d = 1/4$.

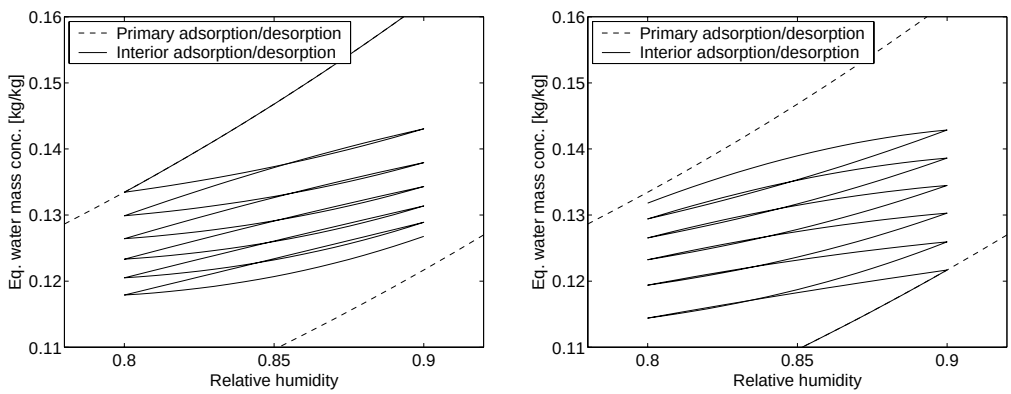

Figure 3: a) Cyclic hardening, $K_a = 1/4, K_d = 3/4$, b) Cyclic softening, $K_a = 3/4$, $K_d = 1/4$.

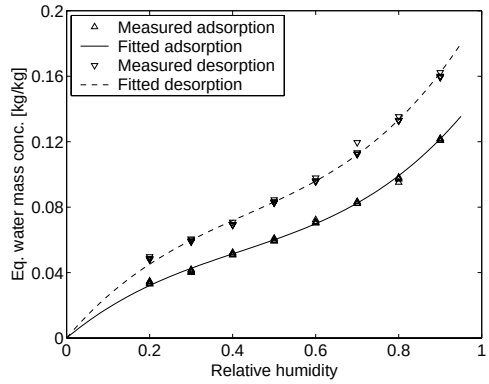

Figure 4: Fitted adsorption and desorption curves.

If not else stated, the temperature used in analysis is 23 °C. A very fine mesh, 50 elements, is used in order to produce comparable results to analytical solutions.

Table 1: Material properties used in numerical examples.

ε_v [15]	0.54
D_v [17] [m^2/s]	2.95×10^{-8}
k_c [17] [1/s]	7.67×10^{-3}
k_b [17] [m/s]	4.31×10^{-3}
ρ_s [kg/m^3]	748
h [m]	2.65×10^{-4}

Table 2: Fitted sorption parameters, [20].

adsorption		desorption	
${}^a c_1$	0.2118	${}^d c_1$	0.2981
${}^a c_2$	-0.3066	${}^d c_2$	-0.4293
${}^a c_3$	0.2461	${}^d c_3$	0.3314

Performance of time integration, linear sorption law

As seen in the investigation of stability of time integration, the most severe problem is given by the first equation in (16). The variation of the integration parameter α is analyzed for the cases; $\alpha = 1/2$ or the trapezoidal rule, $\alpha = 2/3$ corresponding to Galerkin method and $\alpha = 1$ corresponding to the Euler backward method.

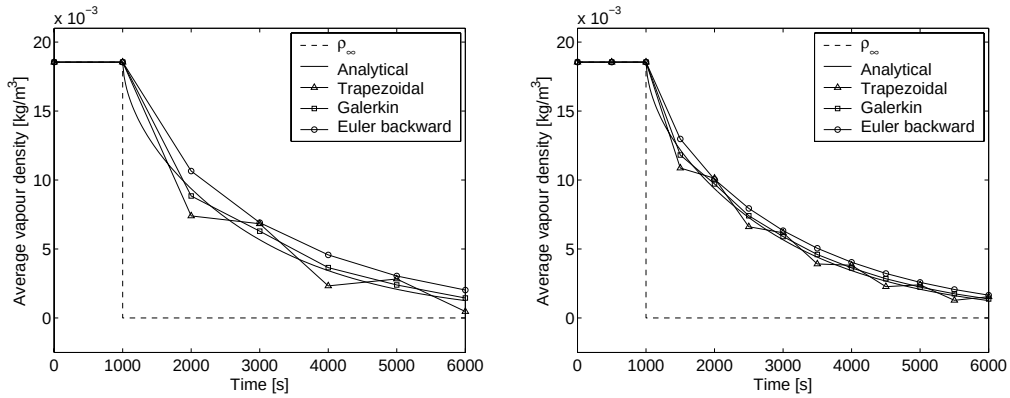

Figure 5: Step boundary conditions; a) $\Delta t = 1000$ s, b) $\Delta t = 500$ s.

An analytical solution to (16) is possible by assuming the sorption process to be infinitely fast, i.e. $c = c_{eq}$. By this assumption (16) reduces to an uncoupled parabolic differential equation for the vapour concentration, still accounting for transport into fibers acting as instantaneous sinks/sources in the material. The condition $c = c_{eq}$ can be numerically invoked in (40) and (41) using a penalty (large) number C_p and

$$k_c(c_{eq} - c) \rightarrow C_p(c_{eq} - c) \tag{57}$$

Furthermore, using

$$\frac{\partial c}{\partial t} = \frac{\partial c_{eq}}{\partial \rho}\frac{\partial \rho}{\partial t} \tag{58}$$

(16) can be written

$$(\varepsilon_v + \rho\frac{\partial c_{eq}}{\partial \rho})\frac{\partial \rho}{\partial t} - D_v\frac{\partial^2 \rho}{\partial x^2} = 0 \tag{59}$$

in the one dimensional case, which for various boundary conditions can be analytically solved for using orthogonal series expansion, see for example [21]. In the examples a constant slope, $\partial q_{eq}/\partial c = 10$, of the sorption isotherm is used.

The first example is a step in surrounding air humidity from $\mathcal{R} = 0.9$ to $\mathcal{R} = 0$. The material is initially in equilibrium with $\mathcal{R} = 0.9$ at 23 °C, that is ρ_0=0.0185 kg/m^3 and c_0=0.1850 kg/kg. In Figures 5a and 5b the response is plotted for a time increment $\Delta t = 1000$ s and $\Delta t = 500$ s, respectively. It is seen that the Trapezoidal rule is producing oscillating results even for the smaller time step. It can be concluded that the Galerkin method produces the most accurate result.

In the second example sinusoidal boundary conditions are applied, $\mathcal{R} = 0.45 + 0.45\sin(\omega t + \psi)$, where $\psi = -\pi/2$ and $\omega = 7\pi/3000$. In Figures 6a and 6b the response is plotted for time increment $\Delta t = 300$ s and $\Delta t = 150$ s, respectively. For this type of loading the best performance is given by the Euler backward method, whereas the Trapezoidal rule overshoots mostly of the three methods investigated.

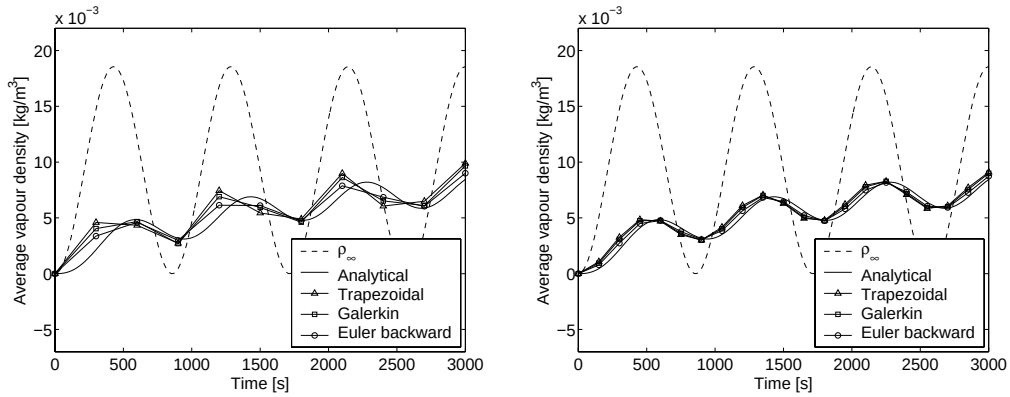

Figure 6: Sinusoidal boundary conditions; a) $\Delta t = 300$ s, b) $\Delta t = 150$ s.

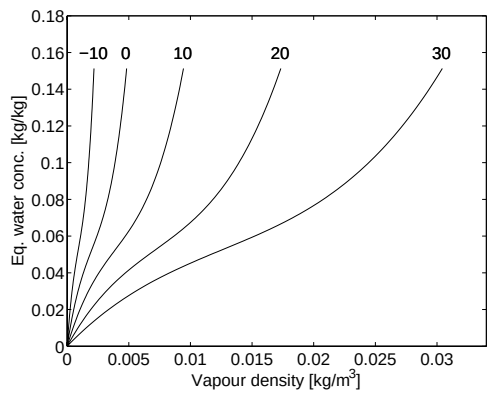

Figure 7: Adsorption isotherms.

Performance of time integration, nonlinear sorption law

In the third example a step in temperature from 23 to 13 °C is applied. The initial conditions $\rho_0 = 0.0103$ kg/m^3 and $c_0 = 0.0782$ kg/kg in conjunction with the boundary condition $\rho_\infty = 0.0103$ is used. Nonlinear adsorption corresponding to the parameters in the left columns of Table 2 is invoked. The temperature influence on the sorption isotherms, due to the variation in saturation concentration ρ_{sat}, is very large. This can been seen in Figure 7, where the adsorption isotherms are plotted for the temperatures -10, 0, 10, 20 and 30 °C. Note that the ultimate values of equilibrium water concentration are identical, induced by the assumption that c_{eq} is a single-valued function of $\mathcal{R}$ only (and not T).

In Figure 8a the step response for both the average vapour density and average water concentration is shown for the case of Euler backward concentration. In addition, a comparison of the response for average vapour concentration is shown for the three different

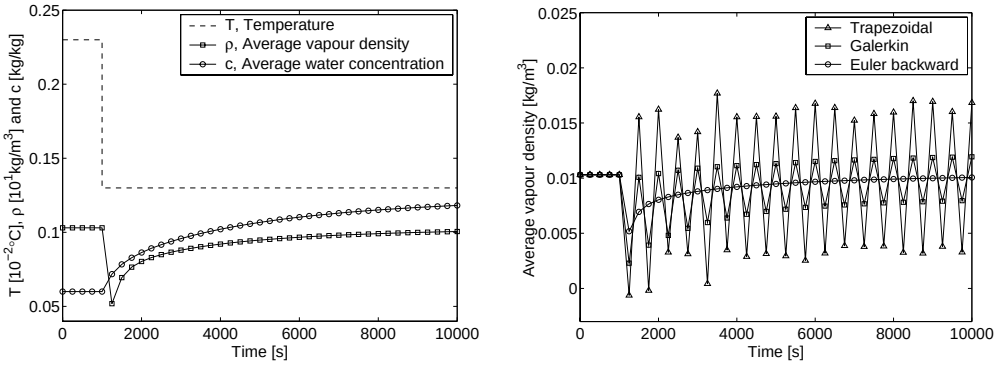

Figure 8: Temperature step; a) Average values of ρ and c, b) Comparison of different integration methods.

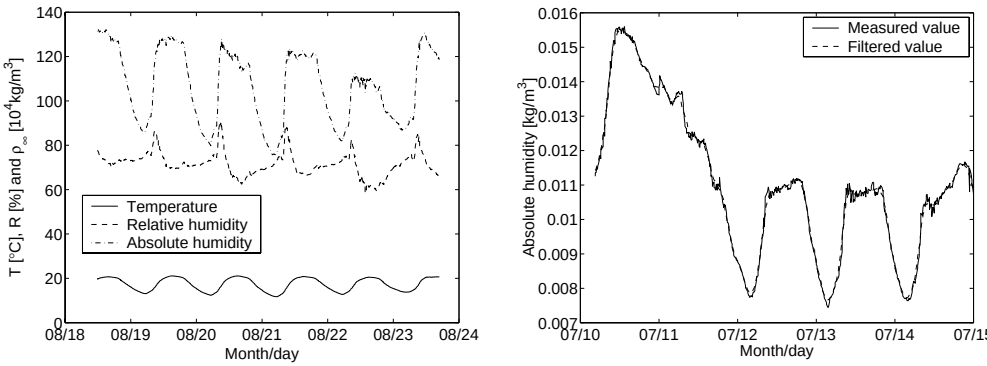

Figure 9: a) Natural variation in temperature and humidity, b) Filtered data for absolute humidity.

types of time integration, see Figure 8b. A very poor performance of the Trapezoidal and Galerkin integration is observed, producing non-physical solutions of (40) and (41). In the following the Euler backward time integration will be used only.

Natural variations in temperature and humidity

Finally, the complete model (40), (41) and (50) including hysteresis is verified by comparison with measured response on water concentration. A paper sample was subjected to one year of natural variations in temperature and humidity, as provided by an untempered indoor climate. The variation of the temperature, relative and absolute humidity of a typical time interval is shown in Figure 9a. The absolute humidity, $\rho = \rho_{\text{sat}}(T)\mathcal{R}$, given by the measured values of T and $\mathcal{R}$, is filtered to produce smooth load data, see Figure 9b.

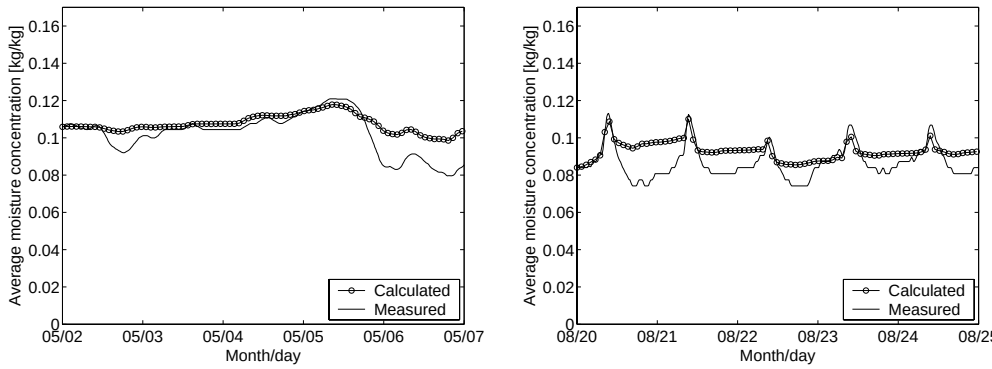

Figure 10: a) and b) Comparison of measured and calculated water concentration, $K_a = K_d = 0$.

In the simulations time integration is performed by using a step length of 1000 sec. Two periods is analyzed, each five days long. As initial value, ρ_0, is chosen the measured value of ρ_∞ at the beginning of the simulation period. The initial value of c is chosen as the boundary adsorption value corresponding to ρ_0. Branch switching of the sorption law according to (54) and (55) is invoked at the boundary sorption lines only, i.e. whenever an interior reversal point occur the old interior branch is used for the new direction.

The mixture average moisture concentration, defined over the thickness of the sample, can be written as

$$\bar{c}_m = \frac{1}{h}\int_0^h (c_g + c_l)\, dL = \frac{1}{h}\int_0^h (\frac{\varepsilon_v \rho_v}{\rho_m} + c_l)\, dL \tag{60}$$

where h is the thickness. In (60) use was made of the relation in (12). In Figures 10a to 14b the simulated transient value of (60) is compared to measured results, for different values of K_a and K_d. It is seen that close agreement is obtained by using $K_a = K_d = 3/4$. It should be noted that the absolute level of the tested moisture concentration is not known due to a considerable drift of the scale over one year. The results from the test are therefore translated so that the level at the starting points of the plotted periods coincide with the calculated results.

Conclusions

A numerical method for the evaluation of transient and cyclic moisture response in paper materials is developed. Tentatively the method could also be used for other cellulosic materials, e.g. wood, if proper material specific parameters are assigned.

The derivation of the model is based on the axiom of mass conservation for a mixture containing a vapour phase and an adsorbed liquid water phase. The principle of virtual moisture concentrations in conjunction with a consistent linearization procedure is used to produce the iterative finite element equations. A model for the development of higher

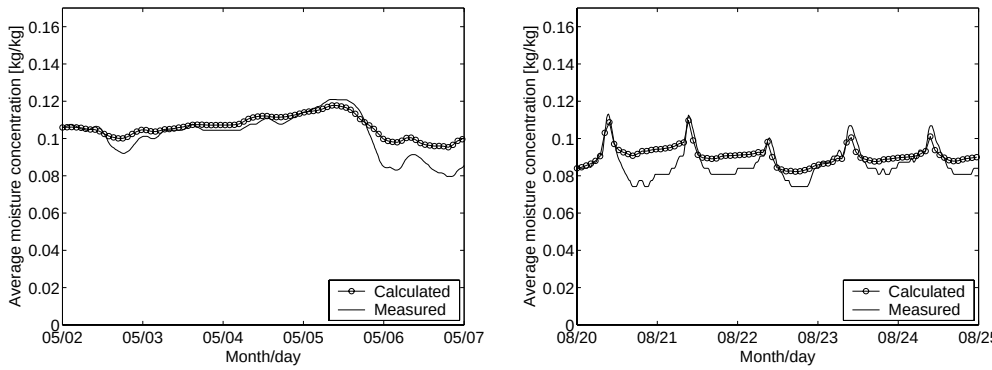

Figure 11: a) and b) Comparison of measured and calculated water concentration, $K_a = K_d = 1/4$.

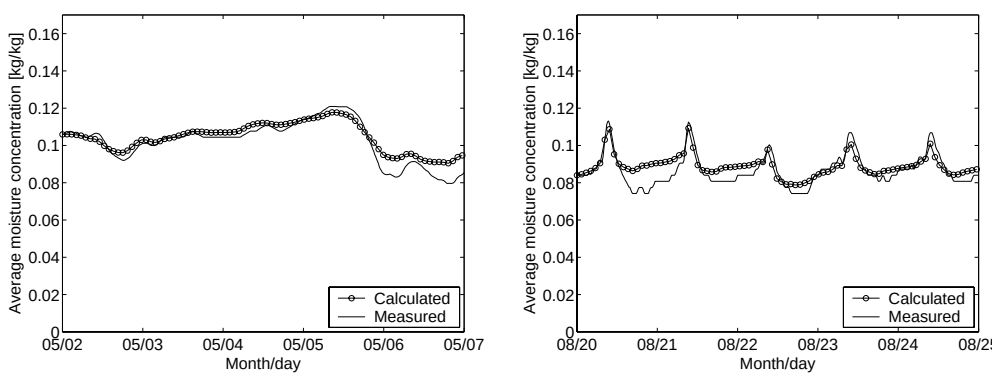

Figure 12: a) and b) Comparison of measured and calculated water concentration, $K_a = K_d = 1/2$.

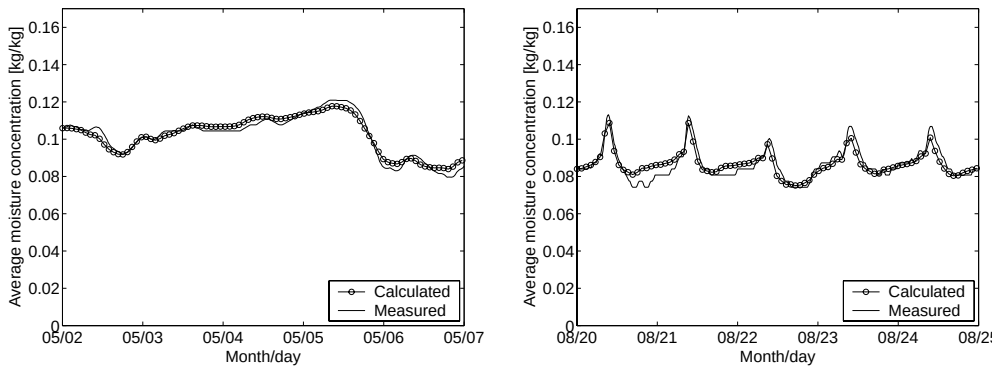

Figure 13: a) and b) Comparison of measured and calculated water concentration, $K_a = K_d = 3/4$.

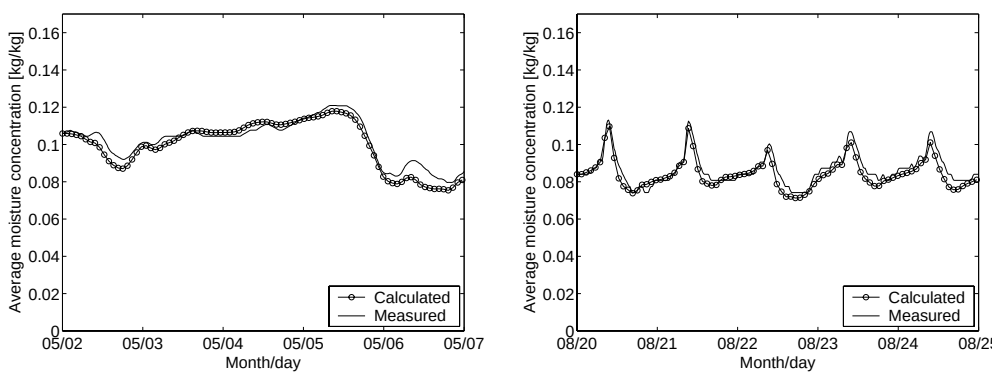

Figure 14: a) and b) Comparison of measured and calculated water concentration, $K_a = K_d = 1$.

order hysteresis is also developed. The model is capable of describing cyclic hardening as well as cyclic softening of the equilibrium water concentration.

In a number of numerical examples the performance of time integration is studied when using different integration methods. It is concluded that the Euler backward method is without hesitation the best method for the given problems. In addition the model is verified by comparison with the measured response to natural variations in temperature and humidity. A close agreement of the simulated results to measured data is found.

Acknowledgements

We gratefully acknowledge “Bo Rydins stiftelse för vetenskaplig forskning” [The Bo Rydin Foundation for Scientific Research] for the support of this research.

References

[1] Luikov A.V. *Heat and Mass Transfer in Capillary-Porous Bodies.* Pergamon Press Ltd, London, 1966.

[2] Truesdell C.A. *Rational Thermodynamics.* Springer, 1984.

[3] Bear J, Buchlin J.M. *Modelling and applications of transport phenomena in porous media.* Kluwer Academic Publishers, The Netherlands, 1991.

[4] Johannesson B. *Modelling of transport processes involved in service life prediction of concrete; Important principles.* Report TVBM - 3083, Licentiate thesis, Division of Building Materials, Lund, Sweden, 1998.

[5] Häupl P, Grunewald J, Fechner H. *Coupled heat and moisture transfer in building structures.* Int. J. Heat Mass Transfer., Vol. 40, No. 7, pp 1633-1642, 1997.

[6] Di Blasi C. *Multi-phase moisture transfer in the high-temperature drying of wood.* Chem. Eng. Sci., Vol. 53, No. 2, pp 353-366, 1998.

[7] Budaiwi I, El-Diasty R, Abdou A. *Modelling of moisture and thermal transient behaviour of multilayer non-cavity walls.* Building and Environment, 34, pp 537-551, 1999.

[8] Roy S, Xu W, Patel S, Case S. *Modelling of moisture diffusion in the presence of bi-axial damage in polymer matrix composite laminates.* Int. J. of Solids and Structures, 38, pp 7627-7641, 2001.

[9] Nilsson L, Wilhelmsson B, Stenström S. *The diffusion of water vapour through pulp and paper.* Drying Technology, 11(6), pp 1205-1225, 1993.

[10] Westerlind B.S., Gustafsson A, Carlsson L.A. *Diffusion of water vapour in paper.* Progress in Paper Physics - A Seminar Proceedings, 1996.

[11] Radhakrishnan H, Chatterjee S.G., Ramarao B.V. *Steady state moisture transport in a bleached kraft paperboard stack.* Journal of Pulp and Paper Science, Vol. 26, No. 4, pp 140 - 144, April, 2000.

[12] Ramarao B.V, Chatterjee S.G. *Moisture transport and sorption by paper under cyclic variations in humidity.* Mechanics of Cellulosic Materials, ASME, AMD-Vol. 209/MD-Vol. 60, 1995.

[13] Foss W.R., Bronkhorst C.A., Bennett K.A., Riedemann J.R. *Transient moisture transport in paper in the hygroscopic range and its role in the mechano-sorptive effect.* Proceedings of the 3:rd International Symposium on Moisture and Creep Effects on Paper, Board and Containers. pp 221 - 236, Rotorua, New Zealand, February 1997.

[14] Ramarao B.V., Chatterjee S.G. *Moisture sorption by paper materials under varying humidity conditions.* Fundamentals of Papermaking Materials, Transaction of the 11:th Fundamental Research Symposium. Vol. 2, pp 703 - 749, Cambridge, September, 1997.

[15] Ramarao B.V. *Moisture sorption and transport processes in paper materials.* Adsorption and its Applications in Industry and Environmental Protection Studies in Surface Science and Catalysis. Vol. 120, pp 531 - 560, 1998.

[16] Bandyopadhyay A, Radhakrishnan H, Ramarao B.V., Chatterjee S.G. *Moisture sorption response of paper subjected to ramp humidity changes: Modelling and experiments.* Ind. Eng. Chem. Res., 39, pp 219 - 226, 2000.

[17] Hägglund R, Westerlind B, Gulliksson M, Nordstrand T. *Diffusion of water vapour in paper.* Fundamental Advances in the Pulp and Paper Industry, AIChE SYmposium Series, Vol. 95, No. 322, pp 71 - 79, 1999.

[18] Tien C. *Adsorption Calculations and Modelling.* Butterworth-Heinemann, Massachusetts, 1994.

[19] Bathe K-J. *Finite Element Procedures.* Prentice-Hall, Inc, New Jersey, 1996.

[20] Lyngå H, Sikö G. *Moisture dynamics in corrugated board boxes.* Master's dissertation, TVSM-5120, 2003.

[21] Carslaw H.S., Jaeger J.C. *Conduction of Heat in Solids.* Oxford University Press, London, 1959.

Appendix

Notation

c_0 =Initial mass concentration of liquid constituent
c_{eq} =Equilibrium mass concentration of water
${}^a c_{eq}$ =Equilibrium boundary adsorption mass concentration
${}^d c_{eq}$ =Equilibrium boundary desorption mass concentration
${}^i c_{eq}$ =Equilibrium interior sorption mass concentration
c_g =Mass concentration of gas constituent
c_l =Mass concentration of liquid constituent
$\bar{c}_m$ =Mixture average moisture concentration
h =Thickness
$\mathbf{j}_g$ =Mass flow of gas relative to mixture
k_b =Mass transfer coefficient at boundary
k_q =Mass transfer coefficient at fiber-void interface
m_i =Rate of mass exchange per unit volume for i:th constituent
$\mathbf{n}$ =Normal vector
t_a, t_b =Critical time steps

$\mathbf{v}_i$ =Relative velocity of i:th constituent
$\mathbf{x}_i$ =Particle position of i:th constituent
C_p =Penalty number
$\mathbf{C}$ =Conductivity matrix
D_v =Vapour diffusivity in voids
$\mathbf{D}$ =Material matrix
$\mathcal{H}$ =Hardening parameters
K_a =Initial slope of interior adsorption
K_d =Initial slope of interior desorption
$\mathbf{K}$ =Stiffness matrix
$\mathbf{Q}_{ext}$ =External flow vector
$\mathbf{Q}_{int}$ =Internal flow vector
$\mathcal{R}$ =Relative humidity
$\mathcal{R}_b$ =Junction point of interior and boundary sorption
T =Temperature
α =Time integration parameter
δc =Virtual moisture concentration
ε_v =Porosity
κ =Discrete memory variables
ρ =Mass density of mixture
ρ_g =Mass density of gas (vapour) constituent
ρ_l =Mass density of liquid (water) constituent
ρ_s =Mass density of solid (fiber) constituent
ρ_v =Mass density of gas constituent, defined over void unit volume element
ρ_0 =Initial mass density of gas constituent
$\rho_{\partial\Omega_b}$ =Vapour mass density at boundary
ρ_∞ =Ambient vapour mass density
Δt =Time increment
$\Delta\mathbf{a}$ =Incremental state variables
Ω =Region occupied by mixture
Ω_v =Region occupied by voids
$\partial\Omega_b$ =Region of boundary
$\dot{(\ )}$ =Time rate of change of quantity
div( ) =Divergence operator
grad( ) =Gradient operator
sgn( ) =Signum function

FE matrices and vectors

One dimensional finite element matrices

$$\mathbf{C}^e_{a\rho} = \frac{\varepsilon_v L_e}{6}\begin{bmatrix} 2 & 0 & 1 & 0 \\ 0 & 0 & 0 & 0 \\ 1 & 0 & 2 & 0 \\ 0 & 0 & 0 & 0 \end{bmatrix}, \qquad \mathbf{C}^e_{bc} = \frac{L_e}{6}\begin{bmatrix} 0 & 0 & 0 & 0 \\ 0 & 2 & 0 & 1 \\ 0 & 0 & 0 & 0 \\ 0 & 1 & 0 & 2 \end{bmatrix}$$

$$\mathbf{K}^e_{av} = \frac{D_v}{L_e}\begin{bmatrix} 1 & 0 & -1 & 0 \\ 0 & 0 & 0 & 0 \\ -1 & 0 & 1 & 0 \\ 0 & 0 & 0 & 0 \end{bmatrix}, \qquad \mathbf{K}^e_{ab} = k_b\begin{bmatrix} \delta^{(1)} & 0 & 0 & 0 \\ 0 & 0 & 0 & 0 \\ 0 & 0 & \delta^{(2)} & 0 \\ 0 & 0 & 0 & 0 \end{bmatrix}$$

$$\mathbf{K}^e_{ai} = \rho_m \frac{k_c L_e}{12}\begin{bmatrix} 3\partial c^{(1)}_{eq}/\partial\rho + \partial c^{(2)}_{eq}/\partial\rho & 0 & \partial c^{(1)}_{eq}/\partial\rho + \partial c^{(2)}_{eq}/\partial\rho & 0 \\ 0 & 0 & 0 & 0 \\ \partial c^{(1)}_{eq}/\partial\rho + \partial c^{(2)}_{eq}/\partial\rho & 0 & \partial c^{(1)}_{eq}/\partial\rho + 3\partial c^{(2)}_{eq}/\partial\rho & 0 \\ 0 & 0 & 0 & 0 \end{bmatrix}$$

$$\mathbf{K}^e_{ac} = -\rho_m \frac{k_c L_e}{6}\begin{bmatrix} 0 & 2 & 0 & 1 \\ 0 & 0 & 0 & 0 \\ 0 & 1 & 0 & 2 \\ 0 & 0 & 0 & 0 \end{bmatrix}, \qquad \mathbf{K}^e_{bc} = \frac{k_c L_e}{6}\begin{bmatrix} 0 & 0 & 0 & 0 \\ 0 & 2 & 0 & 1 \\ 0 & 0 & 0 & 0 \\ 0 & 1 & 0 & 2 \end{bmatrix}$$

$$\mathbf{K}^e_{bi} = -\frac{k_c L_e}{12}\begin{bmatrix} 0 & 0 & 0 & 0 \\ 3\partial c^{(1)}_{eq}/\partial\rho + \partial c^{(2)}_{eq}/\partial\rho & 0 & \partial c^{(1)}_{eq}/\partial\rho + \partial c^{(2)}_{eq}/\partial\rho & 0 \\ 0 & 0 & 0 & 0 \\ \partial c^{(1)}_{eq}/\partial\rho + \partial c^{(2)}_{eq}/\partial\rho & 0 & \partial c^{(1)}_{eq}/\partial\rho + 3\partial c^{(2)}_{eq}/\partial\rho & 0 \end{bmatrix} \tag{61}$$

and vectors

$$\mathbf{Q}^e_{\infty} = k_b\begin{bmatrix} \delta^{(1)}\rho^{(1)}_{\infty} \\ 0 \\ \delta^{(2)}\rho^{(2)}_{\infty} \\ 0 \end{bmatrix}, \ \dot{\mathbf{Q}}^e_{a\rho} = \frac{\varepsilon_v L_e}{6}\begin{bmatrix} 2\dot\rho^{(1)} + \dot\rho^{(2)} \\ 0 \\ \dot\rho^{(1)} + 2\dot\rho^{(2)} \\ 0 \end{bmatrix}, \ \mathbf{Q}^e_{av} = \frac{D_v}{L_e}\begin{bmatrix} \rho^{(1)} - \rho^{(2)} \\ 0 \\ -\rho^{(1)} + \rho^{(2)} \\ 0 \end{bmatrix} \tag{62}$$

$$\mathbf{Q}^e_{\partial\Omega} = k_b\begin{bmatrix} \delta^{(1)}\rho^{(1)}_{\partial\Omega} \\ 0 \\ \delta^{(2)}\rho^{(2)}_{\partial\Omega} \\ 0 \end{bmatrix}, \ \mathbf{Q}^e_{ai} = \frac{\rho_m k_c L_e}{6}\begin{bmatrix} 2\bar c^{(1)}_{eq} + \bar c^{(2)}_{eq} \\ 0 \\ \bar c^{(1)}_{eq} + 2\bar c^{(2)}_{eq} \\ 0 \end{bmatrix}, \ \mathbf{Q}^e_{ac} = -\frac{\rho_m k_c L_e}{6}\begin{bmatrix} 2c^{(1)} + c^{(2)} \\ 0 \\ c^{(1)} + 2c^{(2)} \\ 0 \end{bmatrix}$$

$$\dot{\mathbf{Q}}^e_{bc} = \frac{L_e}{6}\begin{bmatrix} 0 \\ 2\dot c^{(1)} + \dot c^{(2)} \\ 0 \\ \dot c^{(1)} + 2\dot c^{(2)} \end{bmatrix}, \ \mathbf{Q}^e_{bi} = -\frac{k_c L_e}{6}\begin{bmatrix} 0 \\ 2\bar c^{(1)}_{eq} + \bar c^{(2)}_{eq} \\ 0 \\ \bar c^{(1)}_{eq} + 2\bar c^{(2)}_{eq} \end{bmatrix}, \ \mathbf{Q}^e_{bc} = \frac{k_c L_e}{6}\begin{bmatrix} 0 \\ 2c^{(1)} + c^{(2)} \\ 0 \\ c^{(1)} + 2c^{(2)} \end{bmatrix}$$

In (61) and (63) the right superscripts refers to nodal numbers, whereas δ is one if the corresponding node belongs to the boundary and zero else.

Hysteresis parameters

Parameters for interior adsorption

$$\mathcal{R}_b = \frac{\mathcal{A}_b}{\mathcal{B}_b}, \qquad {}^{i}c_1 = \frac{\mathcal{A}_1}{\mathcal{B}_1}, \qquad {}^{i}c_2 = \frac{\mathcal{A}_2}{\mathcal{B}_2}, \qquad {}^{i}c_3 = \frac{\mathcal{A}_3}{\mathcal{B}_3} \tag{63}$$

where

$$\begin{aligned}
&\mathcal{A}_b = (3{}^{i}c_3 - 3K_a{}^{i}c_3)^{t-\Delta t}\mathcal{R}^3 + (-{}^{a}c_2 - 2K_a{}^{i}c_2 + 3{}^{i}c_2)^{t-\Delta t}\mathcal{R}^2 + \\
&(3{}^{i}c_1 - 2{}^{a}c_1 - K_a{}^{i}c_1)^{t-\Delta t}\mathcal{R} \\
&\mathcal{B}_b = (2{}^{a}c_3 - 3K_a{}^{i}c_3 + {}^{i}c_3)^{t-\Delta t}\mathcal{R}^2 + ({}^{i}c_2 - 2K_a{}^{i}c_2 + {}^{a}c_2)^{t-\Delta t}\mathcal{R} + {}^{i}c_1 - K_a{}^{i}c_1 \\
\\
&\mathcal{A}_1 = (-9K_a^{2\,i}c_3^2 - 9{}^{i}c_3^2 + 18K_a{}^{i}c_3^2)^{t-\Delta t}\mathcal{R}^4 + \\
&(-6{}^{a}c_2K_a{}^{i}c_3 - 12K_a^{2\,i}c_2{}^{i}c_3 + 6{}^{a}c_2{}^{i}c_3 - 18{}^{i}c_2{}^{i}c_3 + 30K_a{}^{i}c_3{}^{i}c_2)^{t-\Delta t}\mathcal{R}^3 + \\
&(-12K_a{}^{i}c_3{}^{a}c_1 + 6{}^{i}c_2{}^{a}c_2 + 4{}^{a}c_1{}^{a}c_3 + 24K_a{}^{i}c_3{}^{i}c_1 - {}^{a}c_2^2 + 12K_a{}^{i}c_2^2 - 18{}^{i}c_1{}^{i}c_3 - \\
&4K_a{}^{i}c_2{}^{a}c_2 - 4K_a^{2\,i}c_2^2 - 9{}^{i}c_2^2 - 6K_a^{2\,i}c_1{}^{i}c_3 + 8{}^{i}c_3{}^{a}c_1)^{t-\Delta t}\mathcal{R}^2 + \\
&(-18{}^{i}c_1{}^{i}c_2 - 4K_a^{2\,i}c_2{}^{i}c_1 + 6{}^{i}c_1{}^{a}c_2 - 2K_a{}^{i}c_1{}^{a}c_2 + 8{}^{i}c_2{}^{a}c_1 - \\
&8K_a{}^{i}c_2{}^{a}c_1 + 18K_a{}^{i}c_2{}^{i}c_1)^{t-\Delta t}\mathcal{R} - 4{}^{a}c_1K_a{}^{i}c_1 - 9{}^{i}c_1^2 + 8{}^{a}c_1{}^{i}c_1 - K_a^{2\,i}c_1^2 + 6K_a{}^{i}c_1^2 \\
&\mathcal{B}_1 = (-4{}^{i}c_3 + 4{}^{a}c_3)^{t-\Delta t}\mathcal{R}^2 + (-4{}^{i}c_2 + 4{}^{a}c_2)^{t-\Delta t}\mathcal{R} - 4{}^{i}c_1 + 4{}^{a}c_1 \\
\\
&\mathcal{A}_2 = (9K_a^{2\,i}c_3^2 + 3{}^{i}c_3^2 - 6K_a{}^{i}c_3{}^{a}c_3 + 6{}^{i}c_3{}^{a}c_3 - 12K_a{}^{i}c_3^2)^{t-\Delta t}\mathcal{R}^4 + \\
&(-4K_a{}^{i}c_2{}^{a}c_3 + 6{}^{i}c_2{}^{i}c_3 + 12K_a^{2\,i}c_2{}^{i}c_3 + 6{}^{i}c_2{}^{a}c_3 - 20K_a{}^{i}c_3{}^{i}c_2)^{t-\Delta t}\mathcal{R}^3 + \\
&(4K_a^{2\,i}c_2^2 - 4{}^{a}c_1{}^{a}c_3 + 6K_a{}^{i}c_3{}^{a}c_1 - 8K_a{}^{i}c_2^2 + 6{}^{i}c_1{}^{i}c_3 - 16K_a{}^{i}c_3{}^{i}c_1 + {}^{a}c_2^2 + 3{}^{i}c_2^2 + \\
&6K_a^{2\,i}c_1{}^{i}c_3 - 2{}^{i}c_3{}^{a}c_1 - 2K_a{}^{i}c_1{}^{a}c_3 + 6{}^{i}c_1{}^{a}c_3)^{t-\Delta t}\mathcal{R}^2 + \\
&(6{}^{i}c_1{}^{i}c_2 + 4K_a^{2\,i}c_2{}^{i}c_1 - 2{}^{i}c_2{}^{a}c_1 + 4K_a{}^{i}c_2{}^{a}c_1 - 12K_a{}^{i}c_2{}^{i}c_1)^{t-\Delta t}\mathcal{R} + \\
&2{}^{a}c_1K_a{}^{i}c_1 + 3{}^{i}c_1^2 - 2{}^{a}c_1{}^{i}c_1 + K_a^{2\,i}c_1^2 - 4K_a{}^{i}c_1^2 \\
&\mathcal{B}_2 = (-2{}^{i}c_3 + 2{}^{a}c_3)^{t-\Delta t}\mathcal{R}^3 + (-2{}^{i}c_2 + 2{}^{a}c_2)^{t-\Delta t}\mathcal{R}^2 + (-2{}^{i}c_1 + 2{}^{a}c_1)^{t-\Delta t}\mathcal{R} \\
\\
&\mathcal{A}_3 = (-8{}^{i}c_3{}^{a}c_3 + 6K_a{}^{i}c_3^2 - 9K_a^{2\,i}c_3^2 - {}^{i}c_3^2 + 12K_a{}^{i}c_3{}^{a}c_3)^{t-\Delta t}\mathcal{R}^4 + \\
&(10K_a{}^{i}c_3{}^{i}c_2 + 8K_a{}^{i}c_2{}^{a}c_3 - 2{}^{a}c_2{}^{i}c_3 - 12K_a^{2\,i}c_2{}^{i}c_3 - 2{}^{i}c_2{}^{i}c_3 - 8{}^{i}c_2{}^{a}c_3 + \\
&6{}^{a}c_2K_a{}^{i}c_3)^{t-\Delta t}\mathcal{R}^3 + (-2{}^{i}c_2{}^{a}c_2 + 4K_a{}^{i}c_2^2 - 2{}^{i}c_1{}^{i}c_3 + 4K_a{}^{i}c_1{}^{a}c_3 - {}^{i}c_2^2 - \\
&4K_a^{2\,i}c_2^2 + 4{}^{a}c_1{}^{a}c_3 + 8K_a{}^{i}c_3{}^{i}c_1 + 4K_a{}^{i}c_2{}^{a}c_2 - {}^{a}c_2^2 - 6K_a^{2\,i}c_1{}^{i}c_3 - 8{}^{i}c_1{}^{a}c_3)^{t-\Delta t}\mathcal{R}^2 + \\
&(-2{}^{i}c_1{}^{i}c_2 - 4K_a^{2\,i}c_2{}^{i}c_1 + 2K_a{}^{i}c_1{}^{a}c_2 - 2{}^{i}c_1{}^{a}c_2 + 6K_a{}^{i}c_2{}^{i}c_1)^{t-\Delta t}\mathcal{R} - \\
&{}^{i}c_1^2 + 2K_a{}^{i}c_1^2 - K_a^{2\,i}c_1^2 \\
&\mathcal{B}_3 = (-4{}^{i}c_3 + 4{}^{a}c_3)^{t-\Delta t}\mathcal{R}^4 + (-4{}^{i}c_2 + 4{}^{a}c_2)^{t-\Delta t}\mathcal{R}^3 + (-4{}^{i}c_1 + 4{}^{a}c_1)^{t-\Delta t}\mathcal{R}^2
\end{aligned} \tag{64}$$

The parameters for interior desorption is obtained by simply replacing the index a for d.

Paper III

Finite Element Formulation and Implementation of Nonlinear Shell Reliability

Ulf Nyman and Per Johan Gustafsson

Proceedings of the European Conference on Computational Mechanics, Cracow, Poland, 2001

FINITE ELEMENT FORMULATION AND IMPLEMENTATION OF NONLINEAR SHELL RELIABILITY

Ulf Nyman[1] and Per Johan Gustafsson[2]

ABSTRACT: The reliability of geometrically non-linear composite shells are studied by a finite element procedure. The formulation and implementation of the finite element procedure is described as well as the finite difference method in order to find the gradients of the limit state function. Numerical examples are performed on an in-plane loaded corrugated board panel involving uncertainties in geometrical imperfection, material properties and load.

Introduction

The reliability of structures has attracted an increased attention during recent years. In many applications it is from a lifetime and economic perspective important that a structure under consideration possesses a suitable degree of safety, i.e. the structure should withstand loads under normal conditions, but nevertheless, it must not be exceedable dimensioned in order keep house with resources. One example, which is the focus of this work, is corrugated board panels as, for example, used in packages for the distribution of consumer goods. Corrugated board is a material which to a large extent incorporates uncertainties, manifested as well in material properties, geometrical properties and load conditions under handling. In a reliability analysis, the variables affecting the performance of the structure, called basic variables, are depicted probabilistic measures, i.e. mean and variance. The outcome of the analysis is the share of structures that will fail encountering certain load conditions.

The different techniques existing for reliability analysis can be categorized as either exact or approximate, where in the latter case, some error is inferred from a simplified representation of variation of stochastic variables. Among the exact methods are multifold integration and Monte Carlo simulation techniques. Examples of approximate techniques are methods involving response surface fitting and FORM/SORM (First/Second Order Reliability Methods. The exact methods are numerically intensive and in the analysis of structures, e.g. by the finite element method, the computational cost may be prohibitively large. This is certainly expressed for problems which are numerically intensive in the deterministic case, for example as in non-linear finite element analysis. In this work, FORM is used together with a geometrically non-linear finite element procedure for the solution of in-plane loaded shells.

[1]Division of Structural Mechanics, Lund University, PO Box 118, S-221 00 Lund, Sweden.
[2]Division of Structural Mechanics, Lund University, Sweden.

In using FORM, a limit state function is expressed in terms of the structural resistance and the load. This limit state function represents a n-dimensional surface in the basic variable space. The limit surface can then be mapped into the standard uncorrelated normal space of the basic variables, as proposed in [1]. The idea in FORM is to approximate the limit state surface by a tangent hyper-plane at the design point, which is the point at the limit surface closest to the origin. The design point can be found by an iterative minimization procedure, e.g. as described in [2], and the distance from the origin to the design point is referred to as the reliability index, which provides a first order measure of the probability of failure. The application of reliability methods to the finite element method is currently subject for intensive research activities and examples of work done in this area [3, 4, 5, 6, 7].

The structure analyzed in this work is an in-plane loaded corrugated board panel. The analysis is part of a larger project devoted to reliability design of corrugated board packages. Failure is assumed to take place in either of the facings due to material failure or local buckling. The failure criterion presented in [8] is used for the analysis.

The stability behaviour of a corrugated board panel is analyzed by several numerical examples. The variable uncertainties studied are the magnitude of the geometrical imperfection of the panel, material properties such as strength and stiffness, and load magnitude.

Shell element formulation

As part of the work a geometrically non-linear composite (layered) element is implemented in a structural code for deterministic analysis, CALFEM [9]. The non-linear procedure for evaluation of the response and kinematics of the element is described below.

Equations of motions

In a total Lagrangian formulation, the initial configuration of the deformed body is used as the referential configuration, and the principle of virtual work can be formulated as, see [10],

$$\int_{{}^0V} {}^{t+dt}\mathbf{S} : \delta {}^{t+dt}\boldsymbol{\varepsilon}\, d\,{}^0V = {}^{t+dt}\mathcal{R} \tag{1}$$

where $\mathbf{S}$ is the second Piola Kirchhoff stress tensor and $\boldsymbol{\varepsilon}$ is the Green Lagrange strain tensor. $\mathcal{R}$ is the external work exerted on the body given by

$${}^{t+dt}\mathcal{R} = \int_{{}^0V} {}^{t+dt}\mathbf{f}^B \cdot \delta\mathbf{u}\, d\,{}^0V + \int_{{}^0S} {}^{t+dt}\mathbf{f}^S \cdot \delta\mathbf{u}^S\, d\,{}^0S \tag{2}$$

where $\mathbf{f}^B$ and $\mathbf{f}^S$ are body forces and surface forces, respectively. Using the following decompositions for stresses and strains

$$\begin{aligned} {}^{t+dt}\mathbf{S} &= {}^t\mathbf{S} + d\mathbf{S} \\ {}^{t+dt}\boldsymbol{\varepsilon} &= {}^t\boldsymbol{\varepsilon} + d\boldsymbol{\varepsilon} \end{aligned} \tag{3}$$

and dividing the incremental strain in a linear part, $d\mathbf{e}$, and non-linear part, $d\boldsymbol{\eta}$,

$$d\boldsymbol{\varepsilon} = d\mathbf{e} + d\boldsymbol{\eta} \tag{4}$$

the virtual work equation (1) can be written in incremental form

$$\int_{{}^0V} ({}^t\mathbf{S} : \delta d\mathbf{e} + {}^t\mathbf{S} : \delta d\boldsymbol{\eta} + d\mathbf{S} : \delta d\mathbf{e} + d\mathbf{S} : \delta d\boldsymbol{\eta})\, d\,{}^0V = {}^{t+dt}\mathcal{R} \tag{5}$$

If each step is assumed small, the incremental stress can be expressed as

$$d\mathbf{S} = \mathbb{C} : d\mathbf{e} \tag{6}$$

and (5) can be rewritten as

$$\int_{{}^0V} d\mathbf{e} : \mathbb{C} : \delta d\mathbf{e}\, d\,{}^0V + \int_{{}^0V} {}^t\mathbf{S} : \delta d\boldsymbol{\eta}\, d\,{}^0V = {}^{t+dt}\mathcal{R} - \int_{{}^0V} {}^t\mathbf{S} : \delta d\mathbf{e}\, d\,{}^0V \tag{7}$$

Using the finite element matrices $\mathbf{B}_L$ and $\mathbf{B}_{NL}$, (7) can be expressed in terms of incremental nodal quantities

$$\left[\int_{{}^0V} {}^t\mathbf{B}_L^T \mathbf{D}\, {}^t\mathbf{B}_L\, d\,{}^0V + \int_{{}^0V} \mathbf{B}_{NL}^T\, {}^t\hat{\mathbf{S}}\mathbf{B}_{NL}\, d\,{}^0V\right] d\hat{\mathbf{u}} = {}^{t+dt}\mathbf{R} - \int_{{}^0V} {}^t\mathbf{B}_L^T {}^t\bar{\mathbf{S}}\, d\,{}^0V \tag{8}$$

The finite element equations can then be written as

$${}^t\,[\mathbf{K}_L + \mathbf{K}_{NL}]d\hat{\mathbf{u}} = {}^{t+dt}\mathbf{R} - {}^t\mathbf{F} \tag{9}$$

Kinematics of the element

In the implementation a four node configuration was chosen for the composite element. Following the degenerating principle, [11], the Cartesian coordinates of a point in the element is given by

$$\mathbf{x} = \sum_{k=1}^{4} N_k \hat{\mathbf{x}}_k + \frac{t\zeta}{2} \sum_{k=1}^{4} N_k \mathbf{v}_3^k \tag{10}$$

where $\hat{\mathbf{x}}_k$ are the nodal coordinate points and $\mathbf{v}_3^k$ are the nodal director vectors. ζ is the parent coordinate in the thickness direction. If an isoparametric mapping is used, the incremental displacement is accordingly

$$d\mathbf{u} = \sum_{k=1}^{4} N_k d\hat{\mathbf{u}}_k + \frac{t\zeta}{2} \sum_{k=1}^{4} N_k d\mathbf{v}_3^k \tag{11}$$

The incremental director, $d\mathbf{v}_3^k$, can be expressed approximately, in terms of nodal rotation increments, $d\alpha_k$ and $d\beta_k$,

$$d\mathbf{v}_3^k = -{}^t\mathbf{v}_2^k d\alpha_k + {}^t\mathbf{v}_1^k d\beta_k \tag{12}$$

The total displacements at time t, ${}^t\mathbf{u}$, are given by

$${}^t\mathbf{u} = \sum_{k=1}^{4} N_k\, {}^t\hat{\mathbf{u}}_k + \frac{t\zeta}{2} \sum_{k=1}^{4} N_k({}^t\mathbf{v}_3^k - {}^0\mathbf{v}_3^k) \tag{13}$$

and the vectors ${}^t\mathbf{v}_1^k$ and ${}^t\mathbf{v}_2^k$ are determined by

$$ {}^t\mathbf{v}_1^k = \frac{\mathbf{e}_y \times {}^t\mathbf{v}_3^k}{||\mathbf{e}_y \times {}^t\mathbf{v}_3^k||}, \quad {}^t\mathbf{v}_2^k = {}^t\mathbf{v}_3^k \times {}^t\mathbf{v}_1^k \tag{14} $$

In (11), N_k are the common Lagrange interpolation functions for a four node element. The lamina out-of-plane coordinate in layer i, ζ_i, is mapped to the laminate coordinate, ζ, through

$$ \zeta = -1 + \frac{1}{t}(-t_i(1-\zeta_i) + 2\sum_{j=1}^{i} t_i) \tag{15} $$

in which t is the total thickness of the laminate.

The simple kinematic relation for the laminate deformation given by (11) is a substantial restriction of the true deformation that will develop through the thicknesses of the different layers. In particular, the transverse shear strains will differ substantially from layer to layer, especially if a laminate with largely varying transverse shear stiffnesses is analyzed. In order to capture a more correct stiffness of the laminate, a reduction of the transverse shear stiffness is determined. This is accomplished by matching the shear strain energy obtained from an equilibrium consideration, by the shear strain energy analogous to (11). An equivalent laminate shear stiffness can then be resolved.

In order to prevent shear locking in the element, one integration point is used for the in-plane contribution of the element integrals. In the thickness direction, two points are used. Also, to prevent hour-glass and rhombic patterns to develop, these displacement modes are assigned a penalty.

Reliability finite element procedure (FORM procedure)

The probability of failure P_f, can in terms of the stochastic basic variables $\boldsymbol{\alpha}$, be written

$$ P_f = P[g_\alpha(\boldsymbol{\alpha}) \leq 0] \tag{16} $$

where $g_\alpha(\boldsymbol{\alpha})$ is the limit state function, which is positive when the structure is in a safe state. In using FORM, the basic variables $\boldsymbol{\alpha}$ are mapped to a set of uncorrelated variables, $\mathbf{z}$, in standard normal space. The point at which the structure is most likely to fail, $\mathbf{z}^*$, is called the design point and is the point closest to the origin in the $\mathbf{z}$-coordinate system. This point is found by an iterative search algorithm, for example the iteration points can be determined by [2]

$$ \mathbf{z}_{k+1} = \left(\mathbf{z}_k^T \frac{\nabla g_k}{||\nabla g_k||} + \frac{g_k}{||\nabla g_k||} \right) \frac{\nabla g_k}{||\nabla g_k||} \tag{17} $$

The gradient of g can be found either analytically, by a direct differentiation of the finite element equations, as was done in [5], or numerically. Herein, a finite difference technique is used in order to find the gradient. The gradient can be expressed as

$$ \nabla g = \frac{g(\boldsymbol{\alpha} + \delta\boldsymbol{\alpha}) - g(\boldsymbol{\alpha})}{\delta\boldsymbol{\alpha}} \tag{18} $$

where $\delta\boldsymbol{\alpha}$ is a small variation in the stochastic variables. In an incremental procedure for the calculation of element stresses

$$d\bar{\mathbf{S}}_i(\boldsymbol{\alpha}) = \mathbf{D}(\boldsymbol{\alpha})d\boldsymbol{\epsilon}_i(\boldsymbol{\alpha}) = \mathbf{D}(\boldsymbol{\alpha})\mathbf{B}_L(\boldsymbol{\alpha})d\hat{\mathbf{u}}_i(\boldsymbol{\alpha}) \tag{19}$$

the incremental stress for a small variation in the stochastic variables can be expressed as

$$d\bar{\mathbf{S}}_i(\boldsymbol{\alpha}+\delta\boldsymbol{\alpha}) = \mathbf{D}(\boldsymbol{\alpha}+\delta\boldsymbol{\alpha})\mathbf{B}_L(\boldsymbol{\alpha}+\delta\boldsymbol{\alpha})d\hat{\mathbf{u}}_i(\boldsymbol{\alpha}+\delta\boldsymbol{\alpha}) \tag{20}$$

where $d\hat{\mathbf{u}}_i$ are the nodal increments in the displacement vector for element i. Note that the matrix $\mathbf{B}_L$ is a function of the stochastic variables since variations in geometric properties are included.

The equilibrium of the system before the variation can be obtained by e.g. a Newton Raphson procedure and the residual

$$\mathbf{G}(\boldsymbol{\alpha})_i = \mathbf{R} - \mathbf{F}(\boldsymbol{\alpha})_{i-1} = \lambda(\boldsymbol{\alpha})\mathbf{P} - \mathbf{F}(\boldsymbol{\alpha})_{i-1} \tag{21}$$

tends to zero at convergence. In (21), $\mathbf{P}$ denotes a loading pattern and λ is a scale factor. In this work only proportional loading is considered, that is, $\mathbf{P}$ is a constant vector. The residual for a variation in $\boldsymbol{\alpha}$ is expressed as

$$\mathbf{G}(\boldsymbol{\alpha}+\delta\boldsymbol{\alpha})_i = \lambda(\boldsymbol{\alpha}+\delta\boldsymbol{\alpha})\mathbf{P} - \mathbf{F}(\boldsymbol{\alpha}+\delta\boldsymbol{\alpha})_{i-1} \tag{22}$$

For a geometrically non-linear structure, the response is independent of load history and to obtain equilibrium for a small variation in the stochastic variables it suffices to start the iterations at an arbitrary point of equilibrium. The choice of start point is here chosen as the last point of equilibrium for the current values of the stochastic variables, i.e. when equation (21) vanish for $\boldsymbol{\alpha}_k$.

Numerical examples

Deterministic loading/parameters

The performance of the composite shell element for deterministic parameters is studied by comparison with test results [12] from simply supported edge loaded corrugated board panels, see Figure 1. In the FEM simulation, ten equally large loadsteps are applied on the edge. A small imperfection of the form,

$$z = 8 \cdot 10^{-4} \cos(\frac{\pi x}{L})\cos(\frac{\pi y}{L}) \tag{23}$$

where L is the side length of the panel, is used for the panel. The dimensions and material properties of the board can be found in [12]. In the Figure, the numbers in parentheses is the failure index Φ, see [8], which is equal to one when failure, either due to material failure or structural failure (local buckling), occurs in the facing of the board. Φ is evaluated in the center element, where the stress is calculated as the mean value of the the two gauss points in the facing on the concave side. It should be noted that the failure here was due to local buckling of the facing.

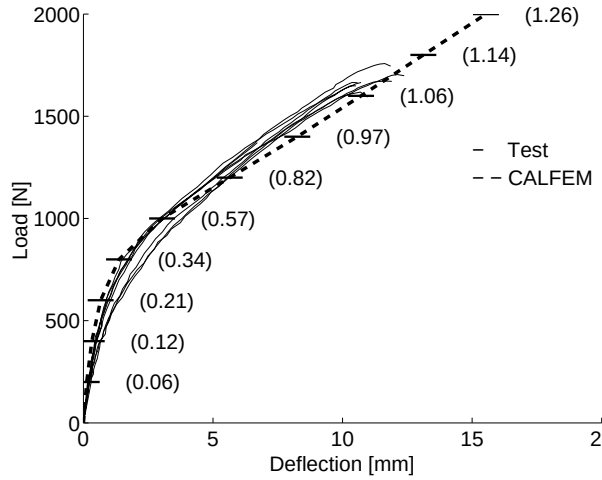

Figure 1: Comparison of test results and composite FEM simulation.

Reliability analysis

The reliability of a corrugated board panel is studied in three cases; influence of the geometrical correlation length, increasing mean value of the edge load and influence of variation of the geometrical imperfection.

The panel is simply supported and quadratic with side dimension 0.5 m. The middle layer is assigned deterministic values and assumed only to contribute with bending stiffness along the corrugations. An effective Young's modulus of the middle layer is calculated as described in [13], where reliability calculations where performed on a surface loaded plate undergoing small deflections.

As stochastic variables are chosen one for the magnitude of the edge load, one for the magnitude of the geometrical imperfection and nine for a geometrically distributed stochastic field for the strength and stiffness variables. The variables for the load and imperfection are chosen to be completely independent stochastic variables. It is known that both the strength and stiffness of paper change drastically when subjected to moisture. It can also be concluded that strong correlation exists between the variation in strength and stiffness. Therefore, the strength and stiffness parameters for a geometric point are here assumed to be be fully correlated. The correlation between two geometric points, i and j, is determined by

$$\rho_{ij} = \mathrm{e}^{-D_{ij}/L} \tag{24}$$

where $L = -D^*/\log \rho^*$. ρ^* is the value of correlation between two points at distance D* from each other. The distance D_{ij} can be obtained as $D_{ij} = \|\mathbf{v}\|$, where $\mathbf{v}$ is the geometric vector between the points, here chosen as the midpoints of the random field elements.

All variables are taken to be log-normally distributed with a coefficient of variation 0.3, unless otherwise stated. The mean values for the stiffness parameters are $E_{11} = 8.36$, $E_{22} = 3.41$, $G_{12} = 2.06$, and $G_{13} = G_{23} = 0.045$ GPa. The in plane Poissons ratio

is $\nu_{12} = 0.17$. Furthermore, the tensile and compressive material strengths in the first direction is $X_t = 85.7$ and $X_c = 25.2$ MPa respectively, and in second direction $Y_t = 35.2$ and $Y_c = 14.7$ MPa. The shear strength is obtained as proposed in [14]. The mean value of the total edge load is 500 N, except for the second analysis case. The mean of the magnitude of the geometrical imperfection is 0.8 mm.

The failure criterion in the reliability analysis is the same as in the deterministic analysis, i.e. the exceedance of $\Phi = 1$ in the facing on the concave side of the center element. The limit state function is then expressed as

$$g = S_f^R - S^R \tag{25}$$

where S_f^R is the failure stress radius and S^R is the evaluated stress radius, see [8].

For the parameters above, $\rho^* = 0.5$ and a large edge load P =1200 N, the probability of failure, P_f, is calculated with both the FORM method described in this paper and Monte Carlo simulations (MCS), see Table 1. The large load is applied for the purpose of reducing the number of MCS.

FORM	MCS (n =100)	MCS (n =500)	MCS (n =2000)
0.4270	0.480	0.398	0.4225

Table 1: P_f, comparison of FORM and MCS.

Influence of the geometrical correlation length

The parameter ρ^* is here varied between 0.01 and 0.9. In Figure 2 the probability of failure is plotted versus ρ^*. For an increasing correlation of the geometrically distributed strength and stiffness variables the probability of failure is seen to increase. The same observation was also done in [13], where a system failure was considered.

Increasing mean value of edge load

In this case the probability of failure is determined for an increasing value of the mean value of the edge load. The analysis is performed for three values of the coefficient of variation, 0.1, 0.2 and 0.3. The value of ρ^* is 0.5. The load is increased in ten load steps to a total edge load of 1200 N, and the probability of failure is evaluated at each load level, see Figure 3.

As seen in the Figure, the probability of failure is very sensitive to the mean value of the applied load. It is interesting to note that the probability of failure is less sensitive to the coefficient of variation. For mean values of the load less than 1150 N, the probability of failure increases with increasing coefficient of variation. In this region the structure is mostly governed by a linear response. However, at larger loads the effect is reversed, and the probability of failure decreases with increasing coefficient of variation. This is due to the highly non-linear response of the structure.

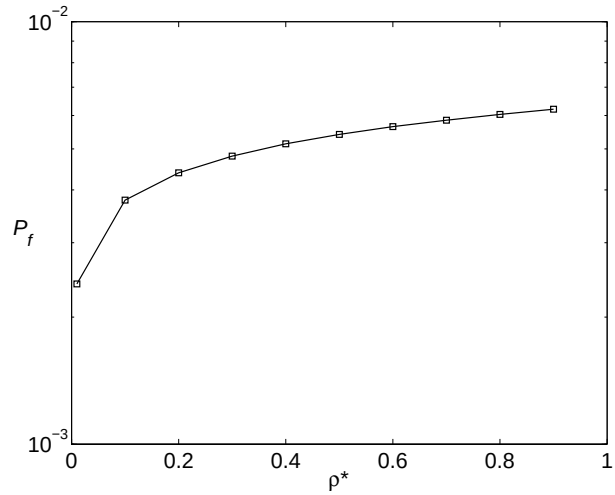

Figure 2: Probability of failure versus correlation length.

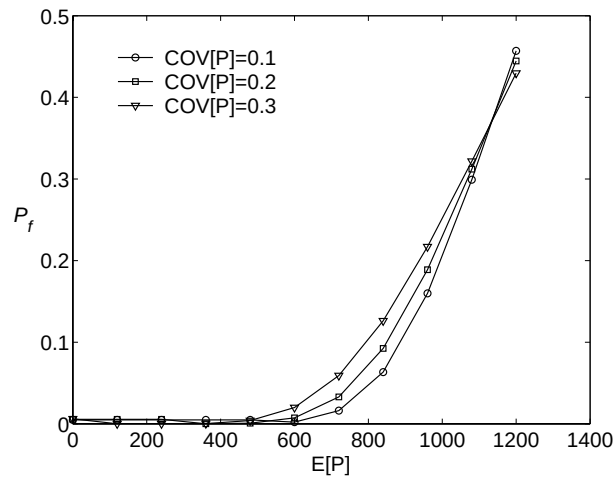

Figure 3: Probability of failure versus increasing edge load.

Influence of variation of the geometrical imperfection

Here the coefficient of variation of the magnitude of the geometrical imperfection, (23), is varied. The value of ρ^* is 0.5. The probability of failure is calculated for the interval of COV=0-0.4, see Figure 4.

It can be seen that the probability of failure is more sensitive to variations in the mean value, than variations in the coefficient of variation. It is also seen that an increasing coefficient of variation tends to strengthen the structure, for this load level.

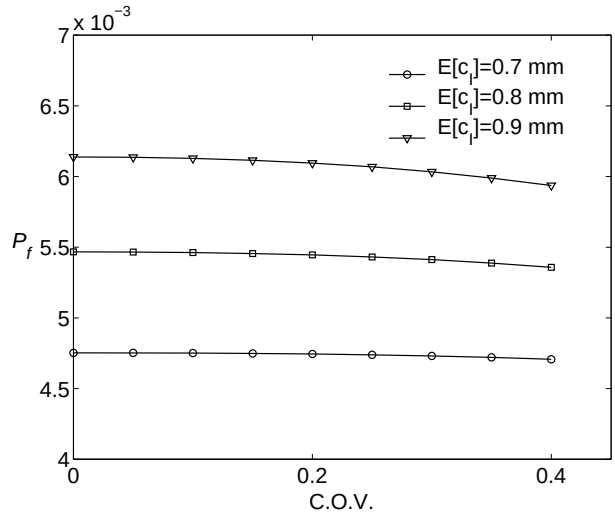

Figure 4: Probability of failure versus increasing coefficient of variation.

Conclusions

The reliability of geometrically non-linear composite shells are studied by a finite element procedure. The finite element formulation and kinematics of the shell element is described, as well as the finite difference method in order to find the gradients of the limit state function. The reliability of an in-plane loaded corrugated board panel, involving uncertainties in geometrical imperfection, material properties and load, is studied through numerical examples.

The composite shell element performs well compared to the measured results of corrugated board panels. It is observed that the FORM procedure used here is very suitable to determine the reliability of this kind of structures. It is also observed that the structure is more sensitive to variations in the mean value of parameters, than variations in the coefficient of variation.

References

[1] A. M. Hasofer and N. C. Lind. An Exact and Invariant First Order Reliability Format, Proc. ASCE, *J. Eng. Mech. Div.*, pp 111-121, (1974).

[2] H. O. Madsen, S. Krenk and N. C. Lind. *Methods of Structural Safety*, Prentice-Hall, New Jersey, (1986).

[3] D. M. Frangopol, Y-H. Lee and K. J. Williams. Nonlinear Finite Element Reliability Analysis of Concrete, *J. Eng. Mech.*, Vol. 122, No. 12., (1996).

[4] P-L. Liu and K-G. Liu. Selection of Random Field Mesh in Finite Element Reliability Analysis, *J. Eng. Mech.*, Vol. 119, No. 4., (1993).

[5] P-L. Liu and A. Der Kiureghian. Finite Element Reliability of Geometrically Nonlinear Uncertain Structures, *J. Eng. Mech.*, Vol. 117, No. 8., (1991).

[6] X. L. Guan and R. E. Melchers. A Load Space Formulation for Probabilistic Finite Element Analysis of Structural Reliability, *Probabilistic Engineering Mechanics*, 14, pp 73-81., (1999).

[7] F. Viadero, J. I. Bueno, L. N. Lopez de Lacalle and R. Sancibrian. Reliability Computation on Stiffened Plates, *Advances in Engineering Software*, **20**, pp 43-48., (1994).

[8] U. Nyman and P. J. Gustafsson. Material and Structural Failure Criterion of Corrugated Board Facings, *Composite Structures*, **50**(1), (2000).

[9] CALFEM 3.3. A finite element toolbox to MATLAB, Jabe Offset AB, Division of Structural Mechanics, Lund University, (1999).

[10] K. J. Bathe. Finite Element Procedures, Prentice Hall, Inc., USA, (1996).

[11] S. Ahmad et. al. Analysis of thick and thin shell structures by curved finite elements, *Int. J. Numer. Meths. Eng.*, 2, 419-451, (1970).

[12] A. Allansson and B. Svärd. Stability and Collapse of Corrugated Board; Numerical and Experimental Analysis, Master's thesis, Structural Mechanics, Lund University, (2001).

[13] U. Nyman and P. J. Gustafsson. Multilayer Composite Reliability Calculations on Corrugated Board, *Proceedings of the International Conference on Wood and Wood Fiber Composites*, April 13-15, Stuttgart, Germany, (2000).

[14] P. J. Gustafsson, et. al. A network mechanics failure criterion. *Report TVSM-7128*, Division of Structural Mechanics, Lund University (2000).

Paper IV

Buckling of Long Orthotropic Plates Including Higher-Order Transverse Shear

Ulf Nyman and Per Johan Gustafsson

Journal of Engineering Mechanics, Vol. 126, No. 12, 2000

BUCKLING OF LONG ORTHOTROPIC PLATES INCLUDING HIGHER-ORDER TRANSVERSE SHEAR

Ulf Nyman[1] and Per Johan Gustafsson[2]

ABSTRACT: The problem of buckling of long orthotropic plates under combined in-plane loading is considered. An approximate analytical solution is presented. The concept of a mixed Rayleigh-Ritz method is used considering higher-order shear deformations. The achieved load function of the half buckling wavelength and the inclination of the nodal lines is minimized via a simplex search method. For low transverse shear stiffnesses the model predicts buckling coefficients under in-plane shear load that are of the same order of magnitude as those resulting from a uniaxial compressive load. For a thin plate the critical shear load is larger by 42% compared to the uniaxial case. The model also suggests that for highly anisotropic materials, such as paper, the critical load solution is still influenced by the shear deformation effect at width-to-thickness ratios above 100.

Introduction

The use of paper as a structural member in a packaging environment has inspired research within the field of modeling corrugated panel structures subject to loads of various kinds. Local buckling of corrugated board facings is a limiting design principle of judgment for packages. Examples of work relating to buckling of the facing of a sandwich panel are mentioned in the following. Johnson and Urbanik (1989) analyzed composite plate structures under uniaxial compression and concluded that, in a triangular core sandwich, the facing initiates buckling. Analysis of an aluminum sheet sandwich plate made by Wittrick (1969) showed that buckling modes with inclined nodal lines (where out-of-plane deflection is equal to zero) are possible. Zahn (1973) studied an orthotropic truss core sandwich in axial compression. Anderson (1958) analyzed the instability of isotropic elements of a truss-core sandwich plate. Harris and Auelmann (1960) presented a buckling solution of finite plates subjected to combined in-plane loads using a first-order shear deformation theory. Norris and Kommers (1952) studied sandwich panels under combined loads.

Originally, instability was examined by a number of authors adopting the Kirchoff-Love assumption (thin plate theory). For plates with reasonable thickness or a very large elastic modulus to transverse shear modulus ratio, the buckling load is considerably over-estimated. Therefore, the plane stress assumption is relaxed and transverse shear stresses are considered. Highly anisotropic behavior is found for many fiber based materials, e.g.

[1]Division of Structural Mechanics, Lund University, PO Box 118, S-221 00 Lund, Sweden.
[2]Division of Structural Mechanics, Lund University, Sweden.

fiber reinforced composite materials, and for paper, with material stiffness ratios as high as 600 being reported (Persson 1991), compared to a typical ratio of 2.6 for isotropic materials. Consequently, the need for using refined plate theories including higher-order shear deformations is clear. A number of plate theories based on an assumed displacement field, taking out-of-plane shear effects into account, have been developed. The Reissner-Mindlin (1945) theory allows for deflection independent rotation of the plate cross-section during deformation. Bert and Chang (1972) introduced in the governing differential equations the slope at which the normal forces act on the plate cross section. However, since the theories assume a constant distribution of shear strains through the plate thickness, a correction factor is needed. An improved higher-order theory was presented by Levinson (1980) and Reddy (1984) where the shear stress distribution in the thickness direction follows a parabolic law, vanishing at the plate surfaces.

Exact solutions of some vibration and buckling problems based on the Reddy theory are presented by Reddy and Phan (1985). The buckling solution of the governing differential equations, for a uniaxial load case, is obtained by the Navier solution method. In the present paper the writers propose an approximate method to find the critical load of an orthotropic plate subjected to an arbitrary in-plane combination of homogeneous shear and compression. The solution makes use of a mixed Rayleigh-Ritz variational method in terms of the minimization procedure. In order to find the Ritz coefficients, the parameters associated with unique terms in the energy functional are first solved for in a linear sense. Successively, a load function is minimized with respect to the remaining parameters via a simplex search to find the critical load. The procedure is useful for obtaining a computationally efficient solution of the critical load. In order to solve the critical state, a numerical procedure is necessary for given material properties and load relations. This can easily be programmed by means of standard methods. The result from the critical state analysis can then be used in combination with a numerical method for structural analysis, such as the finite element method.

The obtained approximate solution is a linear interaction model which enables an arbitrary in-plane homogeneous stress state analysis. The solution is compared with numerical results gained from finite element analysis. The agreement is seen to be very good from an engineering point of view. The need for a computationally efficient solution of the critical load is obvious when the structure analyzed contains a large number of potential locations for buckling. An example structure is one made of corrugated core sandwich elements, e.g. Nyman and Gustafsson (1999).

Problem formulation

The analytical approach in the present study is based upon the principle of stationary total potential strain energy. The study here is restricted to infinitely long plates, see Figure 1, such as a structural member of a corrugated medium.

According to the Levinson and Reddy higher-order shear deformation theory, the plate

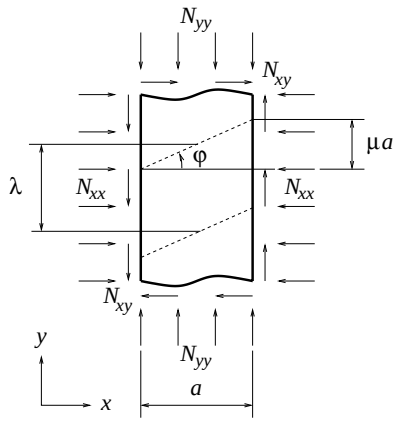

Figure 1: Partial strip of plate.

displacement field is given by

$$\begin{aligned} u &= u^0 + z\psi_x - \frac{4z^3}{3h^2}\left(w^0_{,x} + \psi_x\right) \\ v &= v^0 + z\psi_y - \frac{4z^3}{3h^2}\left(w^0_{,y} + \psi_y\right) \\ w &= w^0 \end{aligned} \tag{1}$$

where u^0, v^0 and w^0 are mid-plane displacements, ψ_x, ψ_y are mid-plane cross section rotations about the y-axis and x-axis respectively, and h is the thickness of the plate. Linearly independent displacement coordinate functions ϕ_i, consistent with the chosen boundary conditions, are used to introduce the displacement distributions

$$\psi_i = q_i\phi_i \qquad i = 1, 2, 3 \tag{2}$$

in which $\psi_1 = w(x, y), \psi_2 = \psi_x(x, y), \psi_3 = \psi_y(x, y)$.

Boundary conditions and coordinate functions

The kinematic boundary conditions of the strip are given by

$$\begin{aligned} \phi_1(x = 0) &= \phi_1(x = a) = 0 \\ \phi_3(x = 0) &= \phi_3(x = a) = 0 \end{aligned} \tag{3}$$

i.e. the strip has zero deflection w and rotation ψ_y at the longitudinal endlines. The nodal lines with zero deflection located in between two half wavelengths (buckling lengths) are assumed to be straight lines: $y = \mu x + p\lambda$ where μ indicates the inclination of the line, λ half the wavelength and $p = 1, 2 \ ... \ \infty$. Transformation of the cross section

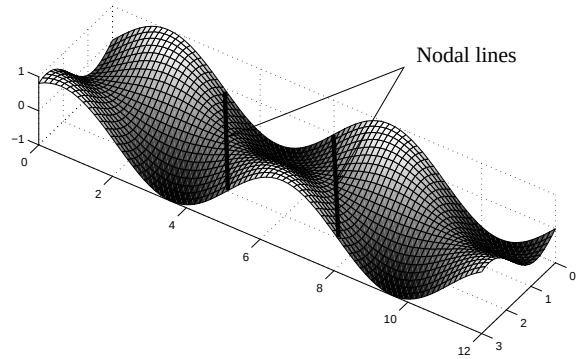

Figure 2: Transformed rotation coordinate function ϕ_2'.

rotations $\boldsymbol{\phi} = [\phi_2\ \phi_3]^T$ to the corresponding rotations in a coordinate system rotated counterclockwise $\varphi = \tan^{-1}(\mu)$ and indicated by $\{\ \}'$ is given by

$$\boldsymbol{\phi}' = \mathbf{A}\boldsymbol{\phi} \tag{4}$$

where the orthogonal transformation matrix $\mathbf{A}$ is given by

$$\mathbf{A} = \begin{bmatrix} \cos(\varphi) & \sin(\varphi) \\ -\sin(\varphi) & \cos(\varphi) \end{bmatrix} \tag{5}$$

Then, the boundary conditions of the joint edges of two half wavelengths in the y-direction are

$$\begin{aligned} &\phi_1(y = \mu x) = \phi_1(y = \mu x + p\lambda) = 0 \\ &\phi_2'(y = \mu x) = \phi_2'(y = \mu x + p\lambda) = 0 \qquad p = 1, 2, 3\ ...\ \infty \end{aligned} \tag{6}$$

i.e. periodic. Since the deflection derivative $\partial w/\partial x'$ is zero along the nodal lines, zero cross section rotation ψ_x' corresponds to zero shear stress σ_{13}'.

The cross section rotation distributions are assumed to have the same form as the deflection derivative, see Harris and Auelmann (1960), i.e. $\phi_2 \sim w^0_{,x}, \phi_3 \sim w^0_{,y}$. Then the present choice of coordinate functions ϕ_i is

$$\begin{bmatrix} \phi_1 \\ \phi_2 \\ \phi_3 \end{bmatrix} = \begin{bmatrix} \mathrm{Im}\, e^{i\frac{\pi}{a}x} \mathrm{Im}\, e^{i[\frac{\pi}{\lambda}(y-\mu x-p\lambda)]} \\ \frac{1}{a}\mathrm{Re}\, e^{i\frac{\pi}{a}x} \mathrm{Im}\, e^{i[\frac{\pi}{\lambda}(y-\mu x-p\lambda)]} - \frac{\mu}{\lambda}\mathrm{Im}\, e^{i\frac{\pi}{a}x} \mathrm{Re}\, e^{i[\frac{\pi}{\lambda}(y-\mu x-p\lambda)]} \\ \mathrm{Im}\, e^{i\frac{\pi}{a}x} \mathrm{Re}\, e^{i[\frac{\pi}{\lambda}(y-\mu x-p\lambda)]} \end{bmatrix} \tag{7}$$

In Figure 2 the transformed rotation coordinate function ϕ_2' is plotted over the plate domain.

Constitutive relations

The elastic orthotropic constitutive behavior is described by the stress-strain relation

$$\boldsymbol{\sigma} = \mathbf{D}\boldsymbol{\varepsilon} \tag{8}$$

or

$$\begin{bmatrix} \sigma_{11} \\ \sigma_{22} \\ \sigma_{12} \\ \sigma_{13} \\ \sigma_{23} \end{bmatrix} = \begin{bmatrix} D_{11} & D_{12} & D_{14} & D_{15} & D_{16} \\ & D_{22} & D_{24} & D_{25} & D_{26} \\ & & D_{44} & D_{45} & D_{46} \\ & sym. & & D_{55} & D_{56} \\ & & & & D_{66} \end{bmatrix} \begin{bmatrix} \varepsilon_{11} \\ \varepsilon_{22} \\ \gamma_{12} \\ \gamma_{13} \\ \gamma_{23} \end{bmatrix} \tag{9}$$

with

$$\begin{aligned} &D_{14} = D_{15} = D_{16} = D_{24} = D_{25} = D_{26} = D_{45} = D_{46} = D_{56} = 0 \\ &D_{11} = \frac{E_{11}}{1 - \nu_{12}\nu_{21}},\ D_{12} = \frac{\nu_{21}E_{11}}{1 - \nu_{12}\nu_{21}},\ D_{22} = \frac{E_{22}}{1 - \nu_{12}\nu_{21}} \\ &D_{44} = G_{12},\ D_{55} = G_{13},\ D_{66} = G_{23} \end{aligned} \tag{10}$$

where E, G and ν are material constants. It is here assumed that the material axes coincide with the coordinate axes of the plate. The kinematic relations are obtained by applying the small strain tensor format on (1)

$$\begin{aligned} \boldsymbol{\varepsilon} = \begin{bmatrix} \varepsilon_{11} \\ \varepsilon_{22} \\ \gamma_{12} \\ \gamma_{13} \\ \gamma_{23} \end{bmatrix} &= \begin{bmatrix} u_{,x} \\ v_{,y} \\ v_{,x} + u_{,y} \\ w_{,x} + \psi_x \\ w_{,y} + \psi_y \end{bmatrix} + z \begin{bmatrix} \psi_{x,x} \\ \psi_{y,y} \\ \psi_{y,x} + \psi_{x,y} \\ 0 \\ 0 \end{bmatrix} \\ -\tfrac{4z^2}{h^2} \begin{bmatrix} 0 \\ 0 \\ 0 \\ w_{,x} + \psi_x \\ w_{,y} + \psi_y \end{bmatrix} &- \tfrac{4z^3}{3h^3} \begin{bmatrix} w_{,xx} + \psi_{x,x} \\ w_{,yy} + \psi_{y,y} \\ \psi_{y,x} + \psi_{x,y} + 2w_{,xy} \\ 0 \\ 0 \end{bmatrix} \end{aligned} \tag{11}$$

Variational formulation

By defining the initial in-plane loading vector $\mathbf{N}$ for the plate

$$\mathbf{N} = \begin{bmatrix} N_{11} \\ N_{12} \\ N_{22} \end{bmatrix} \tag{12}$$

the energy varying during buckling can be obtained, e.g. Bazant (1991), by integrating over the plate region

$$U_1 = \frac{1}{2}\int\int_A N_{ij} w_{,i} w_{,j} dA \qquad i,j = 1,2 \tag{13}$$

$$U_2 = -\frac{1}{2}\int\int\int_V \sigma_{ij}\varepsilon_{ij} dV = -\frac{1}{2}\int\int\int_V \left[D_{11}\varepsilon_{11}^2 + 2D_{12}\varepsilon_{11}\varepsilon_{22} + D_{22}\varepsilon_{22}^2 + D_{44}\gamma_{12}^2\right] dV \qquad i,j = 1,2 \tag{14}$$

$$U_3 = -\frac{1}{2}\int\int\int_V G_{ij}\gamma_{ij}\gamma_{ij} dV \qquad i = 1,2;\ j = 3 \tag{15}$$

where U_1 is the pre-strain energy, U_2 is due to the in-plane stress and U_3 is due to the out-of-plane shear energy. To capture the correct integration of strain energy beyond the plate mid-plane, consideration must be given to the strain variation over the thickness h. In doing so, integration is done over the plate volume. The expressions (14) and (15) can be reduced to area integrals obtaining expressions in terms of the displacement distribution functions. If (2) is substituted in (11) and integration of (14) and (15) is performed over the plate thickness $-h/2..h/2$, the following is obtained

$$\begin{aligned} U_2 = -\frac{1}{2}\int\int_A &\frac{D_{ij}h^3}{315}\left(\frac{5}{4}w_{,ii}w_{,jj} - 4w_{,ii}\psi_{j,j} - 4w_{,jj}\psi_{i,i} + 17\psi_{i,i}\psi_{j,j}\right) \\ &+\frac{D_{kk}h^3}{315}(1-\delta_{ij})\left(\frac{5}{2}w_{,ij}w_{,ji} - 16w_{,ij}\psi_{i,j} + 17\psi_{i,j}\psi_{j,i} + 17\psi_{i,j}\psi_{i,j}\right) dA \end{aligned} \qquad i,j = 1,2;\ k = 4 \tag{16}$$

$$U_3 = -\frac{1}{2}\int\int_A \frac{8h}{15} G_{ij}\left(w_{,i} + \psi_i\right)^2 dA \qquad i = 1,2;\ j = 3 \tag{17}$$

where δ_{ij} is the Kronecker delta function.

The equilibrium condition of the plate can be expressed by a stationary first variation of energy. According to (13), (16) and (17) this is expressed as

$$\delta\Pi = 0 \quad \rightarrow \quad \frac{\partial\Pi}{\partial q_i} = 0 \quad i = 1,2,3, \tag{18}$$

Π being defined as the energy functional $\Pi = U_1 + U_2 + U_3$.

Sectional moments

The section quantity $\tilde{M}_{ij}$ is obtained by the definition

$$\tilde{M}_{ij} = \int_{-h/2}^{h/2} \sigma_{ij} z dz \qquad i,j = 1,2 \tag{19}$$

which yields the constitutive relations in terms of the plate

$$\tilde{M}_{ij} = \tilde{D}_{ij}\kappa_{ij}^D \tag{20}$$

where the flexural stiffness $\tilde{D}_{ij}$ is given by

$$\begin{bmatrix} \tilde{D}_{11} \\ \tilde{D}_{12} \\ \tilde{D}_{22} \end{bmatrix} = \frac{h^3}{12(1-\nu_{12}\nu_{21})} \begin{bmatrix} E_{11} \\ E_{12} \\ E_{22} \end{bmatrix} \tag{21}$$

and the bending deformation κ_{ij}^D

$$\begin{bmatrix} \kappa_{11}^D \\ \kappa_{12}^D \\ \kappa_{22}^D \end{bmatrix} = \frac{1}{5} \begin{bmatrix} w_{,11} - 4\psi_{1,1} + \nu_{21}(w_{,22} - 4\psi_{2,2}) \\ 2w_{,12} - 4(\psi_{2,1} + \psi_{1,2}) \\ \nu_{12}(w_{,11} - 4\psi_{1,1}) + w_{,22} - 4\psi_{2,2} \end{bmatrix} \tag{22}$$

Note that the tilde operator is used on $\tilde{M}_{ij}$ in order not to be confused with the stress resultant M_i given by Reddy (1984).

Resultant moments at the boundary

By recalling the transformation matrix given by (5), the section moments (20) transform according to

$$\tilde{\mathbf{M}}' = \mathbf{A}\tilde{\mathbf{M}}\mathbf{A}^T \tag{23}$$

The resulting moments $\tilde{M}_{11}$ and $\tilde{M}'_{22}$, upon the transformation (23),

$$\begin{aligned} &\tilde{M}_{11}(x=0) = \tilde{M}_{11}(x=a) \\ &\tilde{M}'_{22}(y=\mu x) = \tilde{M}'_{22}(y=\mu x + p\lambda) \qquad p = 1, 2, 3 \ldots \infty \end{aligned} \tag{24}$$

can be obtained from (20)-(22) and (2). It is concluded (calculations not shown here) that section moments develop, symmetrically distributed around the edge midpoints, with zero average value. This is due to the coordinate functions, inferring an approximate displacement field. The moments are proportional to the inclination of the nodal lines; thus the approximation disappears for the simply supported case when no shear load is present.

Buckling solution

In order to find the complete solution, the energy functional in (18) should be minimized with respect to both q_i and λ, μ. This produces a set of equations in q_i and λ, μ which are not linear. However, a non-linear equation system is undesirable since a numerical procedure required to find the critical solution would involve producing initial guess values. This is straightforward for λ and μ, whereas q_i are of more arbitrary form, making it difficult to find an automated solution process. Therefore the solution strategy chosen is first solving for q_i in a linear sense, and then using this solution to find the parameters λ and μ.

The expression for Π can be determined by evaluating (13), (16) and (17) for the given set of displacement functions. By then applying (18) on Π the following homogeneous equation system is obtained

$$\frac{\partial \Pi}{\partial q_j} = B_{ij} q_j = 0 \qquad i,j = 1,2,3 \tag{25}$$

with the coefficients

$$\begin{aligned}
B_{11} &= -\frac{c_1}{5040a^3h^2\lambda^3}\left[-5D_{11}c_1c_3h - 10a^2c_1c_2h(D_{12}+2D_{44}) - 5D_{22}a^4c_1h\right. \\
&\quad \left. -672a^2h\lambda^2(D_{55}c_2 + D_{66}a^2) + 1260a^2\lambda^2(N_{11}c_2 + 2N_{12}a^2\mu + N_{22}a^2)\right] \\
B_{12} &= \frac{\pi h}{315a^3\lambda^3}\left[-D_{11}c_1c_3 - a^2c_1c_2(D_{12}+2D_{44}) + 42D_{55}a^2c_2\lambda^2\right] \\
B_{13} &= -\frac{\pi h}{315a\lambda^2}\left[c_1c_2(D_{12}+2D_{44}) + D_{22}a^2c_1 - 42D_{66}a^2\lambda^2\right] \\
B_{22} &= \frac{h}{1260a^3\lambda^3}\left[17D_{11}c_1c_3 + 17D_{44}a^2c_1c_2 + 168D_{55}a^2c_2\lambda^2\right] \\
B_{23} &= \frac{17c_1c_2h}{1260a\lambda^2}(D_{12}+D_{44}) \\
B_{33} &= \frac{h}{1260a\lambda^3}\left[17D_{44}c_1(4a^4\mu^4 - 5a^2c_2\mu^2 - c_3)\right. \\
&\quad \left. +17D_{22}a^2c_1(c_2 - a^2\mu^2) + 168D_{66}a^2\lambda^4)\right] \\
B_{21} &= B_{12},\ B_{31} = B_{13},\ B_{32} = B_{23} \\
c_1 &= \pi^2h^2,\ c_2 = \lambda^2 + a^2\mu^2,\ c_3 = \lambda^4 + 6a^2\lambda^2\mu^2 + a^4\mu^4
\end{aligned} \tag{26}$$

By observing that B_{ij} in (25) is symmetric the following holds

$$\frac{\partial^2 \Pi}{\partial q_i \partial q_j} = \frac{\partial^2 \Pi}{\partial q_j \partial q_i} \tag{27}$$

and the symmetric property of the stiffness matrix is fulfilled, i.e. the system is conservative; see Bazant (1991) for a more thorough discussion of this subject. The critical state of (25) is given by the singularity condition on B_{ij}, i.e. $\det(B_{ij}) = 0$. Applying this and using the parameterization

$$\mathbf{N} = \begin{bmatrix} N_{11} \\ N_{12} \\ N_{22} \end{bmatrix} = \hat{N} \begin{bmatrix} \alpha \\ \beta \\ \chi \end{bmatrix} \tag{28}$$

the critical stress state is expressed by the load function

$$\hat{N}(\lambda,\mu) = \frac{G}{60a^2\lambda^2\left(c_2\alpha + 2a^2\beta\mu + a^2\chi\right)H} \tag{29}$$

where

$$G = \sum_{i=1}^{33} g_i \qquad H = \sum_{i=1}^{27} h_i \tag{30}$$

The coefficients g_i and h_i are given in Appendix.

The minimum of $\hat{N}$, $\hat{N}_{cr}$, is now exclusively determined by the parameters $\bar{x} = (\lambda/a, \mu)$, which are determined by a numerical minimization procedure. The procedure can be described by

1. Use starting values of $\bar{x}_0 = (\lambda_0/a, \mu_0)$. The appropriate ranges of these values are $1/2 \leq \lambda_0/a \leq 2$ and $0 \leq \mu_0 \leq 2$.

2. Evaluate with the current value of $\bar{x}$ the objective function $\hat{N} = \hat{N}(\bar{x})$. Determine the new values of $\bar{x}$ in terms of the Nelder-Mead simplex method.

3. Repeat step 2 until the termination tolerance is reached. The termination tolerance can be specified for either $\bar{x}$ or $\hat{N}(\bar{x})$.

4. The final value of $\bar{x} = \bar{x}_{cr}$ will yield the critical stress state $\hat{N} = \hat{N}_{cr}$.

The appropriate range of the starting values $\bar{x}_0$ will depend on the degree of orthotropy, and on the load condition. For the load cases studied here, numerical experience shows that choosing the lower limit $\bar{x}_0 = (1/2, 0)$ and the upper limit $\bar{x}_0 = (2, 2)$ is sufficient in order to find the critical solution $\bar{x}_{cr}$.

Numerical results for three materials

In the following, numerical results are presented for the case of three material constitutions under various load conditions. First, an isotropic material is considered, i.e. $\nu_{12} = \nu_{21} = 0.3$. Second, an orthotropic material with stiffness ratios $E_{11}/E_{22} = 2$, $E_{11}/G_{12} = 3$, $E_{11}/G_{13} = E_{11}/G_{23} = 30$ and $\nu_{12} = 0.2$ is considered. Finally, an orthotropic material, typical of corrugated board constituents, is examined. This last material has the same stiffness properties as the second material except that $E_{11}/G_{13} = 300$. The value of E_{11} is taken to be $E_{11} = 7$ GPa and $a = 7$mm, $h = a/20$ for all materials. A non-dimensionalized buckling coefficient is computed according to

$$\hat{K} = \frac{a^2 \hat{N}_{cr}}{\pi^2 \tilde{D}_{11}} (\alpha + \beta + \chi) \tag{31}$$

The termination tolerance used for the simplex search is 1×10^{-8} and 1×10^{-4} for $\bar{x}$ and $\hat{N}$, respectively. The results are presented in Tables 1, 2 and 3.

In addition, the influence of varying plate thickness is examined for the three materials. The results from this analysis are presented in Tables 4, 5 and 6.

In Table 1 it is seen that for $\alpha = \beta = 0, \chi = 1$, i.e. uniaxial load in the y-direction, the ratio of the half buckling wavelength to plate width λ/a is close to unity and the buckling coefficient is slightly lower than the classical plate solution $K = 4.0$. It should be pointed out that the load case $\beta = 0$, i.e. a biaxial load case, provides the exact solution as the displacement distribution functions in the present model have the same form as in Reddy and Phan (1985). Therefore, the top line values in Tables 1, 2 and 3 correspond to the exact solution of a long plate. As the shear stress increases, the inclination of the

Table 1: Nondimensionalized buckling coefficients for the isotropic material.

β	$\bar{x}^a$	$\hat{K}^a$	$\bar{x}^b$	$\hat{K}^b$	$\bar{x}^c$	$\hat{K}^c$
0	(0.993,0)	3.944	(1.281,0)	3.797	(16.815,0)	2.979
0.2	(0.998,0.099)	4.641	(1.279,0.096)	4.366	(7.205,0.08)	3.375
0.4	(1.01,0.188)	5.137	(1.274,0.184)	4.796	(4.034,0.157)	3.759
0.6	(1.025,0.262)	5.455	(1.267,0.257)	5.097	(2.909,0.227)	4.107
1	(1.056,0.369)	5.764	(1.255,0.365)	5.437	(2.073,0.339)	4.639
3	(1.135,0.564)	5.866	(1.23,0.563)	5.714	(1.43,0.556)	5.422
5	(1.162,0.619)	5.788	(1.223,0.618)	5.696	(1.335,0.616)	5.531
10	(1.185,0.664)	5.69	(1.217,0.664)	5.644	(1.271,0.663)	5.569
100	(1.208,0.707)	5.565	(1.212,0.707)	5.56	(1.217,0.707)	5.554

[a] $\alpha = 0, \chi = 1$
[b] $\alpha = 0.2, \chi = 1$
[c] $\alpha = 0.5, \chi = 1$

nodal line converges to $1/\sqrt{2}$, which is valid for a similar analytical analysis[3] of isotropic thin plates, e.g. Timoshenko and Gere (1961). As the stress in the x-direction increases, the half buckling wavelength will become infinitely large and the the buckling problem is similar to that of a hinged column member. However, it is obvious that for very large shear stresses the influence of the normal stresses has little significance. This load condition corresponds to the bottom row in Table 1.

In Table 2 the orthotropic material no. 2 is used. The transverse stiffness is reduced to 1/30 that of the Young's modulus in the x-direction. The value of λ/a in Table 2 is seen to decrease with decreasing transverse stiffness. As the shear load increases, the half buckling wavelength increases. It is seen that the final value of μ corresponding to $\beta = 100$ is lower than for the isotropic material.

The results from material no. 3 are presented in Table 3. The lowered transverse shear stiffness in the xz-plane results in a reduced buckling coefficient, for the case $\alpha = \beta = 0$ and $\chi = 1$, by 32% compared to material no. 2. The same comparison between materials no. 1 and no. 3 shows a reduced buckling coefficient of 56%. The value of μ when $\alpha = 0$ and $\beta = 100$, i.e. close to pure shear, for this material is larger than for both the isotropic material and material no. 2. This indicates that a low transverse shear stiffness will increase the inclination of the nodal lines. It is remarkable to note that for the case $\alpha = 0, \beta = 100$ the buckling coefficient is almost equal that of the pure uniaxial compression case $\alpha = \beta = 0$. This was not the case for the previously examined materials which showed an increased shear buckling coefficient. Both the orthotropic materials show less sensitivity to load in the x-direction in the sense of the solution of λ. In Tables 2 and 3, the last two columns represent the solution for the case $\alpha = 0.6, \chi = 1$. The isotropic material can only be analyzed until $\alpha = 0.5$ before λ becomes very large.

As a comparison with finite element results (Nyman and Gustafsson 1999), the values

[3] Nodal lines considered as straight.

Table 2: Nondimensionalized buckling coefficients for an orthotropic material, no. 2.

β	$\bar{x}^a$	$\hat{K}^a$	$\bar{x}^b$	$\hat{K}^b$	$\bar{x}^c$	$\hat{K}^c$
0	(0.795,0)	2.572	(1.059,0)	2.689	(2.263,0)	2.438
0.2	(0.798,0.078)	3.039	(1.056,0.076)	3.068	(2.166,0.067)	2.734
0.4	(0.804,0.151)	3.397	(1.048,0.147)	3.368	(1.956,0.131)	3.004
0.6	(0.813,0.214)	3.65	(1.038,0.21)	3.59	(1.746,0.191)	3.238
1	(0.831,0.312)	3.934	(1.018,0.307)	3.861	(1.458,0.288)	3.583
3	(0.883,0.504)	4.145	(0.972,0.503)	4.116	(1.093,0.498)	4.043
5	(0.902,0.56)	4.124	(0.959,0.56)	4.111	(1.027,0.558)	4.079
10	(0.919,0.607)	4.079	(0.949,0.607)	4.075	(0.981,0.607)	4.066
100	(0.936,0.652)	4.011	(0.939,0.652)	4.011	(0.942,0.652)	4.011

[a] $\alpha = 0, \chi = 1$
[b] $\alpha = 0.3, \chi = 1$
[c] $\alpha = 0.6, \chi = 1$

Table 3: Nondimensionalized buckling coefficients for an orthotropic material, no. 3.

β	$\bar{x}^a$	$\hat{K}^a$	$\bar{x}^b$	$\hat{K}^b$	$\bar{x}^c$	$\hat{K}^c$
0	(0.867,0)	1.751	(1.179,0)	1.761	(3.477,0)	1.519
0.2	(0.868,0.179)	2.03	(1.158,0.175)	1.984	(2.945,0.12)	1.704
0.4	(0.873,0.341)	2.165	(1.112,0.35)	2.104	(2.172,0.25)	1.864
0.6	(0.882,0.469)	2.204	(1.075,0.497)	2.144	(1.639,0.41)	1.976
1	(0.903,0.634)	2.177	(1.042,0.677)	2.128	(1.259,0.685)	2.036
3	(0.949,0.89)	1.973	(1.009,0.917)	1.959	(1.075,0.942)	1.938
5	(0.963,0.954)	1.892	(1.001,0.972)	1.886	(1.041,0.99)	1.877
10	(0.974,1.005)	1.818	(0.994,1.015)	1.817	(1.015,1.025)	1.814
100	(0.985,1.054)	1.742	(0.988,1.055)	1.742	(0.99,1.056)	1.742

[a] $\alpha = 0, \chi = 1$
[b] $\alpha = 0.3, \chi = 1$
[c] $\alpha = 0.6, \chi = 1$

Table 4: Influence of thickness for the isotropic material.

a/h	$\hat{K}^d$	$\hat{K}^e$	$\hat{K}^f$
5	3.232	4.589	4.207
10	3.784	5.499	5.254
40	3.986	5.833	5.646
80	3.996	5.851	5.666
100	3.998	5.853	5.669
500	4	5.856	5.673

Table 5: Influence of thickness for material no. 2.

a/h	$\hat{K}^d$	$\hat{K}^e$	$\hat{K}^f$
5	0.831	1.088	0.928
10	1.859	2.671	2.457
40	2.826	4.391	4.633
80	2.897	4.517	4.808
100	2.905	4.533	4.829
500	2.92	4.559	4.866

Table 6: Influence of thickness for material no. 3.

a/h	$\hat{K}^d$	$\hat{K}^e$	$\hat{K}^f$
5	0.508	0.497	0.345
10	1.01	1.069	0.771
40	2.443	3.546	3.309
80	2.778	4.26	4.379
100	2.827	4.364	4.546
500	2.917	4.552	4.854

of $\hat{K}^a$ from Table 3 are plotted[4] in Figure 3. It should be noted that the circles in Figure 3 are obtained from a numerical minimization of the parameters λ and μ, in the finite element procedure. In addition, the value of the buckling coefficient when neglecting the transverse shear, a material with large transverse shear modulus is studied, see the upper solid line in Figure 3. It is seen that the difference between considering and not considering the transverse shear is large for all of the analyzed load combinations.

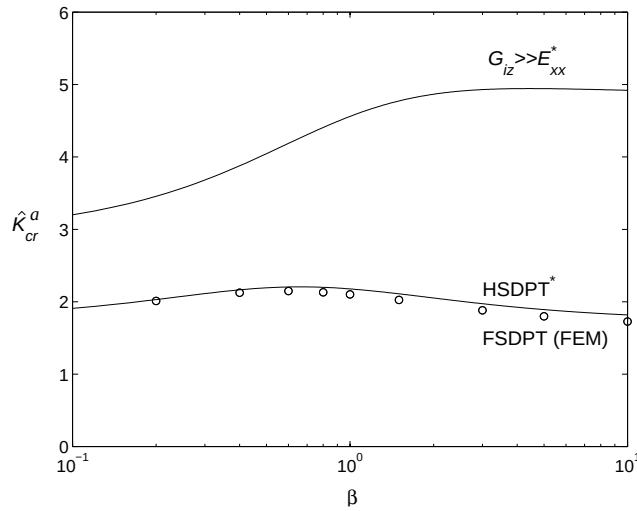

Figure 3: Buckling coefficient with increasing shear load. *Present model.

In Tables 4, 5 and 6 the superscripts d, e and f refer to $\alpha = \beta = 0, \chi = 1$ and $\alpha = 0, \beta = 1, \chi = 1$ and $\alpha = 0, \beta = 100, \chi = 1$, respectively. The results in Table 4 show that for the purely uniaxial load case the critical load converges to the thin plate solution between $10 < a/h < 40$. The same holds for the case of shear load, $\alpha = 0, \beta = 100, \chi = 1$. It is well-known that for isotropic plates, the critical load is fairly close to that of the thin plate solution when the width-to-thickness ratio is ~ 20. For material no. 2, Table 5, the value of the buckling coefficient levels out at $a/h = 80$. For material no. 3 the buckling coefficient has not yet reached a stable level at $a/h = 100$. In Figure 4 the results from Tables 4-6 are also plotted. The figure suggests that for highly anisotropic materials, the critical load solution is still influenced by the shear deformation effect at width-to-thickness ratios above 100. It is expected that the influence is even more significant if the transverse stiffness in the yz-plane is very low, i.e. the same order as G_{13}.

[4]HSDPT – Higher-order shear deformation plate theory.
FSDPT – First-order shear deformation plate theory.

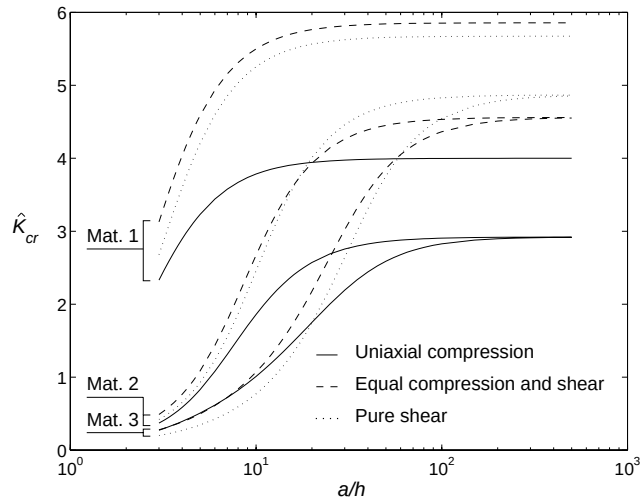

Figure 4: Buckling coefficient with increasing width-to-thickness ratio.

Concluding remarks

An approximate analytical buckling solution of long orthotropic plates under combined in-plane load is presented. A higher-order shear deformation theory is used for the plate displacement field. The solution makes use of a mixed Rayleigh-Ritz variational statement. The Ritz displacement coordinate functions are simple, one-term approximations of the displacement field. The achieved load function of the half buckling wavelength and the inclination of the nodal lines is minimized via a simplex search method.

For low transverse shear stiffnesses the model predicts buckling coefficients under in-plane shear load that are of the same order of magnitude as those resulting from a uniaxial compressive load. For a thin plate the critical shear load is larger by 42% compared to the uniaxial case. The model also suggests that that for highly anisotropic materials, the critical load solution is still influenced by the shear deformation effect at width-to-thickness ratios above 100.

For the analysis cases studied in this paper the present model provides an economic way of performing parameter studies on materials with different stiffness properties subject to various load conditions.

Acknowledgements

This work was supported by "Bo Rydins stiftelse för vetenskaplig forskning" [The Bo Rydin Foundation for Scientific Research] and by FPIRC - Forest Products Industry Research College.

References

[1] Anderson, M. S. (1958). "Local Instability of the Elements of a Truss-Core Sandwich Plate." *NACA Tech.,* Note 4292.

[2] Bazant, Z. P. (1991). "Stability of Structures." *Oxford University Press.*

[3] Bert, C. W., and Chang, S. (1972). "Shear-Flexible Orthotropic Plates Loaded In Plane." *J. Eng. Mech. Division,* Vol. 98, No. EM6, 1499-1509.

[4] Harris, L. A., and Auelmann, R. A. (1960). "Stability of flat simply-supported, corrugated-core sandwich plates under combined loads." *J. Aero/Space Sci.,* **27**, 7, 525-534.

[5] Johnson, M. W., and Urbanik, T. J. (1989). "Analysis of the Localized Buckling in Composite Plate Structures with application to Determining the Strength of Corrugated Fiberboard." *J. of Composites Technology and Research,* Vol. 11, No. 4, 121-127.

[6] Levinson, M. (1980). "An Accurate Simple Theory of the Statics and Dynamics of Elastic Plates." *Mech. Res. Communications,* 7, 343-350.

[7] Norris, C. B., and Kommers, W. J. (1952). "Critical loads of a rectangular, flat sandwich panel subjected to two direct loads combined with a shear load." FPL Report 1833.

[8] Nyman, U., and Gustafsson, P. J. (1999). "Local buckling of corrugated board facings." *Proceedings of the European Conference on Computational Mechanics,* Munich, Germany.

[9] Persson, K. (1991). "Material Model for Paper: Experimental and Theoretical Aspects." Diploma Report, Lund University, Sweden.

[10] Reddy, J. N. (1984). "A Simple Higher-Order Theory for Laminated Composite Plates." *J. Appl. Mech.,* 51(4), 745-752.

[11] Reddy, J. N., and Phan, N. D. (1985). "Stability and Vibration of Isotropic, Orthotropic and Laminated Plates According to a Higher-Order Shear Deformation Theory." *J. of Sound and Vibration,* **98**(2), 157-170.

[12] Reissner, E. (1945). "The Effect of Transverse Shear Deformation on the Bending of Elastic Plates." *J. Appl. Mech.,* 12, A69-A77.

[13] Seide, P. (1961). "Comments on: Stability of flat simply-supported, corrugated-core sandwich plates under combined loads." *J. Aerospace Sci.,* **28**, 3, 248.

[14] Timoshenko, S. P., and Gere, J. M. (1961). "Theory of Elastic Stability." *McGraw-Hill.*

[15] Wittrick, W. H., and Curzon, P. L. V. (1969). "Buckling of a Long Flat Panel with a Series of Equidistant Longitudinal Supports in Combined Longitudinal Compression and Shear." *The Aeronautical Quarterly.*

[16] Wittrick, W. H., and Curzon, P. L. V. (1969). "Nodal Lines for Long Plates in Combined Shear and Compression with Sinusoidal Edge Rotations." *The Aeronautical Quarterly*

[17] Zahn, J. J. (1973). "Local Buckling of Orthotropic Truss-Core Sandwich." Research paper, USDA Forest Service.

Appendix

Notation

$\mathbf{A}$ =Transformation matrix
D_{ij} =Stiffness matrix coefficients
$\tilde{D}_{ij}$ =Flexural stiffness
E_{ij} =Young's Modulus of Elasticity
G_{ij} =Shear Modulus
$\hat{K}$ =Nondimensionalized buckling coefficient
$\tilde{M}_{ij}$ =Section moment
$\mathbf{N}$ =In plane stress matrix
$\hat{N}$ =Parameterized critical stress
$\hat{N}_{cr}$ =Minimum critical stress
U_1 =Pre-strain energy
U_2 =In-plane normal strain energy
U_3 =Out-of-plane shear strain energy
a =Plate width
b =Plate length
h =Plate thickness
q_i =Amplitude functions
(u, v, w) =Plate displacement field
$\bar{x}$ =Vector of shape factors λ and μ
Π =Potential elastic energy
(α, β, χ) =Load parameters
δ =Variational operator
δ_{ij} =Kronecker delta function
ε_{ij} =Elastic strain tensor
ϕ_i =Displacement coordinate functions
κ_{ij}^D =Bending deformation
λ =Half buckling wavelength
μ =Inclination of nodal lines
ν_{ij} =Poisson's ratio
ψ_i =Displacement distribution functions

ψ_x, ψ_y =Cross section rotations
$\{\}_{,i}$ =Partial derivative with respect to coordinate i
$\{\}'$ =Transformed quantity
$\{\}^T$ =Transpose of matrix

Fraction coefficients

$$
\begin{aligned}
&g_1 = 17\pi^6 c_3^2 D_{11}^2 D_{22} a^2 h^7 \quad g_2 = 17\pi^6 c_2 c_3^2 D_{11}^2 D_{44} h^7 \\
&g_3 = 168\pi^4 c_3^2 D_{11}^2 D_{66} a^2 h^5 \lambda^2 \quad g_4 = -17\pi^6 c_3 c_2^2 D_{11} D_{12}^2 a^2 h^7 \\
&g_5 = 34\pi^6 c_2 c_3 D_{11} D_{12} D_{22} a^4 h^7 \quad g_6 = 336\pi^4 c_2 c_3 D_{11} D_{12} D_{66} a^4 h^5 \lambda^2 \\
&g_7 = 17\pi^6 c_3 D_{11} D_{22}^2 a^6 h^7 \quad g_8 = 102\pi^6 c_2 c_3 D_{11} D_{22} D_{44} a^4 h^7 \\
&g_9 = 14280\pi^4 c_2 c_3 D_{11} D_{22} D_{55} a^4 h^5 \lambda^2 \quad g_{10} = 14280\pi^4 c_3 D_{11} D_{22} D_{66} a^6 h^5 \lambda^2 \\
&g_{11} = 68\pi^6 c_3 c_2^2 D_{11} D_{44}^2 a^2 h^7 \quad g_{12} = 14280\pi^4 c_3 c_2^2 D_{11} D_{44} D_{55} a^2 h^5 \lambda^2 \\
&g_{13} = 14952\pi^4 c_2 c_3 D_{11} D_{44} D_{66} a^4 h^5 \lambda^2 \\
&g_{14} = 141120\pi^2 c_2 c_3 D_{11} D_{55} D_{66} a^4 h^3 \lambda^4 \\
&g_{15} = -34\pi^6 c_2^3 D_{12}^3 a^4 h^7 \quad g_{16} = -17\pi^6 c_2^2 D_{12}^2 D_{22} a^6 h^7 \\
&g_{17} = -136\pi^6 c_2^3 D_{12}^2 D_{44} a^4 h^7 \quad g_{18} = -14112\pi^4 c_2^3 D_{12}^2 D_{55} a^4 h^5 \lambda^2 \\
&g_{19} = -14112\pi^4 c_2^2 D_{12}^2 D_{66} a^6 h^5 \lambda^2 \quad g_{20} = 336\pi^4 c_2^2 D_{12} D_{22} D_{55} a^6 h^5 \lambda^2 \\
&g_{21} = -136\pi^6 c_2^3 D_{12} D_{44}^2 a^4 h^7 \quad g_{22} = -27888\pi^4 c_2^3 D_{12} D_{44} D_{55} a^4 h^5 \lambda^2 \\
&g_{23} = -27888\pi^4 c_2^2 D_{12} D_{44} D_{66} a^6 h^5 \lambda^2 \quad g_{24} = 282240\pi^2 c_2^2 D_{12} D_{55} D_{66} a^6 h^3 \lambda^4 \\
&g_{25} = 17\pi^6 c_2 D_{22}^2 D_{44} a^8 h^7 \quad g_{26} = 168\pi^4 c_2 D_{22}^2 D_{55} a^8 h^5 \lambda^2 \\
&g_{27} = 68\pi^6 c_2^2 D_{22} D_{44}^2 a^6 h^7 \quad g_{28} = 14952\pi^4 c_2^2 D_{22} D_{44} D_{55} a^6 h^5 \lambda^2 \\
&g_{29} = 14280\pi^4 c_2 D_{22} D_{44} D_{66} a^8 h^5 \lambda^2 \quad g_{30} = 141120\pi^2 c_2 D_{22} D_{55} D_{66} a^8 h^3 \lambda^4 \\
&g_{31} = 672\pi^4 c_2^3 D_{44}^2 D_{55} a^4 h^5 \lambda^2 \quad g_{32} = 672\pi^4 c_2^2 D_{44}^2 D_{66} a^6 h^5 \lambda^2 \\
&g_{33} = 564480\pi^2 c_2^2 D_{44} D_{55} D_{66} a^6 h^3 \lambda^4
\end{aligned} \tag{32}
$$

$$
\begin{aligned}
&h_1 = 289\pi^4 D_{11} D_{22} a^6 h^4 \mu^4 \quad h_2 = 1734\pi^4 D_{11} D_{22} a^4 h^4 \lambda^2 \mu^2 \\
&h_3 = 289\pi^4 D_{11} D_{22} a^2 h^4 \lambda^4 \quad h_4 = 289\pi^4 D_{11} D_{44} a^6 h^4 \mu^6 \\
&h_5 = 2023\pi^4 D_{11} D_{44} a^4 h^4 \lambda^2 \mu^4 \quad h_6 = 2023\pi^4 D_{11} D_{44} a^2 h^4 \lambda^4 \mu^2 \\
&h_7 = 289\pi^4 D_{11} D_{44} h^4 \lambda^6 \quad h_8 = 2856\pi^2 D_{11} D_{66} a^6 h^2 \lambda^2 \mu^4 \\
&h_9 = 17136\pi^2 D_{11} D_{66} a^4 h^2 \lambda^4 \mu^2 \quad h_{10} = 2856\pi^2 D_{11} D_{66} a^2 h^2 \lambda^6 \\
&h_{11} = -289\pi^4 D_{12}^2 a^6 h^4 \mu^4 \quad h_{12} = -578\pi^4 D_{12}^2 a^4 h^4 \lambda^2 \mu^2 \\
&h_{13} = -289\pi^4 D_{12}^2 a^2 h^4 \lambda^4 \quad h_{14} = -578\pi^4 D_{12} D_{44} a^6 h^4 \mu^4 \\
&h_{15} = -1156\pi^4 D_{12} D_{44} a^4 h^4 \lambda^2 \mu^2 \quad h_{16} = -578\pi^4 D_{12} D_{44} a^2 h^4 \lambda^4 \\
&h_{17} = 289\pi^4 D_{22} D_{44} a^6 h^4 \mu^2 \quad h_{18} = 289\pi^4 D_{22} D_{44} a^4 h^4 \lambda^2 \\
&h_{19} = 2856\pi^2 D_{22} D_{55} a^6 h^2 \lambda^2 \mu^2 \quad h_{20} = 2856\pi^2 D_{22} D_{55} a^4 h^2 \lambda^4 \\
&h_{21} = 2856\pi^2 D_{44} D_{55} a^6 h^2 \lambda^2 \mu^4 \quad h_{22} = 5712\pi^2 D_{44} D_{55} a^4 h^2 \lambda^4 \mu^2 \\
&h_{23} = 2856\pi^2 D_{44} D_{55} a^2 h^2 \lambda^6 \quad h_{24} = 2856\pi^2 D_{44} D_{66} a^6 h^2 \lambda^2 \mu^2 \\
&h_{25} = 2856\pi^2 D_{44} D_{66} a^4 h^2 \lambda^4 \quad h_{26} = 28224 D_{55} D_{66} a^6 \lambda^4 \mu^2 \\
&h_{27} = 28224 D_{55} D_{66} a^4 \lambda^6
\end{aligned} \tag{33}
$$

Paper V

Local Buckling of Corrugated Board Facings

Ulf Nyman and Per Johan Gustafsson

Proceedings of the European Conference on Computational Mechanics, Munchen, Germany, 1999

LOCAL BUCKLING OF CORRUGATED BOARD FACINGS

Ulf Nyman[1] and Per Johan Gustafsson[2]

ABSTRACT: Local buckling of corrugated board facings is studied numerically through finite element calculations. In addition, an analytical model is developed by the use of the Rayleigh-Ritz method. The facings are modeled as infinite orthotropic plates, resting on parallel free supports and subjected to an arbitrary in-plane stress state. The deflection shape is defined by wave length and displacement of the periodic deflection pattern. Transverse shear strain is considered by first (FEM) and higher order (analytical) shape functions. The results suggest that the low out-of-plane shear stiffness of paper significantly affect the critical load.

Introduction

Corrugated paper board, Figure (1a), is extensively used within the packaging industry as a load bearing structure. Its wide application is due to an outstanding strength/cost value. In addition, the use of raw material from a renewable resource strengthens its position. In this work, local buckling of the facings of the board is studied for general in-plane loading, Figure (1b). The purpose is to find a criterion for local buckling that enables assessment of risk of buckling from state of stress without need for extensive numerical calculations. Such a criterion is needed for rational evaluation of the stresses in various parts of a package as determined by, e.g., linear finite element analysis. An approximate analytical criterion is proposed and compared to finite element analysis. The analytical and numerical analyses are valid for orthotropic plates in a general homogeneous in-plane state of stress and particular considerations are made to the transverse out-of-plane shear strains and to the periodic local buckling pattern of a facing of large size.

The need for orthotropic material modeling and consideration to transverse shear deformation are due to the highly anisotropic stiffness properties of paper [10]. The ratio of the in-plane elastic modulus in the machine direction (MD) of paper to the elastic modulus in the cross-machine direction (CD) is typically in the order of 2, and as high ratio between elastic modulus in MD to transverse shear modulus as 600 is reported [10]. In the present analytical analysis the transverse shear is modeled by a higher order shear deformation theory according to Reddy [12] and Levinson (1980). In the numerical analysis, a finite element with constant shear strain according to the theory of Reissner is employed.

Research relating to buckling of corrugated paper board has recently been presented by Patel [1], including results from experiments on corrugated paper board cylinders

[1]Division of Structural Mechanics, Lund University, PO Box 118, S-221 00 Lund, Sweden.
[2]Division of Structural Mechanics, Lund University, Sweden.

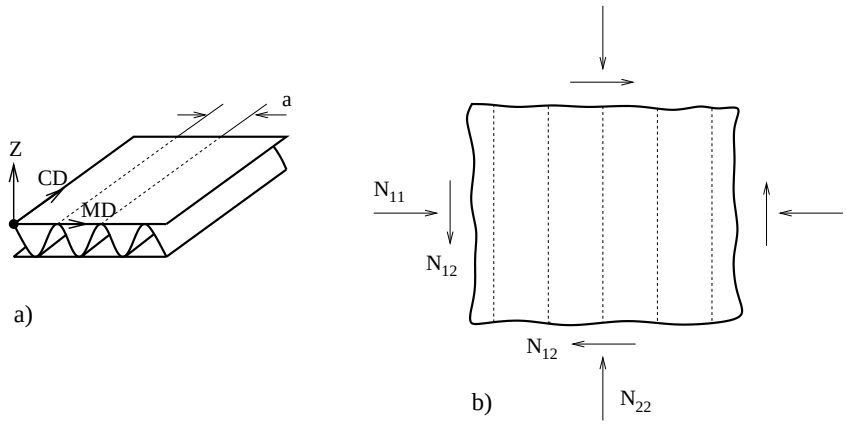

Figure 1: a) Corrugated paper board. b) Facing

subject to biaxial loading and also including references to previous studies of corrugated paper board. Previous theoretical buckling analyses that relate to the present study include work by Johnsson and Urbanik [2], who analyzed a triangular core sandwich under uniaxial compression and concluded that buckling was initiated by local buckling of the facing. Analysis of an isotropic aluminum sheet sandwich carried out by Wittrick and Curzon [3] showed that buckling modes with inclined nodal lines, where the out-of-plane deflection is zero, are possible. A study of the buckling of an in-plane orthotropic truss core sandwich in axial compression has been presented by Zahn [5].

Boundary conditions and periodicity

The plate under consideration is assumed to be of infinite size, Figure (1b), with free parallel supports at distance a. The deflection pattern at buckling can be assumed to be periodic with wavelength 2λ in the direction along the supports and may be assumed to repeat it self from one inter-support strip to the next. Though the inter-support deflection fields are equal, they are in general displaced, i.e. in different phase.

In the analytical analysis approximate boundary conditions are adopted. A cell of length λ and width a is considered, Figure (2a). The deflection along the boundaries of this cell is assumed to be zero, i.e. $w = 0$ along the support lines $x = 0$ and $x = a$ and along inclined nodal lines $y = \mu x$ and $y = \lambda + \mu x$. The height of the cell, λ, and the inclination of the nodal lines, μ, are found by minimization of the critical load. Conditions regarding bending moment and shear strain along the boundaries of the cell can be obtained from the below, where shape functions for deflection and shear strain are defined.

In the finite element analysis a rectangular cell of height λ and width a is considered, see Figure (2b). Along $x = 0$ and $x = a$, w is zero. Other boundary conditions are defined by subsidiary conditions according to the periodic and anti-symmetric character of the

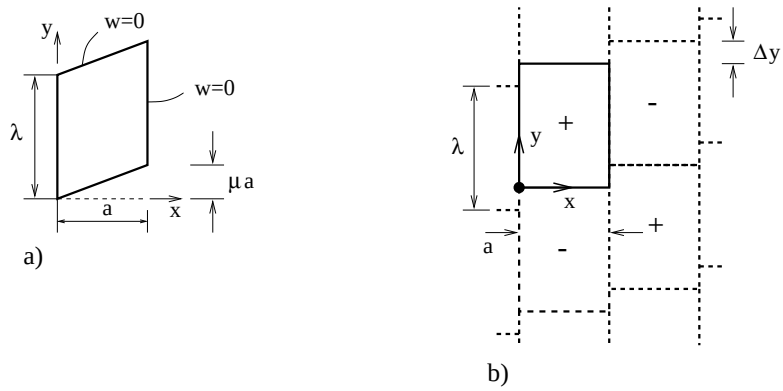

Figure 2: a) Periodic cell analyzed analytically. b) Periodic cell analyzed by FEM

deflection:

$$w(x,0) = -w(x,\lambda), \qquad \frac{\partial w}{\partial x}_{(x,0)} = -\frac{\partial w}{\partial x}_{(x,\lambda)}, \qquad \frac{\partial w}{\partial y}_{(x,0)} = -\frac{\partial w}{\partial y}_{(x,\lambda)} \tag{1}$$

and

$$\begin{aligned} \frac{\partial w}{\partial y}_{(0,y)} &= \frac{\partial w}{\partial y}_{(a,y-\lambda+\Delta y)}, & 0 < y < \lambda - \Delta y \\ \frac{\partial w}{\partial y}_{(0,y)} &= -\frac{\partial w}{\partial y}_{(a,y+\Delta y)}, & \lambda - \Delta y < y < \lambda \end{aligned} \tag{2}$$

Although all values > 0 of parameters λ and Δy yield buckling modes that are possible, only the pair of values that give the smallest critical load is of practical interest. The minimum of the critical load is determined numerically by FE calculations for various values of the parameters.

Analytical approach

The analytical approach in the present study is based upon the principle of stationary total potential strain energy. According to the higher order shear deformation theory due to Reddy [12], the plate displacement field is given by

$$\begin{aligned} u &= u^0 + z\psi_x - \frac{4z^3}{3h^2}\left(\frac{\partial w^0}{\partial x} + \psi_x\right) \\ v &= v^0 + z\psi_y - \frac{4z^3}{3h^2}\left(\frac{\partial w^0}{\partial y} + \psi_y\right) \\ w &= w^0 \end{aligned} \tag{3}$$

where u^0, v^0 and w^0 are mid-plane displacements and ψ_x, ψ_y are cross section rotations about the y-axis and x-axis respectively.

In order to introduce the displacement distribution over the plate region a Rayleigh-Ritz scheme is followed. Approximate displacement coordinate functions in consistency to the boundary conditions are used according to

$$\psi_i = q_i \phi_i \qquad i = 1, 2, 3 \tag{4}$$

in which $\psi_1 = w^{app}(x,y), \psi_2 = \psi_x^{app}(x,y), \psi_3 = \psi_y^{app}(x,y)$. The cross section rotation distributions are assumed to have the same form as the deflection derivative, i.e. $\phi_2 = w^0_{,x}, \phi_3 = w^0_{,y}$. This assumption was used by Harris and Auelmann [14] in analysis of plates considering first order shear deformation theory. Then the coordinate functions ϕ_i are given by

$$\begin{bmatrix} \phi_1 \\ \phi_2 \\ \phi_3 \end{bmatrix} = \begin{bmatrix} \mathrm{Im}\, e^{i\frac{\pi}{a}x} \mathrm{Im}\, e^{i[\frac{\pi}{\lambda}(y-\mu x - p\lambda)]} \\ \frac{1}{a}\mathrm{Re}\, e^{i\frac{\pi}{a}x} \mathrm{Im}\, e^{i[\frac{\pi}{\lambda}(y-\mu x - p\lambda)]} - \frac{\mu}{\lambda}\mathrm{Im}\, e^{i\frac{\pi}{a}x} \mathrm{Re}\, e^{i[\frac{\pi}{\lambda}(y-\mu x - p\lambda)]} \\ \mathrm{Im}\, e^{i\frac{\pi}{a}x} \mathrm{Re}\, e^{i[\frac{\pi}{\lambda}(y-\mu x - p\lambda)]} \end{bmatrix} \tag{5}$$

where $p(x)$ is a polynomial function of the nodal lines. In general, $p(x)$ is symmetric about a point centered in the x-direction. However, in this work the nodal lines are approximated as straight, i.e., $p(x) = \mu x$.

The elastic orthotropic constitutive behaviour is described by the stress-strain relation[3]

$$\boldsymbol{\sigma} = \begin{bmatrix} \sigma_{11} \\ \sigma_{22} \\ \sigma_{12} \\ \sigma_{13} \\ \sigma_{23} \end{bmatrix} = \boldsymbol{D}\boldsymbol{\varepsilon} = \begin{bmatrix} D_{11} & D_{12} & D_{14} & D_{15} & D_{16} \\ & D_{22} & D_{24} & D_{25} & D_{26} \\ & & D_{44} & D_{45} & D_{46} \\ & sym. & & D_{55} & D_{56} \\ & & & & D_{66} \end{bmatrix} \begin{bmatrix} \varepsilon_{11} \\ \varepsilon_{22} \\ \gamma_{12} \\ \gamma_{13} \\ \gamma_{23} \end{bmatrix} \tag{6}$$

with

$$\begin{aligned} &D_{14} = D_{15} = D_{16} = D_{24} = D_{25} = D_{26} = D_{45} = D_{46} = D_{56} = 0 \\ &D_{11} = \frac{E_{xx}}{1 - \nu_{xy}\nu_{yx}},\ D_{12} = \frac{\nu_{yx}E_{xx}}{1 - \nu_{xy}\nu_{yx}},\ D_{22} = \frac{E_{yy}}{1 - \nu_{xy}\nu_{yx}} \\ &D_{44} = G_{xy},\ D_{55} = G_{xz},\ D_{66} = G_{yz} \end{aligned} \tag{7}$$

where E, G and ν are material constants. It is here undertaken that the material axes coincide with the coordinate axes of the plate. The kinematic relations are obtained by applying the small strain tensor format on (3)

$$\begin{aligned} \boldsymbol{\varepsilon} = \begin{bmatrix} \varepsilon_{11} \\ \varepsilon_{22} \\ \gamma_{12} \\ \gamma_{13} \\ \gamma_{23} \end{bmatrix} &= \begin{bmatrix} u^0_{,x} \\ v^0_{,y} \\ v^0_{,x} + u^0_{,y} \\ w^0_{,x} + \psi_x \\ w^0_{,y} + \psi_y \end{bmatrix} + z \begin{bmatrix} \psi_{x,x} \\ \psi_{y,y} \\ \psi_{y,x} + \psi_{x,y} \\ 0 \\ 0 \end{bmatrix} \\ &- \tfrac{4z^2}{h^2} \begin{bmatrix} 0 \\ 0 \\ 0 \\ w^0_{,x} + \psi_x \\ w^0_{,y} + \psi_y \end{bmatrix} - \tfrac{4z^3}{3h^3} \begin{bmatrix} w^0_{,xx} + \psi_{x,x} \\ w^0_{,yy} + \psi_{y,y} \\ \psi_{y,x} + \psi_{x,y} + 2w^0_{xy} \\ 0 \\ 0 \end{bmatrix} \end{aligned} \tag{8}$$

[3]The stiffness coefficients where originally denoted A_{ij}

in which h denotes the thickness of the plate.

By defining the initial in-plane loading matrix $\mathbf{N}$ for the plate

$$\mathbf{N} = \begin{bmatrix} N_{11} \\ N_{12} \\ N_{22} \end{bmatrix} \tag{9}$$

the elastic strain energy varying during buckling can be obtained [7] by integrating over the plate region

$$U_1 = \frac{1}{2}\int\int_A N_{ij} w_{,i} w_{,j} dA \qquad i,j = 1,2 \tag{10}$$

$$U_2 = -\frac{1}{2}\int\int\int_V \sigma_{ij}\varepsilon_{ij} dV = -\frac{1}{2}\int\int\int_V \left[D_{11}\varepsilon_{11}^2 + 2D_{12}\varepsilon_{11}\varepsilon_{22} + D_{22}\varepsilon_{22}^2 + D_{44}\gamma_{12}^2\right] dV \qquad i,j = 1,2 \tag{11}$$

$$U_3 = -\frac{1}{2}\int\int\int_V G_{ij}\gamma_{ij}\gamma_{ij} dV \qquad i = 1,2;\ j = 3 \tag{12}$$

where U_2 is addressed to the in plane stress whereas U_3 is due to the out-of-plane shear stress. If (4) is substituted in (8) and integration of (11) and (12) is performed over the plate thickness from $z = -h/2$ to $z = h/2$, the following is obtained

$$\begin{aligned} U_2 = -\frac{1}{2}\int\int_A & \frac{D_{ij}h^3}{315}\left(\frac{5}{4}w_{,ii}w_{,jj} - 4w_{,ii}\psi_{j,j} - 4w_{,jj}\psi_{i,i} + 17\psi_{i,i}\psi_{j,j}\right) \\ & + \frac{D_{kk}h^3}{315}(1-\delta_{ij})\left(\frac{5}{2}w_{,ij}w_{,ji} - 16w_{,ij}\psi_{i,j} + 17\psi_{i,j}\psi_{j,i} + 17\psi_{i,j}\psi_{i,j}\right) dA \end{aligned} \qquad i,j = 1,2;\ k = 4 \tag{13}$$

$$U_3 = -\frac{1}{2}\int\int_A \frac{8h}{15} G_{ij}\left(w_{,i} + \psi_i\right)^2 dA \qquad i = 1,2;\ j = 3 \tag{14}$$

where δ_{ij} is the Kronecker delta function. The equilibrium condition of the plate can be expressed by a stationary first variation of energy. According to (10), (11) and (12) this is expressed as

$$\delta\Pi = 0 \quad \rightarrow \quad \frac{\partial\Pi}{\partial q_i} = 0 \quad i = 1,2,3 \tag{15}$$

Π being defined as the energy functional[4] $\Pi = U_1 + U_2 + U_3$.

In order to find the complete solution of the critical state the energy functional in (15) should be minimized with respect to both q_i and λ, μ. The approximative displacement coordinate functions given by (4) will produce a set of equations in w^{app}, ψ_x^{app} and ψ_y^{app} which are not linear. However, a non-linear equation system in q_i and λ, μ is not desired since a numerical procedure required to find the critical solution would involve producing initial guess values. This is straight forward for λ and μ, whereas q_i are of more arbitrary form making it difficult to find an automated solution process. Therefore the solution strategy chosen is first solving for q_i in a linear sense, and then use this solution to find the parameters λ and μ.

[4]Original sign convention; $\Pi = U_1 - U_2 - U_3$

The expression for Π can be determined by evaluating (10), (13) and (14) for the given set of displacement functions. By then applying (15) on Π the following homogeneous equation system is obtained

$$B_{ij}\psi_j = 0 \qquad i,j = 1,2,3 \tag{16}$$

where the coefficients B_{ij} are given in Appendix.

The critical state of (16) is given by the singularity condition on B_{ij}, i.e. $\det(B_{ij}) = 0$. Applying this and using the parameterization

$$\mathbf{N} = \hat{N} \begin{bmatrix} \alpha \\ \beta \\ \chi \end{bmatrix} \tag{17}$$

the critical stress state is expressed by the load function

$$\hat{N}(\lambda,\mu) = \frac{G}{60a^2\lambda^2\left(c_2\alpha + 2a^2\beta\mu + a^2\chi\right)H} \tag{18}$$

where

$$G = \sum_{i=1}^{33} g_i \qquad H = \sum_{i=1}^{27} h_i \tag{19}$$

The coefficients g_i, h_i and c_2 are given in Appendix.

The minimum of $\hat{N}$, $\hat{N}_{cr}$, is now only determined by the parameters $\bar{x} = (\lambda/a, \mu)$. In order to find the values of $\bar{x}$ that minimizes (18) a simplex search [8] is used.

Finite element setup

The finite element calculations are performed for the purpose of studying the character of the periodicity and finding the conditions under which the true critical load is present for the complete structure.

The two parameters to be studied are λ and Δy in Figure (2b). The variation of λ is performed by adding one element for each step considered. The application of the periodic boundary conditions as well as the reference edge loads is automatically created for every mesh. The variation of Δy is carried out by initially couple two horizontal nodes equally in magnitude but opposite sign, i.e. $\Delta y = 0$, for every mesh. Then a phase difference is incorporated by gradually increase the y-distance for which two nodes are coupled.

For the convenience, by means of programming, a four node linear interpolation element is chosen. The element incorporates constant shear deformation through the thickness. This makes the comparison with the analytical solution somewhat awkward but the only available since higher order shear elements are not implemented. The element has six degrees of freedom per node and uses reduced stiffness integration, see Hibbitt et al. [9]. Different mesh densities was tried for a uniaxially loaded simply supported quadratic plate and it was concluded that a 20×20 mesh only differed from the exact solution [13] by 1%, in terms of the critical load. Considering the large number of problems to solve, no finer resolution of the mesh was chosen for the parameter study.

The stiffness and geometrical properties, chosen as an example of representative properties for corrugated board facings, are listed in Table (7).

Parameter	*Value*
E_{xx}	7 [GPa]
E_{yy}	$E_{xx}/2$
G_{xy}	$E_{xx}/3$
G_{xz}	$E_{xx}/300$
G_{yz}	$E_{xx}/30$
ν_{xy}	0.2
a	7 [mm]
h	$a/20$ [mm]

Table 1: Stiffness and geometrical properties.

Results

In the following results are presented for the material parameters in Table (7). The reference load in the y-direction is held constant at $\chi = 1$ and the in-plane shear load is increased at steps in the interval $0 < \beta < 10$. For the purpose of comparison a non-dimensionalized buckling coefficient is computed according to

$$K_{cr} = \frac{a^2 \hat{N}_{cr}}{\pi^2 D_{11}} (\alpha + \beta + \chi) \tag{20}$$

In the FEM calculations λ/a is defined as the ratio of the number of elements in the y-direction to the number of elements in the x-direction. In a similar manner $\Delta y/a$ is defined as the ratio of the number of elements the phase shift is applied in the current solution to the number of elements in the x-direction. μ is measured in an approximate manner from the deformation plots, as the slope of the line between two points where $w = 0$, located at $x = 0.2\,a$ and $x = 0.8\,a$, respectively. An example of an array of unified cells is showed in Figure (3), where the absolute deformations larger than 1% of the maximum deformation is filtered for clarity.

For every set of reference loads the FEM parameter solution that yields the least buckling coefficient $\min(K) = K_{cr}$ is sought, together with the corresponding parameters $\Delta y/a$ and λ/a. An example of the buckling coefficient K calculated by FEM is given in Figure (4) for the case $\alpha = 0, \beta = 5$ and $\chi = 1$.

From Table (7) it is seen that when the normal load and shear load are of the same the same order of magnitude, the buckling coefficients from the different models are in good agreement. The discrepancy between the FEM solution and the approximate analytical solution is largest at $\beta = 10$, 5%. It should be noted that the case $\beta = 0, \chi = 1$, i.e. the two left columns in the upper row in (7), yields the exact solution, since no enforcement of the boundary conditions is inferred by assuming straight nodal lines.

It is marked that the phase shift $\Delta y/a$ differs from the value of μ for this material. However from Figure (4) it follows that the buckling coefficient is more sensitive for variations in λ than for variations in Δy. This is even more pronounced from the FEM calculations at low values of the shear load, which suggests that the plate can be approximated as finite in the x-direction, i.e. not considering the cyclic boundary conditions at

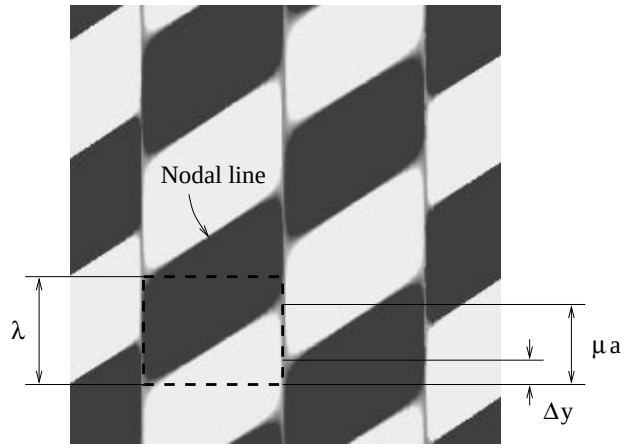

Figure 3: Out-of-plane deformation plot.

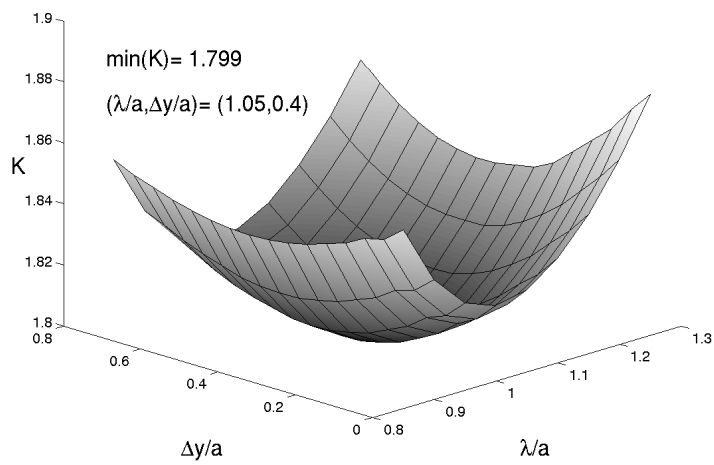

Figure 4: Buckling coefficient calculated by FEM.

the supports, during buckling analysis.

The values of K_{cr} with increasing shear load from Table (7) are also plotted[5] in Figure (5). As a comparison to the value of the buckling coefficient when neglecting the transverse shear, a material with large transverse shear modulus is studied, see the upper solid line in Figure (5). It is seen that the difference between considering and not considering

[5]HSDPT – Higher order shear deformation plate theory.
FSDPT – First order shear deformation plate theory.

β	$\Delta y/a$	$\bar{x}^a$	K^a_{cr}	$\bar{x}^b$	K^b_{cr}
0	0	(0.85,0)	1.742	(0.867,0)	1.751
0.2	0	(0.9,0.2)	2.011	(0.868,0.179)	2.03
0.4	0.1	(0.9,0.35)	2.125	(0.873,0.341)	2.165
0.6	0.2	(0.9,0.5)	2.147	(0.882,0.469)	2.204
0.8	0.25	(0.95,0.6)	2.131	(0.893,0.564)	2.199
1	0.3	(0.95,0.7)	2.101	(0.903,0.634)	2.177
1.5	0.3	(1,0.8)	2.025	(0.922,0.749)	2.11
3	0.35	(1,0.9)	1.881	(0.949,0.89)	1.973
5	0.4	(1.05,0.95)	1.799	(0.963,0.954)	1.892
10	0.45	(1.05,1.1)	1.726	(0.974,1.005)	1.818

[a]FEM
[b]Analytical model

Table 2: Nondimensionalized buckling coefficients.

the transverse shear is large for all of the analyzed load combinations. For the chosen material parameters the buckling coefficient is relatively constant with increasing in-plane shear load. When no transverse shear is present, i.e. pure bending, the buckling load is increased by 56% for the same load case.

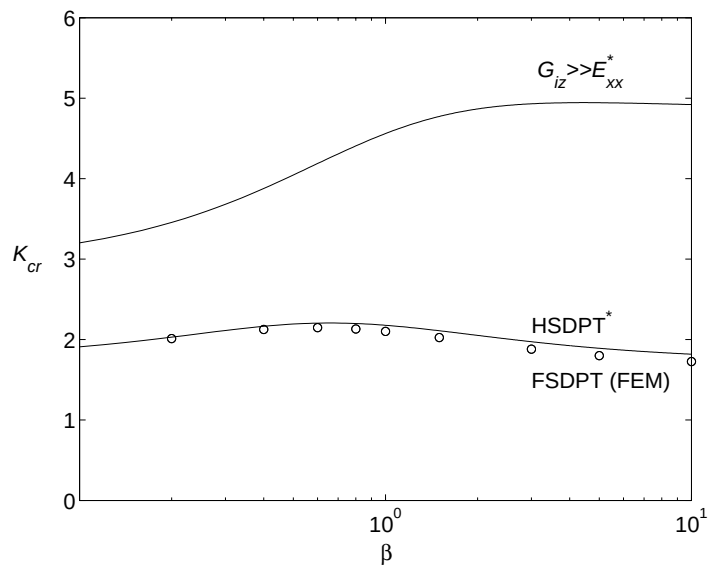

Figure 5: Buckling coefficient with increasing shear load. *Present model.

Conclusions

A method of finding the critical load for a transverse shear flexible plate subject to arbitrary in-plane load is developed. The plate is in the analytical model treated as long, simply supported along the long end lines. In the FEM calculations a cell periodically repeating itself is studied. Cyclic boundary conditions are applied along all edges of the cell. The proposed method is in good agreement with the results gained from the finite element analysis. The method also proves to be computationally efficient.

For the chosen material properties, representative that of paper, the buckling coefficient is significantly reduced by the transverse shear deformations, even though the plate width to thickness ratio is 20. For the uniaxial load case, the buckling coefficient is lowered by 39%, whereas under in plane shear load, the same reduction is 64%. It is observed that in contrast to the case when no shear deformations are considered, the buckling coefficient is relatively constant with increasing in plane shear load. When no transverse shear is present, i.e. pure bending, the buckling load is increased by 56% for the same load case.

References

[1] P. Patel. *Biaxial Failure of Corrugated Board.* KFS AB, (1996)

[2] M. W. Johnson and T. J. Urbanik. *Analysis of the Localized Buckling in Composite Plate Structures with application to Determining the Strength of Corrugated Fiberboard.* J. of Composites Technology and Research, Vol. 11, No. 4, pp. 121-127, (1989)

[3] W. H. Wittrick and P. L. V. Curzon. *Buckling of a Long Flat Panel with a Series of Equidistant Longitudinal Supports in Combined Longitudinal Compression and Shear.* The Aeronautical Quarterly, (1969)

[4] W. H. Wittrick and P. L. V. Curzon. *Nodal Lines for Long Plates in Combined Shear and Compression with Sinusoidal Edge Rotations.* The Aeronautical Quarterly, (1969)

[5] J. J. Zahn. *Local Buckling of Orthotropic Truss-Core Sandwich.* Research paper, USDA Forest Service, (1973)

[6] M. S. Anderson. *Local Instability of the Elements of a Truss-Core Sandwich Plate.* NACA Tech, Note 4292, July (1958)

[7] Z. P. Bazant *Stability of Structures.* Oxford University Press, (1991)

[8] J. A. Nelder and R. Mead. *A Simplex Method for Function Minimization*, Computer Journal, vol. 7, pp 308-313

[9] Hibbitt, Karlsson, Sorensen Inc., *ABAQUS/Standard Version 5.8*, Pawtucket, RI, (1998)

[10] K. Persson, *Material Model for Paper: Experimental and Theoretical Aspects*, Diploma Report, Lund University, Sweden, (1991)

[11] E. Reissner, *The Effect of Transverse Shear Deformation on the Bending of Elastic Plates*, J. Appl. Mech., 12, A69-A77, (1945)

[12] J. N. Reddy, *A Simple Higher-Order Theory for Laminated Composite Plates*, J. Appl. Mech., 51(4), 745-752, Dec. (1984)

[13] J. N. Reddy and N. D. Phan, *Stability and Vibration of Isotropic, Orthotropic and Laminated Plates According to a Higher-Order Shear Deformation Theory*, J. of Sound and Vibration, **98**(2), 157-170, (1985)

[14] L. A. Harris and R. A. Auelmann, *Stability of flat simply-supported, corrugated-core sandwich plates under combined loads.*, J. Aero/Space Sci., **27**, 7, pp 525-534 July (1960)

[15] P. Seide, *Comments on "Stability of flat simply-supported, corrugated-core sandwich plates under combined loads".*, J. Aerospace Sci., **28**, 3, p 248 March (1961)

Appendix

The coefficients B_{ij}

$$
\begin{aligned}
B_{11} &= -\frac{c_1}{5040a^3h^2\lambda^3}\left[-5D_{11}c_1c_3h - 10a^2c_1c_2h(D_{12}+2D_{44}) - 5D_{22}a^4c_1h\right. \\
&\quad \left. -672a^2h\lambda^2(D_{55}c_2 + D_{66}a^2) + 1260a^2\lambda^2(N_{11}c_2 + 2N_{12}a^2\mu + N_{22}a^2)\right] \\
B_{12} &= \frac{\pi h}{315a^3\lambda^3}\left[-D_{11}c_1c_3 - a^2c_1c_2(D_{12}+2D_{44}) + 42D_{55}a^2c_2\lambda^2\right] \\
B_{13} &= -\frac{\pi h}{315a\lambda^2}\left[c_1c_2(D_{12}+2D_{44}) + D_{22}a^2c_1 - 42D_{66}a^2\lambda^2\right] \\
B_{22} &= \frac{h}{1260a^3\lambda^3}\left[17D_{11}c_1c_3 + 17D_{44}a^2c_1c_2 + 168D_{55}a^2c_2\lambda^2\right] \\
B_{23} &= \frac{17c_1c_2h}{1260a\lambda^2}(D_{12}+D_{44}) \\
B_{33} &= \frac{h}{1260a\lambda^3}\left[17D_{44}c_1(4a^4\mu^4 - 5a^2c_2\mu^2 - c_3)\right. \\
&\quad \left. +17D_{22}a^2c_1(c_2 - a^2\mu^2) + 168D_{66}a^2\lambda^4)\right] \\
B_{21} &= B_{12},\ B_{31} = B_{13},\ B_{32} = B_{23} \\
c_1 &= \pi^2h^2,\ c_2 = \lambda^2 + a^2\mu^2,\ c_3 = \lambda^4 + 6a^2\lambda^2\mu^2 + a^4\mu^4
\end{aligned}
\tag{21}
$$

The fraction coefficients g_i and h_i

$$
\begin{aligned}
&g_1 = 17\pi^6 c_3^2 D_{11}^2 D_{22} a^2 h^7 \quad g_2 = 17\pi^6 c_2 c_3^2 D_{11}^2 D_{44} h^7 \\
&g_3 = 168\pi^4 c_3^2 D_{11}^2 D_{66} a^2 h^5 \lambda^2 \quad g_4 = -17\pi^6 c_3 c_2^2 D_{11} D_{12}^2 a^2 h^7 \\
&g_5 = 34\pi^6 c_2 c_3 D_{11} D_{12} D_{22} a^4 h^7 \quad g_6 = 336\pi^4 c_2 c_3 D_{11} D_{12} D_{66} a^4 h^5 \lambda^2 \\
&g_7 = 17\pi^6 c_3 D_{11} D_{22}^2 a^6 h^7 \quad g_8 = 102\pi^6 c_2 c_3 D_{11} D_{22} D_{44} a^4 h^7 \\
&g_9 = 14280\pi^4 c_2 c_3 D_{11} D_{22} D_{55} a^4 h^5 \lambda^2 \quad g_{10} = 14280\pi^4 c_3 D_{11} D_{22} D_{66} a^6 h^5 \lambda^2 \\
&g_{11} = 68\pi^6 c_3 c_2^2 D_{11} D_{44}^2 a^2 h^7 \quad g_{12} = 14280\pi^4 c_3 c_2^2 D_{11} D_{44} D_{55} a^2 h^5 \lambda^2 \\
&g_{13} = 14952\pi^4 c_2 c_3 D_{11} D_{44} D_{66} a^4 h^5 \lambda^2 \\
&g_{14} = 141120\pi^2 c_2 c_3 D_{11} D_{55} D_{66} a^4 h^3 \lambda^4 \\
&g_{15} = -34\pi^6 c_2^3 D_{12}^3 a^4 h^7 \quad g_{16} = -17\pi^6 c_2^2 D_{12}^2 D_{22} a^6 h^7 \\
&g_{17} = -136\pi^6 c_2^3 D_{12}^2 D_{44} a^4 h^7 \quad g_{18} = -14112\pi^4 c_2^3 D_{12}^2 D_{55} a^4 h^5 \lambda^2 \\
&g_{19} = -14112\pi^4 c_2^2 D_{12}^2 D_{66} a^6 h^5 \lambda^2 \quad g_{20} = 336\pi^4 c_2^2 D_{12} D_{22} D_{55} a^6 h^5 \lambda^2 \\
&g_{21} = -136\pi^6 c_2^3 D_{12} D_{44}^2 a^4 h^7 \quad g_{22} = -27888\pi^4 c_2^3 D_{12} D_{44} D_{55} a^4 h^5 \lambda^2 \\
&g_{23} = -27888\pi^4 c_2^2 D_{12} D_{44} D_{66} a^6 h^5 \lambda^2 \quad g_{24} = 282240\pi^2 c_2^2 D_{12} D_{55} D_{66} a^6 h^3 \lambda^4 \\
&g_{25} = 17\pi^6 c_2 D_{22}^2 D_{44} a^8 h^7 \quad g_{26} = 168\pi^4 c_2 D_{22}^2 D_{55} a^8 h^5 \lambda^2 \\
&g_{27} = 68\pi^6 c_2^2 D_{22} D_{44}^2 a^6 h^7 \quad g_{28} = 14952\pi^4 c_2^2 D_{22} D_{44} D_{55} a^6 h^5 \lambda^2 \\
&g_{29} = 14280\pi^4 c_2 D_{22} D_{44} D_{66} a^8 h^5 \lambda^2 \quad g_{30} = 141120\pi^2 c_2 D_{22} D_{55} D_{66} a^8 h^3 \lambda^4 \\
&g_{31} = 672\pi^4 c_2^3 D_{44}^2 D_{55} a^4 h^5 \lambda^2 \quad g_{32} = 672\pi^4 c_2^2 D_{44}^2 D_{66} a^6 h^5 \lambda^2 \\
&g_{33} = 564480\pi^2 c_2^2 D_{44} D_{55} D_{66} a^6 h^3 \lambda^4
\end{aligned} \tag{22}
$$

$$
\begin{aligned}
&h_1 = 289\pi^4 D_{11} D_{22} a^6 h^4 \mu^4 \quad h_2 = 1734\pi^4 D_{11} D_{22} a^4 h^4 \lambda^2 \mu^2 \\
&h_3 = 289\pi^4 D_{11} D_{22} a^2 h^4 \lambda^4 \quad h_4 = 289\pi^4 D_{11} D_{44} a^6 h^4 \mu^6 \\
&h_5 = 2023\pi^4 D_{11} D_{44} a^4 h^4 \lambda^2 \mu^4 \quad h_6 = 2023\pi^4 D_{11} D_{44} a^2 h^4 \lambda^4 \mu^2 \\
&h_7 = 289\pi^4 D_{11} D_{44} h^4 \lambda^6 \quad h_8 = 2856\pi^2 D_{11} D_{66} a^6 h^2 \lambda^2 \mu^4 \\
&h_9 = 17136\pi^2 D_{11} D_{66} a^4 h^2 \lambda^4 \mu^2 \quad h_{10} = 2856\pi^2 D_{11} D_{66} a^2 h^2 \lambda^6 \\
&h_{11} = -289\pi^4 D_{12}^2 a^6 h^4 \mu^4 \quad h_{12} = -578\pi^4 D_{12}^2 a^4 h^4 \lambda^2 \mu^2 \\
&h_{13} = -289\pi^4 D_{12}^2 a^2 h^4 \lambda^4 \quad h_{14} = -578\pi^4 D_{12} D_{44} a^6 h^4 \mu^4 \\
&h_{15} = -1156\pi^4 D_{12} D_{44} a^4 h^4 \lambda^2 \mu^2 \quad h_{16} = -578\pi^4 D_{12} D_{44} a^2 h^4 \lambda^4 \\
&h_{17} = 289\pi^4 D_{22} D_{44} a^6 h^4 \mu^2 \quad h_{18} = 289\pi^4 D_{22} D_{44} a^4 h^4 \lambda^2 \\
&h_{19} = 2856\pi^2 D_{22} D_{55} a^6 h^2 \lambda^2 \mu^2 \quad h_{20} = 2856\pi^2 D_{22} D_{55} a^4 h^2 \lambda^4 \\
&h_{21} = 2856\pi^2 D_{44} D_{55} a^6 h^2 \lambda^2 \mu^4 \quad h_{22} = 5712\pi^2 D_{44} D_{55} a^4 h^2 \lambda^4 \mu^2 \\
&h_{23} = 2856\pi^2 D_{44} D_{55} a^2 h^2 \lambda^6 \quad h_{24} = 2856\pi^2 D_{44} D_{66} a^6 h^2 \lambda^2 \mu^2 \\
&h_{25} = 2856\pi^2 D_{44} D_{66} a^4 h^2 \lambda^4 \quad h_{26} = 28224 D_{55} D_{66} a^6 \lambda^4 \mu^2 \\
&h_{27} = 28224 D_{55} D_{66} a^4 \lambda^6
\end{aligned} \tag{23}
$$

Paper VI

Material and Structural Failure Criterion of Corrugated Board Facings

Ulf Nyman and Per Johan Gustafsson

Composite Structures, Vol. 50, No. 1, 2000

MATERIAL AND STRUCTURAL FAILURE CRITERION OF CORRUGATED BOARD FACINGS

Ulf Nyman[1] and Per Johan Gustafsson[2]

ABSTRACT: A failure stress criterion for corrugated board facings is presented. The failure criterion is based on material failure and structural local buckling failure, which are evaluated in a combined analysis procedure. The failure stress is compared with collapse experiments on corrugated board cylinders and the failure stress presented herein is seen to be in much better agreement with the measured stresses than the Tsai-Wu failure criterion alone. The fluting wavelength of the corrugated board is also varied for the purpose of strength sensitivity analysis of corrugated board.

Introduction

The strength of corrugated board is of great importance within the industry. Accurate design methods are crucial in determining the load capacity of corrugated board. Strength analysis of corrugated board has previously been devoted to calculations on material failure criterions, such as the Tsai-Wu [8] tensor polynomial criterion and modifications of this [7].

Reduction of strength in the compressive region due to local instability of the facing has been found in several investigations [6, 3, 9], and recently, a buckling criterion for the facing was developed for evaluation of the bifurcation load given a general in-plane stress state [5]. For potential material failure points it is hence possible to determine the likeliness of local buckling. An example of buckling induced strength reduction in the compressive region is shown in Figure 1.

The development of the finite element method have led to largely extended opportunities by means of calculations on structural response. However, the detailed modeling of corrugated board is both demanding in terms of pre-processing as well as numerical intensive in the solution process. Therefore, a failure criterion for stress evaluation based on simplified finite element calculations, e.g. composite shell analysis, is vindicated. Herein, a comparison between material failure and structural failure is presented along with a method of determining which failure mode is decisive. Numerical results of a representative board are illustrated in figures for various biaxial stresses and shear stresses.

[1]Division of Structural Mechanics, Lund University, PO Box 118, S-221 00 Lund, Sweden.
[2]Division of Structural Mechanics, Lund University, Sweden.

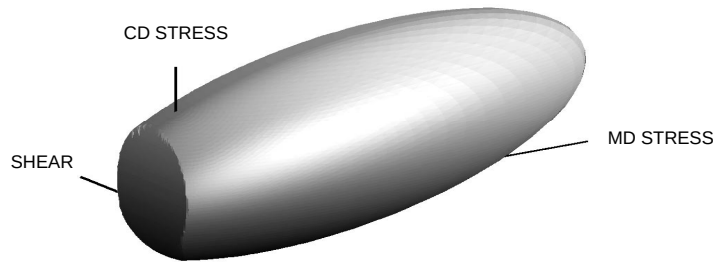

Figure 1: Reduction of strength in compressive region.

Choice of coordinate system

The in-plane stresses in the facings are referred to as normal stresses in the machine direction (MD) and cross direction (CD), and shear. However, for convenience, in further calculations the stresses σ_{11}, σ_{22} and σ_{12} will be used, ordered as previously, given in the coordinates x_1, x_2 and x_4.

Generally, material failure defines a limit surface about the origin in stress space $\{\sigma_{11}, \sigma_{12}, \sigma_{22}\}$. Therefore, in analyzing the in-plane stresses, it may be suitable to express the stresses in spherical coordinates. Then, the Cartesian stresses transform according to

$$\begin{aligned} \sigma_{11} &= \sigma^R \sin\phi \cos\theta \\ \sigma_{12} &= \sigma^R \sin\phi \sin\theta \qquad\qquad 0 \le \phi \le \pi,\ 0 \le \theta \le 2\pi \\ \sigma_{22} &= \sigma^R \cos\phi \end{aligned} \tag{1}$$

where σ^R is the length of a stress vector $\boldsymbol{\sigma}$, from the the origin O to the stress point S in stress space, i.e. $\sigma^R = \|\boldsymbol{\sigma}\|$. Moreover, ϕ is the angle $\boldsymbol{\sigma}$ makes with the positive direction of the x_2-axis, and θ is the angle between the plane containing S and the x_2-axis and the plane containing the x_1-axis and the x_2-axis, see Figure 2.

Material failure

A commonly used material failure criterion for paper is the Tsai-Wu orthotropic tensor polynomial [8]. In using the Tsai-Wu criterion, tensile and compressive strength parameters must be measured for both MD and CD. In addition, the shear strength and the equibiaxial tensile strength must be determined. The latter is determined by equally increasing the MD-stress and CD-stress to the limit state. However, approximations for the shear strength and equibiaxial strength have proven to be reasonable for paper [1].

The Tsai-Wu criterion for plane stress is given by

$$\Phi_{tw} = F_1\sigma_{11} + F_2\sigma_{22} + F_{11}\sigma_{11}^2 + F_{22}\sigma_{22}^2 + F_{66}\sigma_{12}^2 + 2F_{12}\sigma_{11}\sigma_{22} \le 1 \tag{2}$$

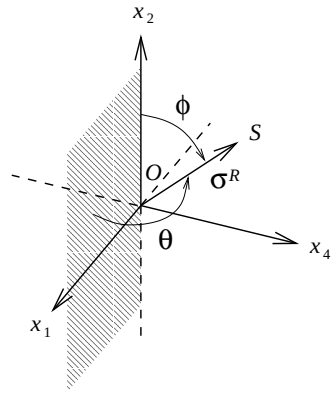

Figure 2: Coordinate system.

where

$$F_1 = \frac{1}{X_t} + \frac{1}{X_c}, \quad F_2 = \frac{1}{Y_t} + \frac{1}{Y_c}, \quad F_{11} = -\frac{1}{X_t X_c}, \quad F_{22} = -\frac{1}{Y_t Y_c}, \quad F_{66} = \frac{1}{T^2} \tag{3}$$

with the notation

$$\begin{aligned} X_t &= \text{Tensile strength in MD} \\ X_c &= \text{Compressive strength in MD} \\ Y_t &= \text{Tensile strength in CD} \\ Y_c &= \text{Compressive strength in CD} \\ T &= \text{Shear strength} \end{aligned} \tag{4}$$

An approximation for F_{12} is given by $F_{12} = f\sqrt{F_{11}F_{22}}$, where the constant $f = -0.36$ can be used for paper, see [1]. Moreover, the shear strength can be calculated as $T = \alpha\sqrt{X_c Y_c}$, where the parameter α can be derived using a maximum strain theory, where the compressive strengths X_c and Y_c are transformed to an equivalent shear stress, see [2]. The usefulness of the formulas for F_{12} and T is certainly justified by the difficulties emerging in corresponding experimental procedures.

Structural failure

The local buckling criterion given in [5] can be used to determine the stress state at which the facing becomes instable. The buckling equation is given by

$$\hat{N}_{cr} = \frac{\sum_{i=1}^{33} g_i}{60a^2\lambda^2\left(c_2\alpha + 2a^2\beta\mu + a^2\chi\right)\sum_{i=1}^{27} h_i} \qquad [\lambda, \mu] \in \mathbf{x}_{cr} \tag{5}$$

where α, β and χ relates to the MD-load, shear load and CD-load, respectively. Moreover, λ is the half buckling wavelength and μ is the inclination of nodal lines, indicating the

slope of the buckling deformation pattern. The parameter a denotes the wavelength of the corrugated core, where the corrugations are oriented in the facing machine direction. See [5] for the coefficients g_i and h_i.

In (5), $\mathbf{x}_{cr}$ is the solution of λ and μ at the buckling load, i.e. the bifurcation point. The solution $\mathbf{x}_{cr}$ is found by numerical minimization of the buckling load equation, which can be performed at points where buckling is suspected.

The buckling solution given in (5) relates to the edge load, i.e. force per unit length. The relation between the critical stress and the critical edge load is found from

$$\boldsymbol{\sigma}_{cr} = \begin{bmatrix} \sigma_{11} \\ \sigma_{12} \\ \sigma_{22} \end{bmatrix}_{cr} = \frac{1}{h}\mathbf{N}_{cr} = \frac{\hat{N}_{cr}}{h} \begin{bmatrix} \alpha \\ \beta \\ \chi \end{bmatrix} \tag{6}$$

in which h is the facing thickness.

Combined failure criterion

In order to determine which failure mode is most significant, material failure and structural failure must be compared. This seems to be of relevance when either some of the normal stresses is dominantly compressive or the shear stress is large. Below, the material failure criterion is reformulated followed by a similar modification of the structural failure criterion, i.e. the buckling equation.

Firstly, by using the transformation in (1), the Tsai-Wu criterion (2) takes the form

$$\begin{aligned} &(F_{11}\sin^2\phi\cos^2\theta + F_{22}\cos^2\phi + F_{66}\sin^2\phi\sin^2\theta + 2F_{12}\sin\phi\cos\phi\cos\theta)(\sigma_{tw}^R)^2 + \\ &(F_1\sin\phi\cos\theta + F_2\cos\phi)\sigma_{tw}^R - 1 = 0, \qquad\qquad \sigma_{tw}^R > 0 \end{aligned} \tag{7}$$

and the radius σ_{tw}^R can be found explicitly at a given stress state from (7), where ϕ and θ is given by the inverse of (1).

Next, in a similar manner, the buckling equation (5) can be rewritten using (1). As the load defined in (5) takes positive sign for compressive load, the normal in-plane loads change sign using the same convention as in (7). Moreover, the absolute value for shear load is used, due to symmetry. Then, (5) takes the form

$$\sigma_{cr}^R = \frac{\sum_{i=1}^{33} g_i}{60a^2h\lambda^2\left(-c_2 n_{11} + 2a^2\mu|n_{12}| - a^2 n_{22}\right)\sum_{i=1}^{27} h_i} \qquad \sigma_{cr}^R > 0,\ [\lambda,\mu] \in \mathbf{x}_{cr} \tag{8}$$

where

$$n_{11} = \sin\phi\cos\theta \qquad n_{12} = \sin\phi\sin\theta \qquad n_{22} = \cos\phi \tag{9}$$

To find the buckling load parameter σ_{cr}^R, 8 is minimized numerically with respect to λ and μ. This minimization is sensitive to the principles in how the initial values of $\mathbf{x}_{cr}$, $\mathbf{x}_0$, are chosen. By inspection of (8), it can be concluded that $\sigma^R(\lambda,\mu)$ is discontinuous at $\lim_{\sigma^R\to\infty}\mathbf{x}$. This is certainly expressed when the load changes from a dominant compressive σ_{11}-stress, yielding a very large buckling wavelength and zero inclination of nodal lines, to a shear buckling mode with $\lambda \approx a$ and non-zero μ. The relation between λ and

μ, at a given relation of stresses, by which $\sigma^R \to \infty$, can be obtained from (8). In order to find the true solution of σ^R, σ^R_{cr}, the initial values $\mathbf{x}_0$ must be chosen on both sides of the values $\lim_{\sigma^R \to \infty} \mathbf{x}$.

When analyzing the stresses in the facing, e.g. corrugated board design, the least of σ^R_{cr} and σ^R_{tw} should be chosen. This is done by defining the distance from the origin to the stress point at failure, either material failure or structural failure, as the failure stress radius σ^R_f

$$\sigma^R_f = \min\left\{\sigma^R_{tw}, \sigma^R_{cr}\right\} \tag{10}$$

In Figure 3 the failure stress radius is shown as the least envelope of material failure and structural failure. From a given state of stress $\boldsymbol{\sigma}$, provided by e.g. finite element analysis,

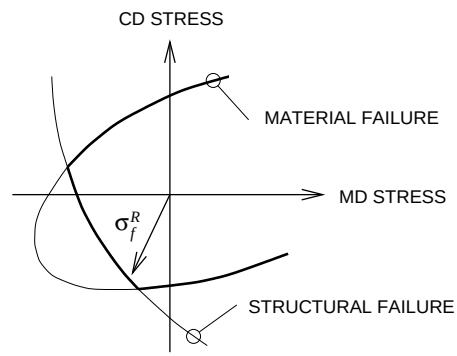

Figure 3: Failure stress radius.

a failure index Φ can be calculated

$$\Phi(\sigma_{11}, \sigma_{12}, \sigma_{22}) = \frac{||\boldsymbol{\sigma}||}{\sigma^R_f} \tag{11}$$

This failure index increases as the actual stress increases and takes the unity value at failure. It should be observed that the failure index, Φ, is not fundamentally the same as the Tsai-Wu index, Φ_{tw}, i.e. the left side of equation (2). Φ, but not Φ_{tw}, is proportional to the stress radius σ^R, defined in the second chapter.

The procedure for stress evaluation in a design process can be explained in the following chronological sequence

1. From finite element analysis, e.g. composite shell calculations, determine the stresses at various points of the corrugated panel. Perform the following steps for all of the points at which failure analysis is of interest.

2. Calculate by equation (1) the parameters ϕ and θ from the given MD stress, CD stress and shear stress.

3. Determine σ^R_{tw} by solving equation (7).

4. Determine the critical point, $\mathbf{x}_{cr}$ and σ_{cr}^R, by minimization of (5). For this minimization, a non-linear unconstrained procedure should be used, e.g. as provided by [4]. Choose the initial guesses of $\mathbf{x}$ as $\frac{1}{\rho}[a, 1]$, $\frac{1}{\rho}[a, \frac{1}{5}]$ and $\rho[a, \frac{1}{5}]$. Numerical experiments have shown that using $\rho = 10$ will provide the true solution $\mathbf{x}_{cr}$ and σ_{cr}^R.

5. Choose σ_f^R as the least of σ_{tw}^R and σ_{cr}^R and calculate the failure index Φ from equation (11).

Numerical example with experimental validation

In the following, an example of corrugated board is analyzed with respect to material failure and structural failure. Experimental data from [6] is used for comparison of measured collapse stresses versus the failure stress calculated by (10). In the reference, experiments are performed on cylinders which dimensions are sized to avoid global buckling. Furthermore, the influence of structural failure on overall collapse of the corrugated board and the change of failure stress with varied wavelength of the fluting is investigated. The board dimensions and experimental data of stiffnesses and strengths of the facing material are presented in Table 1.

Table 1: Experimental data of the facing material.

Board dimensions [mm]	Data from Patel et. al. [6][a]
Thickness, h	0.248
Wavelength of fluting, a	7.2
Tensile and compressive strengths [MPa]	
X_t	85.7
X_c	25.2
Y_t	35.2
Y_c	14.7
Stiffness properties [GPa]	
E_{11}	8.36
E_{22}	3.41
G_{12}	2.06
G_{13}	0.045
G_{23}	0.045
ν_{12}	0.17

[a] Average values of inner and outer liner, see [6].

The tensile and compressive properties from Table 1 are used for the solution of equation (7) and the board dimensions and stiffness properties are used for solution of (8). The parameter α, for the given relation of $X_c/Y_c = 1.71$, is calculated to $\alpha = 0.78$, which yields the shear strength $T = 15$ MPa. Since the measured stress values from [6] are

based on average stresses between the facings, the figures in Table 1 are also averaged for use in the failure calculations.

In Figure 4 the failure stress is plotted in the compressive $\{\sigma_{11}, \sigma_{22}\}$-region, i.e. $\sigma_{12} = 0$, together with the measured collapse stress and the Tsai-Wu envelope. It can be seen that

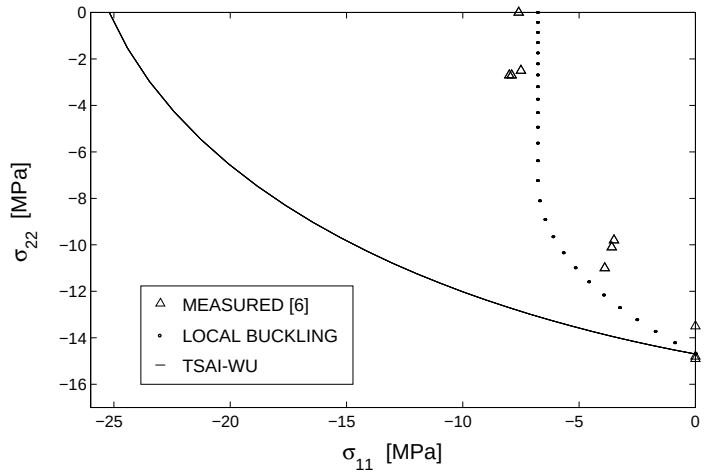

Figure 4: Failure stress in the compressive biaxial region, $\sigma_{12} = 0$.

the measured collapse stress fits very well to the failure stress radius, which is governed completely by local buckling in this stress region.

In Figure 5 the failure stress is plotted for combined shear and normal stress, i.e. σ_{22} versus σ_{12}. For this load combination it is seen that the failure stress radius is governed by material failure when the shear stress is large, and local buckling, or material failure, when the normal stress is large.

It may be useful to picture the failure stress radius for the general in-plane stress state, i.e. all stresses $\{\sigma_{11}, \sigma_{12}, \sigma_{22}\}$ non-zero. This is shown in Figure 6, where σ_{22} is plotted versus σ_{11} for various levels of σ_{12}. The shear stress levels are given as the outermost curve corresponding to the first value, $\sigma_{12} = 0$.

In Figure 7, the ratio of structural to material strength with decreasing fluting wavelength is plotted. A parameter η, defined by $a = a_0/\eta$, is used for lowering a from $a = a_0 = 7.2$ mm. The stress state is equibiaxial compressive, i.e. $\sigma_{11} = \sigma_{22}$, $\sigma_{11} \leq 0$ and $\sigma_{12} = 0$. This corresponds to the intersections of a straight line, forming 45 deg to the negative x-axis, and the curves corresponding to local buckling and Tsai-Wu failure in Figure 4. For values of $\eta \leq 1.4$, i.e. for $a \geq 5.1$ mm, the failure is seen to be governed by structural failure. At $a = 5.1$ mm, i.e. a 29% decrease of the fluting wavelength, the values of structural failure and material failure are equal. Note that for the stiffness parameters, typical for paper, a linear relation is found in Figure 7, i.e. $\sigma_{cr}^R \sim \frac{1}{a}$, while for isotropic thin plate bending a relation $\sigma_{cr}^R \sim \frac{1}{a^2}$ should be expected.

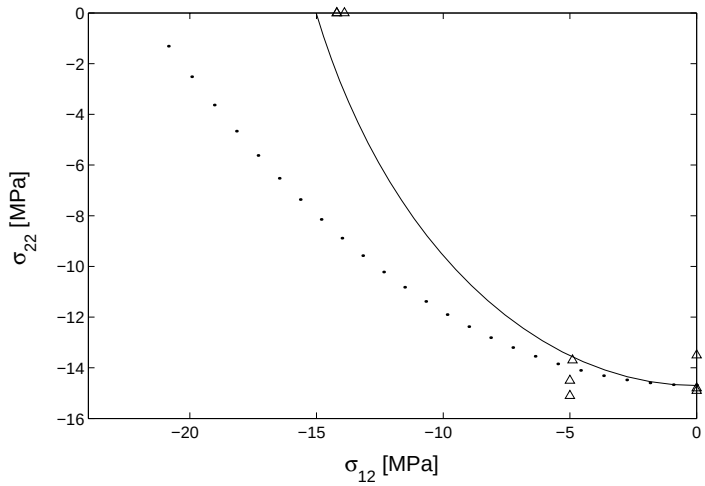

Figure 5: Failure stress in shear-compressive region, $\sigma_{11} = 0$.

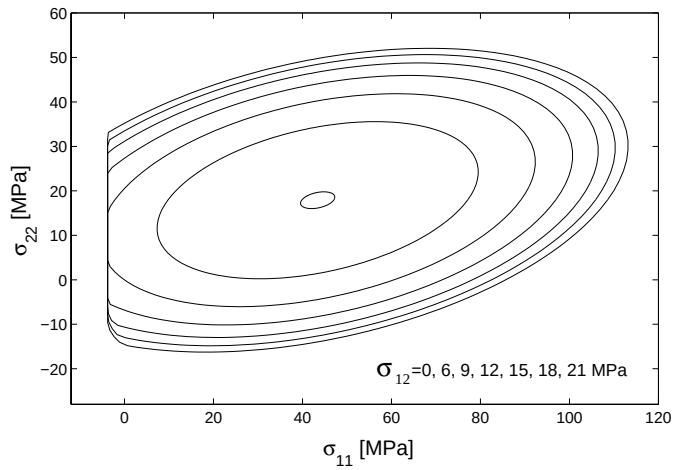

Figure 6: Failure stress for various shear levels.

Concluding remarks

A failure stress criterion for corrugated board facings has been presented. The criterion is based on material failure and structural failure, which are evaluated in a combined analysis procedure. The failure stress is compared with collapse experiments on corrugated board cylinders and the failure stress presented herein is seen to be in much better agreement with the measured stresses than the Tsai-Wu failure criterion alone. The procedure for finding the failure stress can be implemented in a finite element program for failure

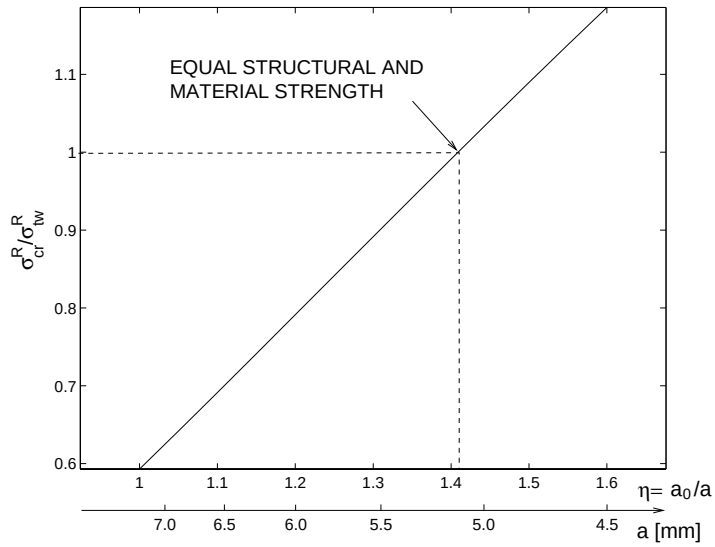

Figure 7: The ratio of structural to material strength with decreasing fluting wavelength for uniform biaxial compressive stress.

evaluation of e.g. corrugated containers.

Acknowledgements

The work herein was supported by "Bo Rydins stiftelse för vetenskaplig forskning" [The Bo Rydin Foundation for Scientific Research] and by FPIRC - Forest Products Industry Research College.

References

[1] C. Fellers, B. Westerlind and A. de Ruvo, *An Investigation of the Biaxial Failure Envelope of Paper: Experimental Study and Theoretical Analysis*. In Transaction of the Symposium, Cambridge, Vol. 1, pp. 527-559, (1983)

[2] P. J. Gustafsson, U. Nyman and S. Heyden, *A Network Mechanics Failure Criterion*. report TVSM-7128, Division of Structural Mechanics, Lund University, To be published

[3] M. W. Johnson and T. J. Urbanik, *Analysis of the Localized Buckling in Composite Plate Structures with application to Determining the Strength of Corrugated Fiberboard*. J. of Composites Technology and Research, Vol. 11, No. 4, pp. 121-127, (1989)

[4] MATLAB, *High Performance Numerical Computation and Visualization Software*. The Math Works Inc., Natick, Ma, USA, (1992)

[5] U. Nyman and P. J. Gustafsson, *Local buckling of corrugated board facings*. Proceedings of the European Conference on Computational Mechanics, Munich, Germany, (1999)

[6] P. Patel, T. Nordstrand, L. A. Carlsson, *Local Buckling and Collapse of Corrugated Board Under Biaxial Stress*. KFS AB, (1996)

[7] J. Tryding, *A Modification of the Tsai-Wu failure criterion of the Biaxial Strength of Paper*. Vol. 77, No. 8, Tappi Journal, (1994)

[8] S. W. Tsai and E. M. Wu, *A General Theory of Strength for Anisotropic Materials*. **5**, pp 58-80, J. Comp. Mater., (1971)

[9] J. J. Zahn, *Local Buckling of Orthotropic Truss-Core Sandwich*. Research paper, USDA Forest Service, (1973)

Paper VII

Multilayer Reliability Analysis of Corrugated Board

Ulf Nyman

Report, TVSM-3049, Structural Mechanics, Lund University, 2000

MULTILAYER RELIABILITY ANALYSIS OF CORRUGATED BOARD

Ulf Nyman[1]

ABSTRACT: The reliability of corrugated board is studied by finite element Monte Carlo simulations and by a first order reliability method, with the use of a failure criterion that includes both material failure and structural failure. The stiffness and strength parameters of the board are given as scalar multipliers of a geometrically distributed stochastic field. For the case of pure bending stresses, it is concluded that the failure is almost completely governed by structural failure. It is also seen that the board is very sensitive to compressive stresses in the machine direction (MD).

Introduction

The concept of reliability of engineering structures has focused increased attention during the last decades. In many applications one is interested in assessing the quality and safety of structures which may include strength and/or load variables that are represented by stochastic distributions. Basically, the establishment of structural reliability can be formulated by a limit state function, involving restrictions of a response quantity as well as the calculated response. The problem is devoted to determine the distribution parameters or the reliability index of the exceedance of structural strength to calculated response. The reliability index is a direct measure of the probability of failure.

Several methods are available for the settlement of the reliability index and the probability of failure. The methods can be classified as exact, e.g. Monte Carlo simulations (MCS), and approximative, e.g. First/Second Order Reliability Methods (FORM/SORM). In using the former example, a suitable number of samples are created as input variables to the structural model. The distribution for the limit state functions are then evaluated as the outcome from the MCS. In the latter example, the limit state functions are calculated in an iterative manner and the reliability index is directly obtained at the point of convergence. The usefulness of FORM/SORM is certainly expressed when the limit state function involves only a single performance quantity, for example the maximum displacement allowed at a generic point. Then, a reliability solution is achieved to a comparably low computational cost.

The treatment of the reliability of corrugated board, Figure 2, has received little attention so far. Previously, work has been devoted to deterministic calculations. The need for predicting the strength of packages/corrugated board has led to the development of various models in order to characterize the board, e.g. [2, 5, 6]. The aim of this paper is to present an analysis of corrugated board for which the reliability is studied by finite

[1]Division of Structural Mechanics, Lund University, PO Box 118, S-221 00 Lund, Sweden.

element MCS and FORM. It is also the aim to investigate the applicability of FORM to finite element analysis in terms of accuracy, complexity and numerical efficiency. The report presented here is an extension of the work presented in [1], where only MCS was performed.

Variations in material parameters due to variations in strength variables such as moisture exposure is considered to affect the overall board performance. As stochastic variables are chosen the stiffness matrix components and the material directional strengths. A stochastic field is applied as a geometrical distribution of the variables. The failure criterion presented in [4], which was proven to provide an accurate agreement of the board failure compared to test data, is used in the settlement of the limit state functions. In the analysis, the variation of the probability of failure due to different extent of correlation at a certain length, is examined. Furthermore, studies of the likeliness of failure at specific geometrical points of the board are performed.

Limit state functions

The failure of corrugated board is assumed to take place in either of the facings. Studies of the board behaviour [2, 8, 9] prior and at the moment of collapse strongly indicates that the failure is influenced by local stability. In [4] a combined failure criterion was developed, based on the calculation of a failure stress radius. From a sandwich plate stress estimation, a failure mode evaluation can be done whether the failure stress radius is due to material or structural failure. For the stress state in an outer layer, a limit state function can be formulated for each random field element i as

$$g(\boldsymbol{\alpha}_i) = \sigma_f^R(\boldsymbol{\alpha}_i) - \sigma^R(\boldsymbol{\alpha}_i) \leq 0 \tag{1}$$

where σ^R is the evaluated stress radius, σ_f^R is the failure stress radius and $\boldsymbol{\alpha}_i$ are the stochastic variables.

Structural failure surface

If the number of elements is large, or a large amount of simulations are performed, the calculation of the structural failure stress radius may be costly. However, from [4] it was concluded that most of the part of the surface defining structural failure, interior material failure, is a plane surface. In [1], the failure due to instability was given by the stress plane corresponding to a constant stress $\sigma_{11} = k_{cr}$ in the first direction (MD). This is the critical stress corresponding to uniaxal structural failure. An explicit expression for k_{cr} is then found as the limit value

$$k_{cr} = \lim_{\lambda \to \infty,\, \mu = 0} \sigma^R(\mathbf{n} = [-1, 0, 0]), \quad k_{cr} < 0 \tag{2}$$

where $\mathbf{n}$ is the directional stress vector, $\mathbf{n} = [n_{11}, n_{12}, n_{22}]$ (unit vector), and λ and μ are the half buckling wavelength in the second direction (CD) and slope of nodal lines [4], respectively. Then the critical stress radius is given by

$$\sigma_{cr}^R = \frac{k_{cr}}{n_{11}}, \quad \sigma_{cr}^R > 0 \tag{3}$$

However, in a reliability analysis using minimization algorithms, the open failure surface defined by (2) might cause numerical problems when the initial search values are chosen far apart from the minimum distance point. Therefore, the plane is substituted for by a quadratic closed surface according to

$$(\sigma_{11} - b)^2 + \sigma_{12}^2 + \sigma_{22}^2 = R^2 \tag{4}$$

where R is assigned some large value and b should be given so as to fulfil

$$R - b = |k_{cr}|, \quad R > b \tag{5}$$

Since n_{11} is less than zero for structural failure to take place, and σ_{cr}^R must be positive, the critical stress radius is given by

$$\sigma_{cr}^R = bn_{11} + \sqrt{b^2 n_{11}^2 + R^2 - b^2} \tag{6}$$

It is worth noting that the larger R is chosen, the more (6) will approach (3). However, in order not to create a badly conditioned problem, R should be chosen as a reasonable factor of $|k_{cr}|$, for example as $R = 5|k_{cr}|$.

Finite element response

In the solution of the reliability index for a given material point, or random field element, it is required to achieve the gradient of (1) at each iteration point in the minimization procedure. This involves the calculation of the stresses as function of the stochastic variables, which could be achieved by a series expansion of the response variables. In this work, however, the determination of the gradients of the limit state function is performed by the full finite element solution, i.e. numerically. The procedure is to solve $\mathbf{a}^{(k)}(\boldsymbol{\alpha}_i)$ from

$$\mathbf{K}^{(k)}(\boldsymbol{\alpha}_i)\mathbf{a}^{(k)}(\boldsymbol{\alpha}_i) = \mathbf{f}^{(k)}(\boldsymbol{\alpha}_i) \tag{7}$$

at the iteration points k. The stresses are then given by

$$\boldsymbol{\sigma}^{(k)}(\boldsymbol{\alpha}_i) = \mathbf{D}^{(k)}(\boldsymbol{\alpha}_i)\boldsymbol{\varepsilon}^{(k)}(\boldsymbol{\alpha}_i) = \mathbf{D}^{(k)}(\boldsymbol{\alpha}_i)\mathbf{B}\mathbf{a}^{(k)}(\boldsymbol{\alpha}_i) \tag{8}$$

from where the failure stress radius can be calculated for evaluation of the limit state function.

The solution of (7) is obtained as the Cholesky decomposition of $\mathbf{K}^{(k)}$

$$\mathbf{K}^{(k)} = \left(\mathbf{G}\mathbf{G}^T\right)^{(k)} \tag{9}$$

where $\mathbf{G}$ is a lower triangular matrix. Further on, $\mathbf{a}^{(k)}$, can be determined by the solution of the triangular systems

$$\begin{aligned} \mathbf{G}^{(k)}\tilde{\mathbf{a}}^{(k)} &= \mathbf{f}^{(k)} \\ \left(\mathbf{G}^T\right)^{(k)}\mathbf{a}^{(k)} &= \tilde{\mathbf{a}}^{(k)} \end{aligned} \tag{10}$$

It is interesting to observe that, if the load variables are the only variables that contain uncertainties, the stiffness matrix will not change during the iterations and the Cholesky decomposition in (9) needs to be done only initially. This is attractive in terms of the computation time required for the iteration process.

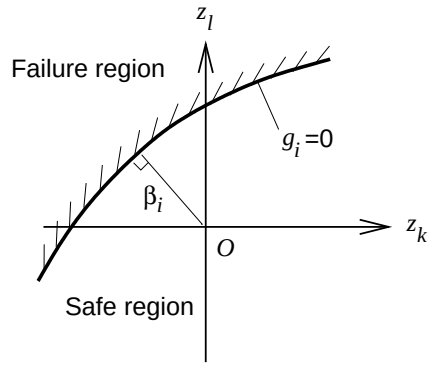

Figure 1: Reliability index in z-coordinate system.

FORM procedure for calculation of reliability indices

For reasons that will be obvious in the next section the basic variables will now be denoted as $\mathbf{x}$, instead of $\boldsymbol{\alpha}$ as before. Initially, the basic variables, $\mathbf{x}$, may not be normally distributed. In a FORM procedure, it is required that the variables $\mathbf{x}$ are transformed from the initial distribution to an equivalent normal distribution. This can be done approximately, e.g. by the transformation given by Rackwitz and Fiessler [11]. If the basic variables are log-normally distributed, an exact mapping is possible by using

$$\mathbf{y} = \log \mathbf{x} \tag{11}$$

and determining the parameters

$$\begin{aligned} \mathrm{E}[y_i] &= \log\left(\mathrm{E}[x_i]\right) - \frac{1}{2}\mathrm{Var}[y_i] \\ \mathrm{Var}[y_i] &= \log\left[\frac{\mathrm{Var}[x_i]}{\left(\mathrm{E}[x_i]\right)^2} + 1\right] \end{aligned} \tag{12}$$

respectively the correlation matrix components

$$\rho_{ij}^{(y)} = \log\left(1 + \rho_{ij}^{(x)} V_{x_i} V_{x_j}\right) \left(\log\left(1 + V_{x_i}^2\right) \log\left(1 + V_{x_j}^2\right)\right)^{-1/2} \tag{13}$$

where V_x is the coefficient of variation of $\mathbf{x}$.

The basic idea in using FORM is to use a reliability index β, see Figure 1, which is invariant of a coordinate system rotation. This is accomplished by a mapping of the stochastic variables according to Hasofer and Lind, [13],

$$\mathbf{z} = \hat{\mathbf{C}}_y^{-1/2} \left(\hat{\mathbf{y}} - \mathrm{E}[\hat{\mathbf{y}}]\right) \tag{14}$$

where $\hat{\mathbf{y}}$ are the uncorrelated normal distributed variables. The variables $\hat{\mathbf{y}}$ are chosen mutually independent by the orthogonal transformation matrix $\mathbf{A}$

$$\hat{\mathbf{y}} = \mathbf{A}^T \mathbf{y} \tag{15}$$

so that

$$\mathrm{E}[\hat{\mathbf{y}}] = \mathbf{A}^T \mathrm{E}[\mathbf{y}] \tag{16}$$

and $\hat{\mathbf{C}}_y$ is a diagonal matrix

$$\hat{\mathbf{C}}_y = \mathbf{A}^T \mathbf{C}_y \mathbf{A} \tag{17}$$

where $\mathbf{C}_y$ is the covariance matrix of $\mathbf{y}$.

In evaluating the limit state function in the original coordinate system, the basic variables $\mathbf{x}$ needs to be determined. By using (14) and (15), the following is obtained

$$\mathbf{y} = \mathbf{A}\hat{\mathbf{y}} = \mathbf{A}\left(\hat{\mathbf{C}}_y^{1/2}\mathbf{z} + \mathrm{E}[\hat{\mathbf{y}}]\right) = \mathbf{A}\left(\hat{\mathbf{C}}_y^{1/2}\mathbf{z} + \mathbf{A}^T\mathrm{E}[\mathbf{y}]\right) \tag{18}$$

From (18) the basic variables $\mathbf{x}$ are then determined as

$$\mathbf{x} = \mathrm{e}^{\mathbf{y}} \tag{19}$$

In an iteration procedure, of course, the eigenvalues of $\mathbf{C}_y$ needs to be determined only initially.

The reliability index is determined as the point of convergence, the minimum distance from the origin to the point $\mathbf{z}^*$ in the z-coordinate system, from a sequence of the iteration points, $\mathbf{z}^{(k)}$. For a general limit state surface, an approximation of the probability of failure, P_f, is given by

$$P_f = \Phi(-\beta_i) \tag{20}$$

where Φ is the standard normal distribution function and β_i is the reliability index of a generic material point i.

When the system failure is analyzed, as in the case of a structure discretized by finite elements, the failure probability is determined for all points of prospective failure, as given by the random field discretization. The system failure can be chosen as the union of failures for a series system, and the probability of failure can be given between upper and lower bounds, [12]. The calculation of the bounds uses the two-fold joint probabilities of failures, P_{ij}.

At the design point, the linearized limit state function is given by

$$g_i^* = \sum_{k=1}^{n} \frac{\partial g_i(z^*)}{\partial z_k}(z_k - z_k^*) = 0 \tag{21}$$

which can be rewritten on normal form

$$g_i^* = \frac{1}{\left[\sum_{k=1}^{n}\left(\partial g(z^*)/\partial z_k\right)^2\right]^{1/2}} \sum_{k=1}^{n} \frac{\partial g(z^*)}{\partial z_k} z_k + \beta_i = 0 \tag{22}$$

or

$$g_i^* = \sum_{k=1}^{n} a_{ik} z_k + \beta_i = 0 \tag{23}$$

The linearized limit state functions g_i^* and g_j^* are standard normally distributed with correlation coefficient ρ_{ij}. The correlation coefficient is given as

$$\rho_{ij} = \sum_{k=1}^{n} a_{ik} a_{jk} \tag{24}$$

Then, the joint probability of failure, P_{ij}, can be determined from the numerical integration of

$$P_{ij} = \int_{-\infty}^{-\beta_i} \int_{-\infty}^{-\beta_j} \varphi(x, y; \rho_{ij}) dx dy \tag{25}$$

where $\varphi(x, y; \rho_{ij})$ is the joint standardized normal probability density function.

Random field representation

In addressing the safety of the corrugated board, subjected to any kind of load, it is crucial to identify a set of variables that incorporate uncertain properties. In this case the purpose is to analyze a physical variation of moisture exposure of the board. It is known that both the strength and stiffness of paper change drastically when subjected to moisture. It can also be concluded that strong correlation exists between the variation in strength and stiffness. Therefore, in order to reduce the number of stochastic variables to a reasonable amount, the strength and stiffness variables $\boldsymbol{\alpha}$ can be chosen as a scalar multiplier to a spatially distributed variable, $\mathbf{x}$ so that for a given geometric point i

$$\boldsymbol{\alpha}_i = \mathbf{c} x_i \tag{26}$$

In this case, for example the stiffness and material tensile strength the in first direction are determined by

$$E_{11}^{(i)} = C_{E_{11}} x_i, \quad X_t^{(i)} = C_{X_t} x_i \tag{27}$$

respectively. The constants $C_{E_{11}}$ and C_{X_t} are the measured parameters under normal conditions. Other stiffness and material strength parameters, assumed to be orthotropic, are made proportional to $E_{11}^{(i)}$ and $X_t^{(i)}$, respectively. Poissons ratio is assumed to be deterministic in this case. The matrix defining the covariance over the plate region is defined by

$$C_{ij} = \begin{bmatrix} \mathrm{Var}[x_1] & \mathrm{Cov}[x_1, x_2] & \dots & \mathrm{Cov}[x_1, x_n] \\ \mathrm{Cov}[x_2, x_1] & \mathrm{Var}[x_2] & \dots & \mathrm{Cov}[x_2, x_n] \\ \vdots & \vdots & \ddots & \vdots \\ \mathrm{Cov}[x_n, x_1] & \mathrm{Cov}[x_n, x_2] & \dots & \mathrm{Var}[x_n] \end{bmatrix} \tag{28}$$

where n is the number of stochastic variables. The covariance between the two points, i and j, at a distance D_{ij} from each other, is taken as

$$C_{ij} = (\mathrm{Var}[x_i]\mathrm{Var}[x_j])^{1/2} \rho_{ij} = (\mathrm{Var}[x_i]\mathrm{Var}[x_j])^{1/2} \, \mathrm{e}^{-D_{ij}/L} \tag{29}$$

where ρ_{ij} is the correlation coefficient between the points and $L = -D^*/\log \rho^*$. ρ^* is the value of correlation between two points at distance D* from each other. The distance D_{ij} can be obtained as

$$D_{ij} = \|\mathbf{v}\| \tag{30}$$

where $\mathbf{v}$ is the geometric vector between the points, here chosen as the midpoints of the random field elements.

Finite element model

In the calculations of the structural response the finite element toolbox CALFEM [7] is used. The bending behaviour is modelled by a quadrilateral multilayered composite plate element, see Figure 2, using bi-linear interpolation functions for the nodal quantities.

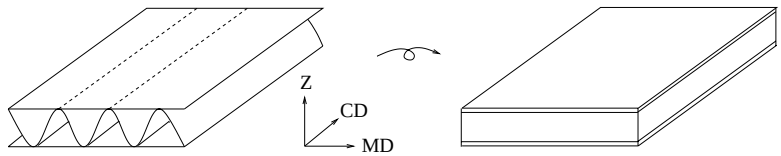

Figure 2: Finite element model of corrugated board.

In determining the effective elastic modulus of the core the procedure described in [3] is used. The counterpart element sides are parallel to each other which enables the stiffness matrix to be determined analytically. The thickness integration part of the stiffness matrix is given by

$$\tilde{\mathbf{D}} = \int_{-h/2}^{h/2} \mathbf{D}(z) z^2 dz \tag{31}$$

where $\mathbf{D}(z)$ is the in plane orthotropic material matrix in the current layer. The matrix $\mathbf{D}$ must be calculated for each layer and element for every new set of values of $\boldsymbol{\alpha}_i$.

Based on the curvature, $\boldsymbol{\kappa}$, the stresses in layer k are determined from

$$\boldsymbol{\sigma}^{(k)} = -z^{(k)} \mathbf{D}^{(k)} \boldsymbol{\kappa} \tag{32}$$

where $z^{(k)}$ is the distance from the plate system line to the center line of the layer.

Numerical results

The system reliability of a simply supported composite plate, subjected to a surface normal pressure, is studied. The plate is quadratic with side dimension 0.5 m. The middle layer is assigned deterministic values and assumed only to contribute with bending stiffness along the corrugations. An effective Young's modulus of the middle layer is calculated by multiplying the paper modulus with $\gamma t_2/h_2$, see [3], where γ is the ratio of the corrugated wave intrinsic length to the wavelength. Moreover t_2 and h_2 is the paper and core thickness, respectively. The value of h_2 is 3.6 mm and the paper thicknesses for all three layers are 0.248 mm. The wavelength of the core corrugations is 7.2 mm, which yields $\gamma \sim 1.4$.

The material parameters of the paper material, referred to as C_E and C_X previously, are used as scalar multipliers to the distribution variables x_i. The values for the stiffness parameters are $C_{E_{11}} = 8.36$, $C_{E_{22}} = 3.41$, $C_{G_{12}} = 2.06$, and $C_{G_{13}} = C_{G_{23}} = 0.045$ GPa. The in plane Poissons ratio is $\nu_{12} = 0.17$. Furthermore, the tensile and compressive material strengths in the first direction is $C_{X_t} = 85.7$ and $C_{X_c} = 25.2$ MPa respectively, and in second direction $C_{Y_t} = 35.2$ and $C_{Y_c} = 14.7$ MPa. The shear strength is obtained as proposed in [10].

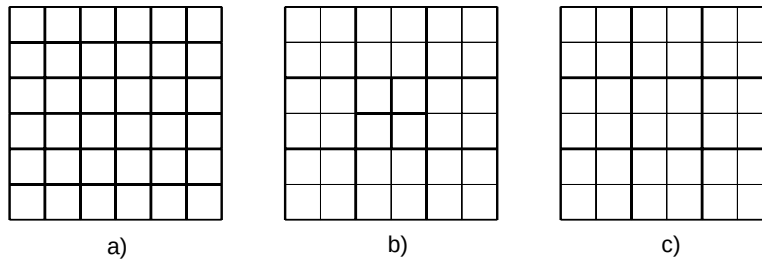

Figure 3: Different resolutions of the random field mesh.

An isotropic probabilistic distribution for the geometric variables x_i is assumed. The distribution for x_i is taken to be log-normal with mean $\mathrm{E}[x_i] = 1$ and variance $\mathrm{Var}[x_i] = 0.09$. It should be noted that in [1], a normal distribution, truncated at zero, was chosen for the geometric variables. However, it was observed that for the case of using FORM, this led to numerical problems in terms of a singular stiffness matrix. The reason for this is that the modulus of elasticity is a strength variable in the case of structural failure. For the low amount of load applied, yielding small values of the probabilities of failure, this results in strength variables tending to be very small, i.e. close to zero, in the iteration procedure.

Two numerical examples are examined. The first example is a comparison of MCS and FORM. Three different types of random field meshes are investigated in the FORM procedure, see Figure 3 where the random field elements are drawn with bold lines. In case (a) the random field elements are coinciding with the finite elements, in case (b) 12 random field elements are used and in case (c) 9 random field elements are used. In addition, a case (d), with the same random field mesh as in (a) but with a reduced number of searches for the reliability index, is investigated. In this case, only the elements with a deterministic ratio of the stress radius to the failure stress radius of 0.3 is used in the search (the four center elements along with their neighbour elements, corner elements excluded). At all MCS, the random field mesh is coinciding with the finite element mesh.

Also the variation of probability of failure due to different extent of correlation at a certain length, is investigated. A surface pressure of 175 Pa is applied on each element, which results in a maximum deterministic deflection of 4.5 mm, see Figure 4.

The second example uses MCS to study the likeliness of failure at specific geometrical points of the board. Here, a larger surface pressure is applied, 500 Pa. The values of D^* and ρ^* are both 0.5.

In the first example the correlation between the geometric variables is varied. This is accomplished by calculating the probability content for values of ρ^*=0.01 to ρ^*=0.9. The result is plotted in Figure 5, where the circles are results from MCS and the solid lines are results from FORM. The failure probability increases with increasing correlation length and takes the value 0.0017 when all the elements are strongly correlated. This is quite lower than the value obtained in [1], even though the surface pressure applied is larger. The reason for this is the low density function values for the log-normal distribution, for the level of the applied load. However, it can be seen that the results from MCS and FORM are very close.

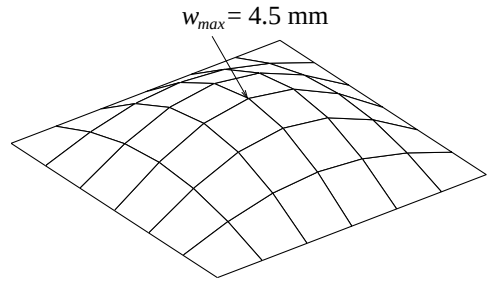

Figure 4: Deflection of composite plate.

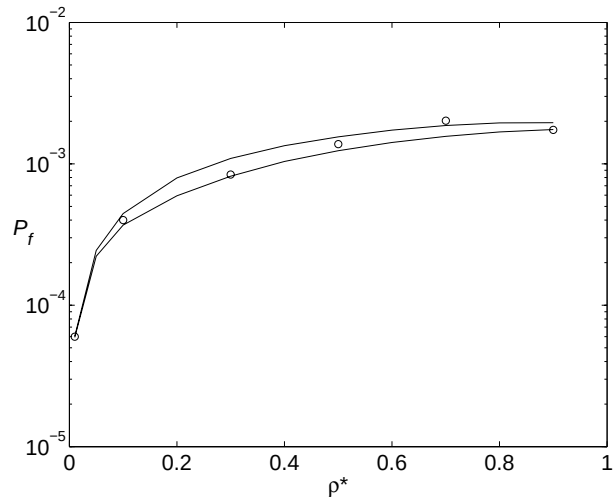

Figure 5: P_f as function of correlation length coefficient.

In Table 1, the results from the three different random field meshes are listed, where the probabilities of failure are given as the mean value of the upper and lower bounds. The value of ρ^* is 0.5 in all cases.

Table 1: Probability of failure for different random field meshes.

	MCS	FORM			
		a	b	c	d
Prob. of failure, 10^{-3}	1.38	1.30	0.77	0.51	1.30
No. Chol. decomp.	50000	8695	936	570	2220

It is seen that when the random field mesh is coinciding with the finite element mesh, the number of required Cholesky decompositions is 8695, for the FORM solution, compared to 50000 for the MCS solution. Furthermore, the probability of failure is a little less than for the case of MCS. For the random field mesh (b) the probability of failure is far from the value in case (a), which indicates that the random field discretization is to coarse. The same holds for case (c). In case (d), however, the reduced number of search elements do not deteriorate the result from (a), where the probability of failure is the same, 0.0013. The number of Cholesky decompositions needed for FORM in (d) is 2220.

It can be concluded from the cases (a)-(d) that the number of random field elements, and thereby the number of stochastic variables, largely affects the rate at which a solution is obtained for the probability of failure. In case (d) the number of search points was 12, the same as the number of random field elements in (b). Despite this, the number of required Cholesky decompositions is more than twice than in case (b).

In the second example the number of fractures in each layer, element and whether the failure is due to structural or material failure, is determined. The number of simulations is 50000. It was noted during the simulations that no failures in the upper layer occurred (where tensile stresses are developed). It should be noted that in [1], where normal distributed variables where used, a few number of failures occurred in the upper layer.

In Figure 6, the numbers in braces are failures due to material failure. As can be seen, material failure only develop in the corner elements, where the shear stress is large. In addition, it can be seen that the number of failures in regions where the curvature in MD is larger compared to CD, exceeds the number of failures in regions where the opposite holds for the curvature. As a conclusion, the board is more sensitive to compressive stresses in MD, than in CD. This result was also confirmed in [1], where an added tensile stress in the MD largely reduced the number of structural failures at the compressive side of the plate.

Conclusions

The reliability of corrugated board, subject to plate bending, is studied both by MCS and by a FORM procedure applied to finite element calculations. The stiffness and strength parameters of the board are given as scalar multipliers of a geometrically distributed stochastic field.

{1}	5	7	6	6	
18	7609	17274	17230	7399	19
82	21987	36545	36441	21994	86
74	22084	36582	36385	22056	94
11	7422	17427	17303	7449	22
{1}	6	8	8	3	{1}

Figure 6: Number of failures in each element.

For the case of pure bending stresses, it is concluded that the failure is almost completely governed by structural failure. It is also seen that the board is sensitive to stresses in the first direction (MD).

Also the variation of probability of failure due to different correlation lengths is studied. The system failure probability is seen to increase with increasing correlation length coefficient.

With the use of MCS, it is recognized that a very large number of Cholesky decompositions is needed for determining the probabilistic characteristics of the board. This is certainly expressed when low failure probabilities are studied. The method of FORM was shown to be a numerically efficient method, even though the failure surface is not explicitly given, but determined by the finite element solution. It should be noted that the response gradients could have been calculated analytically, thus saving a lot of computation time. However, the calculations done here shows that even if the gradients are computed by the full finite element solution, there is significant computational effort to save. This is also attractive since general purpose FEM codes could be used together with FORM without modifications.

It should be mentioned that the example studied here consists of rather few elements representing the structure. If larger problems are studied, and the correlation between each element is high, there could arise problems with widening reliability bounds for the system failure.

In analyzing corrugated board in a broader sense, as in the case of corrugated board packages, a very common load case is in-plane loaded panels. A detailed analysis would require a geometrically non-linear finite element analysis. Studying the reliability of e.g. boxes by MCS, this would lead to a prohibitive computational effort needed. A possible choice would be to extend the limit surface iterations to involve also equilibrium iterations in a buckling analysis.

Acknowledgements

The economic support for this work from the Foundation for Strategic Research (SSF) Forest Products Industry Research College program and from Bo Rydins stiftelse för vetenskaplig forskning is gratefully acknowledged.

References

[1] Nyman, U., and Gustafsson, P. J., (2000) *Multilayer Composite Reliability Calculations on Corrugated Board*, Proceedings of the International Conference on Wood and Wood Fiber Composites, April 13-15, Stuttgart, Germany

[2] Johnson, M. W. and Urbanik, T. J. (1989) *Analysis of the Localized Buckling in Composite Plate Structures with application to Determining the Strength of Corrugated Fiberboard.* J. of Composites Technology and Research, Vol. 11, No. 4, 121-127

[3] Nordstrand, T. M. (1995) *Parametric Study of the Postbuckling Strength of Structural Core Sandwich Panels.* Composite Structures, 30, 441-451

[4] Nyman, U. and Gustafsson, P. J. (2000) *Material and Structural Failure Criterion of Corrugated Board Facings.* Composite Structures, **50**(1).

[5] Patel, P. (1996) *Biaxial Failure of Corrugated Board.* KFS AB, Lund

[6] Urbanik, T. J. (1997) *Linear and Nonlinear Effects on Postbuckling Strength of Corrugated Containers.* Mechanics of Cellulosic Materials, AMD-Vol. 221/MD-VOI. 77, ASME

[7] CALFEM 3.3, (1999) *A finite element toolbox to MATLAB*, Jabe Offset AB, Division of Structural Mechanics, Lund University

[8] Patel, P., Nordstrand T. M. and Carlsson, L. A. (1997) *Local Buckling and Collapse of Corrugated Board Under Biaxial Stress.* Composite Structures, Vol. 39, No 1-2, 93-110

[9] Zahn, J. J. (1973) *Local Buckling of Orthotropic Truss-Core Sandwich.* Research paper, USDA Forest Service

[10] Gustafsson, P. J., Nyman, U. and Heyden, S. (2000) *A network mechanics failure criterion.* Report TVSM-7128, Division of Structural Mechanics, Lund University

[11] Rackwitz, R., and Fiessler, B., (1977) *An algorithm for Calculation of Structural Reliability under Combined Loading.* Berichte zur Sicherheitstheorie der Bauwerke, Lab. f. Konstr. Ingb., Munchen

[12] Ditlevsen, O., (1979) *Narrow Reliability Bounds for Structural Systems.* J. Struct. Mech., Vol. 7, pp. 435-451

[13] Hasofer, A. M, and Lind, N. C., (1974) *An Exact and Invariant First Order Reliability Format.* Proc. ASCE, J. Eng. Mech. Div., pp 111-121

Appendices

Appendix A

ESTIMATION OF RANDOM FIELD PROPERTIES OF PAPER

Introduction

Paper is a structural material consisting of randomly distributed plane-oriented wood fibers. The orientation of fibers with respect to an aligned coordinate system with the material axes, MD and CD, is stochastic, and largely influenced by the prevailing conditions during the papermaking process. Naturally, as a result the mechanical properties will incorporate variabilities due to the randomness in orientation. Furthermore, randomness in density and thickness of the paper is also a sequel of the process. In addition, the mechanical properties will be affected by humidity changes and stress fields introduced on the paper in successive events to the papermaking process, such as the converting process of corrugated board. In a realistic mechanical analysis of paper elements, represented by homogenized material parameters, consideration to variabilities of the material properties is logical. A relevant example is the reliability analysis of long term strength of corrugated board boxes in compression load, where the strength variabilities of paper will give rise to large deviations of the lifetime.

The stochastic variation of parameters can be represented by a random field, extended over a two-dimensional region analogous to an area persistent with the paper sheet used for the assembly of a corrugated board box. A brief description of the random field parameters, which are subsequently determined in an experimental procedure, is given in the following section.

Random field representation

Consider a randomly varying parameter space in two dimensions for paper $\boldsymbol{\alpha}(\mathbf{x})$, $\mathbf{x} \in \Omega \in \mathbb{R}^2$, where $\boldsymbol{\alpha}(\mathbf{x}) = [{}^1\alpha(\mathbf{x}), ..., {}^m\alpha(\mathbf{x})]$ is a m-dimensional vector defining strength properties, stiffness properties and geometrical properties in the region Ω. Then, if

$$\omega \subset \Omega, \tag{A.1}$$

a number of measured values within ω is an observation of $\boldsymbol{\alpha}$. In this application ω can be interpreted as the region occupied by a corrugated board box whereas Ω is the set of all papers used for the converting of boxes. If $m \times n$ observations are collected within Ω, the entire collection, $\boldsymbol{\alpha}_q\,(q = 1, ..., n)$, forms an ensemble of observations. At a geometric location, $\mathbf{x}_i, (i = 1, ..., p)$, the expectation value of ${}^r\alpha$ can be written as

$$E[{}^r\alpha(\mathbf{x}_i)] = \frac{1}{n}\sum_{q=1}^{n} {}^r\alpha_q(\mathbf{x}_i) \qquad r = 1, ..., m \tag{A.2}$$

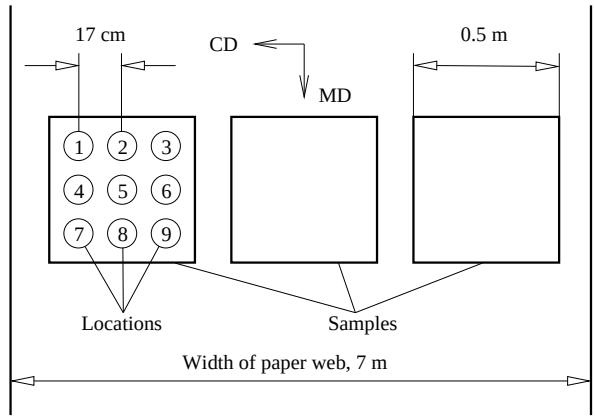

Figure A.1: Collection of samples.

The covariance of the parameters at two different points $\mathbf{x}_i$ and $\mathbf{x}_j$ is given by the matrix

$$Cov[^r\alpha(\mathbf{x}_i),^r\alpha(\mathbf{x}_j)] = \frac{1}{n}\sum_{q=1}^{n}(E[^r\alpha(\mathbf{x}_i)] - {}^r\alpha_i^{(q)})(E[^r\alpha(\mathbf{x}_j)] - {}^r\alpha_j^{(q)}) \qquad r = 1, ..., m \quad \text{(A.3)}$$

The variation of the random variables characterized by (A.3) can also be given in normalized form, by the correlation matrix

$$\rho[^r\alpha(\mathbf{x}_i),^r\alpha(\mathbf{x}_j)] = \frac{Cov[^r\alpha(\mathbf{x}_i),^r\alpha(\mathbf{x}_j)]}{D[^r\alpha(\mathbf{x}_i)]D[^r\alpha(\mathbf{x}_j)]} \qquad r = 1, ..., m \quad \text{(A.4)}$$

where $D[^r\alpha(\mathbf{x}_i)]$ is the standard deviation or the square root of the i:th diagonal element of (A.3). The equations (A.2-A.4) represents the second order information of the random field.

Collection of samples

The materials used for the estimation of parameters are liners and flutings which are in frequent commercial use, see the next section. In order to achieve the amount of variations in the data which is the case in reality the samples (observations) of the random field are extracted from different reels. The samples are cut out from the outer layers, medium layers and inner layers of the reels. The appropriate geometric length interval for the correlation field to be measured is 0-0.5 m, corresponding to a corrugated board box of medium size. Therefore, the samples are collected in approximately the same size. Within this sample, a number of specimens are cut out, clustered at geometric locations which form a matrix pattern, see Figure A.1. Totally, nine samples are collected for each material. This corresponds to 81 specimens for each property and material to be measured. In the following the geometric locations are numbered from one to nine within a sample, starting in the upper left corner proceeding along rows, with reference to Figure A.1. The distances between the different locations are listed in Table A.1.

(location,location)	Distance [cm]
(1,2), (2,3), ...	17
(1,5), (3,5), ...	24
(1,3), (4,6), ...	34
(1,6), (1,8), ...	38
(1,9), (3,7)	48

Table A.1: Distances between different locations.

Materials and parameters tested

Three types of liners and three types of flutings are chosen for the estimation of the random field data. The materials and properties used in the parameter estimation procedure are listed in Table A.2.

The tensile strength and stiffness properties are determined according to the standard SCAN-P 67:93 test method, see [1], whereas the compressive strength properties are determined according to the standard SCAN-P 46:83 test method, see [2]. All tests are performed in 50% relative humidity and 23°C. Before testing the sheets are preconditioned in 30% relative humidity and 23°C for 24 hours and then conditioned in 50% relative humidity and 23°C for 24 hours.

Homogeneity and isotropy

The basic hypothesis on the random field is that is it homogeneous and isotropic. Homogeneity implies that the joint probability density function (jpdf) between different material points will only depend on the relative distance between the points and not on the absolute locations. Furthermore, isotropy implies that the jpdf is independent of a rotation of the configuration points. This is equivalent with constant mean values and variances over the actual locations. In Figures A.2a-A.7b the mean values and variances are plotted for different geometric locations. The values at specific points are normalized with respect to average values (space average) over the entire set of points.

It is obvious from the figures that the deviations from the space average are small. It is also recognized that, despite the general systematic variation of parameters over the paper web, due to differences in tension of the web, no particular pattern can be found with respect to locations. This is explained by the region size of the random field. From this it can be concluded that the random variations are reasonably described by a homogeneous and isotropic field.

Distribution function

When assigning a suitable probability density function on a physical variable it is essential that the shape of the function can be recovered from the density of the measured data. Nevertheless, an evident property of the parameters studied here is that the values are

Liner materials
SCA 200WT
SCA 200KL
SCA 150TL

Fluting materials
SCA 150HK
SCA 112RF
SCA 112HK

In-plane strength
X_t=Tensile strength in MD
X_c=Compressive strength in MD
Y_t=Tensile strength in CD
Y_c=Compressive strength in CD

In-plane stiffness
E_x=Young's modulus in MD
E_y=Young's modulus in CD

Geometrical parameters
t=Liner thickness
G=Grammage

Table A.2: Materials and properties used in the parameter estimation procedure.

restricted to be positive. A density function commonly used for this type of parameters is the log-normal distribution. In Figures A.8a-A.14b the histograms of different material parameters are shown together with a fitted log-normal distribution function.

For the majority of the material parameters the agreement of the estimated distribution with the histogram is acceptable. For the material parameters with obvious deviations from the distribution function the log-normal distribution is still adopted, for convenience.

Correlation pattern

For a randomly varying material parameter field over a geometric region two conditions are observed on the correlation function for two points, i and j, located on a distance D (not to be confused with the standard deviation estimate in (A.4)) from each other

$$\lim_{D\to 0} \rho_{ij} = 1, \qquad \lim_{D\to \infty} \rho_{ij} = 0 \tag{A.5}$$

In (A.5) the first condition follows by definition, whereas the second can be related to practical reasons. A function commonly used for this purpose, satisfying (A.5), is the exponential function. Usually this function is parameterized so that at a certain distance, D^*, the desired correlation ρ^* is obtained. A fitting procedure is employed for determination of correlation parameters in order to achieve a correlation function in agreement with test data. Herein, the parameter ρ^* is fitted so that

$$\rho(D) = e^{-\frac{D}{L}}, \qquad L = -\frac{D^*}{\log \rho^*} \qquad D^* = 0.1 \text{ m} \tag{A.6}$$

under the condition

$$\min ||\rho(D_i) - e^{-\frac{D_i}{L}}||, \qquad i = 1, \ldots, r \tag{A.7}$$

where r is the number of different distances between locations within a sample. In the processing of data the distance correlation within one material property is considered only. This means that zero correlation between different material properties is assumed. This might be questionable for example concerning the correlation between stiffness and strength variables equivalent with the same material direction, such as X_t and E_x or Y_t and E_y.

In Figures A.15a-A.26b scatter plots for different material parameters and different material points are shown. The dashed line in the plots show the least square fitted correlation curve. A large variation of correlation between different material parameters is found. From this it can be concluded that the best agreement of correlation pattern to measured data is obtained if individual correlation parameters are used for the material parameters. In Figures A.27a-A.50b fitted correlation functions to test data are shown for a set of material parameters.

Experimental results

Numerical values of the estimated field parameters for the different materials are presented in Tables A.3-A.8. For all materials the grammage presents the lowest coefficient of

variation, from 0.005 for the liner 200WT to 0.021 for the fluting 150HK. The largest coefficient of variation, 0.211, is found for the tensile strength in CD for the fluting 112HK. It is also observed that, for all materials, a large distance correlation is valid for Young's modulus in CD.

	$E[\alpha]$	$D[\alpha]$	C.O.V.	ρ^*
X_t [MPa]	101.89	4.44	0.044	0.001
Y_t [MPa]	44.26	2.31	0.052	0.543
X_c [MPa]	29.71	1.63	0.055	0.604
Y_c [MPa]	17.00	0.85	0.050	0.001
E_x [MPa]	8690.71	300.07	0.035	0.450
E_y [MPa]	3249.75	137.79	0.042	0.885
t [μm]	265.16	4.30	0.016	0.526
G [g/m^2]	198.39	0.96	0.005	0.602

Table A.3: Estimated field parameters for material SCA 200WT.

	$E[\alpha]$	$D[\alpha]$	C.O.V.	ρ^*
X_t [MPa]	88.97	4.58	0.051	0.540
Y_t [MPa]	32.76	2.76	0.084	0.801
X_c [MPa]	27.67	1.89	0.068	0.120
Y_c [MPa]	15.64	1.02	0.065	0.419
E_x [MPa]	7791.24	244.59	0.031	0.643
E_y [MPa]	2913.15	155.69	0.053	0.868
t [μm]	252.37	3.71	0.015	0.001
G [g/m^2]	198.69	1.30	0.007	0.148

Table A.4: Estimated field parameters for material SCA 200KL.

	$E[\alpha]$	$D[\alpha]$	C.O.V.	ρ^*
X_t [MPa]	67.78	9.78	0.144	0.933
Y_t [MPa]	27.01	2.52	0.093	0.460
X_c [MPa]	25.16	1.53	0.061	0.372
Y_c [MPa]	14.40	1.08	0.075	0.738
E_x [MPa]	6995.71	333.63	0.048	0.803
E_y [MPa]	2767.13	211.79	0.077	0.917
t [μm]	194.67	3.55	0.018	0.824
G [g/m^2]	149.31	0.86	0.006	0.629

Table A.5: Estimated field parameters for material SCA 150TL.

	$E[\alpha]$	$D[\alpha]$	C.O.V.	ρ^*
X_t [MPa]	50.92	3.53	0.069	0.169
Y_t [MPa]	20.96	1.28	0.061	0.732
X_c [MPa]	22.44	1.38	0.062	0.001
Y_c [MPa]	12.99	1.07	0.082	0.155
E_x [MPa]	5641.25	280.36	0.050	0.287
E_y [MPa]	2348.17	154.92	0.066	0.787
t [μm]	251.27	8.10	0.032	0.225
G [g/m^2]	146.42	3.01	0.021	0.902

Table A.6: Estimated field parameters for material SCA 150HK.

	$E[\alpha]$	$D[\alpha]$	C.O.V.	ρ^*
X_t [MPa]	46.85	4.16	0.089	0.514
Y_t [MPa]	15.96	1.23	0.077	0.555
X_c [MPa]	21.41	1.55	0.073	0.001
Y_c [MPa]	11.74	0.95	0.081	0.306
E_x [MPa]	5331.61	389.29	0.073	0.468
E_y [MPa]	2015.73	142.01	0.070	0.571
t [μm]	182.58	7.63	0.042	0.188
G [g/m^2]	113.63	1.58	0.014	0.275

Table A.7: Estimated field parameters for material SCA 112RF.

	$E[\alpha]$	$D[\alpha]$	C.O.V.	ρ^*
X_t [MPa]	52.01	5.37	0.103	0.308
Y_t [MPa]	19.52	4.12	0.211	0.001
X_c [MPa]	22.22	1.95	0.088	0.001
Y_c [MPa]	11.84	1.50	0.127	0.001
E_x [MPa]	5818.86	506.37	0.087	0.001
E_y [MPa]	2230.55	458.31	0.205	0.260
t [μm]	196.68	8.88	0.045	0.001
G [g/m^2]	111.50	1.69	0.015	0.644

Table A.8: Estimated field parameters for material SCA 112HK.

Conclusions

Herein, a procedure for estimating random field parameters for paper is presented. The assigned random field can be used for further reliability analysis on e.g. corrugated boxes.

From the analysis of the measured data it is concluded that proper random field characteristics, for a random field of region size equivalent with a corrugated board box, is given by a homogeneous and isotropic jpdf. That is, the second order information

of the field is established by constant mean value and variance over the sample region. Moreover, it is concluded that different correlation parameters for the individual material parameters are needed to produce correlation patterns in agreement to the measured data. Numerical results for the random field parameters are presented for three liner materials and three fluting materials, used in daily production lines in corrugated board plants.

References

[1] SCAN-P 67:93, (1993) Scandinavian pulp, paper and board testing committee, Box 5604, S-114 86, Stockholm, Sweden.

[2] SCAN-P 46:83, (1983) Scandinavian pulp, paper and board testing committee, Box 5604, S-114 86, Stockholm, Sweden.

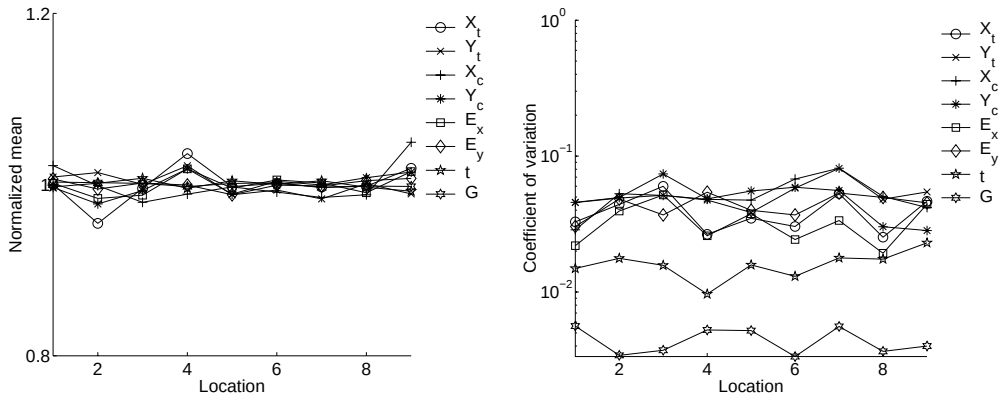

Figure A.2: Normalized a) mean values and b) coefficient of variation for SCA 200WT.

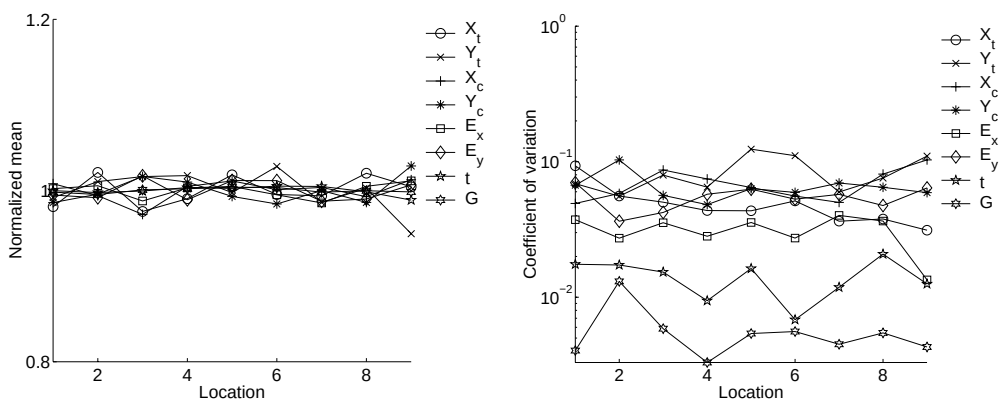

Figure A.3: Normalized a) mean values and b) coefficient of variation for SCA 200KL.

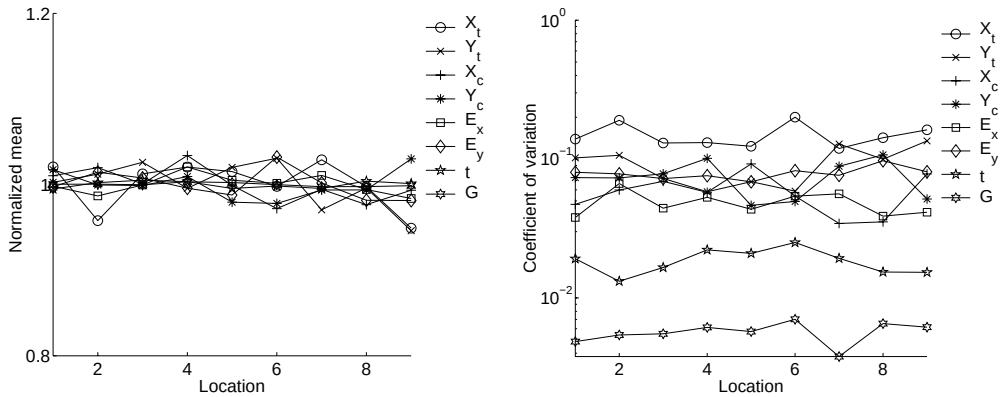

Figure A.4: Normalized a) mean values and b) coefficient of variation for SCA 150TL.

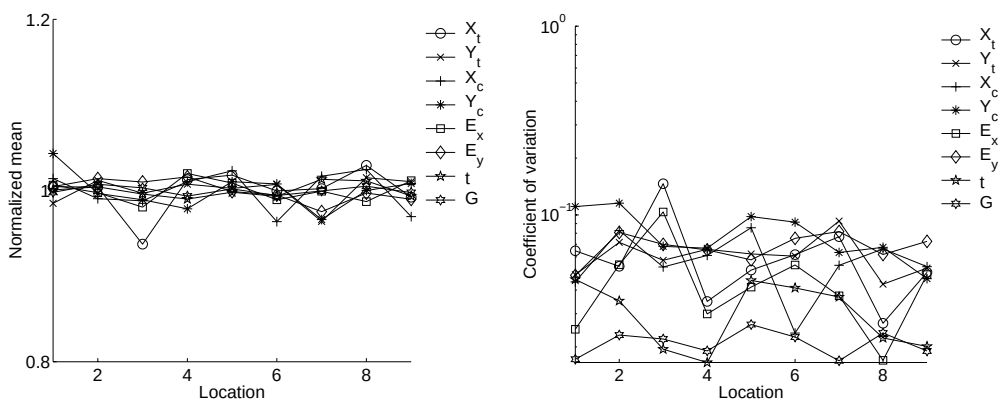

Figure A.5: Normalized a) mean values and b) coefficient of variation for SCA 150HK.

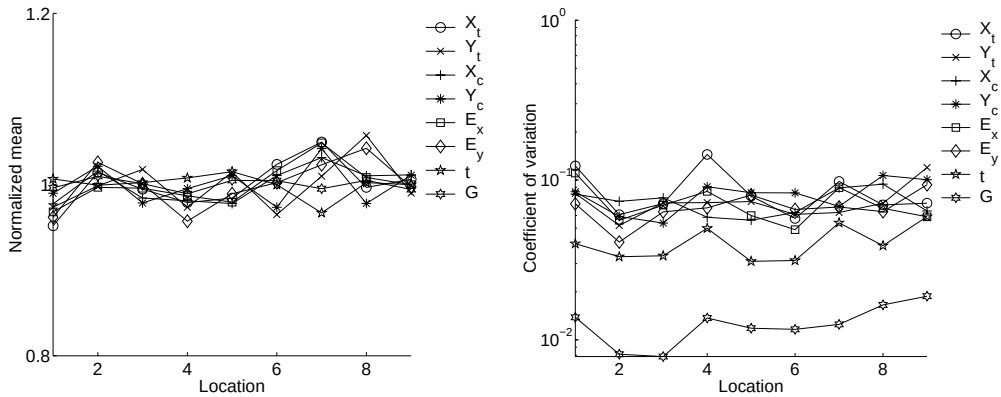

Figure A.6: Normalized a) mean values and b) coefficient of variation for SCA 112RF.

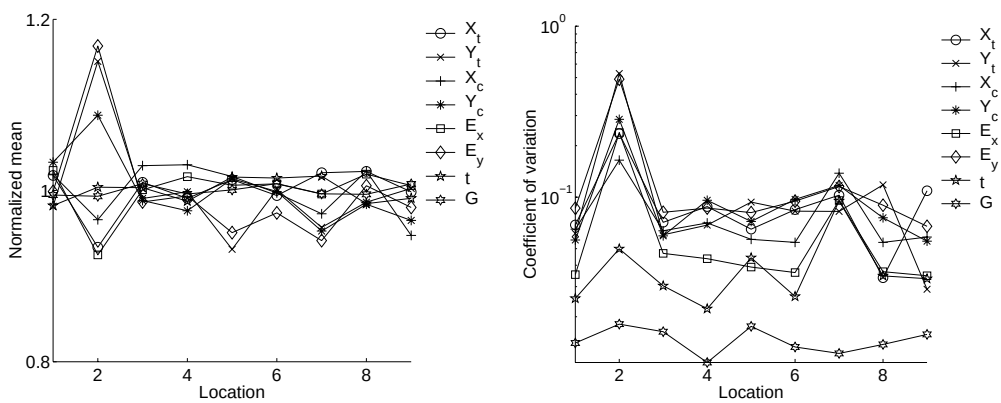

Figure A.7: Normalized a) mean values and b) coefficient of variation for SCA 112HK.

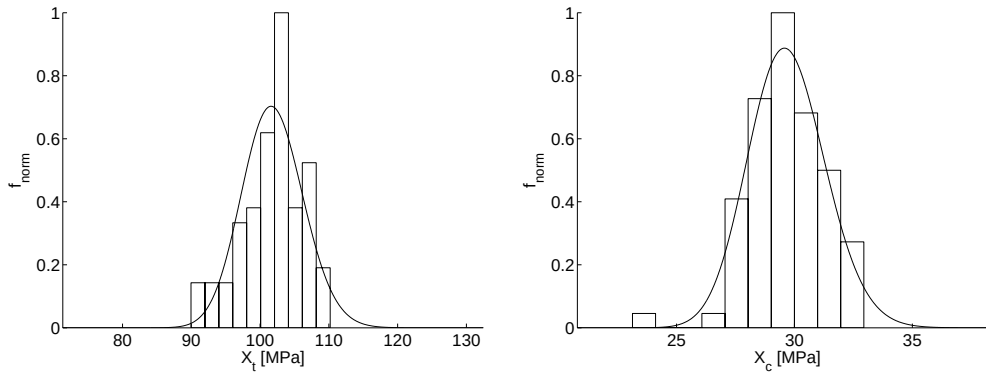

Figure A.8: Distribution of a) X_t and b) X_c, for SCA 200WT.

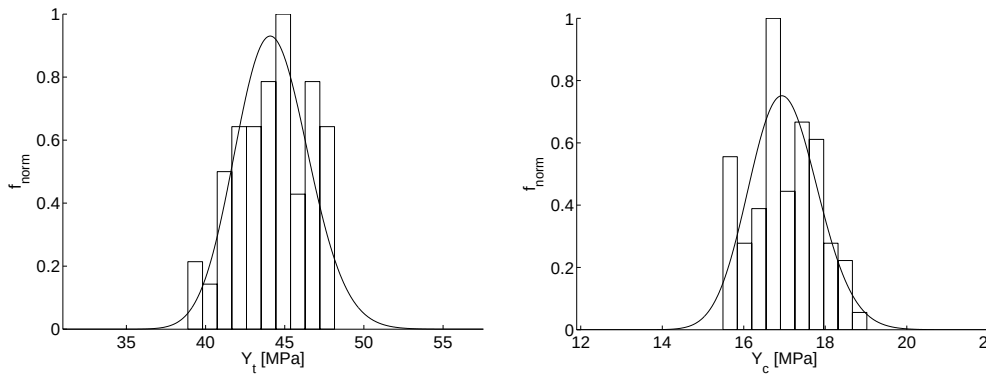

Figure A.9: Distribution of a) Y_t and b) Y_c, for SCA 200WT.

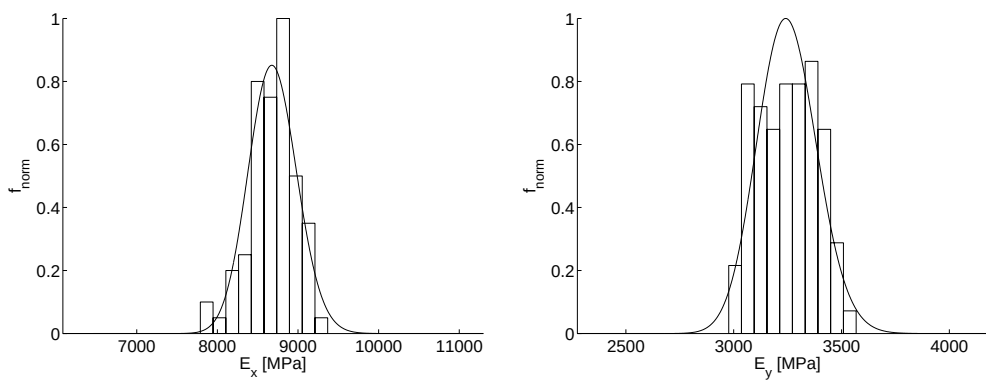

Figure A.10: Distribution of a) E_x and b) E_y, for SCA 200WT.

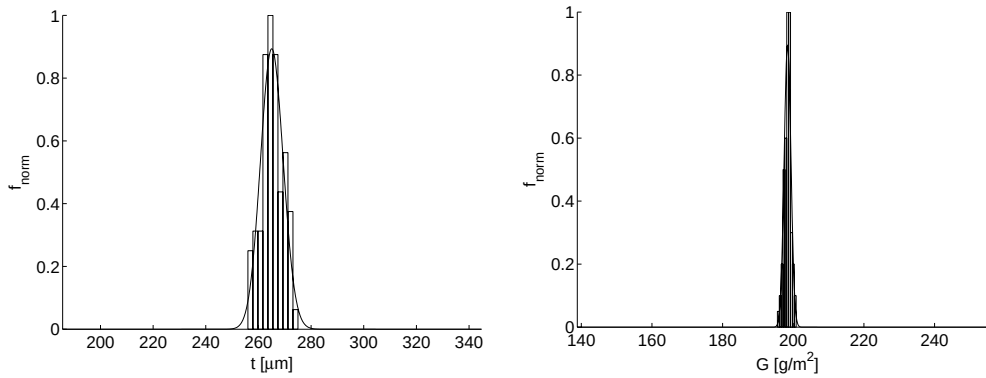

Figure A.11: Distribution of a) t and b) G, for SCA 200WT.

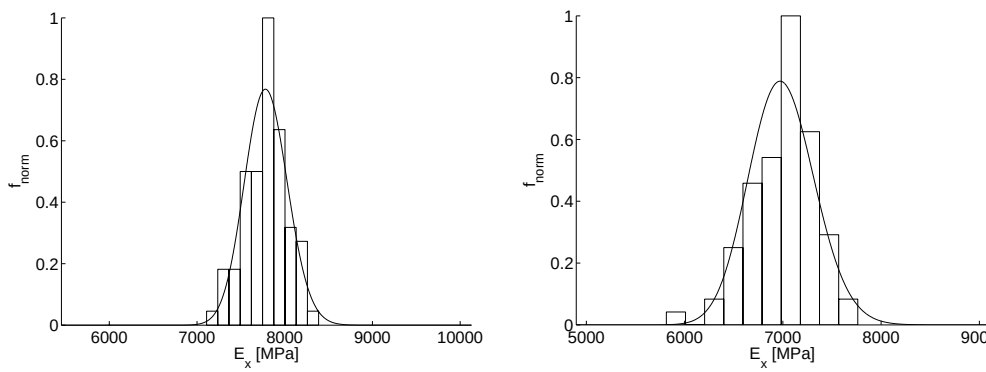

Figure A.12: Distribution of E_x for a) 200KL and b) 150TL.

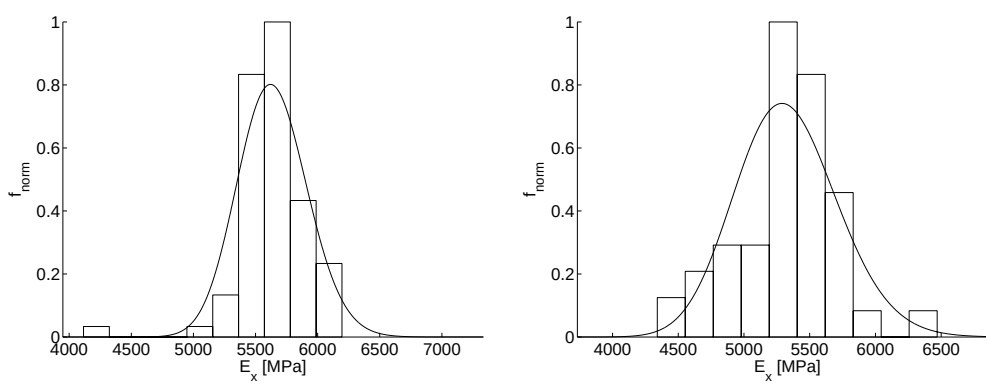

Figure A.13: Distribution of E_x for a) 150HK and b) 112RF.

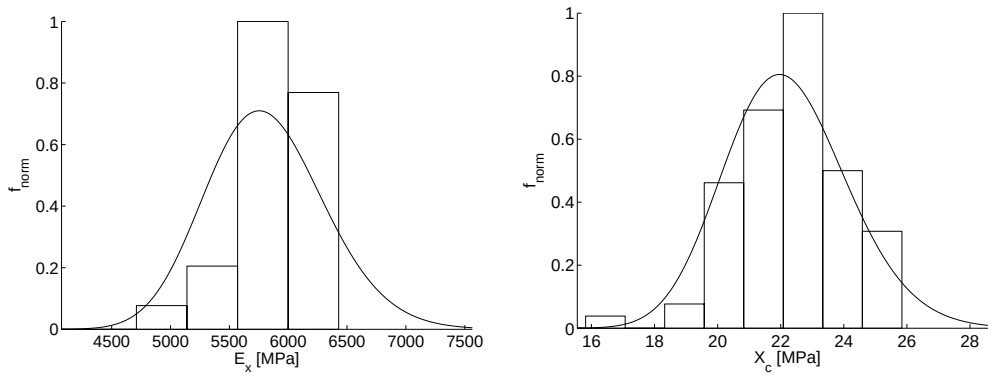

Figure A.14: Distribution of a) E_x and b) X_c for 112HK.

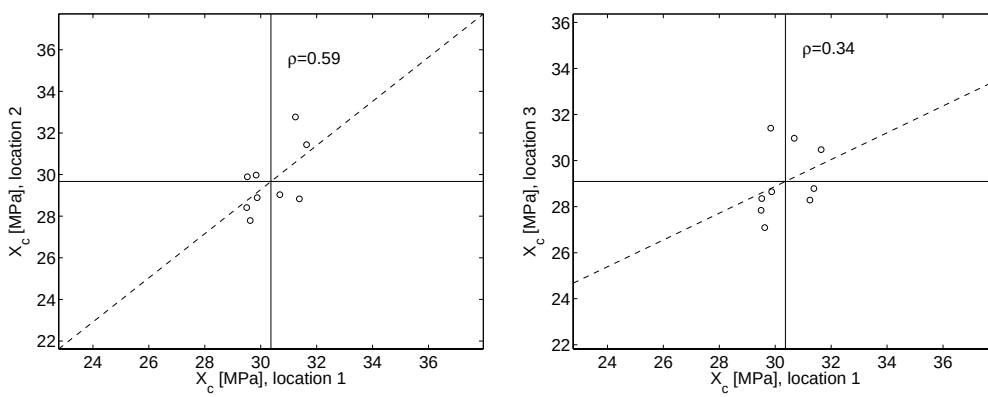

Figure A.15: Scatter of X_c for a) location 1 versus location 2 and b) location 1 versus location 3, material SCA 200WT.

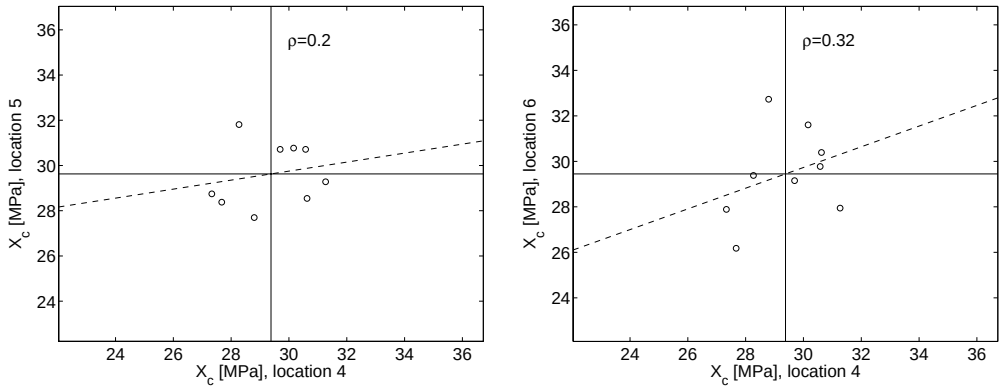

Figure A.16: Scatter of X_c for a) location 4 versus location 5 and b) location 4 versus location 6, material SCA 200WT.

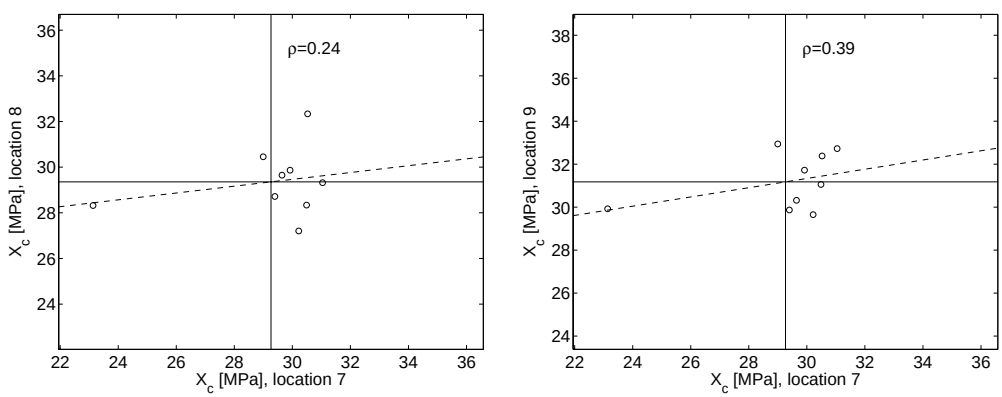

Figure A.17: Scatter of X_c for a) location 7 versus location 8 and b) location 7 versus location 9, material SCA 200WT.

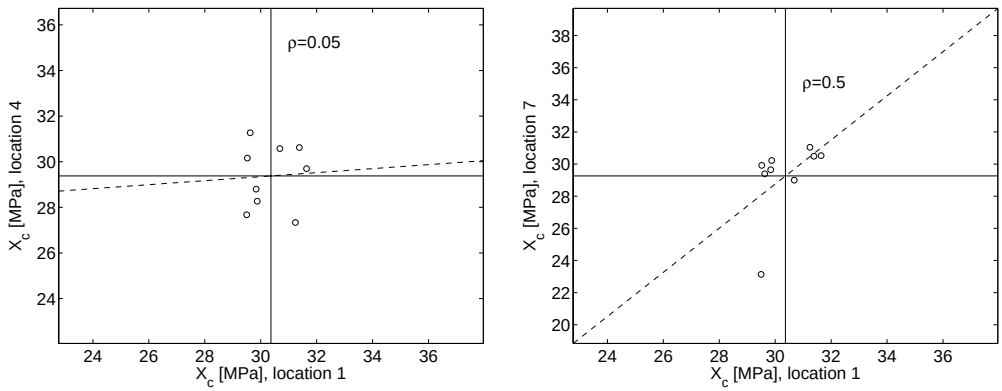

Figure A.18: Scatter of X_c for a) location 1 versus location 4 and b) location 1 versus location 7, material SCA 200WT.

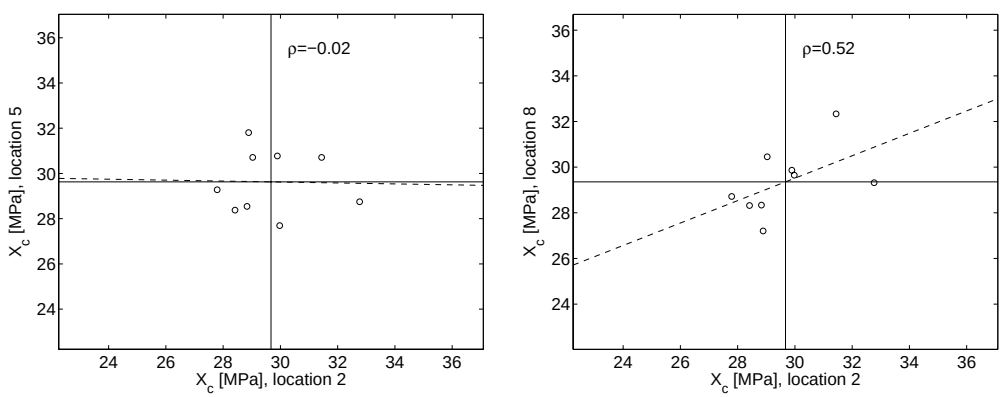

Figure A.19: Scatter of X_c for a) location 2 versus location 5 and b) location 2 versus location 8, material SCA 200WT.

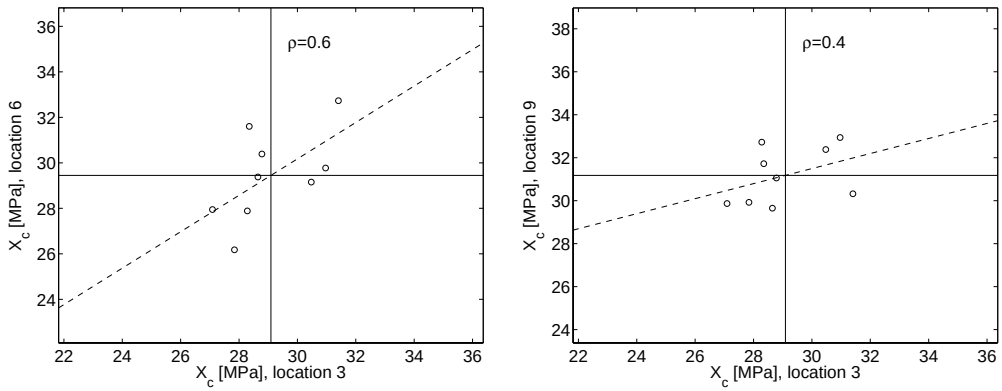

Figure A.20: Scatter of X_c for a) location 3 versus location 6 and b) location 3 versus location 9, material SCA 200WT.

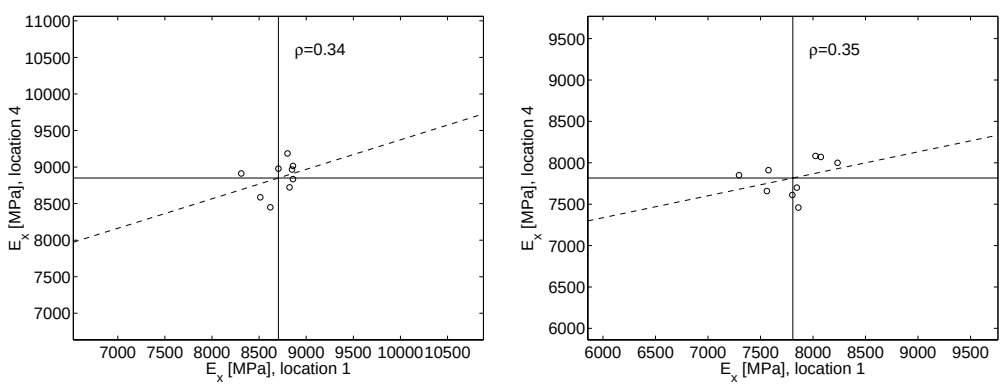

Figure A.21: Scatter of E_x for location 1 versus location 4, a) SCA 200WT and b) SCA 200KL.

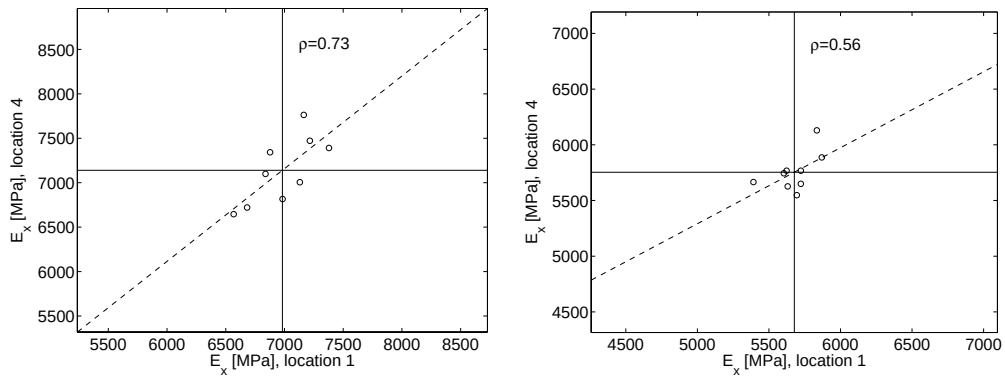

Figure A.22: Scatter of E_x for location 1 versus location 4, a) SCA 150TL and b) SCA 150HK.

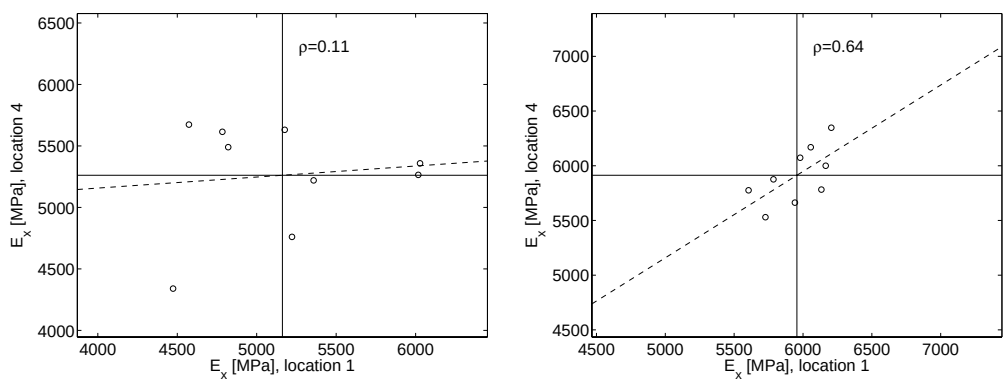

Figure A.23: Scatter of E_x for location 1 versus location 4, a) SCA 112RF and b) SCA 112HK.

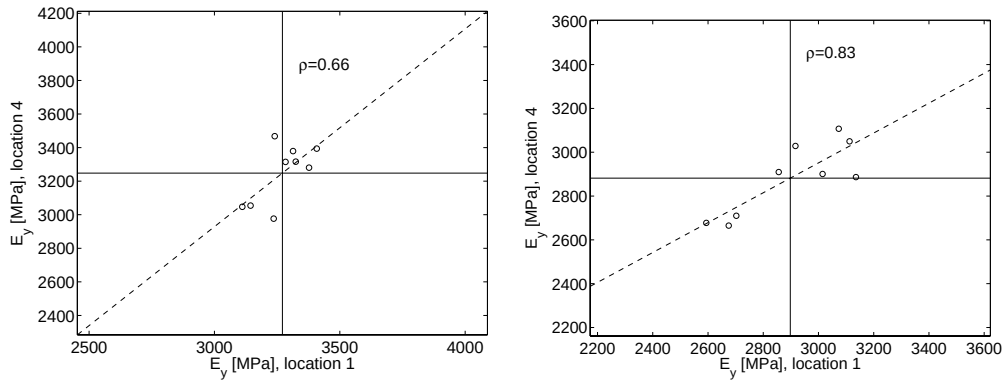

Figure A.24: Scatter of E_y for location 1 versus location 4, a) SCA 200WT and b) SCA 200KL.

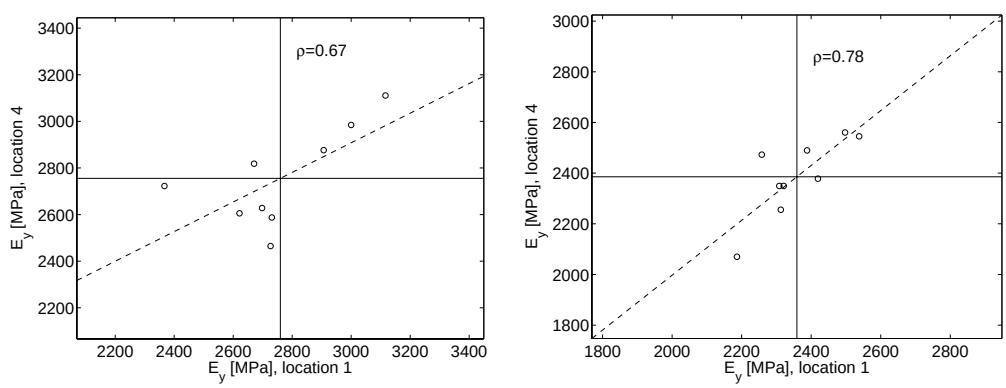

Figure A.25: Scatter of E_y for location 1 versus location 4, a) SCA 150TL and b) SCA 150HK.

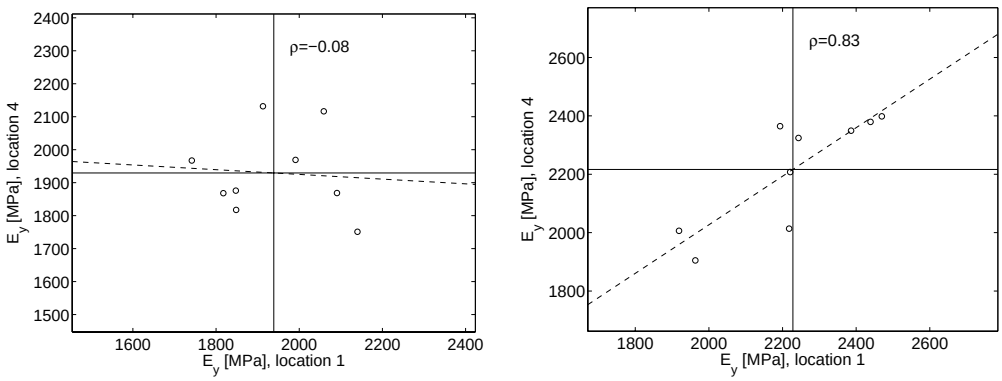

Figure A.26: Scatter of E_y for location 1 versus location 4, a) SCA 112RF and b) SCA 112HK.

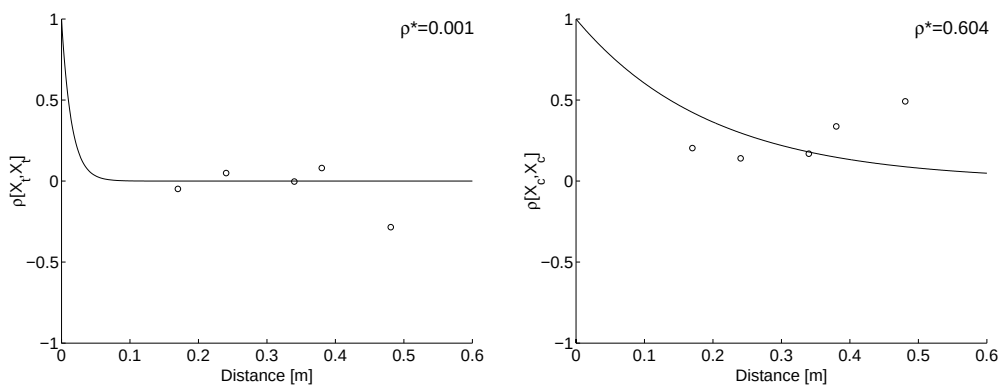

Figure A.27: LS-fitted correlation function for a) X_t and b) X_c, SCA 200WT.

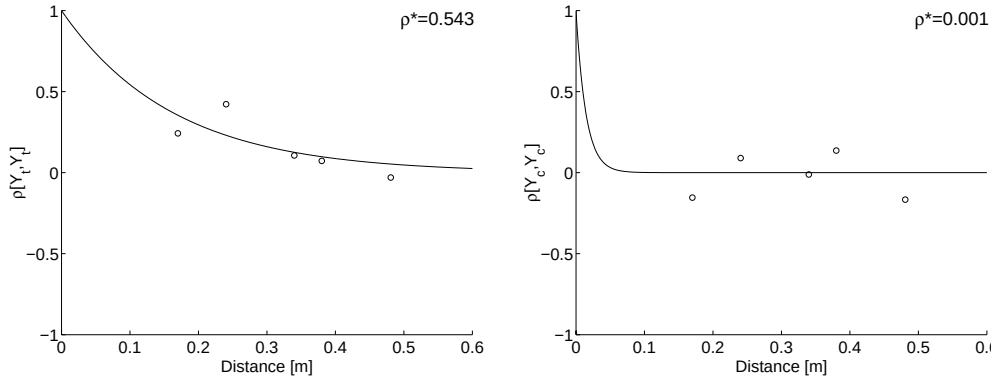

Figure A.28: LS-fitted correlation function for a) Y_t and b) Y_c, SCA 200WT.

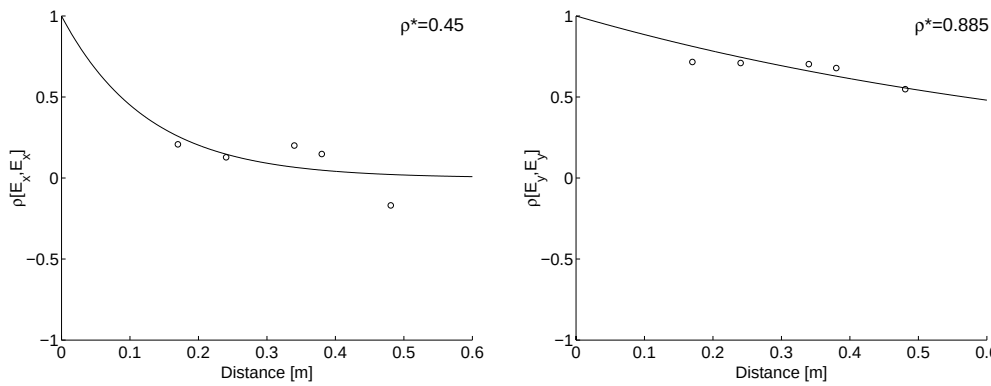

Figure A.29: LS-fitted correlation function for a) E_x and b) E_y, SCA 200WT.

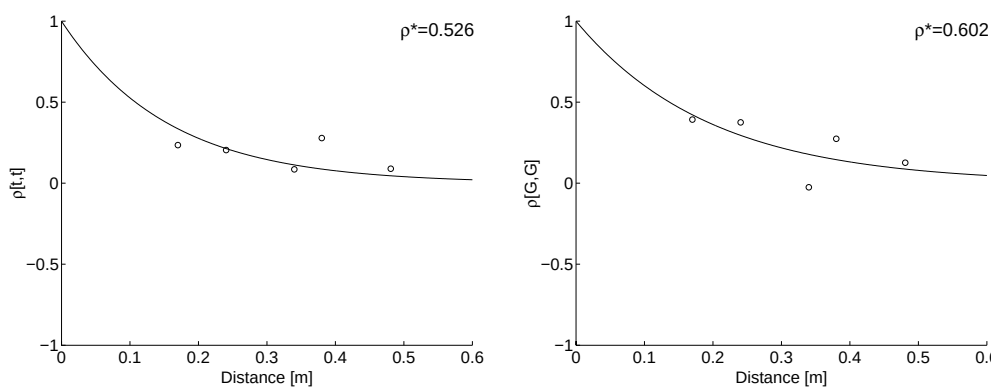

Figure A.30: LS-fitted correlation function for a) t and b) G, SCA 200WT.

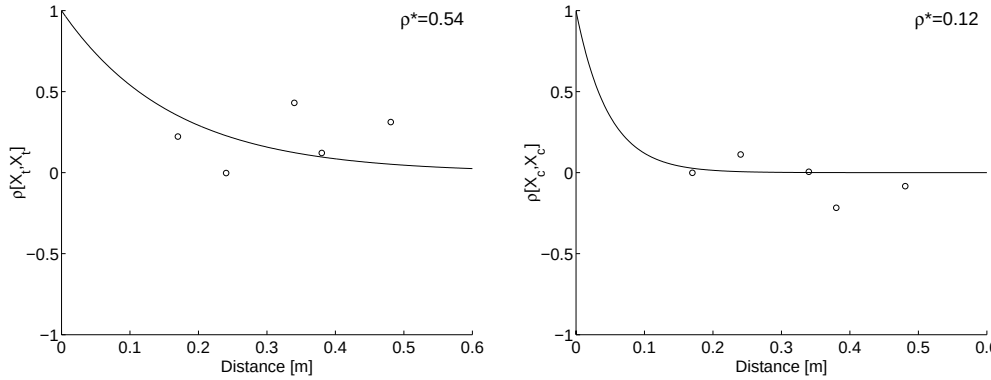

Figure A.31: LS-fitted correlation function for a) X_t and b) X_c, SCA 200KL.

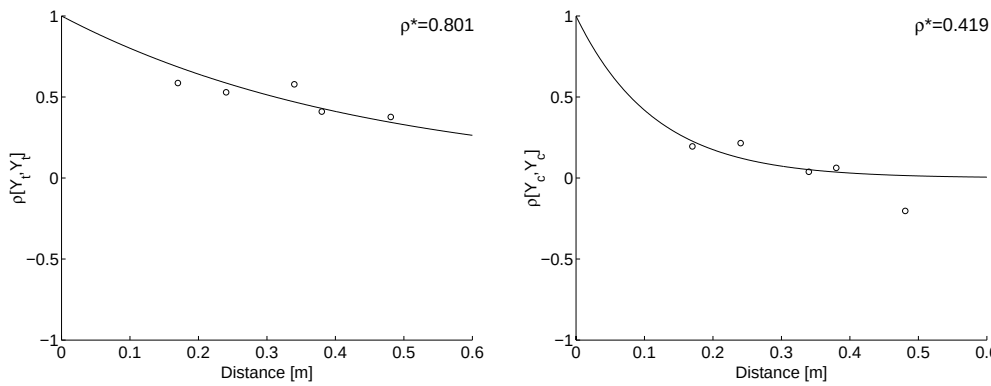

Figure A.32: LS-fitted correlation function for a) Y_t and b) Y_c, SCA 200KL.

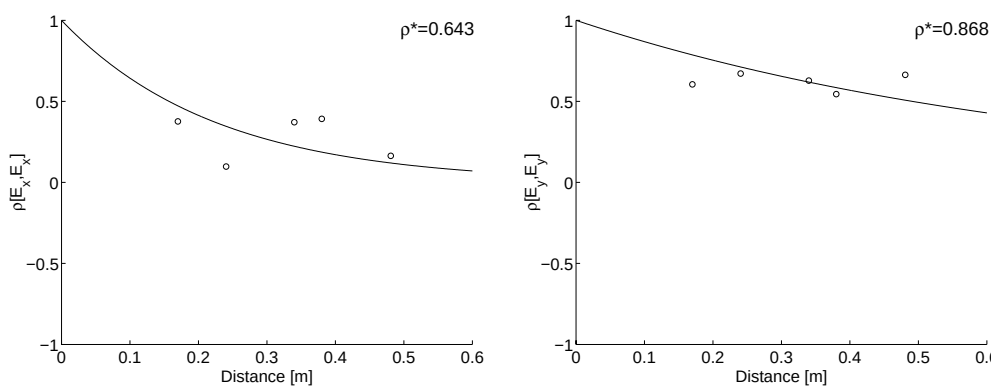

Figure A.33: LS-fitted correlation function for a) E_x and b) E_y, SCA 200KL.

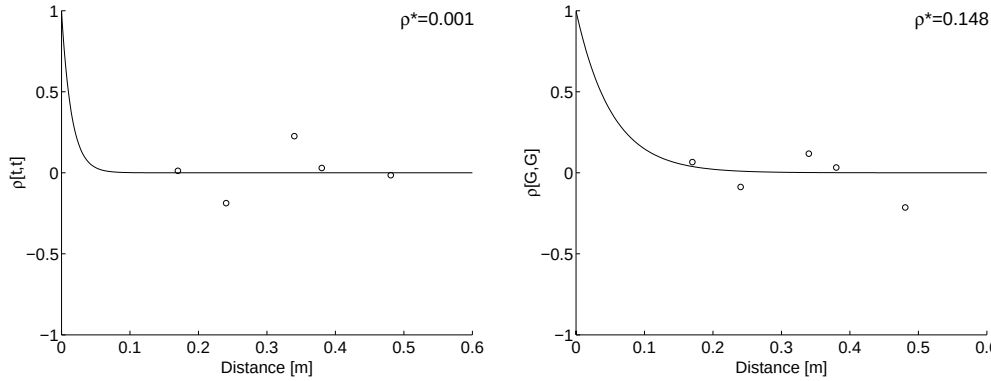

Figure A.34: LS-fitted correlation function for a) t and b) G, SCA 200KL.

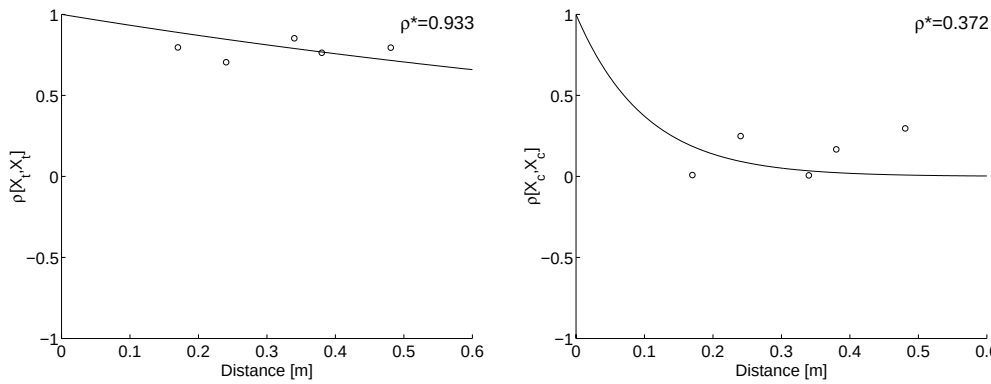

Figure A.35: LS-fitted correlation function for a) X_t and b) X_c, SCA 150TL.

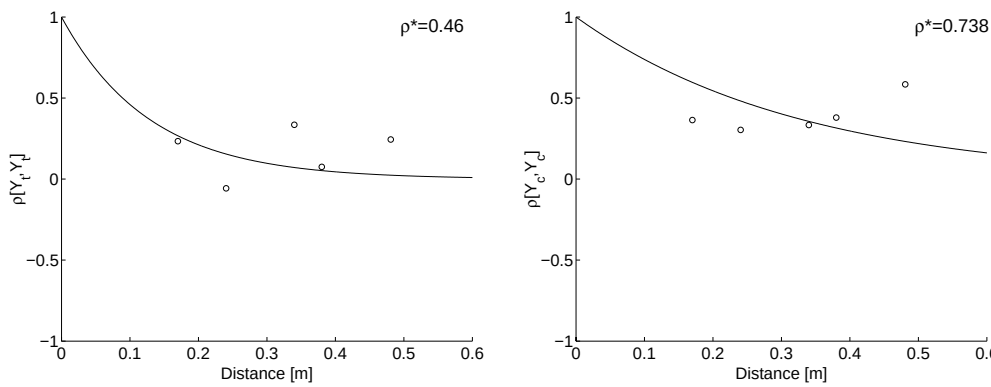

Figure A.36: LS-fitted correlation function for a) Y_t and b) Y_c, SCA 150TL.

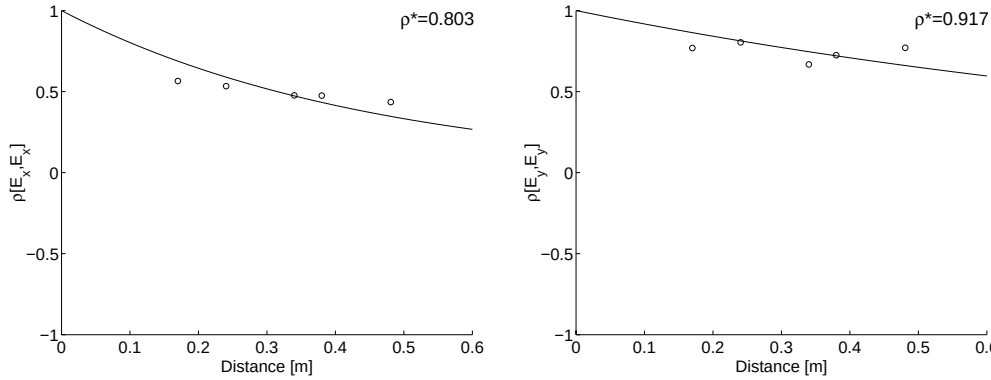

Figure A.37: LS-fitted correlation function for a) E_x and b) E_y, SCA 150TL.

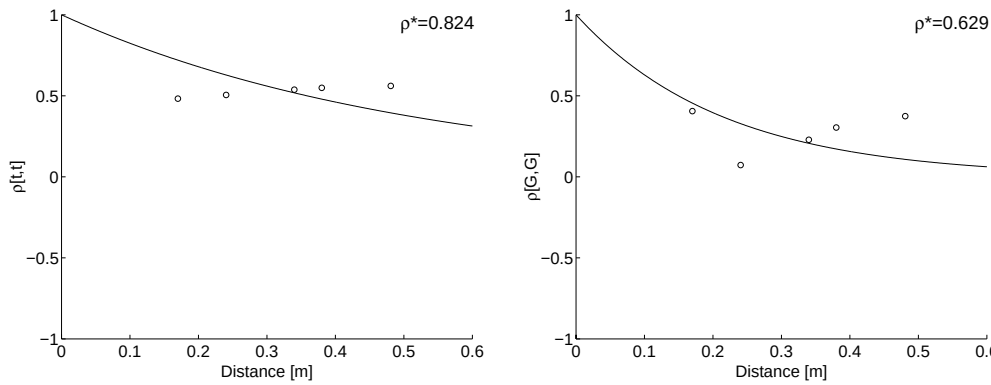

Figure A.38: LS-fitted correlation function for a) t and b) G, SCA 150TL.

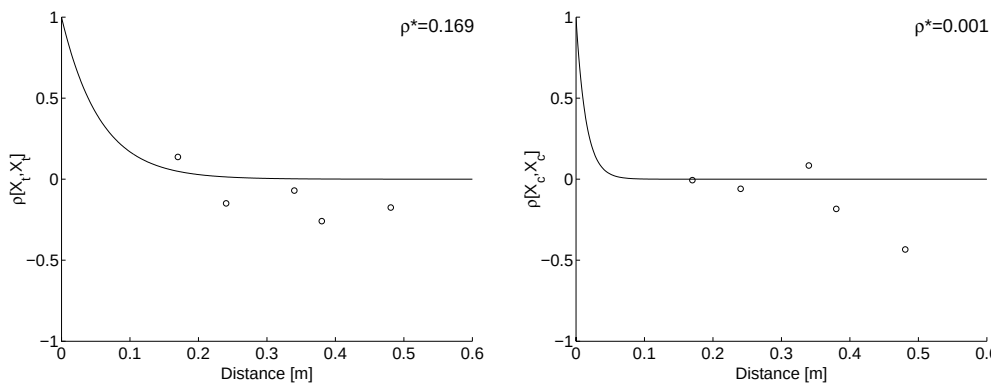

Figure A.39: LS-fitted correlation function for a) X_t and b) X_c, SCA 150HK.

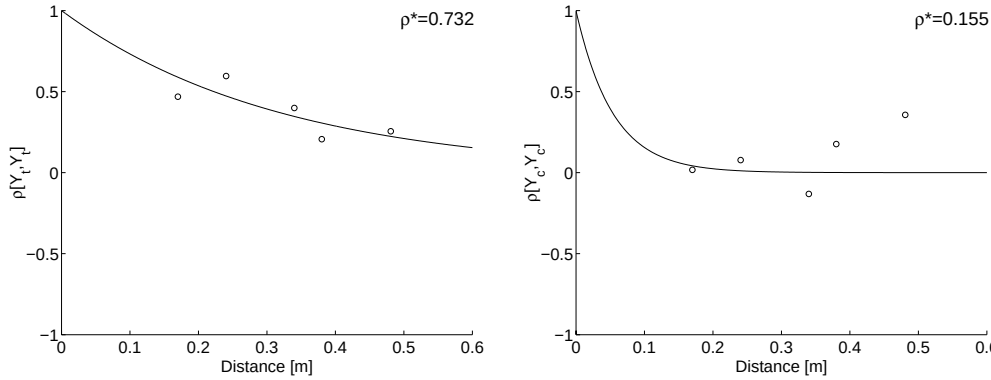

Figure A.40: LS-fitted correlation function for a) Y_t and b) Y_c, SCA 150HK.

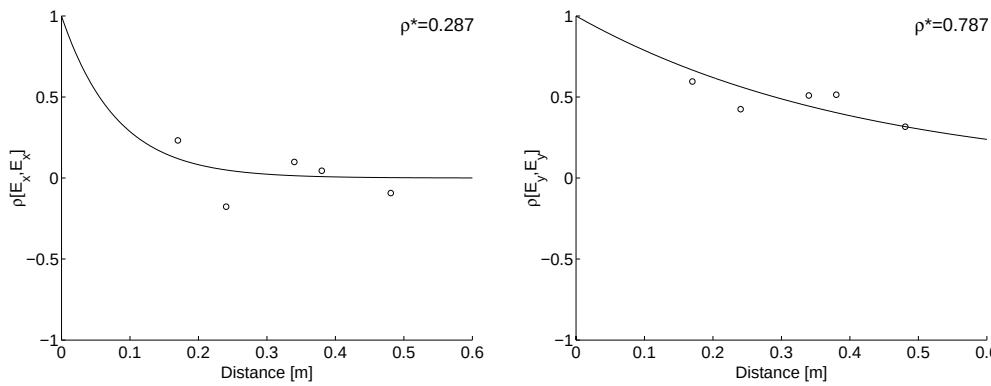

Figure A.41: LS-fitted correlation function for a) E_x and b) E_y, SCA 150HK.

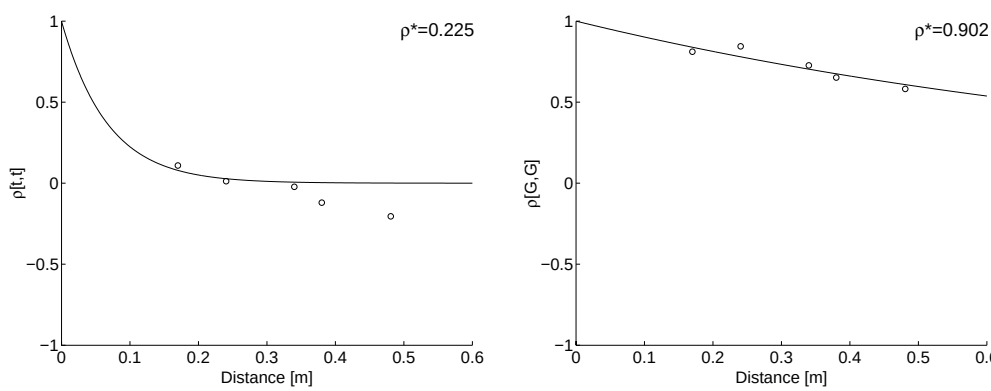

Figure A.42: LS-fitted correlation function for a) t and b) G, SCA 150HK.

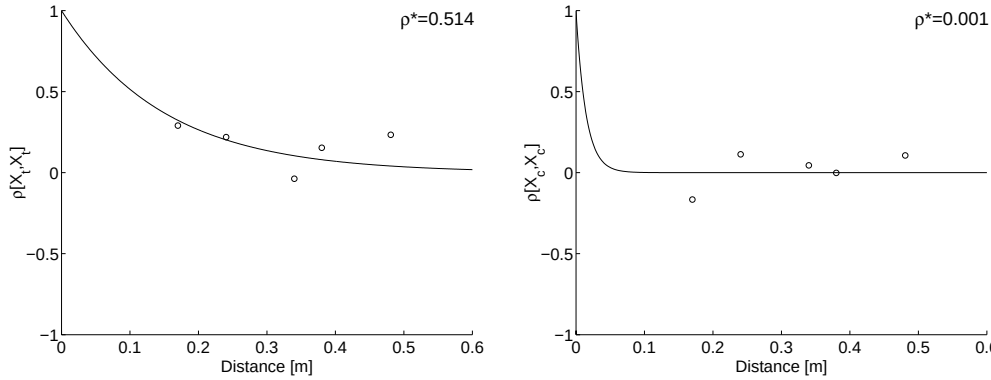

Figure A.43: LS-fitted correlation function for a) X_t and b) X_c, SCA 112RF.

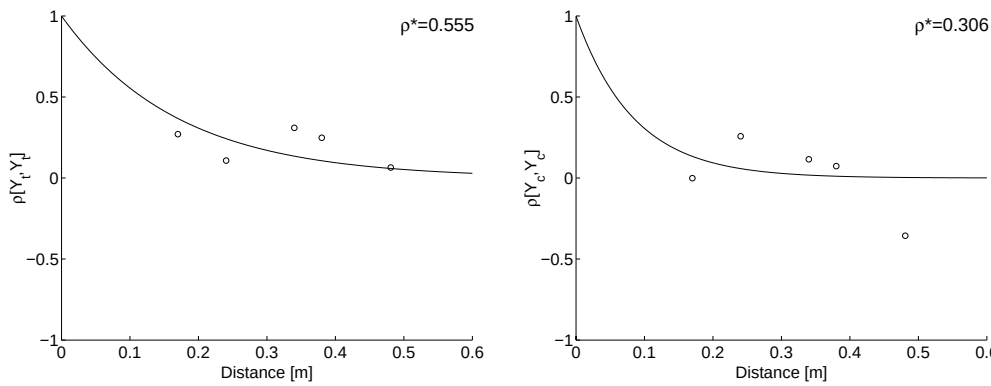

Figure A.44: LS-fitted correlation function for a) Y_t and b) Y_c, SCA 112RF.

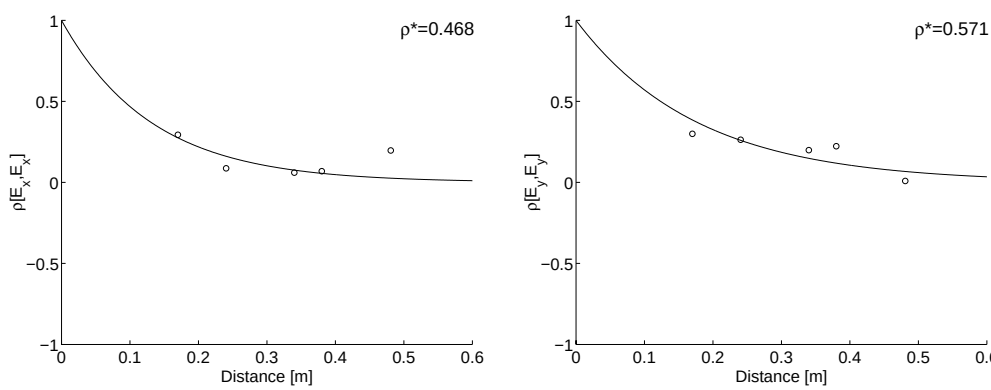

Figure A.45: LS-fitted correlation function for a) E_x and b) E_y, SCA 112RF.

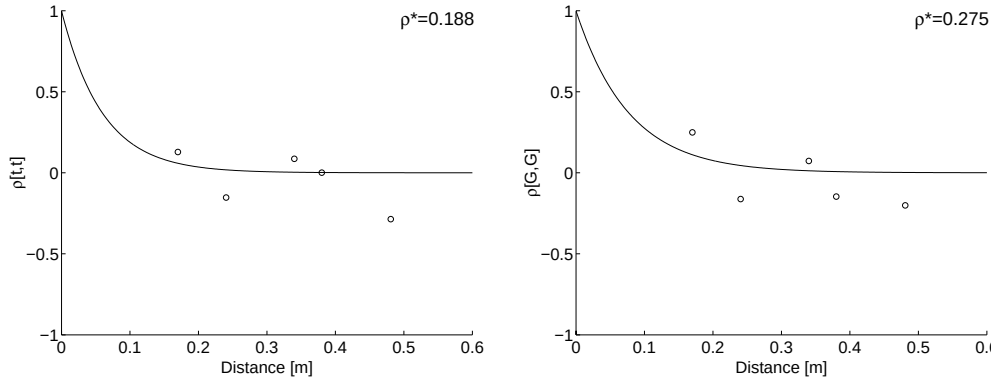

Figure A.46: LS-fitted correlation function for a) t and b) G, SCA 112RF.

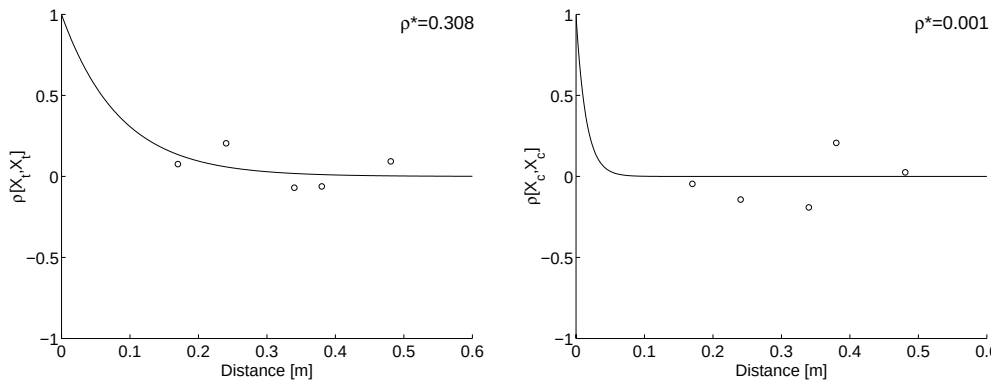

Figure A.47: LS-fitted correlation function for a) X_t and b) X_c, SCA 112HK.

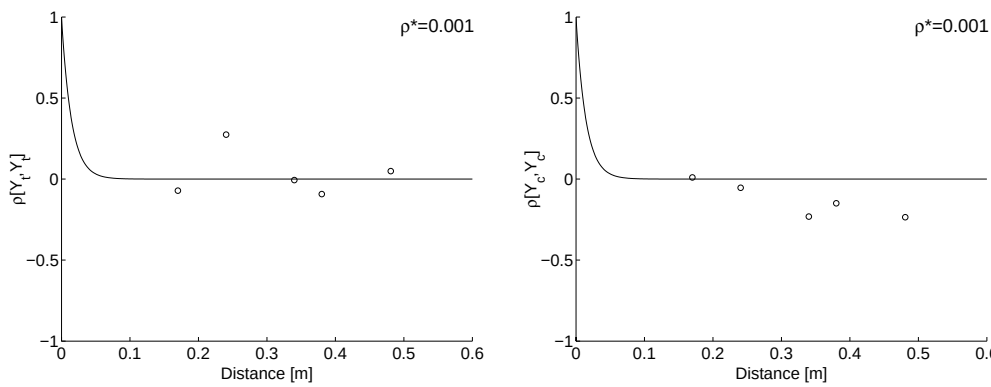

Figure A.48: LS-fitted correlation function for a) Y_t and b) Y_c, SCA 112HK.

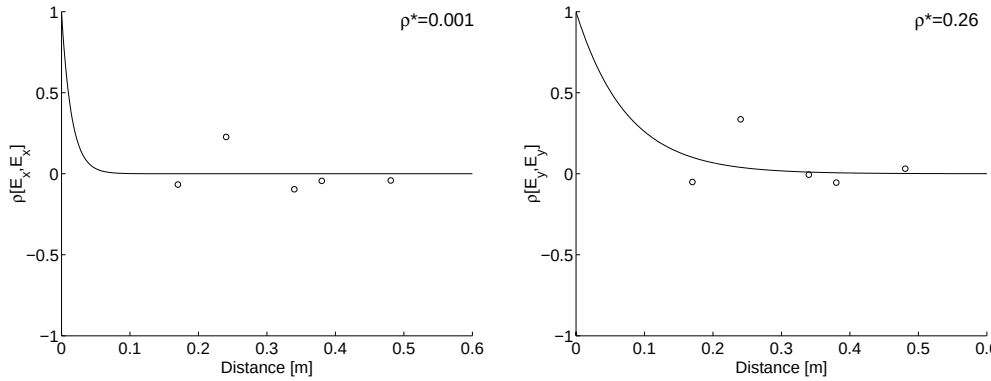

Figure A.49: LS-fitted correlation function for a) E_x and b) E_y, SCA 112HK.

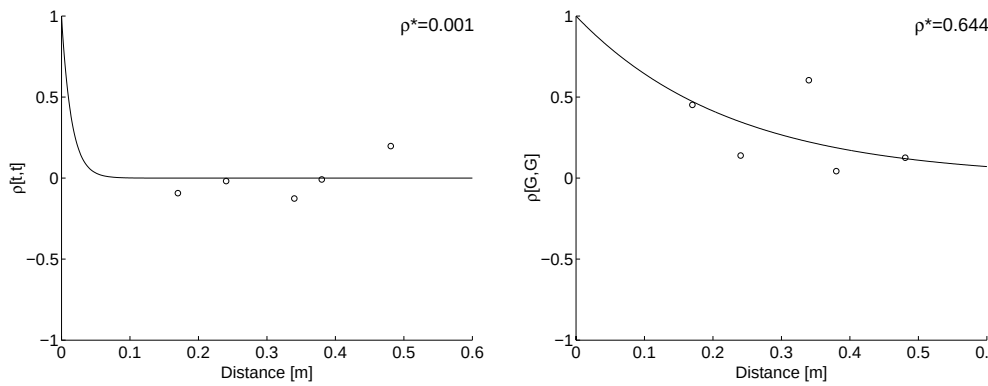

Figure A.50: LS-fitted correlation function for a) t and b) G, SCA 112HK.

Appendix B

STRENGTH TESTING OF CORRUGATED BOARD BOXES IN NATURALLY VARYING CLIMATE

Introduction

The rate of creep and damage growth in paper materials are known to be highly influenced by shifts in the level of surrounding relative humidity. As an example, the strength of corrugated board boxes with a constant compression top load will be substantially reduced. Qualitatively, boxes loaded by a compressive load which is 60% of the short time failure load will fail after two to four weeks when the surrounding relative humidity is constant. If the surrounding relative humidity is varying the compressive load equivalent with the same time to failure is only 20% of the short time failure load.

An important observation of long term loaded boxes is that the deviation of time to failures is large. Normally, the coefficient of variation of the time to failure of regular boxes is between 0.3 and 0.5. Comparatively, the coefficient of variation of the short term collapse load is 0.05. Obviously, the large deviation of time to failure is a result of the flat relation of applied load to the time to failure.

If a measure of the reliability of long term loaded boxes is desired, i.e. the cumulative probability of box failure at a certain moment, knowledge of the probability density function for the time to failure is needed. This may be determined from the density function for the short term load, if the relation of applied load to time to failure is known. However, if the relative humidity is varying this relation is a very complex function and an explicit relation for the density function is hard to achieve.

Herein an experimental procedure is presented, describing the measurement of reliability of long term loaded boxes in a naturally varying surrounding relative humidity. The time to failures are experimentally determined for the purpose of comparison with numerical modelling concerning lifetime of corrugated board boxes.

Materials and types of boxes

Two types of regular boxes are employed in the long term tests. The first box, later referred to as box type 1, is a cubic box with the outer liner coated with a white surface. The length, width and height of the box is 400 mm and the board, termed SCA 171C, is consisting of two liners and a C-flute. The second box, referred to as box type 2, has the same shape, dimensions and profile of the flute but with naturally coloured liners. The board in this box is termed SCA 140C. The specification of boxtypes and liner and fluting materials can be found in Tables B.1 and B.2.

Table B.1: Types of boxes.

Box type	Dimension, L×W×H [mm]	Board	Compr. strength [kN]	C.O.V.
1	400×400×400	171C	3.706	0.052
2	400×400×400	140C	2.120	0.036

Table B.2: Types of boards.

Board	Outer liner[a]	Fluting[a]	Inner liner[a]
SCA 171C	200WT	150HK	200KL
SCA 140C	150TL	112RF	150TL

[a]Numbers indicate the grammage [g/m^2].

Experimental method

The experiments on long term strength of boxes is performed in an airy untempered building located at the inland part of southern Sweden (Asa, Småland). The test equipment consists of 60 steel frames, each with two projecting beams over the space intended for the boxes. A chain is attached to the beams in one end and to a sheet metal cassette in the other end. The bottom of the cassette is consisting of a plane surface to be stacked on top of the boxes. The cassette can be filled with a variable number of sheet metals in order to produce a suitable mechanical compressive load of the boxes. To the cassette is also attached a flexible cord with a pin on the end which is disconnected at the moment of collapse of the box.

Two load levels is used in every set of experiments, which implies that 30 boxes are simultaneously subjected to identical loading conditions. Before loading the open slots of the boxes are sealed with tape and the box is left unloaded in at least 24 hours before the start of the test. Two sheets of corrugated board is also used as bottom and top protection of the box against condensed water.

In addition to the top loaded boxes is measured the relative humidity and temperature inside and outside of a sealed corrugated board box. The purpose of this is to determine the moisture transport in the box. Supplementary to the relative humidity and temperature is measured the moisture content in two liner specimens by the use of inside and outside placed scales. The accuracy of the relative humidity and temperature probes are ±3% RH and ±0.7 °C, respectively. The readability and accuracy of the scales is 0.01 g ±0.02 g. A computer is used for recording the moments of collapse of boxes and logging of relative humidities, temperatures and weights of the liner specimens.

A number of sets of boxes are tested during a period of eight months. The tests started in December 2001 and ended in august 2002. For future reference each set of the experiments is labeled to discern the start of the test, the box type used and the load levels applied, see Table B.3. The load ratio is the applied load divided by the short term

strength in 50% relative humidity, see Table B.1 for the short term strength and Section 5.1 for specification of the experimental procedure concerning the short term strength. The times indicated as start of the tests is the median time for the mounting of the compressive loads. The approximate time duration for the mounting of one set is three hours.

Table B.3: Experimental sets.

Set	Box type	Load [N]	Load ratio	Start of test	Sample size
1a	1	1000	0.270	011228 17:20	24
1b	1	500	0.135	011228 18:45	30
2a	2	500	0.236	020215 15:10	30
2b	2	250	0.118	020215 11.30	30
3a	1	1500	0.405	020508 14:10	25
3b	1	1000	0.270	020508 15:30	30
4a	2	1000	0.472	020617 14:10	30
4b	2	500	0.236	020617 12:30	19

In order to limit the time extension of the tests some of the sets was interrupted before all of the boxes collapsed. In set 1b five boxes were not collapsed when the test was interrupted. The entire set 2b is discarded since no boxes were collapsed after 10 weeks. Unfortunately, the entire set 3b also has to be discarded since a failure of the measuring system occurred due to a thunderstorm.

For some of the sets a few pins was not properly pulled out at the moment for collapse of the boxes. In this case the corresponding set is reduced with respect to the number of tested boxes, i.e. sample size. In set 1a, 3a and 4b the number of boxes that are discarded are six, five and eleven, respectively. The right column in Table B.3 indicates the reduced number of boxes in the set.

Results

In Figures B.1a to B.6c are plotted the temperatures, relative humidities and the estimated probability of collapsed boxes for sets 1a-4b. The estimation of failure probability is given as the number of collapsed boxes divided by the sample size, as given in Table B.3.

In set 1a all 24 boxes were collapsed after 16 days. The majority of the collapses occurred between 12 and 15 days which implies that the deviation in time to failure is very small. In set 1b the deviation is much larger, the first boxes collapse after 23 days while after 46 days five boxes were not collapsed. A concentration of failures is found between 25 and 30 days. In set 2a the majority of the boxes collapsed between seven and 14 days. Six days from the start of the test period there is a drop in relative humidity from 90% to 70%. After this there are two humps in relative humidity, each resulting in a large amount of box failures. After this the relative humidity is oscillating between 80% and 90% and the failures are more scattered over time. In set 3a the variation in relative

humidity is very large, between 40% and 80%. It is observed that there is a time lag of the relative humidity inside the box compared to the outside. In addition, the curve of the relative humidity inside the box is smoother than the curve corresponding to the relative humidity outside of the box. The failures are very dispersed, the first collapse occurred after two days whereas the final collapse occurred after more than six days. Due to the large load ratio in set 4a, all boxes collapsed within 19 hours. The first collapse occurred after 8 minutes only. In set 4b the relative humidity is oscillating between 60% and 90%. Typical for the summer, the daily variation in relative humidity is very large. An extremely large scatter in the time to failures is observed. The first collapses occurred after 2 days only, whereas the final collapse occurred after 56 days. After approximately 18 days the whether conditions are very humid and a concentration of box failures is persistently observed here.

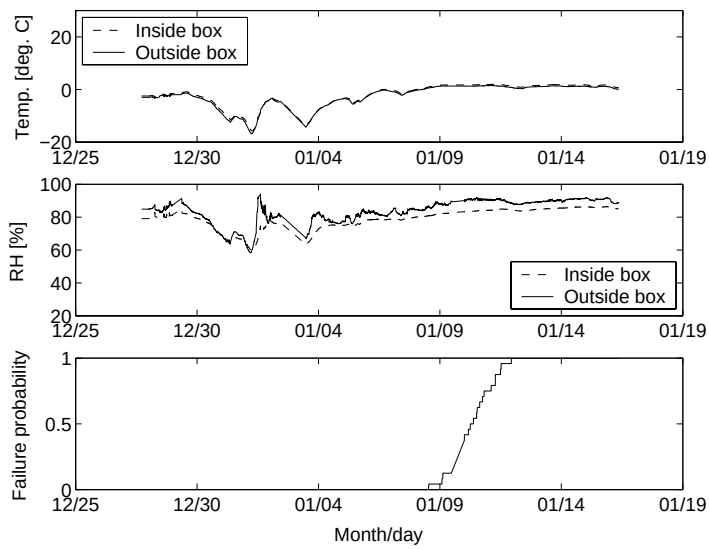

Figure B.1: a) Temperature, b) relative humidity and c) failure probability for set 1a.

In Figures B.7a to B.9b the distribution of failures during 24 hours is plotted. The time span of each bin is one hour, for example the first bin in Figure B.7a indicates that seven failures occcured between midnight and one during the test period. It is observed that, despite the periodic daily variation in relative humidity, the collapses occurred quite evenly distributed during the day.

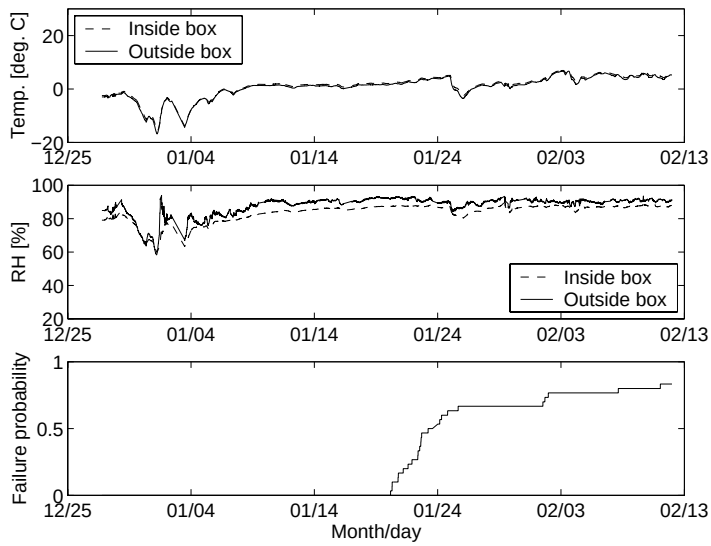

Figure B.2: a) Temperature, b) relative humidity and c) failure probability for set 1b.

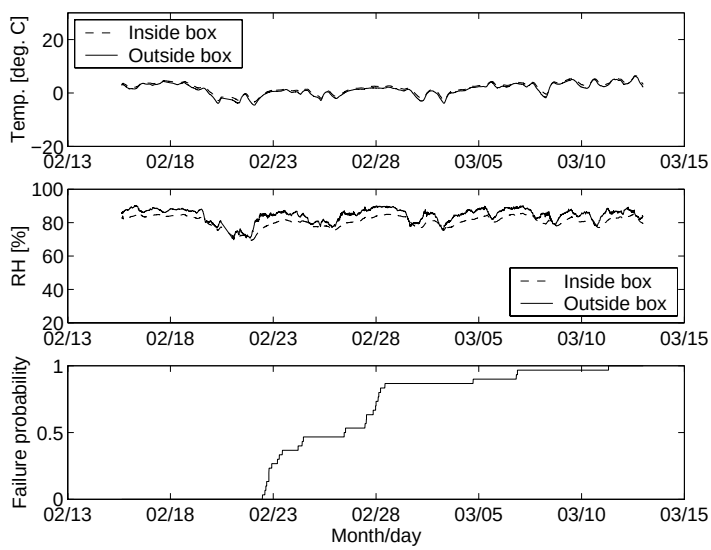

Figure B.3: a) Temperature, b) relative humidity and c) failure probability for set 2a.

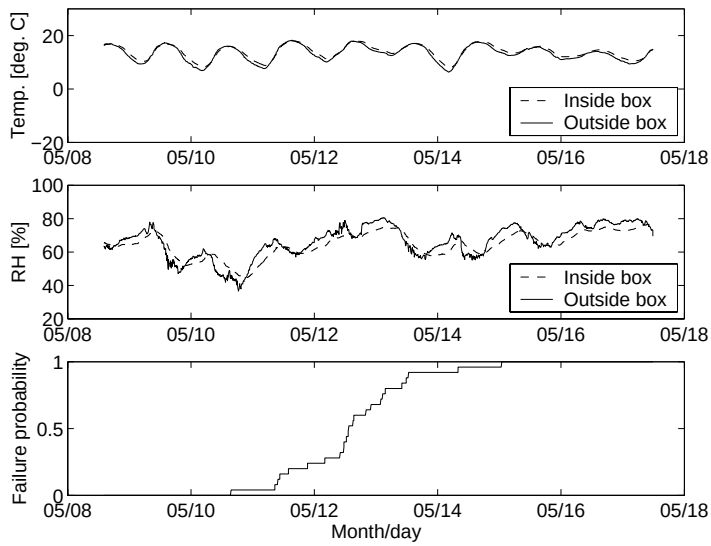

Figure B.4: a) Temperature, b) relative humidity and c) failure probability for set 3a.

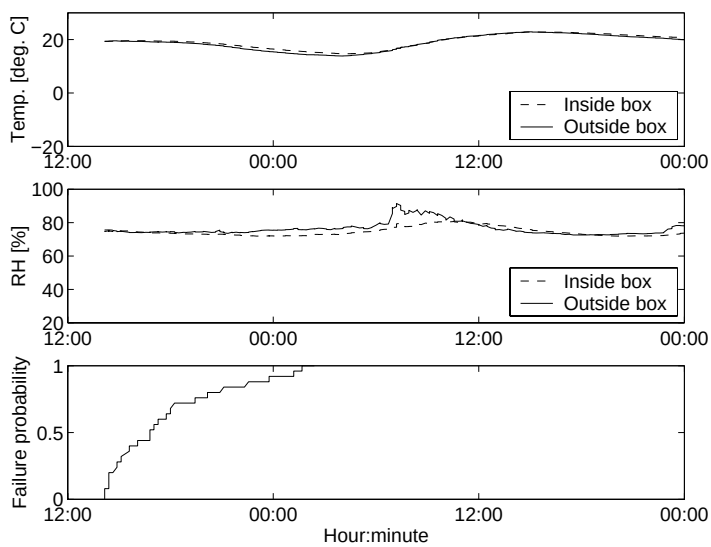

Figure B.5: a) Temperature, b) relative humidity and c) failure probability for set 4a.

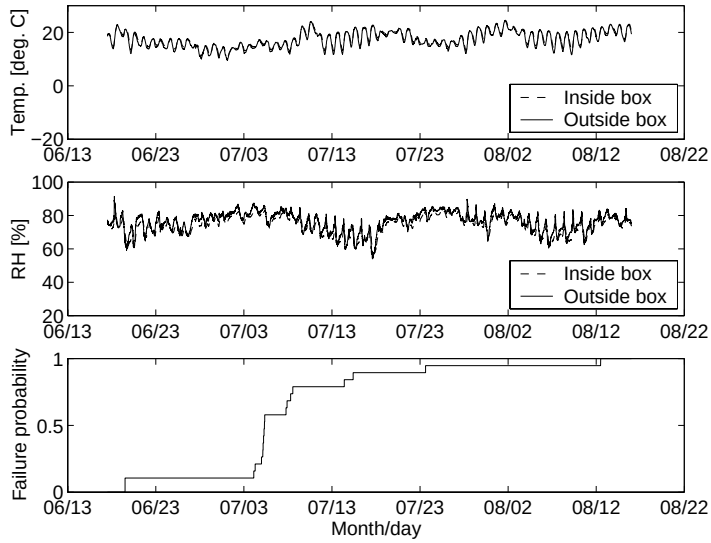

Figure B.6: a) Temperature, b) relative humidity and c) failure probability for set 4b.

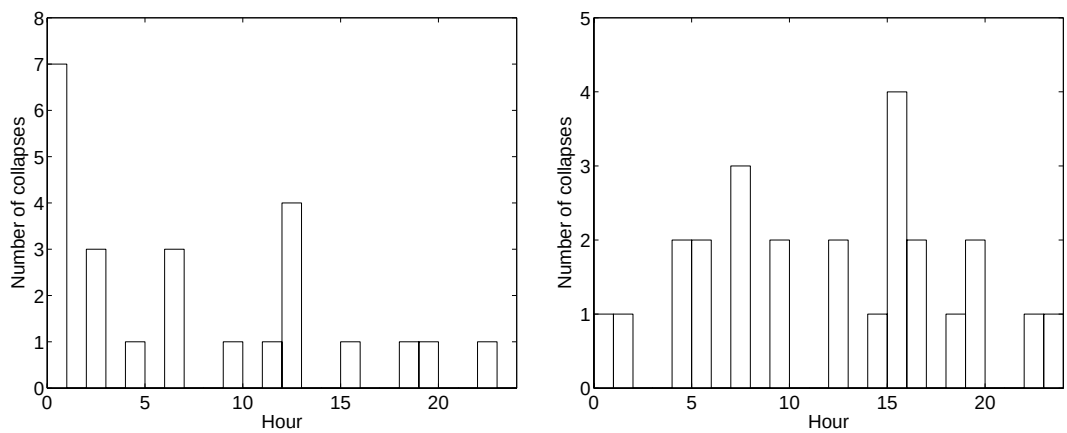

Figure B.7: Daily distribution of collapses a) for set 1a and b) for set 1b.

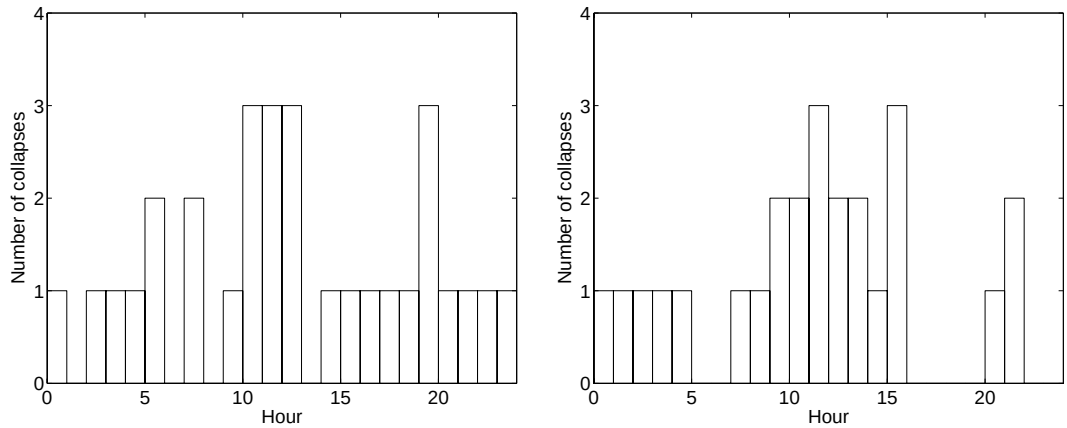

Figure B.8: Daily distribution of collapses a) for set 2a and b) for set 3a.

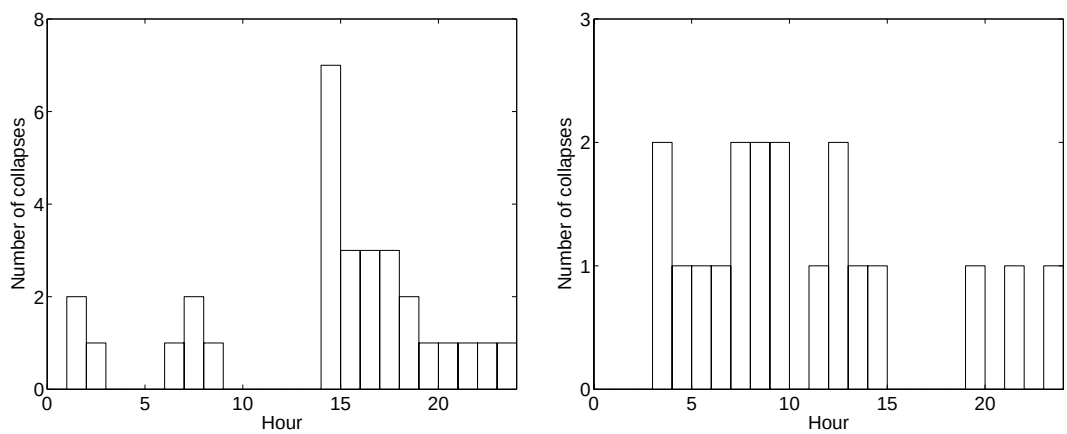

Figure B.9: Daily distribution of collapses a) for set 4a and b) for set 4b.

Appendix C

METHODS FOR RELIABILITY ANALYSIS

Introduction

Many different techniques for the study of structural reliability are available. The techniques can be categorized as exact, e.g. Monte Carlo methods, multi-fold integral evaluation, and approximate, e.g. series expansion methods, response surface fitting and FORM/SORM (First/Second Order Reliability Methods [1].

In using the Monte Carlo method, a suitable number of samples are created as input variables to the structural model. The computation effort with this method is obvious and will, of course, increase with the effort needed for the basic deterministic model. In contrary, it is the most versatile method in terms of problem definition and the solution is always convergent. In order to reduce the computational effort, different methods to reduce the number of samples in structural analysis has been proposed, e.g. Olsson [2]. In using FORM or SORM, limit state functions are formulated which contain both the structural permissible response and the response as a function of load. The next step is to determine the probability content in terms of a minimization procedure. The attractiveness of FORM/SORM lies in the comparably speed by which an engineering solution is attained. However, the method has mostly found its application on simple structures and the application to finite element methods is currently an intensive research field. Examples of work within reliability finite element analysis are Frangopol et. al. [3], Liu and Liu [4], Liu and Der Kiureghian [5], Guan and Melchers [6], and Viadero et. al. [7].

The first order reliability method

The probability of failure P_f, can in terms of the stochastic basic variables $\boldsymbol{\alpha}$, be written

$$P_f = P[g_\alpha(\boldsymbol{\alpha}) \leq 0] = \int_{g_\alpha(\alpha)\leq 0} f(\boldsymbol{\alpha}) d\alpha \tag{C.1}$$

where $g(\boldsymbol{\alpha})$ is the limit state function, which is positive when the structure is in a safe state, and $f(\boldsymbol{\alpha})$ is the joint probability density function of $\boldsymbol{\alpha}$. The general solution of the multifold integral in (C.1) provides a prohibitive task, which has led to the development of approximate techniques. One of the approximate techniques is FORM, in which the limit state function can be mapped to the standard uncorrelated normal space of the basic variables

$$T: \quad g_{\hat{\alpha}} \leq 0 \quad \rightarrow \quad g_z \leq 0 \tag{C.2}$$

where $\mathbf{z}$ are the standard normal variables and $\hat{\boldsymbol{\alpha}}$ is the set of uncorrelated basic variables. According to the mapping given by Hasofer and Lind, [8], the relation between $\mathbf{z}$ and $\hat{\boldsymbol{\alpha}}$

reads

$$\mathbf{z} = \hat{\mathbf{C}}_{\alpha}^{-1/2} \left(\hat{\boldsymbol{\alpha}} - \mathrm{E}[\hat{\boldsymbol{\alpha}}] \right) \tag{C.3}$$

The uncorrelated basic variables are related to $\boldsymbol{\alpha}$ by the orthogonal transformation matrix $\mathbf{A}$

$$\hat{\boldsymbol{\alpha}} = \mathbf{A}^T \boldsymbol{\alpha} \tag{C.4}$$

so that the covariance matrix $\hat{\mathbf{C}}_{\alpha}$ is diagonal

$$\hat{\mathbf{C}}_{\alpha} = \mathbf{A}^T \mathbf{C}_{\alpha} \mathbf{A} \tag{C.5}$$

In using FORM, the reliability index, β, is found as the minimum distance from the origin to the failure surface $g_z(\mathbf{z}) = 0$. This is expressed as

$$\beta = \min \|\mathbf{z}\| \quad \mathbf{z} \in L_z \tag{C.6}$$

where L_z defines the failure surface. The point in the z-coordinate system where the minimum distance is found is referred to as the design point. This point is found by the use of an iterative search algorithm.

For a generic failure surface, an approximation to the probability of failure is given by

$$P_f = \Phi(-\beta) \tag{C.7}$$

where Φ is the standard normal distribution function.

Implemented iterative search algorithm

There are many available iterative algorithms for constrained minimization problems. A search algorithm which is found to be practical in structural minimization problems and used for the calculations presented in Paper III and Paper VII, is described in [1]. This algorithm uses the projection of the current point $\mathbf{z}^{(k)}$ on the failure surface gradient in a sequence of values of $\mathbf{z}$. The gradient pointing towards the failure region can be expressed as

$$\tilde{\mathbf{z}}^{(k)} = -\frac{\partial g(z^{(k)})/\partial z_i}{\left[\sum_{i=1}^{n} \left(\partial g(z^{(k)})/\partial z_i \right)^2 \right]^{1/2}} \tag{C.8}$$

where n is the number of stochastic variables. The projection of $\mathbf{z}^{(k)}$ on $\tilde{\mathbf{z}}^{(k)}$ is given by

$$\mathbf{v}_a^{(k)} = (\mathbf{z}^{(k)} \cdot \tilde{\mathbf{z}}^{(k)}) \tilde{\mathbf{z}}^{(k)} \tag{C.9}$$

The point at the end of this vector is put closer to the actual failure surface $g_z(\mathbf{z}) = 0$ by

$$\mathbf{v}_b^{(k)} = \frac{g(\mathbf{z}^{(k)})}{\left[\sum_{i=1}^{n} \left(\partial g(z^k)/\partial z_i \right)^2 \right]^{1/2}} \, \tilde{\mathbf{z}}^{(k)} \tag{C.10}$$

The next iteration point is then given by

$$\mathbf{z}^{(k+1)} = \mathbf{v}_a^{(k)} + \mathbf{v}_b^{(k)} \tag{C.11}$$

and the iterations are continued until the convergence criterion

$$\begin{aligned} \|\mathbf{z}^{(k+1)} - \mathbf{z}^{(k)}\| &\leq \epsilon_1 \\ |g(\mathbf{z}^{(k+1)})| &\leq \epsilon_2 \end{aligned} \tag{C.12}$$

is fulfilled.

At the point of convergence, z^*, the limit surface can be given as a linearized surface, which has the equation

$$\sum_{i=1}^{n} \frac{\partial g(z^*)}{\partial z_i}(z_i - z_i^*) - g^* = 0 \tag{C.13}$$

or on normal form

$$\frac{1}{\left[\sum_{i=1}^{n} \left(\partial g(z^*)/\partial z_i\right)^2\right]^{1/2}} \sum_{i=1}^{n} \frac{\partial g(z^*)}{\partial z_i} z_i + \beta - g^* = 0 \tag{C.14}$$

It should be pointed out that if the limit state function is a convex function with very large curvature, the projection given by (C.9) will be directed to a point far apart from the limit state surface, and the solution is not convergent. If the failure criterion is a concave and closed function, the algorithm can be expected to converge to the design point.

References

[1] Madsen, H. O., Krenk, S., and Lind, N. C., (1986) *Methods of Structural Safety*, Prentice-Hall, New Jersey.

[2] Olsson, A., (1999) *Modelling Damage and Stochastic Properties in Engineering Structures*, Licentiate thesis, Dept. of Struc. Mech., Lund University.

[3] Frangopol, D. M., Lee, Y-H., and Williams, K. J., (1996) *Nonlinear Finite Element Reliability Analysis of Concrete*, J. Eng. Mech., Vol. 122, No. 12.

[4] Liu, P-L., and Liu, K-G., (1993) *Selection of Random Field Mesh in Finite Element Reliability Analysis*, J. Eng. Mech., Vol. 119, No. 4.

[5] Liu, P-L., and Der Kiureghian, A., (1991) *Finite Element Reliability of Geometrically Nonlinear Uncertain Structures*, J. Eng. Mech., Vol. 117, No. 8.

[6] Guan, X. L., and Melchers, R. E.., (1999) *A Load Space Formulation for Probabilistic Finite Element Analysis of Structural Reliability*, Probabilistic Engineering Mechanics 14, pp 73-81.

[7] Viadero, F., Bueno, J. I., Lopez de Lacalle, L. N., and Sancibrian R., (1994) *Reliability Computation on Stiffened Plates*, Advances in Engineering Software, **20**, pp 43-48.

[8] Hasofer, A. M, and Lind, N. C., (1974) *An Exact and Invariant First Order Reliability Format*, Proc. ASCE, J. Eng. Mech. Div., pp 111-121

Appendix D

LAMINATED QUADRILATERAL SHELL WITH ASSUMED NATURAL STRAIN FIELD

Introduction

The formulation of a shell element quadrilateral which is robust and applicable to a variety of plate structures has for a long time been a challenging task. It is common knowledge that, due to non-zero transverse shear stresses, lower order elements which employ full integration suffer from shear locking as the shell thickness diminish. One solution to defeat the shear locking phenomena is to perform underintegration over the area defining the surface of the shell. As a trivial case the element is uniformly underintegrated with one gauss point over the shell plane. A severe complication is, however, the spurious modes emanating from rank deficiency of the stiffness matrix. The number of spurious modes can be reduced by utilizing selective underintegration of the transverse shear terms, see for example [1]. A very attractive solution is to enable vanishing of transverse shear stress by interpolating the corresponding shear strains with a priori chosen sampling points, as proposed in [2, 3]. This method, the Assumed Natural Strain method (ANS), is used for the implementation of a four node isoparametric shell element applicable to large deflections, rotations and strains.

The element described in [3] is extended to apply also to laminated (composite) shells. Also, in contrast to [3] the numerical integration is performed in a local Cartesian coordinate system. The transverse shear stiffnesses of the composite are reduced using a technique which matches the shear strain energy obtained from equilibrium of the laminate with the strain energy given by the simple displacement assumption. In the strain energy equivalence the shear strains are assumed to be small.

A complete derivation of the shell element is provided starting with the linearized form of the virtual work equation. In the final section an obstacle course of test examples are constructed to validate the numerical performance.

Description of element formulation

Tensors in covariant and contravariant bases

Of particular use in the formulation of shell elements employing mixed interpolation of strains is the expression of tensors in components of a basis of nonorthogonal base vectors. A convected coordinate system is introduced with the base vectors

$$\mathbf{G}_1 = \frac{\partial \mathbf{X}}{\partial \xi} \qquad \mathbf{G}_2 = \frac{\partial \mathbf{X}}{\partial \eta} \qquad \mathbf{G}_3 = \frac{\partial \mathbf{X}}{\partial \zeta} \tag{D.1}$$

where $\mathbf{X}$ is the referential position vector and ξ, η and ζ are the natural finite element coordinates. In a deformed state (D.1) takes the form

$$\mathbf{g}_1 = \frac{\partial \mathbf{x}}{\partial \xi} \qquad \mathbf{g}_2 = \frac{\partial \mathbf{x}}{\partial \eta} \qquad \mathbf{g}_3 = \frac{\partial \mathbf{x}}{\partial \zeta} \tag{D.2}$$

where $\mathbf{x} = \mathbf{X} + \mathbf{u}$ is the displaced position vector. The contravariant counterpart, $\mathbf{G}^i$, of $\mathbf{G}_j$ is given by

$$\mathbf{G}^i = G^{ij}\mathbf{G}_j, \qquad [G^{ij}] = [G_{ij}]^{-1}, \qquad G_{ij} = \mathbf{G}_i \cdot \mathbf{G}_j \tag{D.3}$$

The Green Lagrange strain tensor, $\mathbf{E}$, can be expressed by an orthogonal Cartesian basis or a nonorthogonal contravariant basis as

$$\mathbf{E} = E_{ij}\mathbf{e}_i \otimes \mathbf{e}_j = \tilde{E}_{ij}\mathbf{G}^i \otimes \mathbf{G}^j \tag{D.4}$$

where the covariant components, $\tilde{E}_{ij}$, are given by the initial and displaced covariant basis vectors

$$\tilde{E}_{ij} = \frac{1}{2}(\mathbf{g}_i \cdot \mathbf{g}_j - \mathbf{G}_i \cdot \mathbf{G}_j) \tag{D.5}$$

The Cartesian components of the strain, E_{ij}, are related to $\tilde{E}_{ij}$ by

$$E_{ij} = \tilde{E}_{mn}(\mathbf{G}^m \cdot \mathbf{e}_i)(\mathbf{G}^n \cdot \mathbf{e}_j) = \tilde{E}_{mn}(\mathbf{G}^m \otimes \mathbf{G}^n) : (\mathbf{e}_i \otimes \mathbf{e}_j) \tag{D.6}$$

whereas the inverse relation of (D.6) is

$$\tilde{E}_{ij} = E_{mn}(\mathbf{e}_m \cdot \mathbf{G}_i)(\mathbf{e}_n \cdot \mathbf{G}_j) = E_{mn}(\mathbf{e}_m \otimes \mathbf{e}_n) : (\mathbf{G}_i \otimes \mathbf{G}_j) \tag{D.7}$$

The second Piola-Kirchhoff stress tensor, $\mathbf{S}$, can be expressed by an orthogonal Cartesian basis or a nonorthogonal covariant basis as

$$\mathbf{S} = S_{ij}\mathbf{e}_i \otimes \mathbf{e}_j = \tilde{S}^{ij}\mathbf{G}_i \otimes \mathbf{G}_j \tag{D.8}$$

The Cartesian components of the stress, S_{ij}, are related to $\tilde{S}^{ij}$ by

$$S_{ij} = \tilde{S}^{mn}(\mathbf{G}_m \cdot \mathbf{e}_i)(\mathbf{G}_n \cdot \mathbf{e}_j) = \tilde{S}^{mn}(\mathbf{G}_m \otimes \mathbf{G}_n) : (\mathbf{e}_i \otimes \mathbf{e}_j) \tag{D.9}$$

whereas the inverse relation of (D.9) is

$$\tilde{S}^{ij} = S_{mn}(\mathbf{e}_m \cdot \mathbf{G}^i)(\mathbf{e}_n \cdot \mathbf{G}^j) = S_{mn}(\mathbf{e}_m \otimes \mathbf{e}_n) : (\mathbf{G}^i \otimes \mathbf{G}^j) \tag{D.10}$$

Incremental equations of motion

The linearized principle of virtual displacements for a three-dimensional body, $\mathcal{B} \in \mathbb{R}^3$, undergoing compatible deformations, i.e. boundary conditions are fulfilled, is expressed by

$$\int_{\Omega_0} \delta\mathbf{E} : \mathbb{C} : \Delta\mathbf{E}\,\mathrm{d}V + \int_{\Omega_0} \mathbf{S} : \Delta\delta\mathbf{E}\,\mathrm{d}V = \int_{\partial\Omega_0} \delta\mathbf{u}^T\mathbf{T}\,\mathrm{d}S + \int_{\Omega_0} \delta\mathbf{u}^T\mathbf{B}\,\mathrm{d}V - \int_{\Omega_0} \delta\mathbf{E} : \mathbf{S}\,\mathrm{d}V \tag{D.11}$$

where $\delta\mathbf{E}$ and $\Delta\delta\mathbf{E}$ denote the first and second variation of the Green Lagrange strain tensor, $\mathbb{C}$ is the fourth order elasticity tensor and Ω_0 is the referential volume of $\mathcal{B}$. $\mathbf{T}$ and $\mathbf{B}$ are the applied surface tractions and body forces, respectively. Observing that the first and second variation of $\mathbf{E}$ is given by

$$\begin{aligned}\delta\mathbf{E} &= \mathrm{sym}(\mathbf{F}^T\mathrm{Grad}\delta\mathbf{u}) \\ \Delta\delta\mathbf{E} &= \mathrm{sym}((\mathrm{Grad}\delta\mathbf{u})^T\mathrm{Grad}\Delta\mathbf{u})\end{aligned} \tag{D.12}$$

and noting the symmetry properties of $\mathbb{C}$ and $\mathbf{S}$, (D.11) can be written as

$$\begin{aligned}\int_{\Omega_0}(\mathbf{F}^T\mathrm{Grad}\delta\mathbf{u}) : \mathbb{C} : (\mathbf{F}^T\mathrm{Grad}\Delta\mathbf{u})\,\mathrm{d}V + \int_{\Omega_0}\mathbf{S} : ((\mathrm{Grad}\delta\mathbf{u})^T\mathrm{Grad}\Delta\mathbf{u})\,\mathrm{d}V = \\ \int_{\partial\Omega_0}\delta\mathbf{u}^T\mathbf{T}\,\mathrm{d}S + \int_{\Omega_0}\delta\mathbf{u}^T\mathbf{B}\,\mathrm{d}V - \int_{\Omega_0}(\mathbf{F}^T\mathrm{Grad}\delta\mathbf{u}) : \mathbf{S}\,\mathrm{d}V\end{aligned} \tag{D.13}$$

or

$$\begin{aligned}\int_{\Omega_0}((\mathrm{Grad}\mathbf{u}+\mathbf{I})^T\mathrm{Grad}\delta\mathbf{u}) : \mathbb{C} : ((\mathrm{Grad}\mathbf{u}+\mathbf{I})^T\mathrm{Grad}\Delta\mathbf{u})\,\mathrm{d}V + \\ \int_{\Omega_0}\mathbf{S} : ((\mathrm{Grad}\delta\mathbf{u})^T\mathrm{Grad}\Delta\mathbf{u})\,\mathrm{d}V = \\ \int_{\partial\Omega_0}\delta\mathbf{u}^T\mathbf{T}\,\mathrm{d}S + \int_{\Omega_0}\delta\mathbf{u}^T\mathbf{B}\,\mathrm{d}V - \int_{\Omega_0}((\mathrm{Grad}\mathbf{u}+\mathbf{I})^T\mathrm{Grad}\delta\mathbf{u}) : \mathbf{S}\,\mathrm{d}V\end{aligned} \tag{D.14}$$

Displacements and mapping of coordinates

In the formulation of general shell elements the position vector, ${}^0\mathbf{x} = \mathbf{X}$, of a point in the reference configuration, is a function of the parent domain coordinates (ξ, η, ζ) by the interpolated in-plane position of the shell reference surface, ${}^0\bar{\mathbf{x}}$, plus a contribution of the out-of-plane coordinate, ζ.The shell reference surface is defined as the mid-plane of the laminate. Introducing the Lagrange interpolation functions for a four node element, $N_k(\xi, \eta)$, the position vector can be expressed by

$${}^0\mathbf{x}(\xi,\eta,\zeta) = \sum_{k=1}^{4} N_k(\xi,\eta)\,{}^0\bar{\mathbf{x}}^{(k)} + \frac{\zeta}{2}\sum_{k=1}^{4} h_k N_k(\xi,\eta)\,{}^0\mathbf{v}_3^{(k)} \tag{D.15}$$

where ${}^0\mathbf{v}_3$ is the referential nodal director given by

$${}^0\mathbf{v}_3 = \frac{\frac{\partial^0\bar{\mathbf{x}}}{\partial\xi}\times\frac{\partial^0\bar{\mathbf{x}}}{\partial\eta}}{\left|\left|\frac{\partial^0\bar{\mathbf{x}}}{\partial\xi}\times\frac{\partial^0\bar{\mathbf{x}}}{\partial\eta}\right|\right|} \tag{D.16}$$

where for $\xi = \eta = -1$

$$\begin{aligned}\frac{\partial^0\bar{\mathbf{x}}}{\partial\xi} &= -\frac{1}{2}{}^0\bar{\mathbf{x}}^{(1)} + \frac{1}{2}{}^0\bar{\mathbf{x}}^{(2)} \\ \frac{\partial^0\bar{\mathbf{x}}}{\partial\eta} &= -\frac{1}{2}{}^0\bar{\mathbf{x}}^{(1)} + \frac{1}{2}{}^0\bar{\mathbf{x}}^{(4)}\end{aligned} \tag{D.17}$$

The geometrically consistent displacement at time t is given by

$$ {}^t\mathbf{u} = {}^t\mathbf{x} - {}^0\mathbf{x} = \sum_{k=1}^{4} N_k d\bar{\mathbf{x}}^{(k)} + \frac{\zeta}{2}\sum_{k=1}^{4} h_k N_k d\mathbf{v}_3^{(k)} \tag{D.18} $$

where

$$ d\bar{\mathbf{x}}^{(k)} = {}^t\bar{\mathbf{x}}^{(k)} - {}^0\bar{\mathbf{x}}^{(k)} \qquad d\mathbf{v}_3^{(k)} = {}^t\mathbf{v}_3^{(k)} - {}^0\mathbf{v}_3^{(k)} \tag{D.19} $$

The incremental displacement of a particle, $\Delta\mathbf{u}$, from the position ${}^t\mathbf{x}$ to ${}^{t+\Delta t}\mathbf{x}$ is

$$ \Delta\mathbf{u} = \sum_{k=1}^{4} N_k \Delta\bar{\mathbf{u}}^{(k)} + \frac{\zeta}{2}\sum_{k=1}^{4} h_k N_k(\xi,\eta)\Delta\mathbf{v}_3^{(k)} \tag{D.20} $$

where $\Delta\mathbf{v}_3^{(k)}$ is approximately given by

$$ \Delta\mathbf{v}_3^{(k)} = -{}^t\mathbf{v}_2^{(k)}\Delta\alpha^{(k)} + {}^t\mathbf{v}_1^{(k)}\Delta\beta^{(k)} \tag{D.21} $$

where $\Delta\alpha, \Delta\beta$ denote the rotations around two orthonormal vectors, ${}^t\mathbf{v}_1$ and ${}^t\mathbf{v}_2$ respectively (see Figure D.1), defined by

$$ {}^t\mathbf{v}_1 = \frac{\mathbf{e}_y \times {}^t\mathbf{v}_3}{||\mathbf{e}_y \times {}^t\mathbf{v}_3||}, \qquad {}^t\mathbf{v}_2 = {}^t\mathbf{v}_3 \times {}^t\mathbf{v}_1 \tag{D.22} $$

i.e. ${}^t\mathbf{v}_1$ corresponds to the projection of the global x-axis onto the current shell surface.

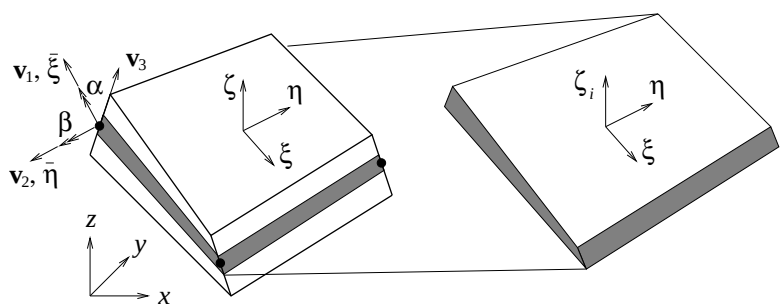

Figure D.1: Coordinate systems of laminate.

The lamina out-of-plane coordinate, ζ_i, is mapped to the laminate coordinate, ζ, through

$$ \zeta = -1 + \frac{1}{h}(-h_i(1-\zeta_i) + 2\sum_{j=1}^{i} h_i) \tag{D.23} $$

in which h is the total thickness of the laminate. In Figure D.2, the two different parent domains in the thickness direction is shown.

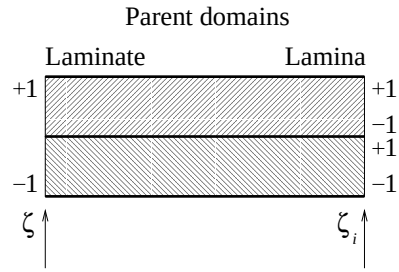

Figure D.2: Parent domains of laminate.

Element matrices

To avoid shear locking an auxiliar interpolation of the covariant transverse shear strain increments is employed according to

$$\begin{aligned}\Delta\tilde{E}_{13} &= N_A\Delta\tilde{E}^A_{13} + N_B\Delta\tilde{E}^B_{13} = \frac{1}{2}(1-\eta)\Delta\tilde{E}^A_{13} + \frac{1}{2}(1+\eta)\Delta\tilde{E}^B_{13}\\ \Delta\tilde{E}_{23} &= N_C\Delta\tilde{E}^C_{23} + N_D\Delta\tilde{E}^D_{23} = \frac{1}{2}(1-\xi)\Delta\tilde{E}^C_{23} + \frac{1}{2}(1+\xi)\Delta\tilde{E}^D_{23}\end{aligned} \tag{D.24}$$

where the superscripts A to D denote evaluation of increments in sampling points located equivalent with

$$\begin{aligned}A:&\ \{\xi,\eta,\zeta\} = \{0,-1,0\}\\ B:&\ \{\xi,\eta,\zeta\} = \{0,1,0\}\\ C:&\ \{\xi,\eta,\zeta\} = \{-1,0,0\}\\ D:&\ \{\xi,\eta,\zeta\} = \{1,0,0\}\end{aligned} \tag{D.25}$$

Considering the symmetry of $\mathbb{C}$ and introducing covariant interpolation matrices the element version of (D.14) can be written as

$$\begin{aligned}&\int_{\Omega^e_0}\delta\mathbf{a}^T\tilde{\mathbf{B}}^T_L\mathbf{A}^T\mathbf{D}\mathbf{A}\tilde{\mathbf{B}}_L\Delta\mathbf{a}\,\mathrm{d}V + \int_{\Omega^e_0}\delta\mathbf{a}^T\,{}^a\tilde{\mathbf{B}}^T_{NL}\mathbf{H}^T\hat{\mathbf{S}}_a\mathbf{H}\,{}^a\tilde{\mathbf{B}}_{NL}\Delta\mathbf{a}\,\mathrm{d}V +\\ &\int_{\Omega^e_0}\delta\mathbf{a}^T\,{}^b\tilde{\mathbf{B}}^T_{NL}\mathbf{H}^T\hat{\mathbf{S}}_b\mathbf{H}\,{}^b\tilde{\mathbf{B}}_{NL}\Delta\mathbf{a}\,\mathrm{d}V + \int_{\Omega^e_0}\delta\mathbf{a}^T\,{}^c\tilde{\mathbf{B}}^T_{NL}\mathbf{H}^T\hat{\mathbf{S}}_c\mathbf{H}\,{}^c\tilde{\mathbf{B}}_{NL}\Delta\mathbf{a}\,\mathrm{d}V =\\ &\int_{\partial\Omega^e_0}\delta\mathbf{a}^T\mathbf{N}^T\mathbf{T}\,\mathrm{d}S + \int_{\Omega^e_0}\delta\mathbf{a}^T\mathbf{N}^T\mathbf{B}\,\mathrm{d}V - \int_{\Omega^e_0}\delta\mathbf{a}^T\tilde{\mathbf{B}}^T_L\mathbf{A}^T\bar{\mathbf{S}}\,\mathrm{d}V\end{aligned} \tag{D.26}$$

where $\mathbf{D}$ is the six by six constitutive matrix in local shell Cartesian basis with zero elements in the third row and column, respectively, and $\tilde{\mathbf{B}}_L$, ${}^a\tilde{\mathbf{B}}_{NL}$, ${}^b\tilde{\mathbf{B}}_{NL}$ and ${}^c\tilde{\mathbf{B}}_{NL}$ are

the covariant interpolation matrices

$$\tilde{\mathbf{B}}_L = \begin{bmatrix} \frac{\partial N_k}{\partial \xi}\mathbf{g}_1^T & \frac{\zeta}{2}h_k\frac{\partial N_k}{\partial \xi}\mathbf{g}_1^T[-\mathbf{v}_2^{(k)} \;\; \mathbf{v}_1^{(k)}] \\ \frac{\partial N_k}{\partial \eta}\mathbf{g}_2^T & \frac{\zeta}{2}h_k\frac{\partial N_k}{\partial \eta}\mathbf{g}_2^T[-\mathbf{v}_2^{(k)} \;\; \mathbf{v}_1^{(k)}] \\ \mathbf{0}_{1,3} & \mathbf{0}_{1,2} \\ \frac{\partial N_k}{\partial \eta}\mathbf{g}_1^T + \frac{\partial N_k}{\partial \xi}\mathbf{g}_2^T & \frac{\zeta}{2}h_k\left(\frac{\partial N_k}{\partial \eta}\mathbf{g}_1^T + \frac{\partial N_k}{\partial \xi}\mathbf{g}_2^T\right)[-\mathbf{v}_2^{(k)} \;\; \mathbf{v}_1^{(k)}] \\ N_A\frac{\partial N_k}{\partial \xi}\Big|_A{}^A\mathbf{g}_3^T + N_B\frac{\partial N_k}{\partial \xi}\Big|_B{}^B\mathbf{g}_3^T & \frac{1}{2}h_k\left(N_AN_k^{AA}\mathbf{g}_1^T + N_BN_k^{BB}\mathbf{g}_1^T\right)[-\mathbf{v}_2^{(k)} \;\; \mathbf{v}_1^{(k)}] \\ N_C\frac{\partial N_k}{\partial \eta}\Big|_C{}^C\mathbf{g}_3^T + N_D\frac{\partial N_k}{\partial \eta}\Big|_D{}^D\mathbf{g}_3^T & \frac{1}{2}h_k\left(N_CN_k^{CC}\mathbf{g}_2^T + N_DN_k^{DD}\mathbf{g}_2^T\right)[-\mathbf{v}_2^{(k)} \;\; \mathbf{v}_1^{(k)}] \end{bmatrix}$$

$${}^a\tilde{\mathbf{B}}_{NL} = \begin{bmatrix} \frac{\partial N_k}{\partial \xi}\mathbf{I}_{3,3} & \frac{\zeta}{2}h_k\frac{\partial N_k}{\partial \xi}[-\mathbf{v}_2^{(k)} \;\; \mathbf{v}_1^{(k)}] \\ \frac{\partial N_k}{\partial \eta}\mathbf{I}_{3,3} & \frac{\zeta}{2}h_k\frac{\partial N_k}{\partial \eta}[-\mathbf{v}_2^{(k)} \;\; \mathbf{v}_1^{(k)}] \\ \mathbf{0}_{3,3} & \frac{1}{2}h_kN_k[-\mathbf{v}_2^{(k)} \;\; \mathbf{v}_1^{(k)}] \end{bmatrix} \tag{D.27}$$

$${}^b\tilde{\mathbf{B}}_{NL} = \begin{bmatrix} \left(N_A\frac{\partial N_k}{\partial \xi}\Big|_A + N_B\frac{\partial N_k}{\partial \xi}\Big|_B\right)\mathbf{I}_{3,3} & \frac{\zeta}{2}h_k\left(N_A\frac{\partial N_k}{\partial \xi}\Big|_A + N_B\frac{\partial N_k}{\partial \xi}\Big|_B\right)[-\mathbf{v}_2^{(k)} \;\; \mathbf{v}_1^{(k)}] \\ \left(N_A\frac{\partial N_k}{\partial \eta}\Big|_A + N_B\frac{\partial N_k}{\partial \eta}\Big|_B\right)\mathbf{I}_{3,3} & \frac{\zeta}{2}h_k\left(N_A\frac{\partial N_k}{\partial \eta}\Big|_A + N_B\frac{\partial N_k}{\partial \eta}\Big|_B\right)[-\mathbf{v}_2^{(k)} \;\; \mathbf{v}_1^{(k)}] \\ \mathbf{0}_{3,3} & \frac{1}{2}h_k(N_AN_k^A + N_BN_k^B)[-\mathbf{v}_2^{(k)} \;\; \mathbf{v}_1^{(k)}] \end{bmatrix}$$

$${}^c\tilde{\mathbf{B}}_{NL} = \begin{bmatrix} \left(N_C\frac{\partial N_k}{\partial \xi}\Big|_C + N_D\frac{\partial N_k}{\partial \xi}\Big|_D\right)\mathbf{I}_{3,3} & \frac{\zeta}{2}h_k\left(N_C\frac{\partial N_k}{\partial \xi}\Big|_C + N_D\frac{\partial N_k}{\partial \xi}\Big|_D\right)[-\mathbf{v}_2^{(k)} \;\; \mathbf{v}_1^{(k)}] \\ \left(N_C\frac{\partial N_k}{\partial \eta}\Big|_C + N_D\frac{\partial N_k}{\partial \eta}\Big|_D\right)\mathbf{I}_{3,3} & \frac{\zeta}{2}h_k\left(N_C\frac{\partial N_k}{\partial \eta}\Big|_C + N_D\frac{\partial N_k}{\partial \eta}\Big|_D\right)[-\mathbf{v}_2^{(k)} \;\; \mathbf{v}_1^{(k)}] \\ \mathbf{0}_{3,3} & \frac{1}{2}h_k(N_CN_k^C + N_DN_k^D)[-\mathbf{v}_2^{(k)} \;\; \mathbf{v}_1^{(k)}] \end{bmatrix}$$

where N_A, N_B, N_C, N_D are the auxiliar shape functions pertinent to the transverse shear sampling points A, B, C, D, evaluated at gauss points. Superscripts of A, B, C, D means evaluation in sampling points. $\hat{\mathbf{S}}_a$, $\hat{\mathbf{S}}_b$ and $\hat{\mathbf{S}}_c$ are the matrices

$$\hat{\mathbf{S}}_a = \begin{bmatrix} S_{11}\mathbf{I}_{3,3} & S_{12}\mathbf{I}_{3,3} & \mathbf{0}_{3,3} \\ & S_{22}\mathbf{I}_{3,3} & \mathbf{0}_{3,3} \\ \text{sym} & & \mathbf{0}_{3,3} \end{bmatrix}$$

$$\hat{\mathbf{S}}_b = \begin{bmatrix} \mathbf{0}_{3,3} & \mathbf{0}_{3,3} & S_{13}\mathbf{I}_{3,3} \\ & \mathbf{0}_{3,3} & \mathbf{0}_{3,3} \\ \text{sym} & & \mathbf{0}_{3,3} \end{bmatrix}$$

$$\hat{\mathbf{S}}_c = \begin{bmatrix} \mathbf{0}_{3,3} & \mathbf{0}_{3,3} & \mathbf{0}_{3,3} \\ & \mathbf{0}_{3,3} & S_{23}\mathbf{I}_{3,3} \\ \text{sym} & & \mathbf{0}_{3,3} \end{bmatrix} \tag{D.28}$$

and $\bar{\mathbf{S}}$ is the vector

$$\bar{\mathbf{S}} = \begin{bmatrix} S_{11} & S_{22} & S_{12} & S_{13} & S_{23} \end{bmatrix}^T \tag{D.29}$$

The matrix $\mathbf{A}$ transforms the linear components of the covariant strain increment to a

local Cartesian shell coordinate system

$$\mathbf{A} = \begin{bmatrix} l_1^2 & m_1^2 & n_1^2 & l_1 m_1 & l_1 n_1 & m_1 n_1 \\ l_2^2 & m_2^2 & n_2^2 & l_2 m_2 & l_2 n_2 & m_2 n_2 \\ l_3^2 & m_3^2 & n_3^2 & l_3 m_3 & l_3 n_3 & m_3 n_3 \\ 2l_1 l_2 & 2m_1 m_2 & 2n_1 n_2 & l_1 m_2 + l_2 m_1 & l_1 n_2 + l_2 n_1 & m_1 n_2 + m_2 n_1 \\ 2l_1 l_3 & 2m_1 m_3 & 2n_1 n_3 & l_1 m_3 + l_3 m_1 & l_1 n_3 + l_3 n_1 & m_1 n_3 + m_3 n_1 \\ 2l_2 l_3 & 2m_2 m_3 & 2n_2 n_3 & l_2 m_3 + l_3 m_2 & l_2 n_3 + l_3 n_2 & m_2 n_3 + m_3 n_2 \end{bmatrix} \tag{D.30}$$

where

$$\begin{aligned} l_1 &= (\mathbf{G}^1)^{T\,0}\mathbf{v}_1 \qquad & m_1 &= (\mathbf{G}^2)^{T\,0}\mathbf{v}_1 \qquad & n_1 &= (\mathbf{G}^3)^{T\,0}\mathbf{v}_1 \\ l_2 &= (\mathbf{G}^1)^{T\,0}\mathbf{v}_2 \qquad & m_2 &= (\mathbf{G}^2)^{T\,0}\mathbf{v}_2 \qquad & n_2 &= (\mathbf{G}^3)^{T\,0}\mathbf{v}_2 \\ l_3 &= (\mathbf{G}^1)^{T\,0}\mathbf{v}_3 \qquad & m_3 &= (\mathbf{G}^2)^{T\,0}\mathbf{v}_3 \qquad & n_3 &= (\mathbf{G}^3)^{T\,0}\mathbf{v}_3 \end{aligned} \tag{D.31}$$

The matrix $\mathbf{H}$ transforms the nonlinear components of the covariant strain increment to a local Cartesian shell coordinate system

$$\mathbf{H} = \begin{bmatrix} l_1 & 0 & 0 & m_1 & 0 & 0 & n_1 & 0 & 0 \\ 0 & l_1 & 0 & 0 & m_1 & 0 & 0 & n_1 & 0 \\ 0 & 0 & l_1 & 0 & 0 & m_1 & 0 & 0 & n_1 \\ l_2 & 0 & 0 & m_2 & 0 & 0 & n_2 & 0 & 0 \\ 0 & l_2 & 0 & 0 & m_2 & 0 & 0 & n_2 & 0 \\ 0 & 0 & l_2 & 0 & 0 & m_2 & 0 & 0 & n_2 \\ l_3 & 0 & 0 & m_3 & 0 & 0 & n_3 & 0 & 0 \\ 0 & l_3 & 0 & 0 & m_3 & 0 & 0 & n_3 & 0 \\ 0 & 0 & l_3 & 0 & 0 & m_3 & 0 & 0 & n_3 \end{bmatrix} \tag{D.32}$$

In (D.26) $\mathbf{N}$ is a matrix containing the Lagrange interpolation functions. The element integral equation (D.26) can be written as a summation over the individual layers of the laminate

$$\begin{aligned} \sum_{j=1}^{n} \Bigg(& \int_{{}_j\Omega_0^e} \delta\mathbf{a}^T {}_j\tilde{\mathbf{B}}_L^T \mathbf{A}^T \mathbf{D}_j \, \mathbf{A}_j \tilde{\mathbf{B}}_L \Delta\mathbf{a} \, \mathrm{d}V + \int_{{}_j\Omega_0^e} \delta\mathbf{a}^T {}_j^a\tilde{\mathbf{B}}_{NL}^T \mathbf{H}^T {}_j\hat{\mathbf{S}}_a \mathbf{H} {}_j^a\tilde{\mathbf{B}}_{NL} \Delta\mathbf{a} \, \mathrm{d}V + \\ & \int_{{}_j\Omega_0^e} \delta\mathbf{a}^T {}_j^b\tilde{\mathbf{B}}_{NL}^T \mathbf{H}^T {}_j\hat{\mathbf{S}}_b \mathbf{H} {}_j^b\tilde{\mathbf{B}}_{NL} \Delta\mathbf{a} \, \mathrm{d}V + \int_{{}_j\Omega_0^e} \delta\mathbf{a}^T {}_j^c\tilde{\mathbf{B}}_{NL}^T \mathbf{H}^T {}_j\hat{\mathbf{S}}_c \mathbf{H} {}_j^c\tilde{\mathbf{B}}_{NL} \Delta\mathbf{a} \, \mathrm{d}V = \\ & \int_{\partial_j\Omega_0^e} \delta\mathbf{a}^T \mathbf{N}^T \mathbf{T} \, \mathrm{d}S + \int_{{}_j\Omega_0^e} \delta\mathbf{a}^T \mathbf{N}^T \mathbf{B} \, \mathrm{d}V - \int_{{}_j\Omega_0^e} \delta\mathbf{a}_j^T \tilde{\mathbf{B}}_L^T \mathbf{A}^T \bar{\mathbf{S}} \, \mathrm{d}V \Bigg) \end{aligned} \tag{D.33}$$

where n is the number of layers. In (D.33) both ζ and the corresponding integration weights must be determined from (D.23), given a local coordinate ζ_j.

Reduction of transverse shear stiffnesses

The simple kinematic relation for the laminate deformation given by (D.20) is a substantial restriction of the true deformation that will develop through the thicknesses of the different

layers. In particular, the transverse shear strains will differ substantially from layer to layer, especially if a laminate with largely varying transverse shear stiffnesses is analyzed. Therefore, a prerequisite for further use of (D.20) implies a correction of the transverse shear stiffness. This is accomplished by determining the shear strain obtained from an equilibrium consideration. The shear strain is then matched to the strain energy obtained from the deformation given by (D.20). In the following expressions the strains are assumed to be small. Also, for notational simplicity, the indices x_1, x_2 and x_3 are replaced by x, y and z.

Consider the following equilibrium condition of a three dimensional body

$$\frac{\partial \sigma_{xx}}{\partial x} + \frac{\partial \sigma_{xy}}{\partial y} + \frac{\partial \sigma_{xz}}{\partial z} = 0 \tag{D.34}$$

If only unidirectional bending deformation is considered, the transverse shear stress is given by

$$\sigma_{xz} = -\int_{z_1}^{z} \frac{\partial \sigma_{xx}}{\partial x} dx \tag{D.35}$$

where z_1 is the coordinate of the bottom face of the laminate. In the z-coordinate system, the origin is located at the neutral layer of the laminate. The coordinate of the neutral layer of a laminate can be found by considering a coordinate system, $\hat{z}$, aligned at the bottom face, i.e. the origin is located at the bottom face. In this case, the following holds for the coordinate of the neutral layer, $\hat{z}_{nl}$,

$$\int_{\hat{z}_1}^{\hat{z}_{n+1}} \hat{z} E_{xx}(\hat{z}) d\hat{z} = \int_{\hat{z}_1}^{\hat{z}_{n+1}} \hat{z}_{nl} E_{xx}(\hat{z}) d\hat{z} \tag{D.36}$$

in which E_{xx} is the modulus of elasticity. This yields

$$\hat{z}_{nl} = \frac{\sum_{i=1}^{n} E_{xx}^{(i)} (\hat{z}_{i+1}^2 - \hat{z}_i^2)}{2 \sum_{i=1}^{n} E_{xx}^{(i)} (\hat{z}_{i+1} - \hat{z}_i)} \tag{D.37}$$

Assuming a normal strain of the form

$$\varepsilon_{xx}(x, z) = z f(x) \tag{D.38}$$

will result in the corresponding normal stress

$$\sigma_{xx}(x, z) = E_{xx}(z) z f(x) \tag{D.39}$$

and the sectional moment can be written

$$M_{xx}(x) = f(x) \int_{z_1}^{z_{n+1}} z^2 E_{xx}(z) dz \tag{D.40}$$

Combining (D.35), (D.38) and (D.40) yields

$$\sigma_{xz} = -\frac{\partial M_{xx}(x)}{\partial x} \int_{z_1}^{z} \frac{z E_{xx}(z)}{\int_{z_1}^{z_{n+1}} z^2 E_{xx}(z) dz} dz \tag{D.41}$$

where $\partial M_{xx}(x)/\partial x = V_{xz}$, i.e. the sectional shear force.

Consider next the shear strain energy of the section. In an infinitesimal strip of height h and width dx the strain energy intensity, $\mathcal{W}_1$, can be written

$$\mathcal{W}_1 = \frac{dx}{2}\int_{z_1}^{z_{n+1}} \sigma_{xz}(z)\gamma_{xz}(z)dz \tag{D.42}$$

Using (D.41), (D.42) can be rewritten

$$\mathcal{W}_1 = \left(\frac{V_{xz}}{\int_{z_1}^{z_{z+1}} z^2 E_{xx}(z)dz}\right)^2 \frac{dx}{2}\int_{z_1}^{z_{z+1}} \frac{1}{G_{xz}(z)}\left(\int_{z_1}^{z} zE_{xx}(z)dz\right)^2 dz \tag{D.43}$$

Next, the strain energy intensity, $\mathcal{W}_2$, in a homogeneous section with constant shear strain can be written

$$\mathcal{W}_2 = \frac{dx}{2}\int_{z_1}^{z_{n+1}} \sigma_{xz}\gamma_{xz}dz \tag{D.44}$$

Furthermore, equal shear strain in both sections leads to

$$\mathcal{W}_1 - \mathcal{W}_2 = 0 \tag{D.45}$$

Finally, by substituting (D.42) for (D.41) and using (D.45), the equivalent shear stiffness of the section, G_{xe}, can be resolved

$$\begin{aligned}
G_{xe} &= \frac{4}{9h}\left[\sum_{j=1}^{n} E_{xx}^{(j)}(z_{j+1}^3 - z_j^3)\right]^2 \frac{1}{F} \\
F &= \sum_{j=1}^{n} \frac{1}{G_{xz}^{(j)}}\Big[\left(H^2 - 2HE_{xx}^{(j)}z_j^2 + (E_{xx}^{(j)}z_j^2)^2\right)(z_{j+1} - z_j) + \\
&\quad \frac{2}{3}\left(H - (E_{xx}^{(j)}z_j)^2\right)(z_{j+1}^3 - z_j^3) + \frac{1}{5}(E_{xx}^{(j)})^2(z_{j+1}^5 - z_j^5)\Big] \\
H &= \sum_{i=1}^{j-1} E_{xx}^{(i)}(z_{i+1}^2 - z_i^2)
\end{aligned} \tag{D.46}$$

The corresponding equivalent transverse shear stiffness G_{ye} is obtained in a similar manner.

Numerical evaluation

In a number of examples the numerical performance of the implemented element is verified. In the first five sections a linear version of the element is used, i.e. the deformations are assumed to be small. In the two final sections the deflections, rotations and deformations are allowed to be arbitrarily large.

Thickness locking test

In the first example the behaviour of the element in the thin plate limit is analyzed. The out of plane displacement, w, at the center of a uniformly loaded, p, and simply supported square plate is calculated for an increasing side length to thickness ratio, a/h. One quarter of the plate is modelled with 8×8 elements. The material is isotropic and homogeneous, with modulus of elasticity E. The solid line in Figure D.3 is a 29 term series solution according to Reddy's higher order transverse shear plate theory, see [4]. Evidently, the element is free of locking.

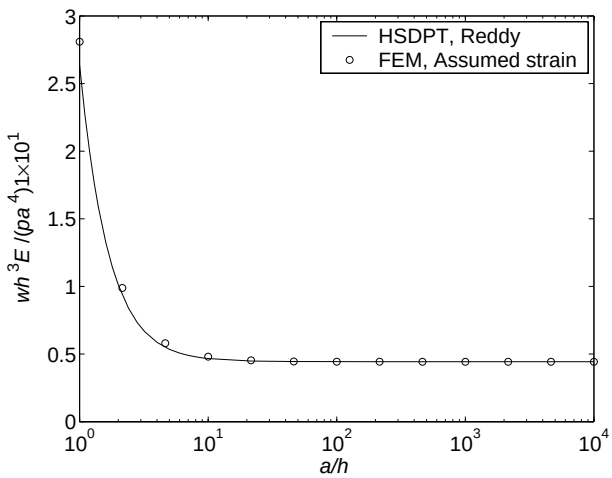

Figure D.3: Normalized deflection versus length to thickness ratio.

Patch test

Here a distorted mesh is used, see Figure D.4. An isotropic and homogeneous material with properties $E = 1 \times 10^{10}$ MPa and $\nu = 0.3$ is used. The thickness of the plate is 50 mm. All the different type of loads below shall produce a constant state of stress over x and y. The mean stress, strain and maximum absolute deviation over all integration points is presented in the Tables D.1 and D.2.

Membrane deformation

A load of $1{\times}10^6$ N is applied at two adjacent corner nodes (in the case of shear load at three adjacent nodes).

Bending and transverse shear deformation

For the case of bending a moment of -$1{\times}10^4$ Nm is applied at the nodes at locations (1,0) and (1,1). In the transverse shear case a load of $1{\times}10^6$ N is applied in the transverse

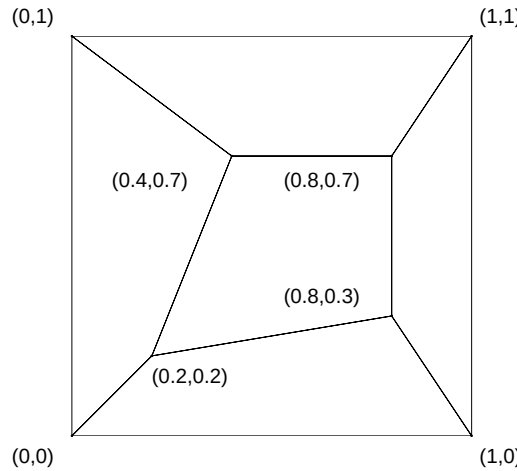

Figure D.4: Distorted mesh used for patch test.

Table D.1: Mean values and maximum absolute deviation at membrane deformation.

		$\sigma_{11}, \varepsilon_{11}$	$\sigma_{22}, \varepsilon_{22}$	τ_{12}, γ_{12}
Uniaxial load in	mean stress [$\times 10^6$Pa]	40	0	0
1:st direction	deviation [$\times 10^{-8}$Pa]	7.45	-	-
	mean strain [$\times 10^{-3}$]	4	-1.2	0
	deviation [$\times 10^{-18}$]	6.07	2.60	-
Uniaxial load in	mean stress [$\times 10^6$Pa]	0	40	0
2:nd direction	deviation [$\times 10^{-8}$Pa]	-	4.47	-
	mean strain [$\times 10^{-3}$]	-1.2	4	0
	deviation [$\times 10^{-18}$]	3.04	5.20	-
Shear load	mean stress [$\times 10^6$Pa]	0	0	40
	deviation [$\times 10^{-8}$Pa]	-	-	8.20
	mean strain [$\times 10^{-3}$]	0	0	10.4
	deviation [$\times 10^{-18}$]	-	-	27.8

direction, at the same locations. Note that the reduced transverse shear modulus results in an increased transverse shear strain compared to the case of membrane shear.

Composite plate test

A 3-layer composite material is analyzed with respect to out of plane deflection in the thick plate limit. A uniform surface pressure is applied in the positive z-direction. The material properties are chosen representative to corrugated board, where the corrugated core is approximated as a homogenized section with equivalent stiffness param-

Table D.2: Mean values and maximum absolute deviation at transverse deformation.

		σ_{11}	σ_{22}	τ_{13}
Bending deformation, lower layer	mean stress [$\times 10^6$Pa]	27.7	0	0
	deviation [$\times 10^{-6}$Pa]	6.76	-	-
	mean strain [$\times 10^{-3}$]	2.77	-0.83	0
	deviation [$\times 10^{-16}$]	5.46	2.35	-
Bending deformation, upper layer	mean stress [$\times 10^6$Pa]	-27.7	0	0
	deviation [$\times 10^{-6}$Pa]	6.77	-	-
	mean strain [$\times 10^{-3}$]	-2.77	0.83	0
	deviation [$\times 10^{-18}$]	5.46	2.34	-
Transverse shear	mean stress [$\times 10^6$Pa]	0	0	40
	deviation [$\times 10^{-8}$Pa]	-	-	3.73
	mean strain [$\times 10^{-3}$]	0	0	12.5
	deviation [$\times 10^{-18}$]	-	-	20.8

eters, see [7]. The stiffness parameters for the facings are E_{xx}=7$\times 10^9$, E_{yy}=3.5$\times 10^9$, G_{xy}=3$\times 10^9$, G_{xz}=G_{yz}=0.045$\times 10^9$ Pa and ν_{xy}=0.2. The stiffness parameters for the core are E_{xx}=0.005$\times 10^9$, E_{yy}=0.2$\times 10^9$, G_{xy}=0.005$\times 10^9$, $G_{xz} = G_{yz}$ =0.0035$\times 10^9$ Pa and ν_{xy}=0.05. The thicknesses of the facings are both chosen as 5% of the total laminate thickness. The circles in Figure D.5 corresponds to reduction of transverse shear modulus based on a complete section strain energy equivalence. The squares corresponds to a simple reduction of each layers transverse shear modulus by a factor 5/6. It should be noted that the reference solution, HSDPT, is likely to be stiffer than the true three dimensional solution. Therefore the FEM solution corresponding to the circles is probably closer to the true solution than the reference solution is.

Transformation test

Rotated composite plate

A single layer composite plate, originally located in the xy-plane, is rotated 90 degrees around the global y-axis, see Figure D.6. This implies that the i:th transformed nodal coordinates, $\mathbf{x}_i^{'} = [x_1^i, x_2^i, x_3^i]^T$, are given by the imposed rotation $\mathbf{x}_i^{'} = \mathbf{R}\mathbf{x}_i$, where $\mathbf{R}$ is given by the permutation matrix

$$\mathbf{R} = \begin{bmatrix} 0 & 0 & 1 \\ 0 & 1 & 0 \\ 1 & 0 & 0 \end{bmatrix} \tag{D.47}$$

With the specified procedure for determining the local Cartesian coordinate axes the local $\bar{\xi}$-axis is oriented parallel to the global z-axis, the local $\bar{\eta}$-axis is oriented parallel to the global y-axis and the local ζ-axis is oriented parallel to the global negative x-axis. The plate is simply supported and loaded with a uniform pressure in the global positive

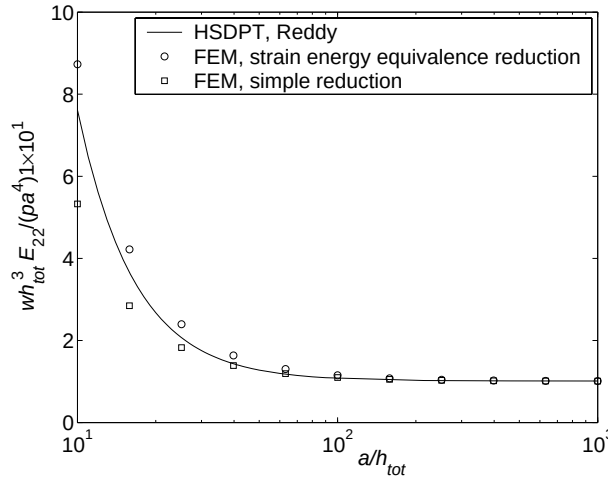

Figure D.5: Response of 3-layer composite for varying length to thickness ratio.

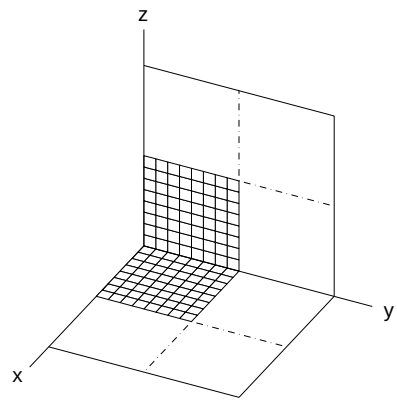

Figure D.6: A plate rotated 90 degrees around the global y-axis.

x-direction. The material properties are orthotropic with the same values as used for the facings of the 3-layer composite plate in the previous example. The nondimensional maximum deflection of the transformed plate, in the global x-direction, and the HSDPT solution is given in Table D.3.

In addition, the stresses in the element exhibiting the largest deflection are calculated. The stresses obtained for the solution of the untransformed plate are the same as the local stresses from the solution of the transformed plate, except that the values are interchanged between the lower and and upper layer of gauss point. This is because in the former case the deflection occurs in the positive direction of the local ζ-axis, while in the latter case the deflection occurs in the negative direction of the local ζ-axis.

Table D.3: Nondimensional maximum deflection of the plate.

	Deflection, $wt^3E_{22}/(pa^4)1 \times 10^2$
Transformed plate	2.868
HSDPT	2.834

Rotated beam

In this example a single layer beam consisting of two elements is rotated 30 degrees around the global x-axis, see Figure D.7. This implies that the i:th transformed nodal coordinates, $\mathbf{x}_i^{'} = [x_1^i, x_2^i, x_3^i]$, are given by the imposed rotation $\mathbf{x}_i^{'} = \mathbf{R}\mathbf{x}_i$, where $\mathbf{R}$ is given by the rotation matrix

$$\mathbf{R} = \begin{bmatrix} 1 & 0 & 0 \\ 0 & \sqrt{3}/2 & -1/2 \\ 0 & 1/2 & \sqrt{3}/2 \end{bmatrix} \tag{D.48}$$

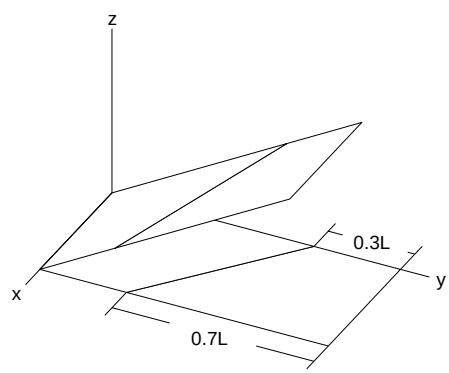

Figure D.7: A beam rotated 30 degrees around the global x-axis.

The material is isotropic with the same properties as used in the patch test. A moment of 1×10^3 Nm is applied to each of the right end nodes. The length, width and thickness of the beam is 2 m, 1 m and 50 mm, respectively. The nodal translations of the transformed beam in the local $\{\bar{\xi}, \bar{\eta}, \zeta\}$-coordinate system, $\mathbf{u}^{'} = [u_{\bar{\xi}}, u_{\bar{\eta}}, u_{\zeta}]^T$, is given by $\mathbf{u}^{'} = \mathbf{R}^T\mathbf{u}$. The local translations $\mathbf{u}^{'}$ and global translations $\mathbf{u}$ at the right end of the beam, together with analytical solution, is given in Table D.4. The local stresses obtained in the rotated beam is identical to the stresses obtained in a beam oriented in the xy-plane.

Table D.4: Translations at the right end of the beam.

[mm]	$u_x, u_{\bar{\xi}}$	$u_y, u_{\bar{\eta}}$	u_z, u_{ζ}
global	0	-19.2	33.3
local	0	0	38.4
analytical	0	0	38.4

Beam of variable thickness

In this example a beam of length L=1 m and width b=0.1 m is analyzed. The thickness h of the beam is given by

$$h(x) = \frac{h_1}{L}(L - x) + \frac{h_2}{L}x \tag{D.49}$$

where h_1=0.05 m and $h_2 = ch_1$ are the thicknesses at the end of the beam. The material properties are E=2.1×10^{11} Pa and ν=0. Adopting the Bernoulli hypothesis for a beam, with one end clamped and the other end subjected to a transversal load (P = 10 kN), the deflection of the beam is easily shown to be

$$w = \left[\frac{6h_2L^4}{(-h_1+h_2)^3(h_1L - h_1x + h_2x)} + \frac{12\ln(h_1L + (-h_1+h_2)x)L^3}{(-h_1+h_2)^3} + \right.$$
$$\left. \frac{6(2\ln(h_1L)h_1 + h_2)L^3}{h_1(h_1^3 - 3h_1^2h_2 + 3h_1h_2^2 - h_2^3)} - \frac{6(2h_1 - h_2)L^2x}{h_1^2(h_1^2 - 2h_1h_2 + h_2^2)} \right] \frac{P}{Eb} \tag{D.50}$$

In Figure D.8 the FEM solution with five elements is compared with the deflection given by (D.50) for different values of c.

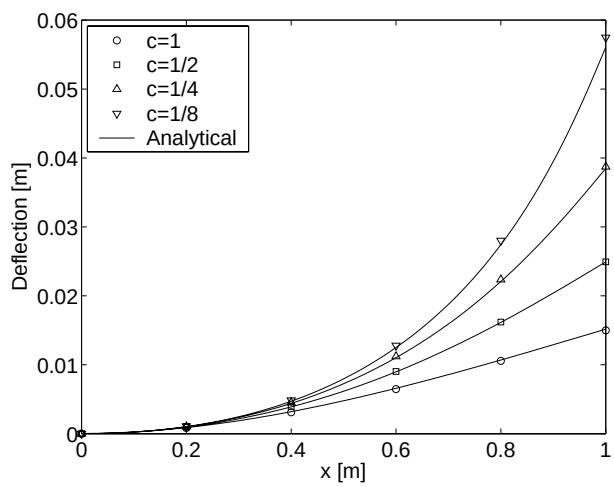

Figure D.8: Deflection of a beam with linearly varying thickness.

Large deflection of beam

A clamped beam undergoing large deflections due to a transversal load is studied. The length of the beam is 10 m which is divided in ten elements. The length to thickness ratio and length to width ratio is 100 and the stiffness properties are E=2.1×10^{11} Pa and ν=0.

By defining ds, which is an infinitesimal beam segment in a deformed configuration, the differential equation and boundary conditions for the beam can be written

$$\frac{d^2\theta}{ds^2} + \frac{P}{EI}\cos\theta = 0, \quad \theta(0) = 0, \quad \left.\frac{d\theta}{ds}\right|_L = 0 \tag{D.51}$$

where P is the current load level at the tip of the beam and θ is the angle between the deformed beam axis and undeformed axis. This second order differential equation can be rewritten as a system of first order equations according to

$$\begin{aligned} \frac{d\theta}{ds} &= \eta, \quad \theta(0) = 0 \\ \frac{d\eta}{ds} &= -\frac{P}{EI}\cos\theta, \quad \eta(L) = 0 \end{aligned} \tag{D.52}$$

which is readily solved numerically. In the deformation corresponding to (D.52) it is assumed that axial stretching and shear deformation are negligible. The solution of (D.52) is compared to the solution obtained by the shell element, see Figure D.9.

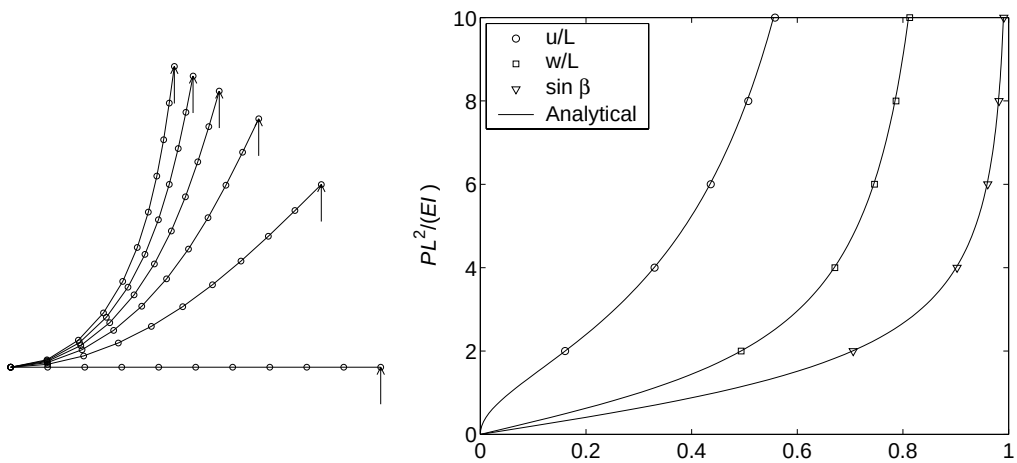

Figure D.9: Large deformation of a transversely loaded beam

Snap through of a shallow spherical shell

I this example the snapping of a shallow spherical shell is analyzed. One quarter of the shell is modelled, see Figure D.10.

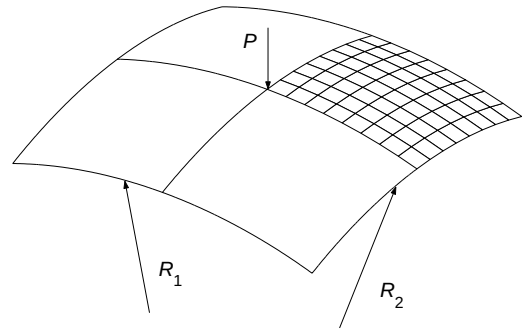

Figure D.10: Initial geometry of the shallow shell.

The value of the two radius parameters are R_1=R_2=2.54 m. Furthermore the thickness of the shell is 99.45 mm and the Euclidean distance between the shell vertices is 1.57 m. The material properties are E=68.95×10^6 Pa and ν=0.3. The response of this type of shell involves a snapping-like deformation at increased load levels. In order to calculate the load deformation path an arc-length time stepping procedure is applied. The arc-length method used here mainly follows the principles developed by Crisfield [5]. In Figure D.11 the load, P, versus transverse center deflection, w_c, is plotted together with the solution presented in [6]. In addition the deformed shape is plotted for the load level P=64.6 kN.

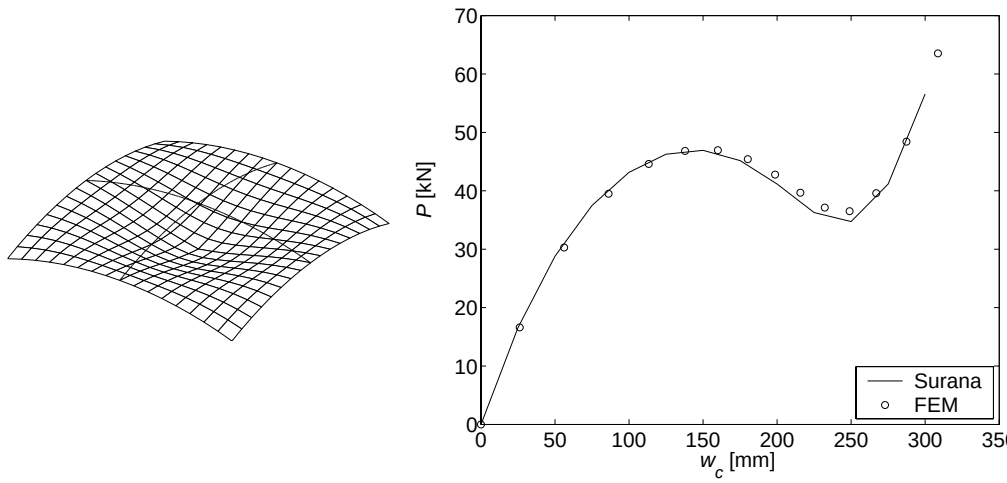

Figure D.11: Final geometry and load path of the shallow shell.

References

[1] Hughes T. J. R., Cohen M., Haroun M., *Reduced and selective integration techniques in the finite element analysis.* Nucl. Engng. Des. **46**, 206-222, 1978.

[2] MacNeal R. H., *Derivation of element stiffness matrices by assumed strain distributions.* Nucl. Engng. Des. **70**, 3-12, 1982.

[3] E. N. Dvorkin and K. J. Bathe, *A continuum mechanics based four-node shell element for general non-linear analysis.* Eng. Comput., Vol 1, (1984)

[4] J. N. Reddy, *A Simple Higher-Order Theory for Laminated Composite Plates*, J. Appl. Mech., 51(4), 745-752, Dec. (1984)

[5] M. A. Crisfield, *A fast incremental/iterative solution procedure that handles "snap-through".* Computers and Structures, Vol 13, pp 55-62 (1980)

[6] K. S. Surana, *Geometrically nonlinear formulation for the curved shell elements.* Int. J. Num. Meth. Eng., **19**, pp 581-615 (1983)

[7] T. M. Nordstrand, *Parametric Study of the Postbuckling Strength of Structural Core Sandwich Panels*, Composite Structures, 30, 441-451, (1995)

Appendix E

SAMPLING OF RELATIVE HUMIDITY ENVIRONMENTS

Introduction

In selected engineering applications the level of relative humidity play an essential role for the strength of materials. A pertinent example is the long term strength of compression loaded corrugated board boxes exposed to natural relative humidity environments. A well established understanding is that the lifetime of corrugated boxes is significantly reduced when subject to fluctuating environments compared to constant environments. Hence, in the modelling of long term strength of boxes, where the influence of moisture content level in the material is considered, a prerequisite is that the variable relative humidity can be defined.

Herein is discerned the characteristics of the random process of relative humidity that is found at the inland part of southern Sweden, in a building that is used for the experimental analysis of reliability and lifetime of corrugated board boxes. It is emphasized that the method applied here for the sampling of relative humidity do not strictly follows the principles of statistical theory for stochastic processes. Instead, the course is to employ functions for relative humidity that is qualitatively extracted from measurement data. Therefore, the statistical correctness of sampled random data in terms of probability density functions associated with the random variable is only checked by means of the interpretation of sampled and measured plots of relative humidities.

Random processes

In a natural fluctuating environment the relative humidity, $\mathcal{R}$, possess the attributes of a random time process. In general, for a statistically regular process the ensemble mean value [1, 2] of relative humidity, $\mu_{\mathcal{R}}$, at a fixed time, τ, is given by

$$\mu_{\mathcal{R}}(\tau) = \lim_{n\to\infty} \frac{1}{n} \sum_{k=1}^{n} \mathcal{R}_k(\tau) \tag{E.1}$$

where summation is performed over an ensemble of sample functions of relative humidity, $\mathcal{R}_k(t)$, evaluated at τ. In a stationary random process $\mu_{\mathcal{R}}$ is constant over time. The autocorrelation function, $c_{\mathcal{R}}$, of relative humidity for a time increment, $\Delta\tau$, is given by

$$c_{\mathcal{R}}(\tau, \tau + \Delta\tau) = \lim_{n\to\infty} \frac{1}{n} \sum_{k=1}^{n} \mathcal{R}_k(\tau)\mathcal{R}_k(\tau + \Delta\tau) \tag{E.2}$$

A less general average of relative humidity can also be defined by using one sample function of relative humidity only. The temporal mean value of relative humidity is given by

$$\mu_{\mathcal{R}}(k) = \lim_{T\to\infty} \frac{1}{T} \int_{-T/2}^{T/2} \mathcal{R}_k(t)dt \tag{E.3}$$

whereas the temporal autocorrelation function is given by

$$c_{\mathcal{R}}(k, \Delta\tau) = \lim_{T\to\infty} \frac{1}{T} \int_{-T/2}^{T/2} \mathcal{R}_k(t)\mathcal{R}_k(t + \Delta\tau)dt \tag{E.4}$$

The statistic information provided by (E.3) and (E.4) comprises the assumption of stationarity, which might not be the case in reality. Even if the use of (E.1) and (E.2) to define a random process for the relative humidity is possible the experimental collection of a sufficiently large number of sample functions might be exceedingly time consuming. Therefore a simplified representation of the random process is desired.

Expectation value functions

In Figure E.1a is plotted the measured relative humidity from an airy untempered building in Asa, Sweden. The measurements of data starts at February 19, 1999, and ends at January 12, 2001. In addition, in Figure E.1b the amplitudes of relative humidity is plotted in the frequency domain. From Figure E.1a it is recognized that the relative

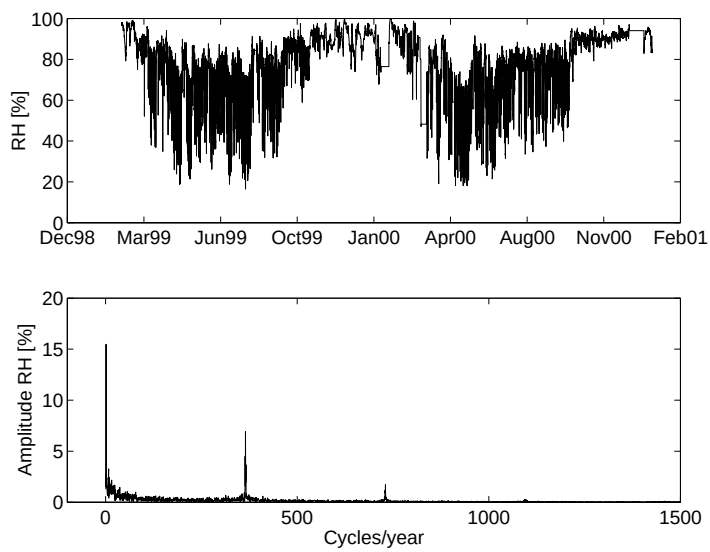

Figure E.1: Measured relative humidity a) in the time domain and b) in the frequency domain.

humidity is not a stationary process if the time average is constructed over intervals of

one year. In general terms, the relative humidity needs not to be stationary even if a very long time interval is used for construction of time average. However, the time history in E.1a is seen to possess some degree of regularity between the two years. In addition, from Figure E.1b the existence of cycles with time periods of one year and one day, respectively, is clear. From this observation it is tempting to assume that the yearly and daily variation can be separated as a sum

$$\mathcal{R}(t) = \mathcal{R}_y(t) + \mathcal{R}_d(t) + C \tag{E.5}$$

where $\mathcal{R}_y(t)$ and $\mathcal{R}_d(t)$ are the yearly and daily variation of relative humidity, respectively, and C is a constant. C can be interpreted as the average relative humidity provided by (E.3). A simple harmonic function for the yearly variation is

$$\mathcal{R}_y(t) = A_y a_y(t) = A_y \cos(2\pi f_y t + \phi_y) \tag{E.6}$$

where A_y is the amplitude of yearly variation and f_y and ϕ_y are fixed values depending on the time scale. A simple harmonic function for the daily variation is

$$\mathcal{R}_d(t) = A_d a_d(t) = A_d \cos(2\pi f_d t + \phi_d) \tag{E.7}$$

where A_d is the amplitude of daily variation and f_d and ϕ_d are fixed values. From Figure E.1a a further important property can be discerned, namely that in the winter the fluctuations are considerably smaller compared to the fluctuations applicable to the summer. This implies that the daily amplitude of variation is a function of time, $A_d = A_d(t)$ with the following restrictions

$$\begin{aligned} \text{On winter :} \quad & A_d = A_{dw} \\ \text{On summer :} \quad & A_d = A_{ds} \end{aligned} \tag{E.8}$$

An explicit form of a weighted amplitude that fulfils the conditions in (E.8) is, for example,

$$A_d(t) = A_{dw}[1 + (1 - a_y(t))\kappa] \tag{E.9}$$

where κ is

$$\kappa = \frac{A_{ds} - A_{dw}}{2A_{dw}} \tag{E.10}$$

Sampling procedure

Using the equations (E.5) to (E.10) a vector containing the time history of expectation values of relative humidity can be determined for a specific time interval. Furthermore, a matrix containing the covariance elements of the time history can be constructed using

$$\text{Cov}[\mathcal{R}(t), \mathcal{R}(t + \Delta t)] = \text{Var}[\mathcal{R}] e^{-|\Delta t/\Delta l|} \tag{E.11}$$

where $\text{Var}[\mathcal{R}]$ is the variance of relative humidity and Δl is a parameter for scaling of the correlation between $\mathcal{R}(t)$ and $\mathcal{R}(t+\Delta t)$. Assuming for example the Gaussian distribution to be valid, the randomized vector of relative humidity can be obtained from a random number generator.

Example of sampling

In order to estimate the performance of the expressions for relative humidity an example of sampling is provided. In the example the following parameters are used

$$\begin{aligned} &f_y = \frac{1}{365}, f_d = 1, \phi_y = 0, \phi_d = -\pi f_d \frac{1}{2} \\ &A_y = 15\%, A_{dw} = 1.5\%, A_{ds} = 18\% \\ &\mathrm{Var}[\mathcal{R}] = 6^2, \Delta l = -3\log(0.5) \end{aligned} \tag{E.12}$$

The value $\phi_d = -\pi f_d/2$ is used in order to produce high relative humidity at 6 hours after midnight, as observed from experiments. The time unit is 24 hours with t=0 at January 1, 1999. In Figures E.2a and E.2b the measured and sampled relative humidity for the time interval April 1, 1999, to Mars 31, 2000, is plotted. It is seen that similar levels of relative humidity is obtained for the sampled data compared to the measured data. In

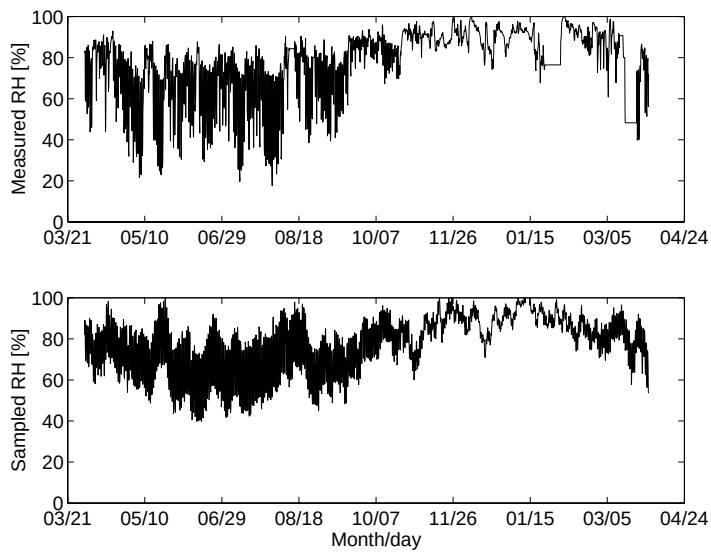

Figure E.2: a) Measured and b) sampled relative humidity from April 1, 1999, to Mars 31, 2000.

Figures E.3a and E.3b a magnification of the measured and sampled data is plotted for July, 1999. In Figures E.4a and E.4b a magnification of the measured and sampled data is plotted for December, 1999. It can be concluded that during summer the sampled data is slightly more regular compared to measured the data. During winter the variations of measured data is somewhat smoother compared to the variations obtained in the sampled data.

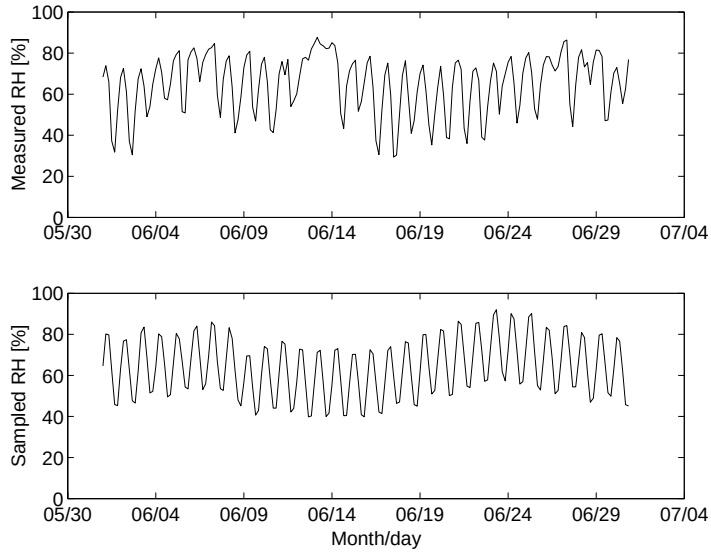

Figure E.3: a) Measured and b) sampled relative humidity from June 1 to June 30, 1999.

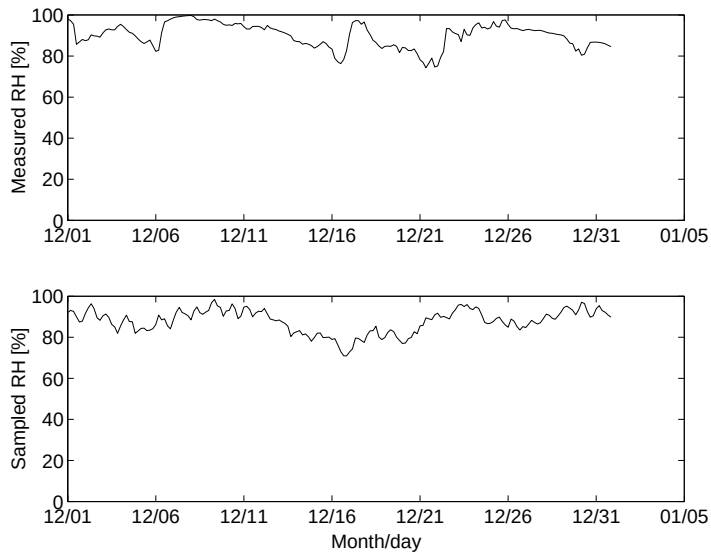

Figure E.4: a) Measured and b) sampled relative humidity from December 1 to December 31, 1999.

Conclusions

A procedure for sampling of random relative humidity levels is described. A representation of the relative humidity is given as the sum of yearly and daily variations. Accessible

parameters are used in the representation of data.

From a sampling example it can be concluded that similar levels of relative humidity is obtained for the sampled data compared to the measured data. During summer the sampled data is slightly more regular compared to measured the data. During winter the variations of measured data is somewhat smoother compared to the variations obtained in the sampled data.

References

[1] Meirovitch, L., (1986) *Elements of Vibration Analysis.* McGraw-Hill, Inc., USA

[2] Vanmarcke, E., (1983) *Random Fields: Analysis and Synthesis.* The MIT Press, Massachusetts, USA.